"Advances in the formulations and accuracy of the method of moments applied to electromagnetics"

Gilles, Thierry

Abstract

The success of electromagnetic analysis and design during the past century would not have been possible without an accurate and complete theory, optimized numerical techniques to solve the complex real-life problems and computers to run the billions of elementary operations required by these techniques. In this work we focused on the scattering by mixed homogeneous linear and isotropic three-dimensional materials solved with the Method of Moments in the harmonic case. The new general methods and expressions that have been derived to this end led incidentally to a new set of theorems forming a generalization of the physical optics approximation. They also allowed to introduce a new numerical formulation able to fully solve metallic sheets. The past two decades have seen the development of many fast methods, acceleration techniques and parallelization strategies, with main objective to solve very to extremely large or complex problems within acceptable time using the available memory. ...

Document type : *Thèse (Dissertation)*

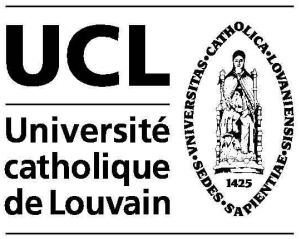

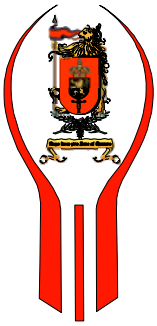

Advances in the Formulations and Accuracy of the Method of Moments Applied to Electromagnetics

PhD thesis

Thierry GILLES

Brussels, September 2011

Contents

List of publications

Conference publications

[C1] T. Gilles, M. Piette, "Controlling the Accuracy of MoM Applied to Complex Shaped Dielectric Objects While Minimizing Computing Time & Memory", *Progress In Electromagnetic Research Symp.*, 22-26 August 2005, Hangzhou, China, Proc. p. 709

[C2] C. Craeye, T. Gilles, "Combination of multipole and macro basis function approaches for the analysis of finite arrays with dielectric elements", *Proc. of the First European Conference on Antennas and Propagation*, Nov. 2006.

[C3] T. Gilles, M. Piette and C. Craeye, "A general treatment for the electromagnetic modelling of composite structures with the method of moments", *Proc. of the First European Conference on Antennas and Propagation*, Nov. 2006.

[C4] T. Gilles, M. Piette, C. Craeye, "A partial analytical solution for the logarithmic singularity associated with MoM applied to dielectrics and its evaluation with polynomial quadratures," *Proc. of 2007 Conf. of the Applied Computational Electromagn. Soc.*, March 20-24, 2007.

[C5] C. Craeye, X. Dardenne, T. Gilles, "Fast method for finite arrays of periodic structures and its relationship with the diakoptic approach," *Proc. of COST_IC0603 meeting*, Bonn, Oct. 25-26, 2007.

[C6] C. Craeye, T. Gilles, X. Dardenne, R. Sarkis, "Fast impedance and pattern evaluation for phased arrays made of complex elements involving finite dielectric material," *Proc. of 2007 Eur. Conf. Antennas Propagat.*, Edinburgh, Nov. 12-16, 2007 (invited).

[C7] T. Gilles, M. Piette, C. Craeye, "An Analytical Solution for the Logarithmic Singularity Associated With MoM Applied to Dielectrics and MFIE and its Optimal Evaluation With Polynomial Quadratures", *Progress In Electromagnetic Research Symp.*, March 2009, Beijing, China

[C8] T. Gilles, M. Piette, C. Craeye, "Electric Current Behavior near Sharp Edges and Corners of Metallic Structures Analyzed with the EFIE and MFIE Comparison with Analytical Well Established Results", *Progress In Electromagnetic Research Symp.*, August 2009, Moskwa, Russia

[C9] T. Gilles, M. Piette, C. Craeye, " Efficient Evaluation of the Logarithmic Singularity on Elongated Triangles With a 16 Nodes Polynomial Quadrature ", *Applied Computational Electromagnetics Symposium*, 26-30 April 2010, Tampere, Finland

[C10] T. Gilles., H. Serizawa, "Scattering by a Perfectly Conducting Square Plate - Comparison between analytical and Numerical Solutions," *ICEAA Symposium*, Sep. 2010, Sydney, Australia

Journal publications

[J1] C. Craeye, T. Gilles, and X. Dardenne, "Efficient full-wave characterisation of arrays of antennas embedded in finite dielectric volumes", *Radio Science*, n°44, February 2009. doi:10.1029/2007RS003806.

[J2] T. Gilles., C. Craeye, M. Piette, "MEFIE Formulation for Arbitrary PEC Sheets," submitted to *IEEE Trans. On Antenna and Propagation*, Mar. 2010.

List of figures

List of Tables

List of abbreviations

ANSI	: American National Standards Institute
CFIE	: Combined Field Integral Equation
CL	: Characteristic Length
CN	: Condition Number
CPU	: Central Processing Unit
E-MFIE	: Electric-Magnetic Field Integral Equation
EFIE	: Electric Field Integral Equation
tEFIE	: Electric Field Integral Equation (tangential component)
nEFIE	: Electric Field Integral Equation (normal component)
MoM	: Method of Moments
MFIE	: Magnetic Field Integral Equation
tMFIE	: Magnetic Field Integral Equation (tangential component)
nMFIE	: Magnetic Field Integral Equation (normal component)
MKS	: Meter Kilogram Second
PEC	: Perfect Electric Conductor
PMC	: Perfect Magnetic Conductor
PMCHWT	: Poggio, Miller, Chang, Harrington, Wu and Tsai
RAM	: Random Access Memory
RWG	: Rao Wilton Glisson (basis function)
TE	: Transvers Electric
TM	: Transverse Magnetic

Acknowledgments

I would like to thank Christophe Craeye for transmitting me his passion and enthousiasm for computational electromagnetics, and for giving me plenty of wise advises that helped me embrace this vast and complex subject with ever growing assurance.

Thanks are also due to U. Jakobus, G. Vandenbosch, D. Van Heule, M. Piette and J.-F. Remacle for their reviews of the manuscript and valuable comments.

I dedicate this book to my beloved wife Khawla and adorable daughter Norah.

Preface

In many engineering fields, the advent of computers has forever changed the type and size of the real-life problems that can be addressed. Burj Khalifa, still the highest skyscraper in the world in 2011, the Bugatti Veyron, world fastest car in 2011 couldn't have been built without an extensive design phase made possible by powerful computers. In electromagnetics as well, numerous modern realizations owe their existence to computer simulation tools : very high frequency passive planar circuits, multiband frequency selective surfaces, metamaterials, corrugated horn antennas optimized through genetic algorithm, just to name a few.

Since the 18th century, various numerical techniques have been developed by many generations of mathematicians and physicists to solve the vast majority of problems for which no analytical solution could ever be found. All those numerical methods had in common that they require a tremendous amount of operations and calculus. Consequently, their practical use remained very limited as long as humans had to do all the work. When the computing power and speed became available in the second half of the 20th century, the theoretical foundations and algorithms were ready, and the millions of repetitive elementary operations necessary to find a good approximation to complex problems had found the perfect machine to perform them.

Since 1965 Moore's law predicts that the computing resources will double every two years, conditioned by the technological capacity of the industry to further miniaturise transistors. But engineers and scientists are always one step ahead with new challenges that exceed the possibilities of their decennia. This situation has stimulated the development of many fast methods, acceleration techniques and parallelization strategies, with main objective to solve very to extremely large or complex problems within acceptable time using the available memory.

In this never ending quest for more and faster, the accuracy of the final solution has received less attention from the electromagnetic community, whereas in essence every numerical method yields an approximate result. To contribute to fill this gap, we made the choice in this book to focus on the quality (accuracy) and less on the price to pay for it (computing time and memory). Aside *accuracy*, another keyword will form the thread of the six upcoming chapters : *generality*. To meet the two objectives of accuracy and generality, high efficiency quadratures have been selected for their ease of implementation in a general code and analyzed in great detail.

In electromagnetics, two independent integral equations can be established from Maxwell's equations. In the Method of Moments, the numerical technique analyzed in this book, the equation based on the electric field is by far the most popular and the most widely used. The other one, based on the magnetic field, is barely considered because it would be less accurate, harder to implement and unsuitable for a large an important family of objects, the metallic sheets. In

electromagnetics, where duality between electric and magnetic magnitudes is a well established principle, this unequal treatment between both approaches incited us to investigate in details the differences between the electric and magnetic formulations. Restoring duality would have been a purist motivation, were it the only one. In fact, except in the case of sheets, both integral equations are most often used side by side, either to analyze dielectric parts, or to eliminate spurious numerical resonances in volumic metallic parts. In this book, one of the objectives was also to establish a general formulation able to solve any combination of geometries (volumes or sheets) and homogeneous linear and isotropic materials (dielectric and perfect conductors). Therefore, both the electric and magnetic formulations had to receive equal attention and be optimized to deliver a similar accuracy, if possible.

In chapter One, the electromagnetic theory relevant to the Method of Moments is reviewed and new formulations are established in their most general form, then cast into a canonical form.

In chapter Two, the Method of Moments is introduced in a practical way. In particular the properties, advantages and limitations of basis functions are reviewed with a critical eye and new light is put on the testing functions.

In chapter Three, the Method of Moments is particularized to the choices made in this book and generalized to any combination of geometries and materials. The general solving scheme that is being proposed fails in some cases with perfectly conducting sheets.

In chapter Four, a novel formulation is established to fully solve perfectly conducting sheets after thorough inspection of the singularities of the electric and magnetic integral equations in this particular case.

In chapter Five, the numerical issues inherent to the Method of Moments are reviewed, then the errors due to numerical integrations with high efficiency polynomial quadratures are analyzed, especially for the singular integrals that appear to play a critical part in the overall accuracy.

To support and illustrate the concepts developed in Part I, a serie of examples has been analyzed in great details, forming Part II.

Part I

1 Electromagnetics

The success of electromagnetic analysis and design during the past century would not have been possible without an accurate and complete theory. This chapter is devoted to exact expressions, formulations and theorems that will form the basis of the Method of Moments, the numerical approximation technique introduced and applied in the subsequent chapters to solve the scattering by three-dimensional linear isotropic and homogeneous bodies. Basic and advanced concepts are reviewed, such as the harmonic Maxwell's equations, the boundary conditions and the Stratton-Chu integral equations. New expressions are also established and presented at the very end of the chapter under a canonical form. They generalize the existing ones in a full vector form, firstly for arbitrary sheets and then for any combination of materials. In the demonstrations, the singular behavior of electromagnetic fields on sharp edges and tips has neither been eluded nor treated in a semi-empirical way, but accounted for very carefully.

This quest for the most general expressions has produced three original results. Firstly an original demonstration that dielectric sheets are transparent to electromagnetic waves. Secondly the discovery of a new set of theorems related to the physical optics approximation. Thirdly and finally the derivation of a novel formulation based on the normal component of the electric and magnetic field integral equations.

1.1 Maxwell's equations

The source of an electromagnetic field is a distribution of electric charge and current densities.

Since we are concerned only with its macroscopic effects we can assume this distribution to be continuous rather than discrete and specified as a function of time and space by the volumic density of charge $\rho(x,y,z,t)$ and the vector current density $\bar{J}(x,y,z,t)$. A brief and interesting discussion about this continuity assumption can be found in [1, *p2*].

If one assumes that an electric current of volumic density $\bar{J}(x,y,z,t)$ is a flow of signed charges of volumic density $\rho(x,y,z,t)$ and that these charges cannot be created nor destroyed, the two quantities $\bar{J}$ and ρ are linked by the following relationship :

$$\nabla \cdot \bar{J} = -\frac{\partial \rho}{\partial t} \tag{1}$$

This equation is often referred to as the *equation of continuity*, because of the assumption made that charges cannot be created or destroyed.

With Maxwell, we will postulate that at every *ordinary point* in space the current density $\bar{J}$ and charge density ρ generates an electromagnetic field that can be

described by the four vectors $\bar{E}$, $\bar{H}$, $\bar{D}$ and $\bar{B}$ subject to the well known Maxwell's equations :

$$\bar{\nabla} \times \bar{E} = -\frac{\partial \bar{B}}{\partial t} \tag{2}$$

$$\bar{\nabla} \times \bar{H} - \frac{\partial \bar{D}}{\partial t} = \bar{J} \tag{3}$$

By an *ordinary point* is meant a point in whose neighbourhood the physical properties of the medium are continuous. At such a point the field vectors and their first derivatives are continuous too.

We cannot determine these four vectors with the two equations (2) and (3) only. Therefore we assume a relationship between the displacement vector $\bar{D}$ and the electric field $\bar{E}$, and also between the magnetic flux density $\bar{B}$ and the magnetic field $\bar{H}$:

$$\bar{D} = \bar{D}(\bar{E}) \tag{4}$$

$$\bar{B} = \bar{B}(\bar{H}) \tag{5}$$

With (6) we also split the total electric current density $\bar{J}$ into a forced part $\bar{J}_{source}$, imposed by a source and maintained independently from the electric field $\bar{E}$ and the magnetic field $\bar{H}$ it creates, and an induced part $\bar{J}(\bar{E})$, due to the action of $\bar{E}$ on the electric charges in the matter.

$$\bar{J} = \bar{J}_{source} + \bar{J}(\bar{E}) \tag{6}$$

The relationships (4), (5) and (6) depend on the matter properties only. It is worth mentioning here already that there are no (known) magnetic charge and current densities.

Equations (4) to (6) prove to be valid in a very wide range of practical situations. Here are the two most common ones :

In vacuum :

$$\begin{aligned} \bar{D} &= \varepsilon_0 \bar{E} \\ \bar{B} &= \mu_0 \bar{H} \\ \bar{J} &= \bar{0} \end{aligned} \tag{7}$$

The values and the dimensions of the constants ε_0 and μ_0 depend on the system of units adopted. In the MKS system, where the speed of light c = 299 792 458 m/s, the following choice has been made :

$$\begin{aligned} \mu_0 &= 4\pi .10^{-7} && \left[Henry/meter\right] \\ \varepsilon_0 &= \frac{1}{\mu_0 c^2} = 8{,}85418782 .10^{-12} && \left[Farad/meter\right] \end{aligned} \tag{8}$$

In a linear, homogeneous, isotropic, conductive and non dispersive material :

$$\begin{aligned} \overline{D} &= \varepsilon \overline{E} \\ \overline{B} &= \mu \overline{H} \\ \overline{J} &= \overline{J}_{source} + \sigma \overline{E} \end{aligned} \tag{9}$$

where the permettivity ε, the permeability μ and the conductivity σ are independent of orientation (isotropy), space (homogeneity), time or frequency (dispersivity) and also independent of the field itself (linearity). One can write $\varepsilon = \varepsilon_r \varepsilon_0$ and $\mu = \mu_r \mu_0$, wherefrom ε_r and μ_r are called relative permittivity (or dielectric constant) and relative permeability.

Such a material is ideal. Any real material presents some degree of anisotropy, inhomogeneity, dispersivity or non linearity. However these assumptions are valid for a great number of materials, at least in a limited range for the field strength and/or frequency. Table 1 shows the minimum and maximum relative permittivity of some dielectrics while Table 2 (p.8) shows the electrical conductivity of some good conductors, semi conductors and air, with three significant digits. More precise values are provided in Table 12 (p.140), for the specific case of air.

Table 1 : Relative dielectric constant (ε_r) of some dielectrics

Material	Min.	Max.	Material	Min.	Max.
Air	1	1	Nylon	3.4	22.4
Amber	2.6	2.7	Paper	1.5	3
Asbestos fiber	3.1	4.8	Paraffin	2	3
Bakelite	5	22	Plexiglass	2.6	3.5
Barium Titanate	100	1250	Polycarbonate	2.9	3.2
Beeswax	2.4	2.8	Polyethylene	2.5	2.5
Cambric	4	4	Polyimide	3.4	3.5
Carbon Tetrachloride	2.17	2.17	Polystyrene	2.4	3
Celluloid	4	4	Porcelain	5	6.5
Cellulose Acetate	2.9	4.5	Quartz	5	5
Durite	4.7	5.1	Rubber	2	4
Ebonite	2.7	2.7	Ruby Mica	5.4	5.4
Epoxy Resin	3.4	3.7	Selenium	6	6
Ethyl Alcohol	6.5	25	Shellac	2.9	3.9
Fiber	5	5	Silicone	3.2	4.7
Formica	3.6	6	Slate	7	7
Glass	3.8	14.5	Soil dry	2.4	2.9
Glass Pyrex	4.6	5	Steatite	5.2	6.3
Gutta Percha	2.4	2.6	Styrofoam	1.03	1.03
Isolantite	6.1	6.1	Teflon	2.1	2.1
Kevlar	3.5	4.5	Titanium Dioxide	100	100
Lucite	2.5	2.5	Vaseline	2.16	2.16
Mica	4	9	Vinylite	2.7	7.5
Micarta	3.2	5.5	Water distilled	34	78
Mycalex	7.3	9.3	Waxes, Mineral	2.2	2.3
Neoprene	4	6.7	Wood dry	1.4	2.9

Table 2 : Electrical conductivity σ of some materials

Material	Electrical Conductivity [S/m]
Silver	63.0×10^6
Copper	56.9×10^6
Gold	45.2×10^6
Aluminium	35.0×10^6
Carbon	0.06×10^6
Sea Water	4.8
Germanium	1.45
Drinking water	0.0005 to 0.05
Silicon	252×10^{-6}
Air	$0.3 \text{ to } 0.8 \times 10^{-12}$

Noting that the divergence of a curl of any vector field $\bar{A}$ with twice continuously differentiable components in the neighbourhood of the *ordinary point* $\bar{r}$ vanishes identically, namely $\nabla \cdot \left(\bar{\nabla} \times \bar{A}(\bar{r}) \right) = 0$, two other conditions satisfied by the vectors $\bar{D}$ and $\bar{B}$ may be deduced directly from Maxwell's equations :

$$\nabla \cdot \bar{D} = \rho \tag{10}$$

$$\nabla \cdot \bar{B} = 0 \tag{11}$$

Equation (10) has as a consequence that $\bar{D}$ field lines start and end up on charges, as illustrated in Figure 1.

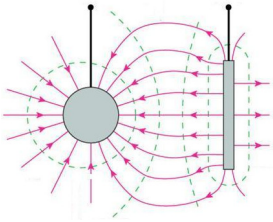

Figure 1 : $\bar{D}$ Field lines starting and ending up on charges

Equation (11) implies that the $\bar{B}$ field is solenoidal : the field lines close on themselves, as illustrated in Figure 2.

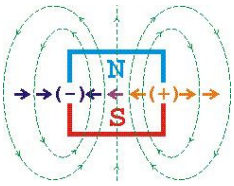

Figure 2 : Solenoidal field

1.2 Harmonic waves

In a non dispersive medium the behavior of a periodic wave of frequency f (or wavelength $\lambda = c/f$) can always be expressed as a sum of sine waves of

frequencies *n.f* (*n* being an integer) while a non periodic wave can be described by its continuous frequency spectrum. The spectral content of those waves being obtained with a Fourier transform it is sufficient to investigate the characteristics of a sine wave at a single frequency *f*, called a time harmonic wave. One can express the field quantities of a time harmonic wave as the real part of a product of a complex spatial form (only function of position) with the factor $e^{j\omega t}$ [1] representing the time variation ($\omega = 2\pi f$).

$$\bar{E}(\bar{r},t) = \mathrm{Re}\left[\bar{E}(\bar{r})e^{j\omega t}\right] = \left|\bar{E}(\bar{r})\right|\cos\left[\omega t + \arg\bar{E}(\bar{r})\right]\hat{u}_E \tag{12}$$

Replacing the instantaneous field vectors by their corresponding complex form, performing the time derivatives and dropping everywhere the $e^{j\omega t}$ term, one obtains from (2) and (3) the time harmonic Maxwell equations in their most general form :

$$\bar{\nabla}\times\bar{E} = -j\omega\bar{B} \tag{13}$$

$$\bar{\nabla}\times\bar{H} = j\omega\bar{D} + \bar{J} \tag{14}$$

The continuity equation (1) becomes :

$$\nabla\cdot\bar{J} = -j\omega\rho \tag{15}$$

In the case of linear, homogeneous and isotropic media, characterised by equations (9), the time harmonic equations (13) and (14) become :

$$\bar{\nabla}\times\bar{E} = -j\omega\mu\bar{H} \tag{16}$$

$$\bar{\nabla}\times\bar{H} = \bar{J}_{source} + \left(j\omega\varepsilon + \sigma\right)\bar{E} \tag{17}$$

The source term $\bar{J}_{source}$ is responsible for the apparition of the fields $\bar{E}$ and $\bar{H}$ while being independent of those fields.

In the case of a lossy dielectric, ie for which σ > 0, these losses can be accounted for by considering the permittivity as a complex value. Considering our $e^{j\omega t}$ choice, the imaginary part of the relative permittivity ε representing the conductivity must be negative :

$$\varepsilon = \varepsilon' - j\varepsilon'' \tag{18}$$

The relation between the imaginary part of ε and σ is then :

$$\sigma = \omega\varepsilon'' \tag{19}$$

When we compare the Maxwell equations a remarkable symmetry appears, but not in every respect, because no magnetic current or charge density exist. Adding

---

[1] Another representation for time harmonic variation is $e^{-j\omega t}$.
This other choice implies sign changes in the harmonic Maxwell equations and produces fields that are complex conjugate of those obtained with the $e^{j\omega t}$ convention.
Indeed: $\bar{E}(\bar{r},t) = \mathrm{Re}\left[\bar{E}(\bar{r})e^{j\omega t}\right] = \mathrm{Re}\left[\bar{E}^*(\bar{r})e^{-j\omega t}\right]$

a fictitious volumic magnetic charge density $\rho_{m,source}$ and a magnetic current density $\bar{M}_{source}$ as well as an additional dual continuity equation (24), symmetric equations can be written :

$$\bar{\nabla}\times\bar{E}+j\omega\mu\bar{H}=-\bar{M}_{source} \tag{20}$$

$$\bar{\nabla}\times\bar{H}-j\omega\varepsilon\bar{E}=\bar{J}_{source} \tag{21}$$

$$\nabla.\bar{E}=\rho_{source}/\varepsilon \tag{22}$$

$$\nabla.\bar{H}=\rho_{m,source}/\mu \tag{23}$$

$$\nabla.\bar{J}_{source}=-j\omega\rho_{source} \tag{24}$$

$$\nabla.\bar{M}_{source}=-j\omega\rho_{m,source} \tag{25}$$

where ε and μ are real for lossless materials and complex for lossy materials.

1.3 The Stratton-Chu equations

Before deriving the vector form of the electric field integral equations (EFIE) and magnetic field integral equations (MFIE), we must establish the Stratton-Chu equations. Only the essential steps are given in this paragraph. All other details and demonstrations can be found for example in [1, Ch.8.14] and in [2, Ch.6.9]. We start from Green's second identity, where S_0 is a closed surface enclosing the volume V_0 :

$$\int_{V_0}\left(\bar{Q}.\bar{\nabla}\times\bar{\nabla}\times\bar{P}-\bar{P}.\bar{\nabla}\times\bar{\nabla}\times\bar{Q}\right)dV=\int_{S_0}\left(\bar{P}\times\bar{\nabla}\times\bar{Q}-\bar{Q}\times\bar{\nabla}\times\bar{P}\right)\hat{n}_0 dS \tag{26}$$

It is a purely mathematical relationship between the vectors of position $\bar{P}$ and $\bar{Q}$ which both need to have continuous first and second derivatives within V_0 and on S_0.

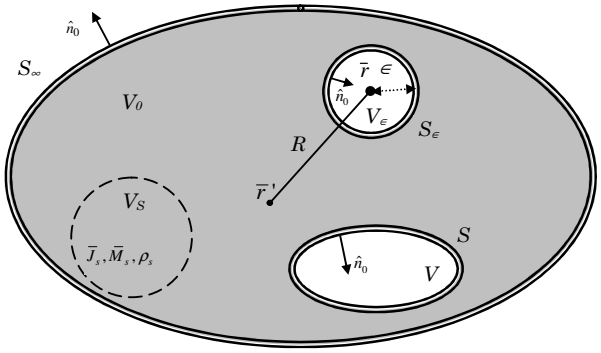

Figure 3 : Geometry for Green's second identity

In Figure 3 the volume V_0 is grey-shaded and the surface S_0 is made of three non intersecting closed surfaces S_∞, S_ϵ and S represented by double lines.

The unit normal $\hat{n}_0$ is defined everywhere on S_0 and points outside V_0. From here on, the subscript "$_0$" will indicate values related to the volume V_0.

In (26) we substitute $\bar{P}$ by the total electric field $\bar{E}_0$ and $\bar{Q}$ by an arbitrary unit vector $\hat{a}$ multiplied by the free-space Green's function :

$$G_0(\bar{r},\bar{r}') = \frac{\exp(-jk_0R)}{4\pi R} \tag{27}$$

with $R = |\bar{r} - \bar{r}'|$ and $k_0 = \omega\sqrt{\varepsilon_0\mu_0}$, where ε_0 and μ_0 are the scalar permittivity and permeability of the homogeneous, linear and isotropic body V_0 (typically : free space). The sources $\bar{J}_s, \bar{M}_s, \rho_s$ of the fields are confined in a volume V_S of finite extent, which is a part of V_0. The volume V is a scattering body having electromagnetic properties different from those of V_0, while V_ϵ is an infinitesimally small sphere of radius ϵ centered on $\bar{r}$ and having the same electromagnetic properties as V_0. After some calculations taking into account Maxwell's equations [1, Ch.8.14] and [2, Ch.6.9], (26) becomes :

$$\begin{aligned}&\int_{V_0}\left\{-j\omega\mu_0 G_0\bar{J}_s - \bar{M}_s\times\bar{\nabla}'G_0 + \frac{\rho_s}{\varepsilon_0}\bar{\nabla}'G_0\right\}dV' \\ &= \int_{S_0}\left\{-j\omega\mu_0 G_0\left[\hat{n}_0\times\bar{H}_0\right] + \left[\hat{n}_0\times\bar{E}_0\right]\times\bar{\nabla}'G_0 + \left(\hat{n}_0.\bar{E}_0\right)\bar{\nabla}'G_0\right\}dS'\end{aligned} \tag{28}$$

Mind that sign differences occur among the various bibliographic sources, depending on the choices made for the time dependence ($e^{j\omega t}$ throughout this book) and for the orientation of normals, inwards or outwards.

The volume and surface integrals as well as the derivatives are computed with regard to the coordinate $\bar{r}'$: this is made clear in the notation by the use of *dS'*, *dV'* and $\bar{\nabla}'$. Note again that sign differences occur in the literature when $\bar{\nabla}G_0 = -\bar{\nabla}'G_0$ is used instead of $\bar{\nabla}'G_0$. The position $\bar{r}$, appearing only in G_0, corresponds to an observation point located outside V_0, and also not on S_0. The free-space Green's function G_0 and its gradient $\bar{\nabla}'G_0$ would become infinite if $\bar{r}'$ could coincide with $\bar{r}$. This would violate the continuity requirements on $\bar{Q}$ necessary to establish (26). Therefore this singular point has been excluded from V_0. To include it inside V_0, we shrink the radius of the sphere V_ϵ to zero. At the limit $\epsilon = 0$, the surface integral on S_ϵ becomes singular. It is shown in [1, p252] that :

$$\lim_{\epsilon\to 0}\int_{S_\epsilon}\left\{\begin{aligned}&-j\omega\mu_0 G_0\left[\hat{n}_0\times\bar{H}_0\right] \\ &+\left[\hat{n}_0\times\bar{E}_0\right]\times\bar{\nabla}'G_0 + \left(\hat{n}_0.\bar{E}_0\right)\bar{\nabla}'G_0\end{aligned}\right\}\ dS' = \bar{E}_0(\bar{r}) \tag{29}$$

where $\bar{E}_0(\bar{r})$ is nothing else than the total electric field at the observation point $\bar{r}$. If we now let S_∞ recede to infinity, while all the sources of the fields are confined in a volume V_s of finite extent, then Sommerfeld's radiation condition at infinity ensures that the integral over S_∞ reduces to zero. With V_ϵ reduced to zero and S_∞ extending to infinity, (28) becomes :

$$\begin{aligned}&\int_{V_0}\left\{-j\omega\mu_0 G_0\bar{J}_s-\bar{M}_s\times\bar{\nabla}'G_0+\frac{\rho_s}{\varepsilon_0}\bar{\nabla}'G_0\right\}dV'\\&=\bar{E}_0(\bar{r})+\int_S\left\{-j\omega\mu_0 G_0\left[\hat{n}_0\times\bar{H}_0\right]+\left[\hat{n}_0\times\bar{E}_0\right]\times\bar{\nabla}'G_0+\left(\hat{n}_0.\bar{E}_0\right)\bar{\nabla}'G_0\right\}dS'\end{aligned}\tag{30}$$

From (30) we recognize that the volume integral over the source terms $\bar{J}_s$, $\bar{M}_s$ and ρ_s is the incident field $\bar{E}^{inc}$ at $\bar{r}$ created by these sources. Indeed if the volume V enclosed by S were removed, then the total field $\bar{E}_0(\bar{r})$ should be equal to $\bar{E}^{inc}(\bar{r})$. Equation (30) finally becomes :

$$\bar{E}_0(\bar{r})=\bar{E}^{inc}(\bar{r})+\int_S\left\{\begin{array}{l}+j\omega\mu_0 G_0\left[\hat{n}_0\times\bar{H}_0\right]\\-\left[\hat{n}_0\times\bar{E}_0\right]\times\bar{\nabla}'G_0-\left(\hat{n}_0.\bar{E}_0\right)\bar{\nabla}'G_0\end{array}\right\}\,dS'\tag{31}$$

With (31), the integral over S appears as the field scattered by the surface S when hit by the incident field $\bar{E}^{inc}$.

If we now choose for $\bar{P}$ the total magnetic field $\bar{H}_0$ instead of $\bar{E}_0$, then we obtain similarly to (31) for the same observation point $\bar{r}$:

$$\bar{H}_0(\bar{r})=\bar{H}^{inc}(\bar{r})+\int_S\left\{\begin{array}{l}-j\omega\varepsilon_0 G_0\left[\hat{n}_0\times\bar{E}_0\right]\\-\left[\hat{n}_0\times\bar{H}_0\right]\times\bar{\nabla}'G_0-\left(\hat{n}_0.\bar{H}_0\right)\bar{\nabla}'G_0\end{array}\right\}\,dS'\tag{32}$$

Equations (31) and (32) are the Stratton-Chu equations.

1.4 Fields on the surface S of a sheet

Following Maue [3], Poggio and Miller [4, pp.159-170] have shown how (31) and (32) must be modified when the observation point lies on the surface S of a non zero volume V. As will be shown in §1.7 this step is essential to incorporate the boundary conditions and solve the integro-differential equations. We don't reproduce here the details of the aforementioned derivation; instead we have generalized it to the limit case of infinitely thin plates - being zero volume bodies - that we call *sheets* in this book. We present in §1.4.1 a complete and original demonstration that takes into account the field singularities that may occur at sharp edges and corners. The electric (EFIE) and magnetic (MFIE) field integral expressions obtained in every possible case are then summarized in §1.5, with equation (57).

1.4.1 Fully embedded sheet

Let us consider first a very general sheet, as the one depicted in Figure 4 (p.13), fully embedded in only one volume V_0 (of infinite extent). The case of a sheet in contact with several volumes is treated in §1.4.2. The sheet is made of several adjacent surfaces, S_1 to S_4, each delimited by a closed curve.

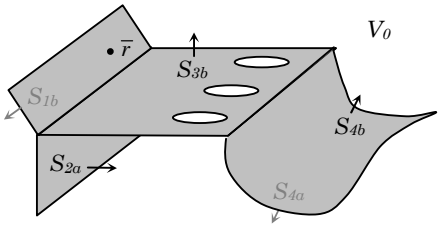

Figure 4 : Sheet with branches and holes

Every surface may contain holes, that are themselves delimited by a closed curve. At any location $\bar{r}$ on every surface S_i, except on the closed curves delimiting them, there are exactly two opposite faces S_{ia} and S_{ib}. Both faces can be identified by the orientation of the unit vector normal to them. Let us now consider all closed curves delimiting the surfaces as rigid seals around them, and that both faces S_{ia} and S_{ib} of all these surfaces i can be stretched away from each other, everywhere except at the rigid seals. This produces new closed surfaces $F_i=F_{ia}+F_{ib}$, enclosing non zero volumes V_i , as shown in Figure 5. The sum of both faces $S_i=S_{ia}+S_{ib}$ can now be viewed as the limit of $F_i=F_{ia}+F_{ib}$ when the stretching tension is released. Note that the seals, corresponding to every sharp edge and corner, are identical for the original sheet and for the volume $V=\sum(V_i)$. We introduce the notation $F_a=\sum(F_{ia})$, $F_b=\sum(F_{ib})$, $F=\sum(F_i)$ and similar expressions for S_a , S_b , S.

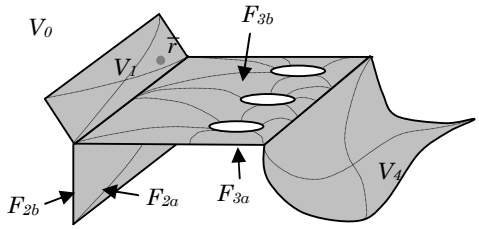

Figure 5 : Non zero volume stretched sheet

We consider next an observation point $\bar{r}$ located inside V, actually on the face S_{1a} inside V_1 , but not on any of the seals around S_1. As $\bar{r}$ is located inside V_1 , thus outside V_0 , the free-space Green's function and its gradient are regular everywhere inside V_0 . Consequently there is no need to isolate $\bar{r}$ inside a small sphere V_ϵ and to calculate the limit of a singular integral over S_ϵ , as we did to obtain (29). The left hand term of (31) and (32) vanishes : inside V the scattered field exactly compensates the incident field to produce a null total field. This property is also called the Ewald-Oseen extinction theorem [2, Ch.6.9]. We can thus write :

$$\bar{0} = \bar{E}^{inc}(\bar{r}) + \int_F \left\{ \begin{array}{l} +j\omega\mu_0 G_0 \left[\hat{n}_0 \times \bar{H}_0 \right] \\ -\left[\hat{n}_0 \times \bar{E}_0 \right] \times \bar{\nabla}' G_0 - \left(\hat{n}_0 . \bar{E}_0 \right) \bar{\nabla}' G_0 \end{array} \right\} dS' \qquad (33)$$

$$\bar{0} = \bar{H}^{inc}(\bar{r}) + \int_F \begin{Bmatrix} -j\omega\varepsilon_0 G_0 \left[\hat{n}_0 \times \bar{E}_0\right] \\ -\left[\hat{n}_0 \times \bar{H}_0\right] \times \bar{\nabla}' G_0 - \left(\hat{n}_0 . \bar{H}_0\right) \bar{\nabla}' G_0 \end{Bmatrix} dS' \qquad (34)$$

From here on we will omit the subscript '$_0$', but we will remember that the fields and the electromagnetic properties under the surface integral are those on F, on the V_0 side. Also the unit normal $\hat{n}_0$ is pointing out of V_0 (thus inside V). In Figure 6 we represent only the volume V_1 containing the observation point $\bar{r}$. If we shrink the volume V to a null volume, such that surfaces F_a and F_b eventually merge with S_a and S_b, then $\bar{r}_{fa} \to \bar{r}_a = \bar{r}$, $\bar{r}_{fb} \to \bar{r}_b = \bar{r}$ and the surface integral over F_{1a}+F_{1b} will become singular twice. The unit normal to F_{1a} (F_{1b}) at $\bar{r}_{fa}$ ($\bar{r}_{fb}$) will be called $\hat{n}_{fa}$ ($\hat{n}_{fb}$) ; it points outside V_0 and towards $\bar{r} = \bar{r}_a = \bar{r}_b$ at all times. Note at this stage that we avoid denominations such as upper and lower, or positive and negative to differentiate the faces of the sheet. Indeed, a sheet can be curved, branched or even twisted, like the Moebius ring (see Figure 43, p.81).

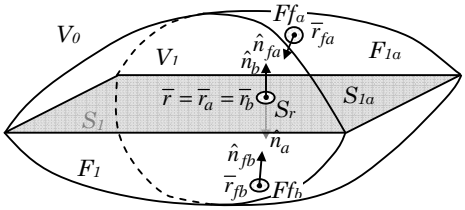

Figure 6 : Volume V_1 containing $\bar{r}$

To determine and extract the two singularities of this doubly singular integral, we circumscribe $\bar{r}_{fa}$ with an infinitesimally small circle with surface F_{fa}, which we exclude from F_{1a}. The surface F_{fa} must be so small and flat that the unit normal $\hat{n}_{fa}$, the electric and magnetic fields $\bar{E}_{fa}$ and $\bar{H}_{fa}$ can all be considered as constant vectors everywhere on F_{fa}. Those requirements exclude that $\bar{r}_{fa}$ (and at the limit, $\bar{r}_a = \bar{r}$) be located on a sharp edge or on a corner, but they don't exclude the possibility for the sheet to have sharp edges or corners elsewhere, as depicted in Figure 4 (p.13). It is well known that the fields may locally become infinite at such geometric discontinuities [5, Ch.4 and 5], but the edge condition, enforced to guarantee a unique solution, also ensures that the fields scattered by any bounded region enclosing these discontinuities remain finite at all other geometrically regular points in space, in particular at $\bar{r}$ [6, Ch.2.1]. The surface integrals in (33) and (34) thus produce a well defined finite value at $\bar{r}$ despite the presence of sharp edges and corners all around and inside the volume (and, at the limit, around and inside the sheet). Similarly, we define the circle with surface F_{fb} around $\bar{r}_{fb}$ and exclude it from F_{1b}. The radii of the circles F_{fa} and F_{fb} will respectively be denoted by ρ_a and ρ_b. The integral over F is then subdivided into :

$$\int_F = \sum_{i \neq 1} \int_{F_i} + \int_{F_{1a} - F_{fa}} + \int_{F_{1b} - F_{fb}} + \int_{F_{fa}} + \int_{F_{fb}} \qquad (35)$$

where the first three integrals are regular at all times and the two last ones become singular when both $\bar{r}_{fa}$ and $\bar{r}_{fb}$ merge with $\bar{r}$. Let us concentrate on the first singular integral on F_{fa}. To determine its limit value when $\bar{r}_{fa} \to \bar{r}_a$, we consider $\bar{r}_{fa}$ to be already located at a very small distance $d_a << \lambda$ from $\bar{r}_a$. We also require ρ_a to be so small that $R = \left|\bar{R}\right| = \left|\bar{r} - \bar{r}'\right| << \lambda$ for any integration point $\bar{r}'$ in F_{fa}. Then we can approximate the free-space Green's function and its gradient on F_{fa} by their asymptotic values :

$$G = \frac{e^{-jkR}}{4\pi R} \cong \frac{1}{4\pi R} \tag{36}$$

$$\bar{\nabla}' G = \frac{1 + jkR}{4\pi R^3} e^{-jkR} \bar{R} \cong \frac{\bar{R}}{4\pi R^3} \tag{37}$$

With (36) and (37), the three components of the integral on the circular and flat infinitesimal surface F_{fa} in (34) can be approximated by :

$$\int_{F_{fa}} j\omega\varepsilon \, G \left[\hat{n} \times \bar{E}\right] dS' \cong \left[\hat{n}_{fa} \times \bar{E}_{fa}\right] \frac{j\omega\varepsilon}{4\pi} \int_{F_{fa}} \frac{dS'}{R} \tag{38}$$

$$\int_{F_{fa}} \left[\hat{n} \times \bar{H}\right] \times \bar{\nabla}' G \, dS' \cong \left[\hat{n}_{fa} \times \bar{H}_{fa}\right] \times \frac{1}{4\pi} \int_{F_{fa}} \frac{\bar{R}}{R^3} dS' \tag{39}$$

$$\int_{F_{fa}} \left[\hat{n} \cdot \bar{H}\right] \; \bar{\nabla}' G \; dS' \cong \left[\hat{n}_{fa} \cdot \bar{H}_{fa}\right] \; \frac{1}{4\pi} \int_{F_{fa}} \frac{\bar{R}}{R^3} dS' \tag{40}$$

Letting then $\bar{r}_{fa}$ merge with $\bar{r}_a$ (and F_{fa} with the disc S_r of radius ρ_r), the first integral (38), involving G, reduces to :

$$\lim_{\bar{r}_{fa} \to \bar{r}_a} \int_{F_{fa}} \frac{dS'}{R} = \int_0^{2\pi} d\theta \int_0^{\rho_r} \frac{\rho \, d\rho}{\rho} = \int_0^{2\pi} \rho_r \, d\theta = 2\pi\rho_r \tag{41}$$

Next, if the (radius ρ_r of the) surface S_r tends to zero, then (41) also reduces to zero. The integrals (39) and (40), involving $\bar{\nabla}' G$, both contain the same singular vector integral. Since $\bar{r}_a$ is not located on a sharp edge or on a corner, we show in Appendix A that :

$$\lim_{\bar{r}_{fa} \to \bar{r}_a} \int_{F_{fa}} \frac{\bar{R}}{4\pi R^3} dS' = \frac{+\hat{n}_a}{2} \tag{42}$$

The result is independent of the size of the surface S_r. Consequently, the limit of (42) remains unchanged when the radius of the surface S_r tends to zero. Note though that (42) is not independent of the shape of S_r : it holds only if S_r is symmetric around $\bar{r}_a$. For asymmetric shapes, a tangential term normal to $\hat{n}_{fa}$ arises that does not cancel out. This unpleasant mathematical peculiarity is very rarely mentioned [3], [7, p.54], and nowhere clarified. We close this debate by observing that the limit value of (35) when F_{1a} merges with S_{1a} has a unique value, independent of the choice of S_r : the additional tangential term is present with opposite signs in both the integrals over S_r and S_{1a}-S_r. In the context of numerical integration, where the surface S_r can be a flat polygon of any shape

and finite extent, Yaghjian [8] proposed a generalized expression for the electric field integral equation (EFIE) including this tangential term. We will assume here that the tangential term vanishes through a proper choice of the principal value area S_r.

Proceeding similarly with $\bar{r}_{fb} \to \bar{r}_b$, we obtain :

$$\lim_{\rho_b \to 0} \left\{ \lim_{\bar{r}_{fb} \to \bar{r}_b} \int_{F_{fb}} \frac{dS'}{R} \right\} = \lim_{\rho_b \to 0} \{ 2\pi \rho_b \} = 0 \tag{43}$$

$$\lim_{\rho_b \to 0} \left\{ \lim_{\bar{r}_{fb} \to \bar{r}_b} \int_{F_{fb}} \frac{\bar{R}}{4\pi R^3} dS' \right\} = \frac{+\hat{n}_b}{2} \tag{44}$$

Finally, we can write :

$$\begin{aligned} \lim_{F \to S} \int_F \; = \bar{\!\!\!\int}_S \; & + \left[\hat{n}_a \times \bar{H}_a \right] \times \frac{\hat{n}_a}{2} + \left[\hat{n}_a \cdot \bar{H}_a \right] \; \frac{\hat{n}_a}{2} \\ & + \left[\hat{n}_b \times \bar{H}_b \right] \times \frac{\hat{n}_b}{2} + \left[\hat{n}_b \cdot \bar{H}_b \right] \; \frac{\hat{n}_b}{2} \end{aligned} \tag{45}$$

where the bar across the integral sign reminds us that the singular terms have been extracted (principal value integral). Noting now that, for any vector $\bar{K}$ and unit vector $\hat{n}$:

$$\left[\hat{n} \times \bar{K} \right] \times \hat{n} + \left[\hat{n} \cdot \bar{K} \right] \hat{n} = \bar{K} \tag{46}$$

we obtain the first vector form of the magnetic field integral equation (MFIE) for an arbitrary sheet, fully embedded in the volume V_0, with opposite faces S_a+S_b=S :

$$\begin{aligned} \bar{H}^{inc}(\bar{r}) = & \frac{1}{2} \left\{ \bar{H}_a(\bar{r}) + \bar{H}_b(\bar{r}) \right\} + \\ & \bar{\!\!\!\int}_{S_a + S_b} \left\{ + j\omega\varepsilon G \left[\hat{n} \times \bar{E} \right] + \left[\hat{n} \times \bar{H} \right] \times \bar{\nabla}' G + \left(\hat{n} \cdot \bar{H} \right) \bar{\nabla}' G \right\} \; dS' \end{aligned} \tag{47}$$

The vector form of the electric field integral equation (EFIE) can likewise be established for the same sheet from (33) :

$$\begin{aligned} \bar{E}^{inc}(\bar{r}) = & \frac{1}{2} \left\{ \bar{E}_a(\bar{r}) + \bar{E}_b(\bar{r}) \right\} + \\ & \bar{\!\!\!\int}_{S_a + S_b} \left\{ - j\omega\mu G \left[\hat{n} \times \bar{H} \right] + \left[\hat{n} \times \bar{E} \right] \times \bar{\nabla}' G + \left(\hat{n} \cdot \bar{E} \right) \bar{\nabla}' G \right\} \; dS' \end{aligned} \tag{48}$$

We recall that all the fields and electromagnetic properties are those (on S) inside V_0 and that the unit normal $\hat{n}$ points outside V_0.

It can now be demontrated with (47), (48) and the unicity theorem that a dielectric sheet of any shape and size is transparent to electromagnetic waves, regardless of its finite complex permittivity ε and permeability μ. In other words, a dielectric sheet does not scatter any fields. The total fields everywhere on both faces of the dielectric sheet are thus equal to the incident fields. This trivial solution is perfectly in line with (47) and (48) : if $\bar{E}(\bar{r}') = \bar{E}_i(\bar{r}')$ and $\bar{H}(\bar{r}') = \bar{H}_i(\bar{r}')$

everywhere around the sheet, then because of the opposite normals on both faces, the integral over S_a exactly cancels the integral over S_b and we are left with the identities :

$$\bar{E}_i(\bar{r}) = \frac{1}{2}\left\{\bar{E}_i(\bar{r}) + \bar{E}_i(\bar{r})\right\} \tag{49}$$

$$\bar{H}_i(\bar{r}) = \frac{1}{2}\left\{\bar{H}_i(\bar{r}) + \bar{H}_i(\bar{r})\right\} \tag{50}$$

The unicity theorem finally ensures that this trivial but correct solution is the only solution in the case of dielectric sheets.

As a result, the EFIE and MFIE formulation for sheets will be specialized in §1.12 to perfect electric conductors (PEC) or perfect magnetic conductors (PMC), for which the conductivity – namely either the imaginary part of ε, see (19), or that of μ – is considered to be infinite.

An important remark must be made here : the factor 1/2 appearing in (42) and (44) is obtained because the surface is locally flat in the neighbourhood of $\bar{r}_a$, where the subtended solid angle equals 2π. Some authors have proposed to generalize this factor when the observation point is located on an edge or on a corner of a volume, taking into account the solid angle Ω subtended on the edge or on the corner [4, p.163][9][10]. It is our opinion though that such a modification is useless : except in a few highly symmetric cases, either the total electric or magnetic field in the right hand sides of (47) and (48) become zero or infinite on sharp edges or corners [5][11], rendering the factor affecting the total field at such locations pointless, as well as the whole evaluation of (47) and (48). In the specific case of sheets, the angle subtended by an edge is always 4π.

1.4.2 Sheet in contact with more than one volume

We must recall that the MFIE (47) and EFIE (48) are not written "for the sheet" but inside the volume V_0, that fully embeds the sheet. These equations are written for any regular observation point $\bar{r}$ on the sheet surface, but inside V_0 . As such, they involve fields inside V_0.

If both faces of the sheet are in contact with two different volumes, as shown in Figure 7 (p.18), then we must write an EFIE and a MFIE in each of these volumes.

The same stretching-unstretching process can be applied to the sheet of Figure 7, followed by the limit process. If we write the MFIE$_1$ inside V_1, then we obtain :

$$\begin{aligned}\bar{H}_1^{inc}(\bar{r}) = {} & \frac{1}{2}\left\{\bar{H}_{1S}(\bar{r})\right\} + \\ & \oint_{S_{1S}+S_{1V}} \left\{ + j\omega\varepsilon_1 G_1\left[\hat{n}_1 \times \bar{E}_1\right] + \left[\hat{n}_1 \times \bar{H}_1\right] \times \bar{\nabla}' G_1 + \left(\hat{n}_1 \cdot \bar{H}_1\right)\bar{\nabla}' G_1 \right\} dS'\end{aligned} \tag{51}$$

where $\bar{H}_1^{inc}(\bar{r})$ is the incident field at $\bar{r}$ created by sources contained in V_1, if any. The subscripts "$_1$" remind us that the fields and electromagnetic properties are those inside V_1. Only $\bar{H}_{1S}/2$ has been extracted, and not $(\bar{H}_{1S} + \bar{H}_{2S})/2$.

Indeed the surface integral over the surface enclosing V_1 is computed on $S_1=S_{1V}+S_{1S}$.

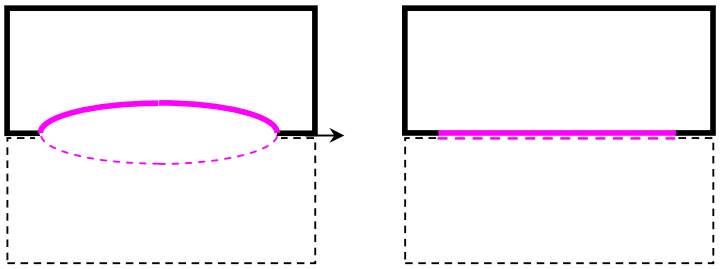

Figure 7 : Sheet squeezed between two volumes

Similarly, the MFIE$_2$ in V_2 is :

$$\bar{H}_2^{inc}(\bar{r}) = \frac{1}{2}\left\{\bar{H}_{2S}(\bar{r})\right\} + \oint_{S_{2S}+S_{2V}} \left\{ +j\omega\varepsilon_2 G_2\left[\hat{n}_2\times\bar{E}_2\right] + \left[\hat{n}_2\times\bar{H}_2\right]\times\bar{\nabla}'G_2 + \left(\hat{n}_2\cdot\bar{H}_2\right)\bar{\nabla}'G_2\right\} dS' \tag{52}$$

Finally, to treat the most general case of a partly embedded sheet, we must remember that the EFIE and MFIE are written for a given observation point $\bar{r}$, located on the enclosing surface S_i of the volume V_i.

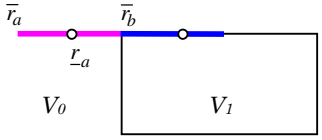

Figure 8 : Partly embedded sheet

In Figure 8 we introduce the notation $\underline{r}_a$ to designate the observation point mathematically collocated with $\bar{r}_a$ but physically situated on the opposite face of the sheet. The EFIE$_0$, inside V_0, at points $\bar{r}_a$ and $\bar{r}_b$ are :

$$\bar{E}^{inc}(\bar{r}_a) = \frac{1}{2}\left\{\bar{E}_0(\bar{r}_a) + \bar{E}_0(\underline{r}_a)\right\} + \oint_{S_0} \left\{ -j\omega\mu_0 G_0\left[\hat{n}_0\times\bar{H}_0\right] + \left[\hat{n}_0\times\bar{E}_0\right]\times\bar{\nabla}'G_0 + \left(\hat{n}_0\cdot\bar{E}_0\right)\bar{\nabla}'G_0\right\} dS' \tag{53}$$

$$\bar{E}^{inc}(\bar{r}_b) = \frac{1}{2}\left\{\bar{E}_0(\bar{r}_b)\right\} + \oint_{S_0} \left\{ -j\omega\mu_0 G_0\left[\hat{n}_0\times\bar{H}_0\right] + \left[\hat{n}_0\times\bar{E}_0\right]\times\bar{\nabla}'G_0 + \left(\hat{n}_0\cdot\bar{E}_0\right)\bar{\nabla}'G_0\right\} dS' \tag{54}$$

It is important to note that :

– The surface S_0 consists of the surface S_1 enclosing V_1 and both superimposed faces of that part of the sheet fully embedded in V_0 (pink coloured)

- The electric fields $\bar{E}_0(\bar{r}_a)$ and $\bar{E}_0(\underline{r}_a)$ on either faces of the sheet are different from each other for a perfectly conducting sheet
- $EFIE_0(\bar{r}_a) = EFIE_0(\underline{r}_a)$

1.5 Generalized formulation for mixed materials

The Stratton-Chu equations and their modification for perfectly conducting sheets are actually dealing with one single body enclosed in a surface S embedded in free space V_0. We already presented a slightly more general situation in §1.4.2 for the case of a sheet in contact with several bodies. In this paragraph we generalize the EFIE and MFIE for the case of several arbitrary bodies, volumes or sheets, perfectly conducting or not, all embedded in one infinite domain : free space. The objective is to determine the electric and magnetic field at any *ordinary* observation point $\bar{r}$ in space, namely a point where the fields as well as their first derivatives are continuous. We exclude thereby every point $\bar{r}$ located on a sharp edge or on a corner.

Let us consider several adjacent domains D_i with volume V_i bounded by a closed surface S_i. Every domain D_i is linear, isotropic and homogeneous. D_0 represents free space, extending to infinity. D_1 and D_2 are dielectric bodies, possibly lossy. D_3 is a perfect conductor, electric or magnetic. We also consider a perfectly conducting sheet made of three branches and three pairs of opposite faces. We do not consider in this book the particular case of imperfectly conducting bodies for which the finite and inhomogeneous conductivity can be replaced by a Leontovitch impedance boundary condition [12][13].

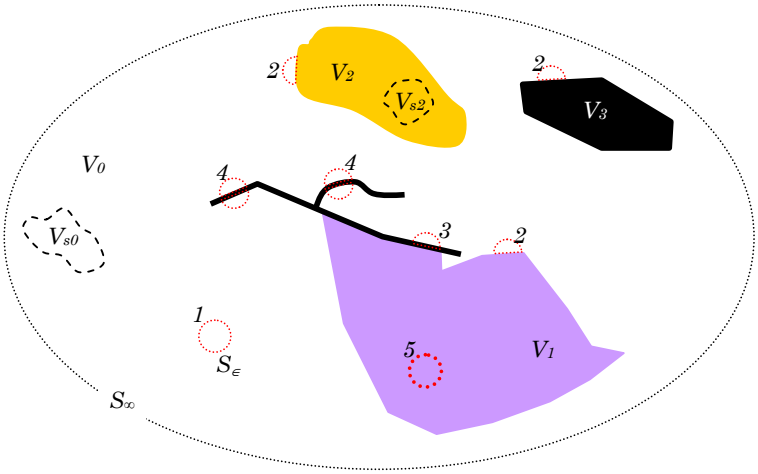

Figure 9 : Geometry for the mixed material problem

We include in every non perfectly conducting domain D_i one or even several harmonic sources $\bar{J}_{si}, \bar{M}_{si}, \rho_{si}$ all operating at the same angular frequency ω, and confined in a volume V_{si} of finite extent. The fields created by the sources in D_i

add up to produce everywhere in space, and in particular at the observation point $\bar{r}$, a primary field $\bar{E}_i^p(\bar{r}),\ \bar{H}_i^p(\bar{r})$.

For scattering problems, sources located sufficiently far away from the scatterers are represented by the plane waves they create, in which case they belong to the unbounded domain D_0 or D_1. For near field excitation, they can be represented by elementary electric or magnetic dipoles or loops and they can be located in any domain. For radiation problems, the sources are confined in generators and only their effects at the end of the feed lines are modelled, for example by delta gaps [14], magnetic frills [15][16] or microstrip transmission lines [17]. All these primary fields combine to form a total primary field $\bar{E}^p(\bar{r}),\ \bar{H}^p(\bar{r})$. The combined reaction of every domain D_i to this total primary field is the creation of a secondary (scattered) field $\bar{E}^s(\bar{r}),\ \bar{H}^s(\bar{r})$. In linear materials, the primary and secondary fields simply add up to establish a total electromagnetic field $\bar{E}(\bar{r}),\ \bar{H}(\bar{r})$ everywhere in space.

Provided the observation point $\bar{r}$ is not situated on a sharp edge or corner, where the fields can be singular, we can write (28) separately for every volume V_i enclosed within S_i :

$$\begin{aligned}&\int_{V_i}\left\{-j\omega\mu_i G_i\bar{J}_{si}-\bar{M}_{si}\times\bar{\nabla}'G_i+\frac{\rho_{si}}{\varepsilon_i}\bar{\nabla}'G_i\right\}.dV'\\&=\int_{S_i}\left\{-j\omega\mu_i G_i\left[\hat{n}_i\times\bar{H}_i\right]+\left[\hat{n}_i\times\bar{E}_i\right]\times\bar{\nabla}'G_i+\left(\hat{n}_i.\bar{E}_i\right)\bar{\nabla}'G_i\right\}dS'\end{aligned}\tag{55}$$

where the free-space Green's function in domain D_i is :

$$G_i(\bar{r},\bar{r}')=\frac{\exp(-jk_iR)}{4\pi R}\tag{56}$$

with $R=\left|\bar{r}-\bar{r}'\right|$ and $k_i=\omega\sqrt{\varepsilon_i\mu_i}$. The electromagnetic properties ε_i and μ_i are the permittivity and permeability of the homogeneous, linear and isotropic body V_i and the sources $\bar{J}_{si},\bar{M}_{si},\rho_{si}$ are confined in a volume V_{si} of finite extent, which is a part of V_i. In the example of Figure 9 (p.19), only V_0 and V_2 contain field sources. The fields $\bar{E}_i$ and $\bar{H}_i$ are the total fields existing inside V_i, possibly on S_i, while $\hat{n}_i$ is the unit normal to S_i pointing outside V_i.

The observation point $\bar{r}$, appearing only in the free-space Green's function G_i , is kept temporarily outside V_i, inside an infinitesimal volume V_ϵ enclosed in the surface S_ϵ. Considering for example $V_i = V_0$, depending on the location of $\bar{r}$ (see Figure 9), the exclusion volume is a sphere (cases 1 and 5), a half sphere (cases 2 and 3), or two half spheres on both sides of a sheet (case 4). Case 1 has been explained in §1.3 to obtain (29). Case 2 has been described by Poggio and Miller [4, pp.159-170]. Cases 3 and 4 are treated in this paragraph in a way similar to case 2, namely with the help of half spheres, but has been demonstrated in §1.4 with a different technique. Case 5 has been explained in §1.4.1 to obtain (33) or (34).

When the radius ϵ of the (half) sphere(s) is reduced to zero, the singular integral over the surface S_ϵ becomes :

$$\lim_{\epsilon\to 0}\int_{S_\epsilon}\Big\{-j\omega\mu_0 G_0\Big[\hat{n}_0\times\bar{H}_0\Big]+\Big[\hat{n}_0\times\bar{E}_0\Big]\times\bar{\nabla}'G_0+\Big[\hat{n}_0.\bar{E}_0\Big]\ \bar{\nabla}'G_0\Big\}.dS'$$

$$=\tilde{E}_0(\bar{r})=\begin{cases}\bar{E}_0(\bar{r}_1) & case\,1\\ \bar{E}_0(\bar{r}_2)/2 & case\,2\\ \bar{E}_0(\bar{r}_3)/2 & case\,3\\ \left\{\bar{E}_0(\bar{r}_4)+\bar{E}_0(\underline{r}_4)\right\}/2 & case\,4\\ \bar{0} & case\,5\end{cases} \tag{57}$$

where the tilde notation $\tilde{E}_0(\bar{r})$ is introduced to summarize all possible cases.

The volume integral over the sources $\bar{J}_{si},\bar{M}_{si},\rho_{si}$ in (55) can be identified as the incident field $\bar{E}_i^{inc}(\bar{r})$ produced by these sources. In the example of Figure 9 (p.19) it is equal to zero in volumes V_1 and V_3, as they contain no sources.

Equation (55) becomes the EFIE$_i$ in domain D_i :

$$\bar{E}_i^{inc}(\bar{r})=\tilde{E}_i(\bar{r})+\int_{S_i}\Big\{-j\omega\mu_i G_i\Big[\hat{n}_i\times\bar{H}_i\Big]+\Big[\hat{n}_i\times\bar{E}_i\Big]\times\bar{\nabla}'G_i+\Big[\hat{n}_i.\bar{E}_i\Big]\ \bar{\nabla}'G_i\Big\}dS' \tag{58}$$

Inside any perfectly conducting volume there can be no sources and the fields are identically zero : equation (58) vanishes identically in the case of V_3.

Similarly for the MFIE$_i$ in domain D_i :

$$\bar{H}_i^{inc}(\bar{r})=\tilde{H}_i(\bar{r})+\int_{S_i}\Big\{+j\omega\varepsilon_i G_i\Big[\hat{n}_i\times\bar{E}_i\Big]+\Big[\hat{n}_i\times\bar{H}_i\Big]\times\bar{\nabla}'G_i+\Big[\hat{n}_i.\bar{H}_i\Big]\ \bar{\nabla}'G_i\Big\}dS' \tag{59}$$

In §1.4 we have interpreted the surface integral as the field scattered by a unique passive body outside D_i enclosed in the surface S_i, while the incident field was created by the unique sources all contained within D_i.

In a multidomain context, and especially a multi-source configuration, this interpretation must be revised. When $\bar{r}$ is not located on the surface S_i, the fields $\tilde{E}_i$, $\tilde{H}_i$ and $\bar{E}_i$, $\bar{H}_i$ are the total fields due to the combined effect of all sources and all domains, but the incident field $\bar{E}_i^{inc}$, $\bar{H}_i^{inc}$ is not the sum of the contribution of all sources contained in every domain, but only the fields created by the sources in domain D_i. The surface S_i is the surface delimiting the domain D_i, and not the surface of a single passive scatterer : outside D_i, also enclosed in S_i, there are possibly many different bodies, and there can be other sources in some of these bodies. The surface integral summarizes the combined contribution of everything outside D_i, namely all sources and all scattering bodies outside D_i. Added to the fields $\bar{E}_i^{inc}$ and $\bar{H}_i^{inc}$ created by the sources inside D_i, the fields created by "everything outside D_i" produces the total field inside D_i.

If there are no sources outside D_i, the surface integral can be interpreted as the scattering contribution from all bodies outside D_i excited by the incident field due to the sole sources contained inside D_i.

If there are sources outside D_i, the surface integral is the sum of the scattering from all bodies outside D_i and the fields generated by the sources outside D_i.

1.6 Equivalent surface current densities

In (28) we observe a great symmetry between $\bar{J}_s$ and $\hat{n}\times\bar{H}$, between $\bar{M}_s$ and $-\hat{n}\times\bar{E}$ and between ρ_s/ε_0 and $\hat{n}.\bar{E}$. This suggests that $\hat{n}\times\bar{H}$ and $-\hat{n}\times\bar{E}$ can be seen as surface current densities (on the surface S) and $-\hat{n}.\bar{E}$ as a surface charge density (on S), all contributing together with the volumic source current and charge densities $\bar{J}_s$, $\bar{M}_s$ and ρ_s in V to the total fields at $\bar{r}$.

We introduce therefore the equivalent surface current densities, defined everywhere inside every domain D_i on its bounding surface S_i :

$$\bar{J}_i = +\hat{n}_i \times \bar{H}_i \tag{60}$$

$$\bar{M}_i = -\hat{n}_i \times \bar{E}_i \tag{61}$$

We remind that $\hat{n}_i$ is the normal to S_i pointing outside V_i. Note also that the volumic source current densities $\bar{J}_s$ and $\bar{M}_s$ have units A/m² and V/m² while equivalent surface current densities $\bar{J}_i$ and $\bar{M}_i$ have units A/m and V/m.

1.7 Boundary conditions

In §1.3, 1.4 and 1.5 we have established the electric (EFIE$_i$) and magnetic (MFIE$_i$) field integral equations valid inside every domain D_i, and in particular at their inner boundary S_i. To solve uniquely this set of equations, the relationships between the fields on both sides of the boundaries of all adjacent domains must be added.

Referring to Figure 10 (p.23), the case of S_∞, the outer surface of the unbounded domain D_0, is particular : when it recedes to infinity, while all the sources of the fields are confined in a volume V_s of finite extent, then Sommerfeld's radiation condition at infinity [18] ensures that a surface integral over S_∞ of the electric and magnetic fields (or their components) reduces to zero.

Every *ordinary* point at the interface between adjacent domains is shared by exactly two domains. The only exceptions to this rule are the points situated on S_∞, treated above, and eventually those situated on sharp edges or corners. These singular points have been excluded when we have established the EFIE$_i$ and MFIE$_i$, as the fields at these points are not necessarily continuous, continusously differentiable and finite.

At the interface separating two domains D_i and D_j the total fields at every *ordinary* point of the interface are related by the boundary conditions listed in

Table 3. The electric fields $\bar{E}_i$ and $\bar{E}_j$ are the fields at the same observation point of the interface, respectively inside D_i and inside D_j. The same applies to $\bar{H}$, $\bar{D}$ and $\bar{B}$.

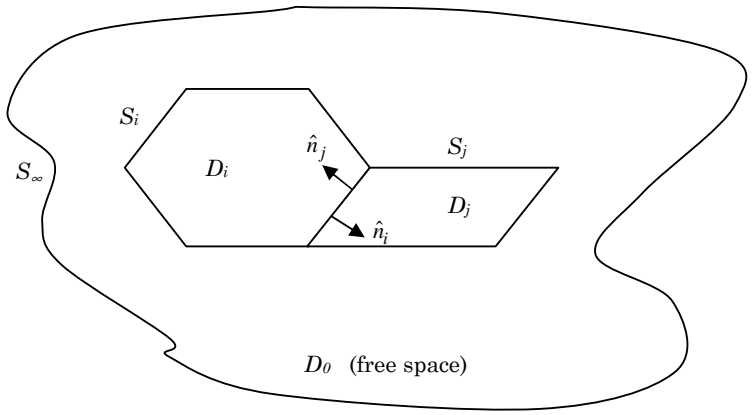

Figure 10 : Geometry for the boundary conditions

Table 3 : Boundary conditions summary

D_i and D_j have finite conductivity	D_i has finite conductivity D_j is PEC	D_i has finite conductivity D_j is PMC
$\hat{n}_i \times \overline{E}_i + \hat{n}_j \times \overline{E}_j = \overline{0}$	$\hat{n}_i \times \overline{E}_i = \overline{0}$ $\overline{E}_j = \overline{0}$	$\overline{E}_j = \overline{0}$
$\hat{n}_i \times \overline{H}_i + \hat{n}_j \times \overline{H}_j = \overline{0}$	$\overline{H}_j = \overline{0}$	$\hat{n}_i \times \overline{H}_i = \overline{0}$ $\overline{H}_j = \overline{0}$
$\hat{n}_i . \overline{D}_i + \hat{n}_j . \overline{D}_j = 0$	$\overline{D}_j = \overline{0}$	$\hat{n}_i . \overline{D}_i = 0$ $\overline{D}_j = \overline{0}$
$\hat{n}_i . \overline{B}_i + \hat{n}_j . \overline{B}_j = 0$	$\hat{n}_i . \overline{B}_i = 0$ $\overline{B}_j = \overline{0}$	$\overline{B}_j = \overline{0}$

These equations are usually said to be related to the normal and tangential components of the fields. It is correct for the normal components but it is a slight abuse of language for the tangential components.

The correct expression for the tangential component of $\overline{E}$ is $\overline{E}_t = -\hat{n} \times \hat{n} \times \overline{E}$. The vector $\hat{n} \times \overline{E}$ has the same amplitude as $\overline{E}_t$, but it is rotated by 90° in the plane of the interface, as shown in Figure 11.

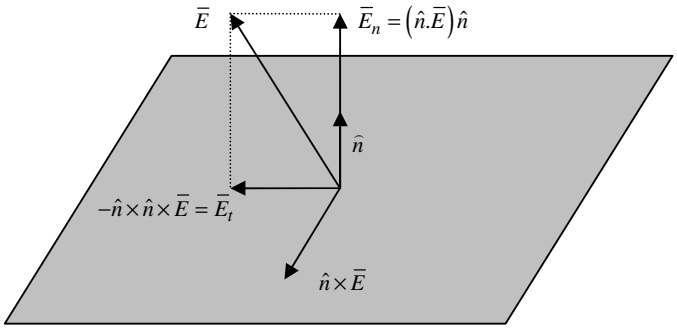

Figure 11 : Normal and tangential components

The classical proof of the boundary equations summarized in Table 3 (p.23) is based on the Stokes' and the divergence theorems [19, pp.19-31] :

$$\oint_C \bar{A}\, dl = \iint_S \left(\bar{\nabla}\times\bar{A}\right) dS \tag{62}$$

$$\oiint_S \left(\bar{A}.\hat{n}\right) dS = \iiint_V \left(\nabla.\bar{A}\right) dV \tag{63}$$

with the contour C, the surface S and the volume V being partly in both domains. This procedure is mathematically questionable because theorems requiring the continuity of $\bar{A}$ and of its first derivative are used to prove the discontinuities of $\bar{A}$ across the boundary. Stratton overcomes this problem by supposing that the fields vary extremely rapidly but continuously at the crossing of the interface [1, p.34].

1.8 Relations between normal and tangential components

Equations (58) and (59) contain both tangential and normal components of the total electric and magnetic fields. Similarly, the boundary conditions at the interface between domains listed in Table 3 (p.23) also involve the normal and tangential components.

Maxwell's equations allow to show that the normal and tangential components of the fields are not independent from each other. The differential form of these relationships can be found for example in [4, p.169] :

$$\hat{n}\cdot\bar{E} = \frac{-1}{j\omega\varepsilon}\nabla'_s\cdot\left(\hat{n}\times\bar{H}\right) \tag{64}$$

$$\hat{n}\cdot\bar{H} = \frac{+1}{j\omega\mu}\nabla'_s\cdot\left(\hat{n}\times\bar{E}\right) \tag{65}$$

Using (64) and (65) the integral relationships (66) and (67), where S is a closed surface and G is the free-space Green's function, are demonstrated in Appendix B :

$$\int_S \left(\bar{\nabla}'G\right)\left[\hat{n}\cdot\bar{E}\right] dS' = \frac{+1}{j\omega\varepsilon}\bar{\nabla}\nabla\cdot\int_S G\left(\hat{n}\times\bar{H}\right) dS' \tag{66}$$

$$\int_S \left(\bar{\nabla}'G\right)\left[\hat{n}\cdot\bar{H}\right]dS' = \frac{-1}{j\omega\mu}\bar{\nabla}\nabla\cdot\int_S G\left(\hat{n}\times\bar{E}\right)dS' \tag{67}$$

These relationships are used in §1.9 to rewrite the surface integrals occurring in the EFIE$_i$ and MFIE$_i$ in function of the normal or tangential components only.

1.9 First and second form of the integro-differential equations

We introduce the impedance Z_i, the admittance Y_i, and reintroduce the wave number k_i inside a domain D_i :

$$Z_i = Y_i^{-1} = \sqrt{\mu_i/\varepsilon_i} \tag{68}$$

$$k_i = \omega\sqrt{\varepsilon_i\mu_i} \tag{69}$$

With (8), the impedance of free space $Z_0 \approx 120\pi \approx 377\Omega$. Considering the definitions (60), (61) and the expressions (68) and (69), we can introduce (64) in (58) for the EFIE$_i$ and (65) in (59) for the MFIE$_i$, to obtain the *first vector form* of the EFIE$_i$ and MFIE$_i$:

$$\bar{E}_i^{inc}(\bar{r}) = \tilde{E}_i(\bar{r}) - \frac{jZ_i}{k_i}\int_{S_i}\left\{ k_i^2 G_i\bar{J}_i - \nabla'_s\cdot\bar{J}_i \;\; \bar{\nabla}'G_i\right\}dS' - \int_{S_i}\left\{\bar{M}_i\times\bar{\nabla}'G_i\right\}dS' \tag{70}$$

$$\bar{H}_i^{inc}(\bar{r}) = \tilde{H}_i(\bar{r}) - \frac{jY_i}{k_i}\int_{S_i}\left\{ k_i^2 G_i\bar{M}_i - \nabla'_s\cdot\bar{M}_i \;\; \bar{\nabla}'G_i\right\}dS' + \int_{S_i}\left\{\bar{J}_i\times\bar{\nabla}'G_i\right\}dS' \tag{71}$$

Introducing instead (66) in (58) for the EFIE$_i$ and (67) in (59) for the MFIE$_i$, we obtain :

$$\bar{E}_i^{inc}(\bar{r}) = \tilde{E}_i(\bar{r}) - \frac{jZ_i}{k_i}\left(k_i^2 + \bar{\nabla}\nabla\cdot\right)\int_{S_i} G_i\bar{J}_i\,dS' - \int_{S_i}\bar{M}_i\times\bar{\nabla}'G_i\,dS' \tag{72}$$

$$\bar{H}_i^{inc}(\bar{r}) = \tilde{H}_i(\bar{r}) - \frac{jY_i}{k_i}\left(k_i^2 + \bar{\nabla}\nabla\cdot\right)\int_{S_i} G_i\bar{M}_i\,dS' + \int_{S_i}\bar{J}_i\times\bar{\nabla}'G_i\,dS' \tag{73}$$

Expanding the differential operators (see Appendix C) we obtain the *second vector form* of the EFIE$_i$ and MFIE$_i$:

$$\bar{E}_i^{inc}(\bar{r}) = \tilde{E}_i(\bar{r}) - Z_i\int_{S_i}\left[\bar{J}_i\,f_{3,i} - \left(\bar{J}_i.\hat{R}\right)\hat{R}\,f_{3r,i}\right]k_i^2 dS' - \int_{S_i}\left\{\bar{M}_i\times\hat{R}\right\}f_{2,i}\,k_i^2 dS' \tag{74}$$

$$\bar{H}_i^{inc}(\bar{r}) = \tilde{H}_i(\bar{r}) - Y_i\int_{S_i}\left[\bar{M}_i\,f_{3,i} - \left(\bar{M}_i.\hat{R}\right)\hat{R}\,f_{3r,i}\right]k_i^2 dS' + \int_{S_i}\left\{\bar{J}_i\times\hat{R}\right\}f_{2,i}\,k_i^2 dS' \tag{75}$$

with the adimensional unit vector and functions :

$$\hat{R} = \frac{\bar{R}}{R} \tag{76}$$

$$f_{3,i} = \left(\frac{j}{k_i R} + \frac{1}{(k_i R)^2} - \frac{j}{(k_i R)^3}\right)\frac{e^{-jk_i R}}{4\pi} \tag{77}$$

$$f_{3r,i} = \left(\frac{j}{k_i R} + \frac{3}{(k_i R)^2} - \frac{3j}{(k_i R)^3} \right) \frac{e^{-jk_i R}}{4\pi} \tag{78}$$

$$f_{2,i} = \left(\frac{j}{k_i R} + \frac{1}{(k_i R)^2} \right) \frac{e^{-jk_i R}}{4\pi} \tag{79}$$

In the first form (70) and (71) the surface current densities $\bar{J}_i$ and $\bar{M}_i$ appear along with their first derivative, as well as the free-space Green's function. In the second form (74) and (75), the free-space Green's function appears up to its second derivative, while the surface current densities appear without any derivative.

Let us remember with (57) that the tilde vector notations $\tilde{E}_i(\bar{r})$ and $\tilde{H}_i(\bar{r})$ represent the total field when the observation point $\bar{r}$ is located inside V_i, only half of it if $\bar{r}$ is on the surface S_i, or the average between the total fields on both faces of S_i in the case of an embedded perfectly conducting sheet. The field itself inside V_i is under consideration when the scattered near or far field must be computed from the surface current densities. The expressions on the surface S_i will be used to solve the integro-differential equations, along with the boundary conditions.

1.10 Near and far scattered fields

We have derived expressions for the $EFIE_i$ and $MFIE_i$ valid inside any linear homogenous isotropic domain D_i. We refer to §1.5 for a discussion about the meaning of the incident and scattered fields inside D_i.

1.10.1 Exact near field expressions

Provided all sources are inside D_i, then in (70) and (74) the scattered electric field can be viewed as the sum of an electric field scattered by the equivalent electric current density (80) and an electric field scattered by the equivalent magnetic current density (81) :

$$\begin{aligned} \bar{E}_i^{sJ}(\bar{r}) &= \frac{jZ_i}{k_i} \int_{S_i} \left\{ k_i^2 G_i \bar{J}_i - \nabla'_s \cdot \bar{J}_i \;\; \bar{\nabla}' G_i \right\} dS' \\ &= Z_i \int_{S_i} \left[\bar{J}_i \, f_{3,i} - \left(\bar{J}_i . \hat{R} \right) \hat{R} \, f_{3r,i} \right] k_i^2 dS' \end{aligned} \tag{80}$$

$$\begin{aligned} \bar{E}_i^{sM}(\bar{r}) &= \int_{S_i} \left\{ \bar{M}_i \times \bar{\nabla}' G_i \right\} dS' \\ &= \int_{S_i} \left\{ \bar{M}_i \times \hat{R} \right\} f_{2,i} \, k_i^2 dS' \end{aligned} \tag{81}$$

Similarly, in (71) and (75), the scattered magnetic field can be viewed as the sum of a magnetic field scattered by the equivalent magnetic current density (82) and a magnetic field scattered by the equivalent electric current density (83) :

$$\begin{aligned}\bar{H}_i^{sM}(\bar{r}) &= \frac{jY_i}{k_i}\int_{S_i}\left\{\, k_i^2 G_i \bar{M}_i - \nabla'_s\cdot \bar{M}_i \;\; \bar{\nabla}' G_i\right\} dS' \\ &= Y_i \int_{S_i}\left[\bar{M}_i\, f_{3,i} - \left(\bar{M}_i.\hat{R}\right)\hat{R}\, f_{3r,i}\right] k_i^2 dS'\end{aligned} \tag{82}$$

$$\begin{aligned}\bar{H}_i^{sJ}(\bar{r}) &= -\int_{S_i}\left\{\, \bar{J}_i \times \bar{\nabla}' G_i\right\} dS' \\ &= -\int_{S_i}\left\{\bar{J}_i \times \hat{R}\right\} f_{2,i}\, k_i^2 dS'\end{aligned} \tag{83}$$

1.10.2 Far field approximation

The expressions (80) to (83) can be greatly simplified in the far field from a scattering or radiating object / antenna.

Considering the patch antenna of Figure 12 the radiated fields at a distant point $\bar{r}$ result from integrals taken over the whole surface of the antenna. The integration point $\bar{r}'$ is therefore running across the whole surface of the patch antenna. We can define a reference point 0 anywhere on this antenna, usually in the feed area, from which the vectors $\bar{r}$ and $\bar{r}'$ are defined.

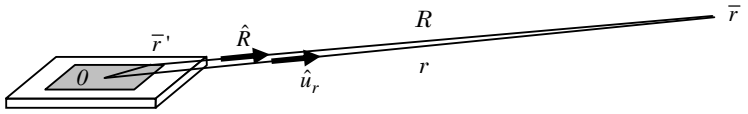

Figure 12 : Far field geometry

If the observation point $\bar{r}$ is sufficiently far away from the antenna, the following approximations can be applied :

- $\hat{R} \approx \hat{u}_r$
- $R \approx r$ for the amplitude terms
- $R \approx r - \bar{r}'.\hat{u}_r$ for the phase term

If we also consider in (77) to (79) that only the dominant term $j/(k_i R)$ remains, then (80) to (83) become in the far field :

$$\bar{E}_i^{sJ}(\bar{r}) \approx jk_i Z_i \frac{e^{-jk_i r}}{4\pi r}\int_{S_i}\left[\bar{J}_i - \left(\bar{J}_i.\hat{u}_r\right)\hat{u}_r\right] e^{jk_i\left(\bar{r}'.\hat{u}_r\right)}\, dS' \tag{84}$$

$$\bar{H}_i^{sJ}(\bar{r}) \approx -jk_i \frac{e^{-jk_i r}}{4\pi r}\int_{S_i}\left[\bar{J}_i \times \hat{u}_r\right] e^{jk_i\left(\bar{r}'.\hat{u}_r\right)}\, dS' \tag{85}$$

$$\bar{E}_i^{sM}(\bar{r}) \approx jk_i \frac{e^{-jk_i r}}{4\pi r}\int_{S_i}\left[\bar{M}_i \times \hat{u}_r\right] e^{jk_i\left(\bar{r}'.\hat{u}_r\right)}\, dS' \tag{86}$$

$$\bar{H}_i^{sM}(\bar{r}) \approx jk_i Y_i \frac{e^{-jk_i r}}{4\pi r}\int_{S_i}\left[\bar{M}_i - \left(\bar{M}_i.\hat{u}_r\right)\hat{u}_r\right] e^{jk_i\left(\bar{r}'.\hat{u}_r\right)}\, dS' \tag{87}$$

1.11 Normal and tangential components of the integro-differential equations on the surface S_i

The integro-differential equations (70), (72) and (74) for the EFIE$_i$ or (71), (73) and (75) for the MFIE$_i$ are vector equations, evaluated at an *ordinary* [2] observation point $\bar{r}$, involving all three components of the electric and magnetic field. For three reasons we will now project these equations either on $\hat{n}_i(\bar{r})$, the unit normal to S_i pointing outside V_i, or on a direction perpendicular to $\hat{n}_i(\bar{r})$.

The first reason is that we need to enforce the boundary conditions at the interface between every pair of adjacent domains; as we have seen in §1.7, the boundary conditions are related to the tangential and to the normal component of these fields, not to the total fields. We also remember from §1.8 that the normal and tangential boundary conditions are not independent from each other.

Secondly we observe under the integrals that the fields are already projected on the two directions prescribed by the boundary conditions, whereas only the extracted principal value term appears as the full three-dimensional field.

Thirdly, we would like integro-differential equations where the only unknowns are the surface current densities $\bar{J}_i$ and $\bar{M}_i$, and not the total fields $\bar{E}_i$ and $\bar{H}_i$.

Therefore we project the EFIE$_i$ and MFIE$_i$ on either the normal to S_i, premultiplying them with $\left[\hat{n}_i(\bar{r})\cdot\right]$, or on S_i, with the $\left[\hat{n}_i(\bar{r})\times\right]$ operation :

$$\begin{aligned}\hat{n}_i(\bar{r})\cdot\bar{E}_i^{inc}(\bar{r}) = &+\frac{jZ_i}{k_i}\nabla_s\cdot\tilde{J}_i(\bar{r}) - \hat{n}_i(\bar{r})\cdot\int_{S_i}\left\{\bar{M}_i\times\bar{\nabla}'G_i\right\}dS' \\ &-\frac{jZ_i}{k_i}\hat{n}_i(\bar{r})\cdot\int_{S_i}\left\{k_i^2G_i\bar{J}_i - \nabla'_s\cdot\bar{J}_i\ \ \bar{\nabla}'G_i\right\}dS'\end{aligned} \tag{88}$$

$$\begin{aligned}\hat{n}_i(\bar{r})\cdot\bar{H}_i^{inc}(\bar{r}) = &+\frac{jY_i}{k_i}\nabla_s\cdot\tilde{M}_i(\bar{r}) + \hat{n}_i(\bar{r})\cdot\int_{S_i}\left\{\bar{J}_i\times\bar{\nabla}'G_i\right\}dS' \\ &-\frac{jY_i}{k_i}\hat{n}_i(\bar{r})\cdot\int_{S_i}\left\{k_i^2G_i\bar{M}_i - \nabla'_s\cdot\bar{M}_i\ \ \bar{\nabla}'G_i\right\}dS'\end{aligned} \tag{89}$$

$$\begin{aligned}\hat{n}_i(\bar{r})\times\bar{E}_i^{inc}(\bar{r}) = &-\tilde{M}_i(\bar{r}) - \hat{n}_i(\bar{r})\times\int_{S_i}\left\{\bar{M}_i\times\bar{\nabla}'G_i\right\}dS' \\ &-\frac{jZ_i}{k_i}\hat{n}_i(\bar{r})\times\int_{S_i}\left\{k_i^2G_i\bar{J}_i - \nabla'_s\cdot\bar{J}_i\ \ \bar{\nabla}'G_i\right\}dS'\end{aligned} \tag{90}$$

$$\begin{aligned}\hat{n}_i(\bar{r})\times\bar{H}_i^{inc}(\bar{r}) = &+\tilde{J}_i(\bar{r}) + \hat{n}_i(\bar{r})\times\int_{S_i}\left\{\bar{J}_i\times\bar{\nabla}'G_i\right\}dS' \\ &-\frac{jY_i}{k_i}\hat{n}_i(\bar{r})\times\int_{S_i}\left\{k_i^2G_i\bar{M}_i - \nabla'_s\cdot\bar{M}_i\ \ \bar{\nabla}'G_i\right\}dS'\end{aligned} \tag{91}$$

We will further call these projections nEFIE$_i$ or nMFIE$_i$ for the normal projections, and tEFIE$_i$ or tMFIE$_i$ for the tangential projections.

[2] See §1.1 for the definition of an *ordinary* point

Similar expressions can be derived from the second form of the EFIE$_i$ (74) and MFIE$_i$ (75) :

$$\begin{aligned}\hat{n}_i(\bar{r})\cdot\bar{E}_i^{inc}(\bar{r}) = &+\frac{jZ_i}{k_i}\nabla_s\cdot\tilde{J}_i(\bar{r})+k_i^2\,\hat{n}_i(\bar{r})\cdot\int_{S_i}\bar{M}_i\times\hat{R}\,f_{2,i}\,dS'\\ &+Z_ik_i^2\,\hat{n}_i(\bar{r})\cdot\int_{S_i}\left[\bar{J}_i\,f_{3,i}-\left(\bar{J}_i.\hat{R}\right)\hat{R}\,f_{3r,i}\right]dS'\end{aligned} \tag{92}$$

$$\begin{aligned}\hat{n}_i(\bar{r})\cdot\bar{H}_i^{inc}(\bar{r}) = &+\frac{jY_i}{k_i}\nabla_s\cdot\tilde{M}_i(\bar{r})-k_i^2\,\hat{n}_i(\bar{r})\cdot\int_{S_i}\bar{J}_i\times\hat{R}\,f_{2,i}\,dS'\\ &+Y_ik_i^2\,\hat{n}_i(\bar{r})\cdot\int_{S_i}\left[\bar{M}_i\,f_{3,i}-\left(\bar{M}_i.\hat{R}\right)\hat{R}\,f_{3r,i}\right]dS'\end{aligned} \tag{93}$$

$$\begin{aligned}\hat{n}_i(\bar{r})\times\bar{E}_i^{inc}(\bar{r}) = &-\tilde{M}_i(\bar{r})+k_i^2\,\hat{n}_i(\bar{r})\times\int_{S_i}\bar{M}_i\times\hat{R}\,f_{2,i}\,dS'\\ &+Z_ik_i^2\,\hat{n}_i(\bar{r})\times\int_{S_i}\left[\bar{J}_i\,f_{3,i}-\left(\bar{J}_i.\hat{R}\right)\hat{R}\,f_{3r,i}\right]dS'\end{aligned} \tag{94}$$

$$\begin{aligned}\hat{n}_i(\bar{r})\times\bar{H}_i^{inc}(\bar{r}) = &+\tilde{J}_i(\bar{r})-k_i^2\,\hat{n}_i(\bar{r})\times\int_{S_i}\bar{J}_i\times\hat{R}\,f_{2,i}\,dS'\\ &+Y_ik_i^2\,\hat{n}_i(\bar{r})\times\int_{S_i}\left[\bar{M}_i\,f_{3,i}-\left(\bar{M}_i.\hat{R}\right)\hat{R}\,f_{3r,i}\right]dS'\end{aligned} \tag{95}$$

The equations obtained with the normal projection are scalar, while those obtained with the tangential projection yield two-dimensional vectors lying on S_i.

It is important to remember that everything outside the integrals, $\hat{n}_i(\bar{r})$, $\bar{E}^{inc}(\bar{r})$, $\bar{H}^{inc}(\bar{r})$, $\tilde{J}(\bar{r})$ and $\tilde{M}(\bar{r})$ depend on a fixed observation point $\bar{r}$ on the surface S_i, and that all derivatives (∇_s and $\bar{\nabla}$) are taken with regard to the coordinate $\bar{r}$. Inside the integrals, the vector functions $\bar{J}(\bar{r}')$ and $\bar{M}(\bar{r}')$ depend on $\bar{r}'$ only whereas the free-space Green's function G_i depends on $|\bar{r}-\bar{r}'|$. The derivatives (∇'_s and $\bar{\nabla}'$) are taken with respect to the coordinate $\bar{r}'$.

1.12 Perfectly conducting sheets

We have seen in §1.4.1 that a dielectric sheet is completely transparent to electromagnetic waves. The boundary conditions listed in

Table **3** (p.23) in §1.7 show that the electric (magnetic) field is normal (tangent) to the surface of a perfect electric conductor (PEC). We turn now our attention to the MFIE (47) and EFIE (48) particularized for a PEC sheet, introducing the electric surface current density $\bar{J}$ defined by (60).

Considering the location $\bar{r}$ in Figure 13 (p.30) where the PEC sheet is embedded on both sides S_a and S_b in one domain (case 4 in Figure 9, p.19) :

$$\bar{E}^{inc}(\bar{r}) = \frac{1}{2}\left\{\bar{E}_a(\bar{r})+\bar{E}_b(\bar{r})\right\}-\frac{jZ}{k}\oint_{S_a+S_b}\left\{k^2G\bar{J}+\nabla'_s\cdot\bar{J}\,\bar{\nabla}'G\right\}dS' \tag{96}$$

$$\bar{H}^{inc}(\bar{r}) = \frac{1}{2}\left\{\bar{H}_a(\bar{r})+\bar{H}_b(\bar{r})\right\}+\oint_{S_a+S_b}\left\{\bar{J}\times\bar{\nabla}'G\right\}dS' \tag{97}$$

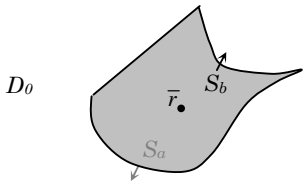

Figure 13 : PEC sheet

In (96) and (97) the integrals on $S_a + S_b$ can be computed as an integral on the face S_a only, but with the sum of the current densities on both faces S_a and S_b in the integrand. If the observation point $\bar{r} = \bar{r}_a$ is situated on the face S_a, projecting the EFIE and MFIE with $\left[\hat{n}_a(\bar{r})\cdot\right]$ or $\left[\hat{n}_a(\bar{r})\times\right]$ we obtain :

$$\begin{aligned}\hat{n}_a(\bar{r})\cdot\bar{E}^{inc}(\bar{r}) = &+\frac{jZ}{k}\nabla_s\cdot\left(\bar{J}_a-\bar{J}_b\right)(\bar{r})\\ &-\frac{jZ}{k}\hat{n}_a(\bar{r})\cdot\oint_{S_a}\left\{k^2G\left(\bar{J}_a+\bar{J}_b\right)+\nabla_s'\cdot\left(\bar{J}_a+\bar{J}_b\right)\bar{\nabla}'G\right\}dS'\end{aligned} \tag{98}$$

$$\hat{n}_a(\bar{r})\cdot\bar{H}^{inc}(\bar{r}) = \hat{n}_a(\bar{r})\cdot\oint_{S_a}\left\{\left(\bar{J}_a+\bar{J}_b\right)\times\bar{\nabla}'G\right\}dS' \tag{99}$$

$$\hat{n}_a(\bar{r})\times\bar{E}^{inc}(\bar{r}) = -\frac{jZ}{k}\hat{n}_a(\bar{r})\times\oint_{S_a}\left\{k^2G\left(\bar{J}_a+\bar{J}_b\right)+\nabla_s'\cdot\left(\bar{J}_a+\bar{J}_b\right)\bar{\nabla}'G\right\}dS' \tag{100}$$

$$\hat{n}_a(\bar{r})\times\bar{H}^{inc}(\bar{r}) = \frac{\left(\bar{J}_a-\bar{J}_b\right)(\bar{r})}{2}+\hat{n}_a(\bar{r})\times\oint_{S_a}\left\{\left(\bar{J}_a+\bar{J}_b\right)\times\bar{\nabla}'G\right\}dS' \tag{101}$$

The important observation is that (99) and (100) contain only $\left(\bar{J}_a+\bar{J}_b\right)$, whereas (98) and (101) also contain $\left(\bar{J}_a-\bar{J}_b\right)$. Either (99) or (100) can therefore be used to determine the sum of the surface current density on both faces of a PEC sheet, but none of these four integral equations allow to find $\bar{J}_a$ and $\bar{J}_b$ isolately. To this end, it is necessary to combine any two equations, except (99) and (100) as they both contain only $\left(\bar{J}_a+\bar{J}_b\right)$.

Dual equations and conclusions can be established for PMC sheets.

1.13 Sum of Fields on both sides of a flat perfectly conducting sheet of arbitrary shape

We now present simple closed form expressions for the sum of the fields on both sides of a flat perfectly conducting sheet such as the one depicted in Figure 14 (p.31). The observation point $\bar{r}$ can be anywhere on the flat sheet, except on a sharp edge or on a corner, where some components of the fields can be infinite.

As the sheet is flat, regardless of its shape and dimensions, then both vectors $\bar{\nabla}'G(\bar{r}-\bar{r}') = C.(\bar{r}-\bar{r}')$ and $\bar{J}(\bar{r}')$ are always lying in the plane of the sheet for every pair $(\bar{r},\bar{r}')$ in the sheet. As a consequence :

$$\hat{n}(\bar{r})\cdot\bar{\nabla}'G(\bar{r}-\bar{r}') = 0 \tag{102}$$

$$\hat{n}(\bar{r})\times\left[J(\bar{r}')\times\bar{\nabla}'G(\bar{r}-\bar{r}')\right]=\bar{0} \tag{103}$$

Starting from (96) and (97) this leads to the two following closed form expressions for the sum of fields on both faces of a flat PEC sheet, where $\hat{n}$ can again be either $\hat{n}_a$ or $\hat{n}_b$:

$$2\hat{n}\times\bar{H}^{inc}=\hat{n}\times\left(\bar{H}_a+\bar{H}_b\right) \tag{104}$$

$$2\hat{n}\cdot\bar{E}^{inc}=\hat{n}\cdot\left(\bar{E}_a+\bar{E}_b\right) \tag{105}$$

Choosing for example $\hat{n}=\hat{n}_a$, (104) and (105) can be rewritten in terms of equivalent surface current densities :

$$2\hat{n}_a\times\bar{H}^{inc}=\bar{J}_a-\bar{J}_b \tag{106}$$

$$2\hat{n}_a\cdot\bar{E}^{inc}=\frac{jZ}{k}\nabla_s\cdot\left(\bar{J}_a-\bar{J}_b\right) \tag{107}$$

Equation (106) is an exact generalization for flat PEC plates of finite extent and arbitrary shape of the well known physical optics approximation : let the incident field come from the a side of a flat PEC plate of infinite extent, then $\bar{J}_b=\bar{0}$ in (106). This result had already been announced [20], but the given demonstration, based on reaction integral equations instead of field integral equations, must be considered as incomplete as it explicitely ignores the edges.

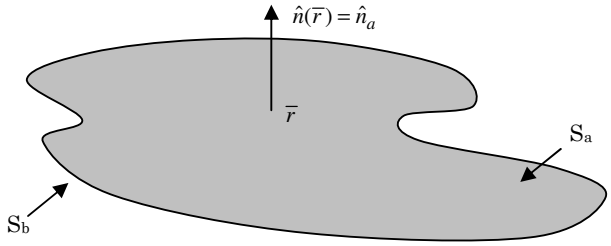

Figure 14 : Flat perfectly conducting sheet of arbitrary shape

To conclude, it is worth mentioning that :

- Equations (104) and (105) could have been derived easily and directly from the (anti)symmetry relationships listed in [21, p.636] or also in [22, p.497] valid for the electric and magnetic field scattered by a flat PEC sheet of any shape and extent
- Dual properties apply to a flat PMC sheet

1.14 Canonical expressions

All the equations obtained in §1.11 can be nicely summarized in a short notation that will be very useful during the discretization steps.

Considering an observation point $\bar{r}$ and the outwards directed unit normal $\hat{n}_i(\bar{r})$ on the surface S_i enclosing domain D_i , we define the vector functions applied to another vector function $\bar{F}$:

$$\tilde{N}_i\left\{\bar{F}\right\}(\bar{r}) = \frac{j}{k_i}\left\{\nabla_s \cdot \tilde{F}(\bar{r})\right\}\hat{n}_i(\bar{r}) \tag{108}$$

$$\tilde{T}_i\left\{\bar{F}\right\}(\bar{r}) = \hat{n}_i(\bar{r}) \times \tilde{F}(\bar{r}) \tag{109}$$

$$\bar{D}_i^{(1)}\left\{\bar{F}\right\}(\bar{r}) = \frac{j}{k_i}\int_{S_i}\left\{\ k_i^2 G_i(\bar{r}-\bar{r}')\bar{F}(\bar{r}') - \nabla'_s \cdot \bar{F}(\bar{r}')\ \ \bar{\nabla}' G_i(\bar{r}-\bar{r}')\right\} dS' \tag{110}$$

$$\bar{D}_i^{(2)}\left\{\bar{F}\right\}(\bar{r}) = k_i^2 \int_{S_i}\left[\bar{F}\, f_{3,i} - \left(\bar{F}\cdot\hat{R}\right)\hat{R}\, f_{3r,i}\right] dS' \tag{111}$$

$$\bar{K}_i^{(1)}\left\{\bar{F}\right\}(\bar{r}) = \int_{S_i}\left\{\bar{F}\times\bar{\nabla}' G_i\right\} dS' \tag{112}$$

$$\bar{K}_i^{(2)}\left\{\bar{F}\right\}(\bar{r}) = k_i^2 \int_{S_i}\left\{\bar{F}\times\hat{R}\right\} f_{2,i}\, dS' \tag{113}$$

where

- $G_i(\bar{r}-\bar{r}')$ is the free-space Green's function in the domain D_i with wavenumber k_i, whose expression is given by (56)
- $\hat{R}$ and the functions $f_{2,i}$, $f_{3,i}$ and $f_{3r,i}$ have been defined by (76), (77), (78) and (79)
- The tilde notation in (108) and (109) has been defined by in §1.5

Note that :

- all these functions have the dimension of the vector function $\bar{F}$
- Only the functions $\tilde{N}_i$ and $\bar{D}_i^{(1)}$ contain the first derivative of the vector function $\bar{F}$
- $\bar{D}_i^{(1)}\left\{\bar{F}\right\}(\bar{r}) = \bar{D}_i^{(2)}\left\{\bar{F}\right\}(\bar{r}) = \bar{D}_i\left\{\bar{F}\right\}(\bar{r})$
- $\bar{K}_i^{(1)}\left\{\bar{F}\right\}(\bar{r}) = \bar{K}_i^{(2)}\left\{\bar{F}\right\}(\bar{r}) = \bar{K}_i\left\{\bar{F}\right\}(\bar{r})$

The first form of the integro-differential equations, (88) to (90), and the second form of the same equations, (92) to (95), can now be rewritten as :

$$\hat{n}_i(\bar{r})\cdot\bar{E}_i^{inc}(\bar{r}) = \hat{n}_i(\bar{r})\cdot\left\{\left[\tilde{N}_i - \bar{D}_i\right]\left\{Z_i\bar{J}_i\right\}(\bar{r}) - \bar{K}_i\left\{\bar{M}_i\right\}(\bar{r})\right\} \tag{114}$$

$$\hat{n}_i(\bar{r})\cdot Z_i\bar{H}_i^{inc}(\bar{r}) = \hat{n}_i(\bar{r})\cdot\left\{+\bar{K}_i\left\{Z_i\bar{J}_i\right\}(\bar{r}) + \left[\tilde{N}_i - \bar{D}_i\right]\left\{\bar{M}_i\right\}(\bar{r})\right\} \tag{115}$$

$$\hat{n}_i(\bar{r})\times\bar{E}_i^{inc}(\bar{r}) = \hat{n}_i(\bar{r})\times\left\{-\bar{D}_i\left\{Z_i\bar{J}_i\right\}(\bar{r}) + \left[\tilde{T}_i - \bar{K}_i\right]\left\{\bar{M}_i\right\}(\bar{r})\right\} \tag{116}$$

$$\hat{n}_i(\bar{r})\times Z_i\bar{H}_i^{inc}(\bar{r}) = \hat{n}_i(\bar{r})\times\left\{-\left[\tilde{T}_i - \bar{K}_i\right]\left\{Z_i\bar{J}_i\right\}(\bar{r}) - \bar{D}_i\left\{\bar{M}_i\right\}(\bar{r})\right\} \tag{117}$$

The sole difference between the first and second form of the equations resides in the use of $\bar{D}_i^{(1)}$ or $\bar{D}_i^{(2)}$ for the integro-differential operator $\bar{D}_i$ and $\bar{K}_i^{(1)}$ or $\bar{K}_i^{(2)}$ for the integral operator $\bar{K}_i$.

Note also with (80), (81), (82) and (83) that the operator $\bar{D}_i$ applied to $Z_i\bar{J}_i$ ($\bar{M}_i$) yields that part of the "scattered" electric (magnetic) field due to the equivalent electric (magnetic) current density, while the operator $\bar{K}_i$ applied to $-\bar{J}_i$ ($Y_i\bar{M}_i$) yields that part of the "scattered" magnetic (electric) field due to the equivalent electric (magnetic) current density. By quoting "scattered" we remind the refer to the actual meaning of "scattered field" in a multidomain and multisources environment (see the end of §1.5).

1.15 Summary

This chapter has laid the theoretical fundations for the following ones, devoted to the numerical resolution of electromagnetic scattering problems with the Method of Moments. To this end, exact integral equations must be derived from Maxwell's equations and boundary conditions must be expressed. In this process, the unknowns appear under the form of equivalent current densities, electric and/or magnetic, defined at the bounding surface of every non perfectly conducting volumic homogenous region.

To analyze any combination of three-dimensional homogeneous, linear and isotropic bodies, new integral expressions have been presented and demonstrated that are very general in many ways : they are given in their full three-dimensional vector form for both the electric and magnetic version, they have been derived for the specific case of sheets, they have been proposed in a first and second form, and they have been cast into canonical forms with the introduction of original notations.

The generalization of the existing EFIE and MFIE to the case of sheets has revealed a new set of theorems valid for flat perfectly conducting sheets of finite extent and arbitrary contour. One of these theorems can be regarded as a generalization of the well-known physical optics approximation.

The generalization to the full three-dimensional vector forms has permitted to derive a new formulation based on the normal components of the EFIE and MFIE, aside those exclusively used, based on the tangential components.

[1] A.J. Stratton, *Electromagnetic Theory*, Mc Graw Hill Book Company New York and London, 1941.

[2] A. Ishimaru, *Electromagnetic Wave Propagation, Radiation and Scattering*, Prentice Hall Inc., 1991.

[3] A.W. Maue, "The formulation of a general diffraction problem by an integral equation", *Zeitschrift für Physik.*, Bd. 126, pp. 601-618, 1949.

[4] A. J. Poggio and E. K. Miller, "Integral equation solutions of three dimensional scattering problems, in *Computer Techniques for Electromagnetics*. Oxford, U.K.: Pergamon, 1973, chap. 4.

[5] J. Van Bladel, *Singular Electromagnetic Fields and Sources*, IEEE Press, New York, 1991.

[6] A. S. Ilyinsky, Yu. G. Smirnov, *Electromagnetic Wave Diffraction by Conducting Screens : Pseudodifferential Operators in Diffraction Problems*, Utrecht, The Netherlands, 1998.

[7] J. Van Bladel, *Electromagnetic Fields*, Mc Graw Hill, New York, 1964.

[8] A. D. Yaghjian, "Augmented Electric- and Magnetic-Field Integral Equations" , *Radio Sci.,* Vol. 16, pp. 987-1001, November 2001.

[9] J.M. Rius, E. Ubeda, J. Parron, "On The Testing of the Magnetic Field Integral Equation With RWG Basis Functions in Method of Moments", *IEEE Transactions on Antennas and Propagation*, Vol. 49, No.11, November 2001.

[10] Ö. Ergül and L. Gürel, "Solid Angle Factor in the Magnetic-Field Integral Equation" , *Microwave and Optical Technology Letters* Vol. 45, No.5, June 2005.

[11] J.-C. Bolomey and A. Wirgin "Sur le comportement du champ électromagnétique aux arêtes" *Annales de l'I.H.P.*, Section A, tome 14, No.2, pp. 97-112, 1971.

[12] M.A. Leontovitch, "Investigations of Propagation of Radiowaves, Part II", Soviet Radio, Moscow, 1948.

[13] D.S. Wang, "Limits and validity of the impedance boundary condition" , *IEEE Transactions on Antennas and Propagation* Vol. 35, No.4, pp. 453-457, April 1987.

[14] G.P. Junker, A.A. Kishk and A.W. Glisson, "A Novel Delta Gap Source Model for Center Fed Cylindrical Dipoles" , *IEEE Transactions on Antennas and Propagation* Vol. 43, No.5, pp. 537-540, May 1995.

[15] L.L. Tsai, "A Numerical Solution for the Near and Far Fields of an Annular Ring of Magnetic Current" , *IEEE Transactions on Antennas and Propagation*, Vol. 20, No.5, pp. 569-576, Sep 1972.

[16] G. Fikioris, J. Lionas and C.G. Lioutas "The Use of Frill Generator in Thin-Wire Integral Equations", *IEEE Transactions on Antennas and Propagation*, Vol. 51, No.8, pp. 1847-1854, Aug 2003.

[17] M. Davidovitz, Y.T. Lo, "Rigorous Analysis of Circular Patch Antenna Excited by a Microstrip Transmission Line" , *IEEE Transactions on Antennas and Propagation*, Vol. 37, No.8, pp. 949-958, Aug 1989.

[18] A. Sommerfeld, *Partial Differential Equations in Physics*, New York: Academic Press, 1949.

[19] J.A. Kong, *Electromagnetic Wave Theory*, EMW Publishing, Cambridge, Massachussets, 2005.

[20] E.H. Newman and M.R. Schrote, "On the Current Distribution for Open Surfaces", *IEEE Transactions on Antennas and Propagation*, Vol. 31, No. 3, pp. 515-518, May 1983.

[21] M. Born, E. Wolf, *Principles of Optics*, 7th (expanded) edition, Cambridge University Press, London, 1999.

[22] A. Hirose, H. Li, S. Livingstone and X.F .Lu, "On diffraction of electromagnetic waves by an aperture in a conducting screen", *Can. J. Phys.*, Vol. 82, pp. 495-500, June 2004.

2 Method of Moments

Despite the existence of a very mature and complete theory of electromagnetics, most real life problems are too complex and would remain unsolvable without the help of numerical approximation techniques. The Method of Moments is one of them, particularly well suited to analyze the harmonic scattering or radiation by the objets under consideration in this book : homogeneous and isotropic bodies that are not too large as compared to the wavelength.

The discretized version of the canonical exact expressions obtained in chapter 1 is kept very general. This allows a detailed discussion on basis functions, for which two important observations are made, explained and illustrated. Firstly curl conforming basis functions cannot be used in conjunction with the electric or magnetic field integral equation. Secondly the limited linearity of the most popular basis functions – RWG and rooftop – is responsible for some erratic behavior in the fine details of the solution, especially but not exclusively close to edges.

Also the testing process and resulting expressions are presented in a very general form based on the full vector expressions, putting new light on the tangential testing and introducing the normal testing. A closer look to the possible testing functions involved in this crucial step reveals why some choices are wrong, acceptable or very good. To illustrate these original considerations, unused testing schemes are successfully applied.

2.1 Preamble

In chapter 1 we have presented harmonic integro-differential equations and boundary conditions that describe exactly electromagnetic problems, such as the radiation by an antenna or the scattering by a complex body, made of dielectric and/or perfectly conducting bodies. After normal or tangential projection, the initial vector equations can all be expressed in function of only two vector unknowns, the equivalent surface electric and magnetic current densities $\bar{J}_i$ and $\bar{M}_i$. If we can solve the integro-differential equations for those current densities, excited at the surface S_i of every domain D_i by the combined effect of all sources, then many interesting properties can be deduced from them : radiated or scattered near and far field, radiation pattern, scattering coefficients, impedance at access feeds if the body is used as an antenna.

Exact solutions for finite-sized volumic structures are only known for a few simple and smooth geometries, like the sphere [1], the tri-axial ellipsoid [2][3] and the torus [4]. No solution is known to date for perfectly conducting or dielectric volumes having sharp edges or corners, the simplest of all being the cube and the cylinder with circular base. For finite-sized PEC sheets, many solutions exist for the circular disc, for example [5][6], and one solution is known to the author for the rectangular sheet [7].

Aside these few canonical but useful examples, one must resort to numerical methods to find an approximation of the solution to real-life problems involving complex-shaped antennas or scatterers. Among the many mature numerical methods available today, the Method of Moments (MoM) will be used and analyzed in this book. It starts from the correct expressions of the integro-differential equations and only introduces errors when solving these numerically.

It is interesting to mention here that even analytical solutions are usually approximate in practice, when it comes to evaluating them; such solutions, derived from separation of variables and suitable special functions, usually involve infinite summations which must be truncated. Furthermore, the evaluation of the special functions is almost exclusively done computationally nowadays, a process not strictly always reliable and sometimes suffering from convergence issues.

Instead of presenting the general theory of the MoM, which can be found in its full extent in the first reference book that introduced it [8], we choose to apply it directly to the integro-differential equations presented in §1.14, showing how a matrix system of equations is created to obtain an approximate solution.

2.2 Basis functions

Except in a few simple cases, it is not possible to find in every domain D_i the analytic expressions for $\bar{J}_i(\bar{r})$ and $\bar{M}_i(\bar{r})$ that would be the exact solution at any location $\bar{r}$ on the boundary S_i. In the MoM, we try to find instead an approximation (see §5.1) in the form of a series expansion :

$$\bar{J}_i(\bar{r}) \cong \sum_{j_i=1}^{N_i^J} J_{j_i} \bar{f}_{j_i}^J(\bar{r}) \tag{118}$$

$$\bar{M}_i(\bar{r}) \cong \sum_{m_i=1}^{N_i^M} M_{m_i} \bar{f}_{m_i}^M(\bar{r}) \tag{119}$$

where the vector functions $\bar{f}_{j_i}^J$ and $\bar{f}_{m_i}^M$ are known basis functions and J_{j_i} , M_{m_i} are unknown complex scalar coefficients to determine.

If the basis functions are defined for every $\bar{r}$ over the entire surface S_i, they are called entire domain basis functions (§2.2.3). Otherwise they are called subdomain basis functions (§2.2.4).

2.2.1 Scalar or vector basis functions

With (118) and (119) we introduced vector basis functions. The two-dimensional vectors $\bar{J}_i(\bar{r})$ and $\bar{M}_i(\bar{r})$ could also be represented by scalar basis functions (for x, y and z components separately for example). This choice is quite natural for flat structures, as will be shown in the entire domain basis function example of §2.2.3, but a major difficulty arises from this choice for non flat structures : the boundary conditions are expressed in terms of normal and tangential components (see §1.7), and they become tedious to enforce on arbitrary three-dimensional

structures because all three components are involved simultaneously. Therefore, vector basis functions are preferred, as they allow easy enforcement of the boundary conditions through decoupled parameters.

2.2.2 Discretized equations

With equations (114) to (117) we have established canonical expressions for the first and second form of the n- or tEFIE$_i$ and n- or tMFIE$_i$, valid inside a volumic dielectric domain D_i possibly enclosing, completely or partially, dielectric or perfectly conducting volumes and/or perfectly conducting sheets, and possibly enclosed itself in surrounding free-space, entirely or partially.

Inserting in (114) to (117) the expansions (118) and (119), we obtain :

$$\hat{n}_i(\bar{r})\cdot\bar{E}_i^{inc}(\bar{r}) = \hat{n}_i(\bar{r})\cdot\left\{\sum_{j_i}^{N_i^J} Z_i J_{j_i}\left[\tilde{N}_i-\bar{D}_i\right]\left\{\bar{f}_{j_i}^J\right\}(\bar{r}) - \sum_{m_i}^{N_i^M} M_{m_i}\bar{K}_i\left\{\bar{f}_{m_i}^M\right\}(\bar{r})\right\} \tag{120}$$

$$\hat{n}_i(\bar{r})\cdot Z_i\bar{H}_i^{inc}(\bar{r}) = \hat{n}_i(\bar{r})\cdot\left\{\sum_{j_i}^{N_i^J} Z_i J_{j_i}\bar{K}_i\left\{\bar{f}_{j_i}^J\right\}(\bar{r}) + \sum_{m_i}^{N_i^M} M_{m_i}\left[\tilde{N}_i-\bar{D}_i\right]\left\{\bar{f}_{m_i}^M\right\}(\bar{r})\right\} \tag{121}$$

$$\hat{n}_i(\bar{r})\times\bar{E}_i^{inc}(\bar{r}) = \hat{n}_i(\bar{r})\times\left\{-\sum_{j_i}^{N_i^J} Z_i J_{j_i}\bar{D}_i\left\{\bar{f}_{j_i}^J\right\}(\bar{r}) + \sum_{m_i}^{N_i^M} M_{m_i}\left[\tilde{T}_i-\bar{K}_i\right]\left\{\bar{f}_{m_i}^M\right\}(\bar{r})\right\} \tag{122}$$

$$\hat{n}_i(\bar{r})\times Z_i\bar{H}_i^{inc}(\bar{r}) = \hat{n}_i(\bar{r})\times\left\{-\sum_{j_i}^{N_i^J} Z_i J_{j_i}\left[\tilde{T}_i-\bar{K}_i\right]\left\{\bar{f}_{j_i}^J\right\}(\bar{r}) - \sum_{m_i}^{N_i^M} M_{m_i}\bar{D}_i\left\{\bar{f}_{m_i}^M\right\}(\bar{r})\right\} \tag{123}$$

These discretized equations contain $N_i^J + N_i^M$ complex scalar unknowns J_{j_i} and M_{m_i} independent of $\bar{r}$ instead of two complex vector unknowns $\bar{J}(\bar{r})$, $\bar{M}(\bar{r})$. To solve them for J_{j_i} and M_{m_i}, we need to generate at least $N_i^J + N_i^M$ independent equations.

The exact and discretized integro-differential equations represent an infinity of equations that must all be verified simultaneously at every possible location $\bar{r}$ on S_i. During the testing process, described in §2.3, we will reduce this infinite number of equations to a finite number.

2.2.3 Entire Domain basis functions

The basis functions used in the analytical methods are of the entire domain type and orthogonal in nature : sinusoidal, Bessel or Legendre functions, Chebyshev polynomials or power series. If the set of basis functions is complete, which most often requires an infinite number of orthogonal functions, the series expansion

can be made equal to the exact solution. Consequently, truncation of the series yields an approximation of the exact solution.

As an example, let us try to model the sum of the electric current density variations on both sides of a *L*x*W* rectangular PEC sheet lying in the $z = 0$ plane with the following expansion :

$$\bar{J}(x,y) \cong \hat{x}\, J_x(x,y) + \hat{y}\, J_y(x,y) \tag{124}$$

with :

$$J_x(x,y) = \sum_m \sum_n a_{mn} J^x_{mn}(x,y) \tag{125}$$

$$J_y(x,y) = \sum_p \sum_q b_{pq} J^y_{pq}(x,y) \tag{126}$$

$$J^x_{mn}(x,y) = \sin\left(\frac{m\pi}{L}\left[x+\frac{L}{2}\right]\right)\cos\left(\frac{n\pi}{W}\left[y+\frac{W}{2}\right]\right) \tag{127}$$

$$J^y_{pq}(x,y) = \cos\left(\frac{p\pi}{L}\left[x+\frac{L}{2}\right]\right)\sin\left(\frac{q\pi}{W}\left[y+\frac{W}{2}\right]\right) \tag{128}$$

The use of entire domain basis functions such as (127) and (128) is efficient only when the first few functions suffice to approximate $\bar{J}_i(\bar{r})$ and $\bar{M}_i(\bar{r})$ to the desired accuracy. This is the case if the expansion functions match the eigenfunctions of the problem and when the eigenfunctions series are rapidly convergent. There are many possible sets of basis functions for a given problem. Some sets may give faster convergence, or matrix elements which are easier to evaluate, or on the contrary divergence. In the example of the rectangular sheet, the convergence can be greatly improved if the growth to infinity in the vicinity of the edges is included, with additional factors like $[1-(2y/W)^2]^{-1/2}$ for (127) and $[1-(2x/L)^2]^{-1/2}$ for (128) [9][10][11]. The function $J^x_{12}(x,y)$ is represented in Figure 15, with and without the additional edge factor.

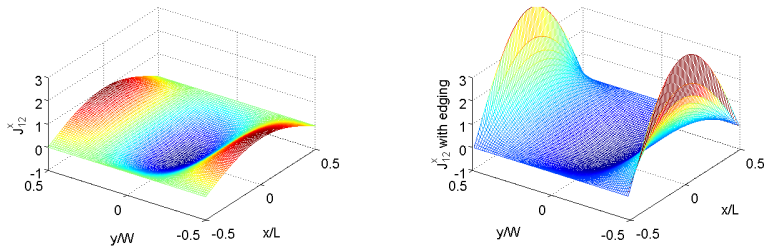

(a) without edge factor (b) with edge factor

Figure 15 : Entire domain basis function over a rectangular sheet

The entire domain basis functions are powerful to model smooth variations such as those encountered on regularly shaped geometries, for example rectangular and circular sheets. However their disadvantages are numerous :

- To benefit from the use of entire domain basis functions it is necessary to guess the function to approximate
- They are not versatile enough to model complex shapes (consider for example slots and notches in the rectangular sheet)
- If elaborate basis functions are used, they can render the computations occurring to fill the MoM matrix tedious and lengthy
- The use of entire domain basis functions is likely to increase the condition number very rapidly with the order of the MoM matrix [12, p.461]. It is therefore vital to use as few terms as possible in the expansion

As we are interested in the modelling of arbitrary three-dimensional geometries, we turn now our attention to subdomain basis functions.

2.2.4 Subdomain basis functions

Subdomain basis functions require that subdomains be defined in all domains D_i. The way of dividing the surface S_i enclosing D_i into subdomains is strongly related to the characteristics of the basis functions, but also to the way boundary conditions between domains are enforced. Remembering that we must discretize integro-differential expressions including integrals over the entire surface S_i, the complete set of subdomains must entirely cover S_i.

Ideally a curved surface S_i should be divided into small curved subdomains conformal to S_i, as shown in Figure 16.

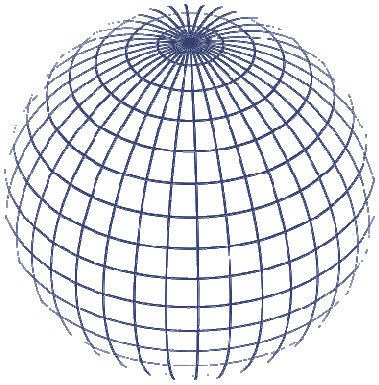

Figure 16 : Curved mesh on a sphere

This requires in turn that vector basis functions be defined on a curved surface. Such subdomain basis functions have been studied [13][14], but are not widely used due to their increased mathematical complexity, but also to the difficulty to model curved surfaces that cannot be represented with polynomial functions.

The most popular way of meshing a surface S_i with elementary subdomains is by far with straight-edged triangles, quadrangles, or a combination of both. A mesh constructed with such subdomains cannot exactly conform to a curved surface S_i, for which this meshing choice introduces an additional discretization error

(see §5.1) : not only the current densities are approximated, but also the surface S_i.

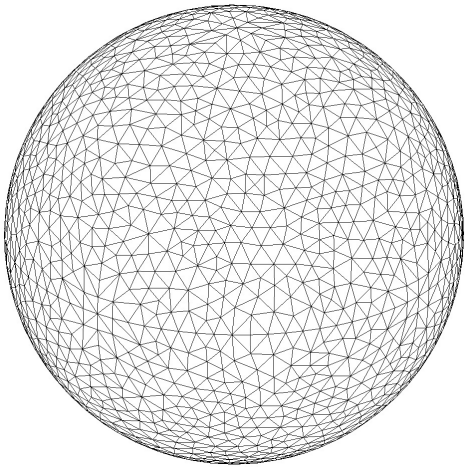

Figure 17 : Mesh of a sphere with flat triangles

Subdomain basis functions can be defined on individual subdomains (pulse basis functions, §2.2.6), pair of subdomains (see §2.2.8), or even larger groups of subdomains (characteristic basis functions [15], synthetic functions [16], multiresolution hierarchical basis functions [17], star loop decomposition of basis functions [18]). Most basis functions defined on two or more subdomains require that all adjacent subdomains share exactly entire edges (Figure 18a,b). Most meshing algorithms produce only such meshes. As a consequence, it is impossible to define zones where the mesh is very fine and others where it is very coarse without a progressive transition region (Figure 18b). If this constraint is relaxed, meshes like the one depicted in Figure 18c permit strong local mesh refinements with much fewer subdomains. In this book we will use meshes based on flat triangular patches of the type (a) and (b) in Figure 18.

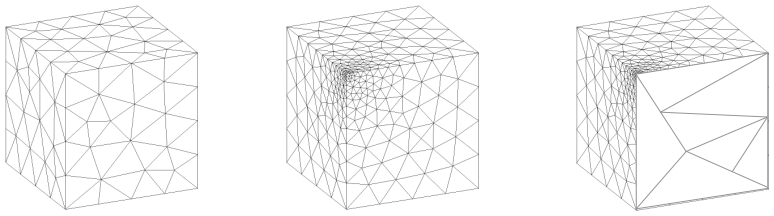

(a) (b) (c)

Figure 18 : Meshes with triangles

Subdomain basis functions are most often polynomial functions of order n. The basis function can be a complete expansion, including all terms up to order n, or not (see §2.2.8). Higher order polynomial functions introduce more unknowns in the subdomain, namely the coefficients of the polynomial expansion, but they

allow the use of larger subdomains [19]. The dimensions of the subdomains are indeed determinant for the accuracy of the approximation of the integro-differential equations by the MoM matrix system of equations. Linear basis functions (see §2.2.7) require subdomains with characteristic dimensions not larger than $\lambda/8$[3], while 8^{th}-order polynomial functions can be used with subdomains as large as 2λ[4]. Defenders of higher order polynomial basis functions claim that the net number of unknowns is in their advantage [20, p.289]. One drawback is the increased complexity in the computation of the MoM matrix elements.

To better model the infinite current densities flowing in the close vicinity ($r << \lambda$) of some sharp edges, modified basis functions are sometimes used that include a $r^{1/2}$ behavior [21]. We did not use such functions in this book.

Basis functions are also categorized as "curl free" or "div free". This property is closely related to the fact that such functions enforce some continuity requirements between adjacent subdomains, typically the continuity of the normal or the tangential component (see §2.2.5).

It is often said that elongated subdomains are not recommended [22][23], the main reason being that the evaluation of numerical integrals is not very accurate, even with a large number of quadrature nodes (see §5.3.1). Opposite conclusions are also reported [24]. In this book we provide numerical evidences that this warning is not entirely justified (§§5.5.3, 6.6, 6.8, 6.9 and 6.10), even if elongated subdomains seem to degrade the condition number of the MoM matrix (see §5.2.2).

2.2.5 Conforming functions

When basis functions span over adjacent subdomains, some continuity requirements can be incorporated in their very definition. In the finite element literature, basis functions that maintain continuity between subdomains are known as conforming functions. Similarly, vector basis functions that impose tangential (normal) continuity between subdomains are called curl (divergence) conforming.

A discretization of the vector Helmholtz equation :

$$\bar{\nabla}\times\left(\frac{1}{\mu_r}\bar{\nabla}\times\bar{E}\right)=k^2\varepsilon_r\,\bar{E} \tag{129}$$

containing curls of curls, should employ a basis functions set that imposes tangential continuity but not normal continuity [10, §9.8].

The integro-differential equations (114) to (117) do not contain the curl of the surface current densities but instead, in most formulations, their surface divergence. As explained hereafter, it is advantageous in such a case to consider

[3] See FEKO™ User's manual
[4] See WIPL-D™ User's manual

basis functions that maintain normal continuity between subdomains. We also show with the example of a dielectric cube (see §6.6.2) why curl conforming basis functions are not physically acceptable to model electric or magnetic current densities on dielectric bodies.

On a closed surface S, we consider a polygonal subdomain with contour Γ and surface S_{patch} carrying the vector basis function $\bar{F}_C$.

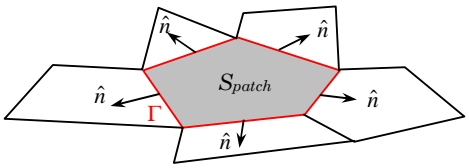

Figure 19 : Polygonal subdomain and its neighbours

Then we define :

- A scalar step function $\Pi(\bar{r})$ which is unity inside the patch and zero outside
- An arbitrary extension $\bar{F}$ to $\bar{F}_C$ extending it outside the patch, with the unique requirement that $\bar{F}$ be continuous and have continuous first derivative everywhere on the patch contour Γ

The surface divergence of the basis function $\bar{F}_C$ can now be written :

$$\nabla_s \cdot \bar{F}_C = \nabla_s \cdot (\Pi \bar{F}) = (\bar{\nabla}_s \Pi) \cdot \bar{F} + \Pi(\nabla_s \cdot \bar{F}) \tag{130}$$

The gradient of the step function $\Pi(\bar{r})$ is a unit vector everywhere normal to the edges of the patch, coplanar with the patch, multiplied by a Dirac function :

$$\bar{\nabla}_s \Pi = -\hat{n}\, \delta(\bar{r} - \bar{r}_\Gamma) \tag{131}$$

Any integral over the total surface S involving the surface divergence of the basis function can now be written as :

$$\iint_S G(\bar{r} - \bar{r}')(\nabla_s \cdot \bar{F}_C) dS = -\oint_\Gamma G(\bar{r} - \bar{r}_\Gamma)(\hat{n} \cdot \bar{F}) dl + \iint_{S_{patch}} G(\bar{r} - \bar{r}')(\nabla_s \cdot \bar{F}) dS \tag{132}$$

The line integral arises from the abrupt discontinuity of the basis function across the patch boundaries. It is usally termed as a line current contribution. Looking carefully at (132) we observe that the line integral can be cancelled in two ways.

- Locally within the patch if the normal component of the basis function is forced to zero on the patch boundaries. In this case, the $(\hat{n} \cdot \bar{F})$ term is reduced to zero.
- Globally over adjacent patches if the normal component of the basis function is forced to be continuous across the patch common boundaries Γ_c. In this case, the $(\hat{n} \cdot \bar{F})$ term changes sign on Γ_c from one patch to the other and the sum of both line integrals is identically zero.

Basis functions with such properties are called divergence conforming. Famous and widely used examples of such functions are the Rao Wilton Glisson, or RWG function (§2.2.8) and the rooftop function (§2.2.9).

Basis functions can be used even if they are not divergence conforming, but the line integral term in (132) should not be omitted [25].

2.2.6 Pulse basis function

The simplest basis functions are pulse basis functions. With this choice, the surface current densities are forced to be constant over every subdomain of the mesh. Considering any flat polygonal subdomain, they can be entirely defined with two independent parameters for the basis function representing $\bar{J}$ and two for the basis function representing $\bar{M}$:

$$\bar{f}_{j_i}^J(\bar{r}) = \hat{x}_{j_i} A_x^J + \hat{y}_{j_i} A_y^J \tag{133}$$

$$\bar{f}_{m_i}^M(\bar{r}) = \hat{x}_{m_i} A_x^M + \hat{y}_{m_i} A_y^M \tag{134}$$

where the unit vectors $\hat{x}$, $\hat{y}$ are local to every subdomain.

For a closed surface containing N_i^J subdomains to represent $\bar{J}$ and N_i^M subdomains to represent $\bar{M}$, there are $2(N_i^J + N_i^M)$ unknowns.

Aside their mathematical simplicity, another advantage of these elementary functions is that they are defined on isolated elements. It is therefore possible to use meshes like the one depicted in Figure 18c (p.42), where very fine elements can be joined to much larger elements without smooth transition. This is not possible with neither RWG nor rooftop functions (see §§2.2.8 and 2.2.9).

Pulse basis functions should only be used if the discretized integro-differential equations contain no derivatives of the equivalent surface current densities, otherwise such terms would be discarded : this would lead to high errors whenever the discarded terms have a significant contribution in the whole equation. In §1.9 we have established (74) and (75), that we called second form of the integro-differential equations. This second form is suitable to be used in conjunction with pulse basis functions as the current densities appear without any derivatives. Neither this second form, nor pulse basis functions have been used in this book.

2.2.7 Linear basis function

A complete linear vector expansion over any flat polygonal subdomain requires six independent parameters for $\bar{J}$:

$$\bar{f}_{j_i}^J(\bar{r}) = \hat{x}_{j_i}\left(A_x^J + B_x^J x + C_x^J y\right) + \hat{y}_{j_i}\left(A_y^J + B_y^J x + C_y^J y\right) \tag{135}$$

and an equivalent expression for the $\bar{M}$ basis functions, with six additional independent parameters. If appropriate continuity relationships are incorporated in the basis functions themselves, independently of the problem to solve, then the

number of unknowns will be reduced while rendering the basis functions more physical in their attempt to represent the equivalent surface current densities.

If we require the normal of the basis function to be continuous across every edge of the polygons, it becomes natural to look for basis functions defined on edges and not on isolated elements.

Let us consider with Figure 20 two triangles T^+ and T^- sharing a common edge *e* delimited by the vertices *1* and *2*. We refer to the two other edges of both triangles as their free edges.

Any location $\bar{r}$ inside T^+ is given by :

$$\bar{r} = \lambda_1^+ \bar{r}_1 + \lambda_2^+ \bar{r}_2 + (1 - \lambda_1^+ - \lambda_2^+)\bar{r}_{p^+} \tag{136}$$

where $\bar{r}_1$, $\bar{r}_2$ and $\bar{r}_{p^+}$ correspond to the vertices *1*, *2* and p^+, while $0 \le \lambda_1^+(\bar{r}) \le 1$ and $0 \le \lambda_2^+(\bar{r}) \le 1$ are the barycentric coordinates of $\bar{r}$.

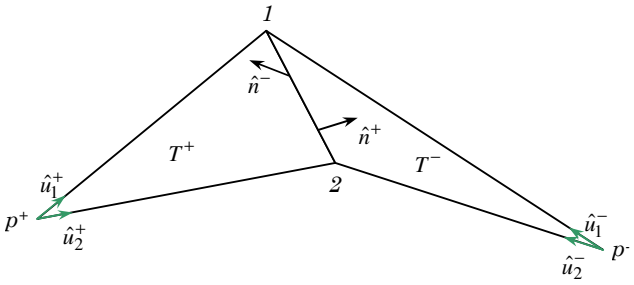

Figure 20 : Geometry for barycentric coordinates in a pair of triangles

The most general expression for a linear vector function lying on T^+ and having no component normal to its two free edges is :

$$\bar{f}^+(\bar{r}) = K^+ \hat{u}_1^+ \lambda_1^+(\bar{r}) + L^+ \hat{u}_2^+ \lambda_2^+(\bar{r}) \tag{137}$$

Where $\hat{u}_1^+$ and $\hat{u}_2^+$ are unit vectors directed from vertex p^+ to 1 and 2, respectively and K^+, L^+ are free parameters. Similarly, within T^- :

$$\bar{f}^-(\bar{r}) = K^- \hat{u}_1^- \lambda_1^-(\bar{r}) + L^- \hat{u}_2^- \lambda_2^-(\bar{r}) \tag{138}$$

A similar pair of positive and negative functions can be defined on every edge of the mesh. A closed surface entirely meshed with *N* triangles counts *1,5N* edges. As every edge supports two basis functions with two degrees of freedom each, the total number of free parameters is *6N*. This is exactly the same as with (135), indicating that any linear vector function can be described either by an element-based representation (135), or an edge-based representation such as the pair of functions (137) and (138).

If we impose now to both edge-based functions the additional constraint that the norm of their normal component be continuous across the common edge at any location $\bar{r}_e$ on the edge, namely :

$$\bar{f}^{+}(\bar{r}_e)\hat{n}^{+} = -\bar{f}^{-}(\bar{r}_e)\hat{n}^{-} \tag{139}$$

then they become coupled in the form :

$$\bar{f}^{+}(\bar{r}) = +K\frac{\lambda_1^{+}(\bar{r})}{\hat{u}_1^{+}\cdot\hat{n}^{+}}\hat{u}_1^{+} + L\frac{\lambda_2^{+}(\bar{r})}{\hat{u}_2^{+}\cdot\hat{n}^{+}}\hat{u}_2^{+} \tag{140}$$

$$\bar{f}^{-}(\bar{r}) = -K\frac{\lambda_1^{-}(\bar{r})}{\hat{u}_1^{-}\cdot\hat{n}^{-}}\hat{u}_1^{-} - L\frac{\lambda_2^{-}(\bar{r})}{\hat{u}_2^{-}\cdot\hat{n}^{-}}\hat{u}_2^{-} \tag{141}$$

and the only two degrees of freedom are now K and L.

The coupled functions (140) and (141) are the most general linear divergence conforming vector functions that can be defined on a surface meshed with triangles [26]. To use these divergence conforming functions in an expansion such as (118), we must define two basis functions for every pair of triangles and their common edge :

$$\bar{f}_1^{\pm}(\bar{r}) = \pm\frac{\lambda_1^{\pm}(\bar{r})}{\hat{u}_1^{\pm}\cdot\hat{n}^{\pm}}\hat{u}_1^{\pm} \tag{142}$$

$$\bar{f}_2^{\pm}(\bar{r}) = \pm\frac{\lambda_2^{\pm}(\bar{r})}{\hat{u}_2^{\pm}\cdot\hat{n}^{\pm}}\hat{u}_2^{\pm} \tag{143}$$

These adimensional functions are a field of parallel vectors aligned with a free edge, with a maximum norm at the vertex of the common edge belonging to this free edge, then linearly decreasing to become zero on the other free edge :

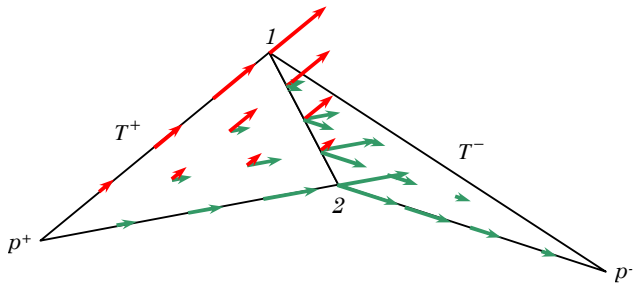

Figure 21 : Coupled linear divergence conforming functions over a pair of adjacent triangles

In Figure 21, $\bar{f}_1^{-}(\bar{r})$ has not been represented to maintain readability.

The divergence of (142) and (143) is constant inside each triangle :

$$\nabla_s \cdot \bar{f}_{1or2}^{\pm}(\bar{r}) = \begin{cases} \pm 1/h^{\pm} & \bar{r} \ in \ T^{\pm} \\ 0 & elsewhere \end{cases} \tag{144}$$

where h^{+} (h^{-}) is the height of triangle T^{+} (T^{-}) on the common edge.

In a mesh containing N triangles, thus $1{,}5N$ edges, the number of unknowns is now $3N$ for $\bar{J}$ and $3N$ for $\bar{M}$.

2.2.8 Rao Wilton Glisson (RWG) basis functions

The RWG function [27] is a special case of the most general divergence conforming linear functions on triangles presented in §2.2.7 : the RWG function imposes that the normal component be not only continuous but also *constant* everywhere on the edge. It is easy to show that this additional constraint leads to K=L in (140) and (141). As a consequence, there is now only one basis function per edge instead of two, and the number of unknown parameters in a mesh with N triangles is reduced to $1{,}5N$ for $\bar{J}$ and $1{,}5N$ for $\bar{M}$.

This now unique basis function on the pair of triangles T^+ and T^- sharing the edge e looks like :

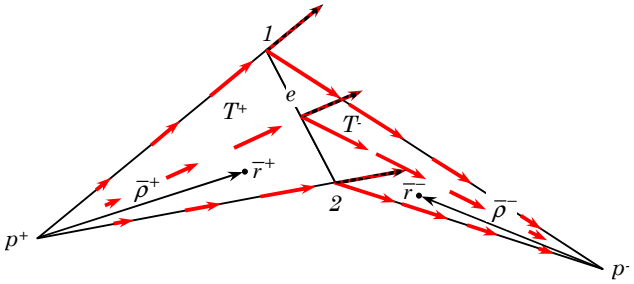

Figure 22 : RWG basis function

and takes a simple mathematical form in local polar coordinates :

$$\bar{f}^{\pm}(\bar{r}) = \begin{cases} \pm\bar{\rho}^{\pm}/h^{\pm} & \bar{r} \ in \ T^{\pm} \\ 0 & elsewhere \end{cases} \tag{145}$$

where h^+ (h^-) is again the height of triangle T^+ (T^-) on the common edge. The surface divergence of a RWG basis function is constant in T^+ and T^-, equal but with opposite signs in both triangles :

$$\nabla_s \cdot \bar{f}^{\pm}(\bar{r}) = \begin{cases} \pm 2/h^{\pm} & \bar{r} \ in \ T^{\pm} \\ 0 & elsewhere \end{cases} \tag{146}$$

To support the RWG functions, the surface S_i of every domain D_i must first be discretized with adjacent and non overlapping flat triangles. Moreover, the definition of RWG requires that every regular[5] edge in the mesh must be shared by exactly two triangles. This excludes meshes like the one depicted in Figure 18c. A mesh of a torus, suitable for RWG functions, is shown in Figure 23 (p.49).

[5] See §3.2 for the definition of regular and singular edges

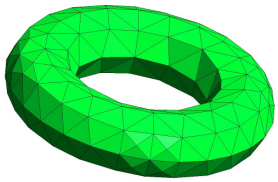

Figure 23 : Mesh of a torus

To compute the current density at any location $\bar{r}$ on the surface S_i inside one of the triangles of the mesh, only three RWG functions (and their associated unknowns $J_{e,i}$ or $M_{e,i}$) are involved : those defined on each of the 3 edges of the triangle, as illustrated in Figure 24.

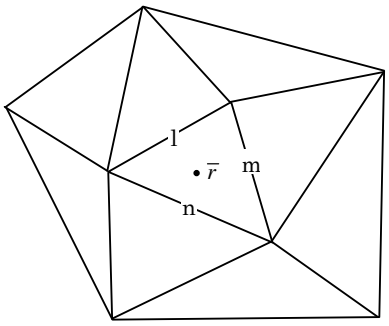

Figure 24 : Current density in a triangle computed with 3 RWGs

Supposing that the same RWG functions $\bar{f}_{e,i}(\bar{r})$ are used to model the electric and magnetic current density :

$$\bar{J}_i(\bar{r}) = J_{l,i}\bar{f}_{l,i}(\bar{r}) + J_{m,i}\bar{f}_{m,i}(\bar{r}) + J_{n,i}\bar{f}_{n,i}(\bar{r}) \tag{147}$$

$$\bar{M}_i(\bar{r}) = M_{l,i}\bar{f}_{l,i}(\bar{r}) + M_{m,i}\bar{f}_{m,i}(\bar{r}) + M_{n,i}\bar{f}_{n,i}(\bar{r}) \tag{148}$$

The price to pay though for this reduction of the number of unknowns per edge is the loss of a degree of freedom : as opposed to (142) and (143), RWG's are unable to model a surface current density with a transverse gradient, as represented in Figure 25 :

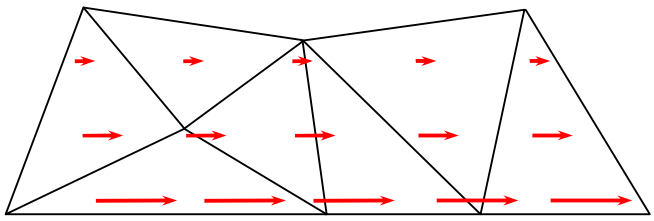

Figure 25 : Surface current density with transverse gradient

Such a current density field implies a normal component through any edge crossed by the current density that is not constant along the edge, but

proportional to the gradient of the current density. Such current density fields are most often encountered in the close vicinity of edges [28]. A direct consequence of the limited linear representation allowed by RWG functions is that current densities flowing parallel to edges where such a gradient is present are forced to zigzag (see §6.9). There are also situations where the normal component of the current density must be allowed to vary along some edges of the mesh. The strong deformations imposed to the current density flow resulting from the use of RWG functions is revealed in §6.7.1 and explained with Figure **116** (p.192).

In this book we are interested in multidomain problems, including dielectric volumes and perfectly conducting plates or sheets. We explain in detail in chapter 3 how to properly define RWG's in such a complex situation.

2.2.9 Rooftop functions

Rooftop functions are defined similarly to RWG's, but on a pair of flat rectangles or parallellograms instead of flat triangles [29].

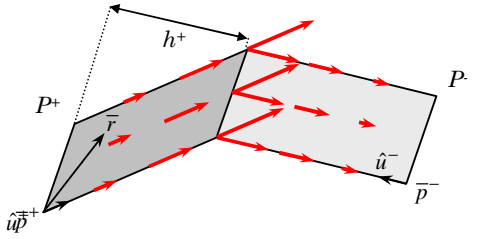

Figure 26 : Rooftop functions

Their mathematical expression, in coordinates local to every parallelogram, is :

$$\bar{f}^{\pm}(\bar{r}) = \begin{cases} \pm(\bar{r} - \bar{p}^{\pm}) \cdot \hat{u}^{\pm} / h^{\pm} & \bar{r} \ \ in \ \ P^{\pm} \\ 0 & elsewhere \end{cases} \tag{149}$$

where h^+ (h^-) is the height of the parallelogram P^+ (P^-) on the common edge and $\hat{u}^{\pm}$ is a unit vector parallel to the two free edges of the parallelogram connected to the common edge.

Similarly to RWG's, they are divergence conforming, exhibit a constant surface divergence over every parallelogram, and cannot represent a transverse current density gradient.

2.3 Testing

In the mathematical theory of linear vector spaces, the process of testing means applying a suitable inner product to a (vector) function to turn it into a scalar. Doing so, we project the function onto a subspace of its original space. The properties of a suitable inner product $\langle f, g \rangle$ between f and g are commutativity, linearity and positive definiteness :

$$\langle f, g \rangle = \langle g, f \rangle \tag{150}$$

$$\langle \alpha f + \beta g, h \rangle = \alpha \langle f, h \rangle + \beta \langle g, h \rangle \tag{151}$$

$$\left\langle f^*, f \right\rangle \begin{array}{ll} > 0 & if \quad f \neq 0 \\ = 0 & if \quad f = 0 \end{array} \tag{152}$$

In electromagnetics, the inner product between two functions is defined as [8][30] :

$$\langle f, g \rangle = \int f(\bar{r}) \cdot g(\bar{r}) dr \tag{153}$$

The product becomes a dot product if the functions are vector functions.

In mathematics (respectively, quantum physics) the function f is complex conjugated in the definition of the inner product, allowing the definition of the norm of a function (respectively, a probability function), two quantities that need to be positive.

2.3.1 Normal and tangential testing

The four discretized equations (120) to (123) actually originate from only two independent three-dimensional vector equations, the $EFIE_i$ and the $MFIE_i$, that we projected on the normal $\hat{n}_i(\bar{r})$ to the surface S_i or onto a direction tangent to S_i, at location $\bar{r}$ on S_i. These projections resulted in two scalar equations, the $nEFIE_i$ (120) and $nMFIE_i$ (121), and two vector equations, the $tEFIE_i$ (122) and $tMFIE_i$ (123).

At this stage, for the sake of generality, we test the scalar equations with sets of arbitrary scalar functions :

$$w_{e_i}(\bar{r}) \qquad \left(e_i = 1..N_i^{E,n}\right) \qquad for\ the\ nEFIE \tag{154}$$

$$w_{h_i}(\bar{r}) \qquad \left(h_i = 1..N_i^{H,n}\right) \qquad for\ the\ nMFIE \tag{155}$$

and we test the vector equations with sets of arbitrary vector functions :

$$\bar{w}_{e_i}(\bar{r}) \qquad \left(e_i = 1..N_i^{E,t}\right) \qquad for\ the\ tEFIE \tag{156}$$

$$\bar{w}_{h_i}(\bar{r}) \qquad \left(h_i = 1..N_i^{H,t}\right) \qquad for\ the\ tMFIE \tag{157}$$

Defining now the arbitrary normal vector testing functions :

$$\bar{N}_{e_i}(\bar{r}) = w_{e_i}(\bar{r}) \hat{n}_i(\bar{r}) \tag{158}$$

$$\bar{N}_{h_i}(\bar{r}) = w_{h_i}(\bar{r}) \hat{n}_i(\bar{r}) \tag{159}$$

and the arbitrary tangential vector testing functions :

$$\overline{T}_{e_i}(\overline{r}) = \hat{n}_i(\overline{r}) \times \overline{w}_{e_i}(\overline{r}) \tag{160}$$

$$\overline{T}_{h_i}(\overline{r}) = \hat{n}_i(\overline{r}) \times \overline{w}_{h_i}(\overline{r}) \tag{161}$$

Equations (120) to (123) become, after multiplying them with the appropriate testing function (158) to (161), integrating over the discretized surface S_i and rearranging the cross and dot products :

$$\begin{aligned} &\int_{S_i} \overline{N}_{e_i}(\overline{r}) \cdot \overline{E}_i^{inc}(\overline{r}) \mathrm{dS} \\ &= \int_{S_i} \overline{N}_{e_i}(\overline{r}) \cdot \left\{ \sum_{j_i}^{N_i^J} Z_i J_{j_i} \left[\tilde{N}_i - \overline{D}_i \right] \left\{ \overline{f}_{j_i}^J \right\}(\overline{r}) - \sum_{m_i}^{N_i^M} M_{m_i} \overline{K}_i \left\{ \overline{f}_{m_i}^M \right\}(\overline{r}) \right\} \mathrm{dS} \end{aligned} \tag{162}$$

$$\begin{aligned} &\int_{S_i} \overline{N}_{h_i}(\overline{r}) \cdot Z_i \overline{H}_i^{inc}(\overline{r}) \mathrm{dS} \\ &= \int_{S_i} \overline{N}_{h_i}(\overline{r}) \cdot \left\{ \sum_{j_i}^{N_i^J} Z_i J_{j_i} \overline{K}_i \left\{ \overline{f}_{j_i}^J \right\}(\overline{r}) + \sum_{m_i}^{N_i^M} M_{m_i} \left[\tilde{N}_i - \overline{D}_i \right] \left\{ \overline{f}_{m_i}^M \right\}(\overline{r}) \right\} \mathrm{dS} \end{aligned} \tag{163}$$

$$\begin{aligned} &\int_{S_i} \overline{T}_{e_i}(\overline{r}) \cdot \overline{E}_i^{inc}(\overline{r}) \mathrm{dS} \\ &= \int_{S_i} \overline{T}_{e_i}(\overline{r}) \cdot \left\{ -\sum_{j_i}^{N_i^J} Z_i J_{j_i} \overline{D}_i \left\{ \overline{f}_{j_i}^J \right\}(\overline{r}) + \sum_{m_i}^{N_i^M} M_{m_i} \left[\tilde{T}_i - \overline{K}_i \right] \left\{ \overline{f}_{m_i}^M \right\}(\overline{r}) \right\} \mathrm{dS} \end{aligned} \tag{164}$$

$$\begin{aligned} &\int_{S_i} \overline{T}_{h_i}(\overline{r}) \cdot Z_i \overline{H}_i^{inc}(\overline{r}) \mathrm{dS} \\ &= \int_{S_i} \overline{T}_{h_i}(\overline{r}) \cdot \left\{ -\sum_{j_i}^{N_i^J} Z_i J_{j_i} \left[\tilde{T}_i - \overline{K}_i \right] \left\{ \overline{f}_{j_i}^J \right\}(\overline{r}) - \sum_{m_i}^{N_i^M} M_{m_i} \overline{D}_i \left\{ \overline{f}_{m_i}^M \right\}(\overline{r}) \right\} \mathrm{dS} \end{aligned} \tag{165}$$

These expressions can be contracted into a global matrix system of equations :

$$\begin{bmatrix} Z_i^{EJ,n} & Z_i^{EM,n} \\ Z_i^{HJ,n} & Z_i^{HM,n} \\ Z_i^{EJ,t} & Z_i^{EM,t} \\ Z_i^{HJ,t} & Z_i^{HM,t} \end{bmatrix} \begin{bmatrix} J_i \\ M_i \end{bmatrix} = \begin{bmatrix} V_i^{E,n} \\ V_i^{H,n} \\ V_i^{E,t} \\ V_i^{H,t} \end{bmatrix} \tag{166}$$

The elements of the eight sub-blocks of the matrix and the four sub-vectors on the right hand side are given below :

$$Z_{(e_i,j_i)}^{EJ,n} = Z_i \int_{S_i} \bar{N}_{e_i}(\bar{r}) \cdot \left(\left[\tilde{N}_i - \bar{D}_i \right] \left\{ \bar{f}_{j_i}^J \right\}(\bar{r}) \right) \mathrm{dS} \tag{167}$$

$$Z_{(e_i,m_i)}^{EM,n} = -\int_{S_i} \bar{N}_{e_i}(\bar{r}) \cdot \left(\bar{K}_i \left\{ \bar{f}_{m_i}^M \right\}(\bar{r}) \right) \mathrm{dS} \tag{168}$$

$$Z_{(h_i,j_i)}^{HJ,n} = Z_i \int_{S_i} \bar{N}_{h_i}(\bar{r}) \cdot \left(\bar{K}_i \left\{ \bar{f}_{j_i}^J \right\}(\bar{r}) \right) \mathrm{dS} \tag{169}$$

$$Z_{(h_i,m_i)}^{HM,n} = \int_{S_i} \bar{N}_{h_i}(\bar{r}) \cdot \left(\left[\tilde{N}_i - \bar{D}_i \right] \left\{ \bar{f}_{m_i}^M \right\}(\bar{r}) \right) \mathrm{dS} \tag{170}$$

$$V_{(e_i)}^{E,n} = \int_{S_i} \bar{N}_{e_i}(\bar{r}) \cdot \bar{E}_i^{inc}(\bar{r}) \mathrm{dS} \tag{171}$$

$$V_{(h_i)}^{H,n} = Z_i \int_{S_i} \bar{N}_{h_i}(\bar{r}) \cdot \bar{H}_i^{inc}(\bar{r}) \mathrm{dS} \tag{172}$$

and

$$Z_{(e_i,j_i)}^{EJ,t} = -Z_i \int_{S_i} \bar{T}_{e_i}(\bar{r}) \cdot \left(\bar{D}_i \left\{ \bar{f}_{j_i}^J \right\}(\bar{r}) \right) \mathrm{dS} \tag{173}$$

$$Z_{(e_i,m_i)}^{EM,t} = \int_{S_i} \bar{T}_{e_i}(\bar{r}) \cdot \left(\left[\tilde{T}_i - \bar{K}_i \right] \left\{ \bar{f}_{m_i}^M \right\}(\bar{r}) \right) \mathrm{dS} \tag{174}$$

$$Z_{(h_i,j_i)}^{HJ,t} = -Z_i \int_{S_i} \bar{T}_{h_i}(\bar{r}) \cdot \left(\left[\tilde{T}_i - \bar{K}_i \right] \left\{ \bar{f}_{j_i}^J \right\}(\bar{r}) \right) \mathrm{dS} \tag{175}$$

$$Z_{(h_i,m_i)}^{HM,t} = -\int_{S_i} \bar{T}_{h_i}(\bar{r}) \cdot \left(\bar{D}_i \left\{ \bar{f}_{m_i}^M \right\}(\bar{r}) \right) \mathrm{dS} \tag{176}$$

$$V_{(e_i)}^{E,t} = \int_{S_i} \bar{T}_{e_i}(\bar{r}) \cdot \bar{E}_i^{inc}(\bar{r}) \mathrm{dS} \tag{177}$$

$$V_{(h_i)}^{H,t} = Z_i \int_{S_i} \bar{T}_{h_i}(\bar{r}) \cdot \bar{H}_i^{inc}(\bar{r}) \mathrm{dS} \tag{178}$$

Note that the impedance Z_i has been incorporated in the expressions of the Z^{EJ}, Z^{HJ} and V^H elements : when the boundary conditions between domains will have to be enforced (see §3.6), it will imply equalities between J_{j_i} (and M_{m_i}), and not between $Z_i J_{j_i}$.

The size of the subblock $Z_i^{EJ,n}$ is ($N_i^{E,n}$ by N_i^J), the size of the subvector $V_i^{H,t}$ is ($N_i^{H,t}$ by 1), and so on for all the other subblocks and subvectors. The global Z matrix has thus size ($N_i^{E,n} + N_i^{H,n} + N_i^{E,t} + N_i^{H,t}$ by $N_i^J + N_i^M$). The matrix system of equations (166) represents the discretized MoM version of the integro-differential equations (114) to (117), valid on the inner discretized surface S_i of domain D_i.

Except in the unique case where domain D_i is free space enclosing a unique PEC object, the matrix system of equations (166) cannot be solved in its own : a similar system of equations must be written for all dielectric domains and the boundary conditions must be enforced between all these domains. This is the topic of chapter 3, particularly in §3.6. In any case, the arbitrary scalar and vector testing functions still need to be specified.

2.3.2 General considerations about testing

Every element $Z_{(t_i,b_i)}$ of the Z_i matrix in (166) results from the testing of a function of $\overline{f}_{bi}$, a basis function defined on the subdomain S_{bi}, by a testing function $\overline{f}_{ti}$ defined on subdomain S_{ti}. We call self terms those obtained when the testing and basis subdomains are identical, and quasi-self terms those where partial overlapping occurs. Self and quasi-self terms should not be annihilated in the testing process as they are relatively large and contribute significantly to the solution [10, p.39]. To understand this statement, we must take a closer look at the vector functions $\tilde{N}_i(\overline{r})$, $\tilde{T}_i(\overline{r})$, $\overline{D}_i(\overline{r})$ and $\overline{K}_i(\overline{r})$, defined in §1.14.

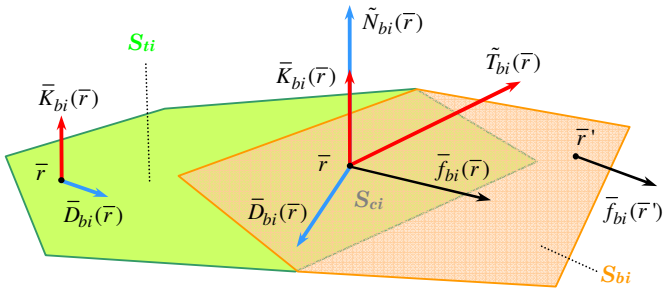

Figure 27 : Quasi self term

We consider a subdomain basis function $\overline{f}_{bi}(\overline{r}\,')$ which is non zero only on the pentagon S_{bi}, a flat portion of the total discretized surface S_i (coloured and delimited in orange in Figure 27). We consider also a subdomain testing function $\overline{f}_{ti}(\overline{r})$ defined only on the hexagon S_{ti} (coloured and delimited in green in Figure 27), another flat portion of S_{di} having some area S_{ci} in common with S_{bi}.

In the testing integrals, for example (169) and (173), the observation point $\overline{r}$ is running everywhere inside S_{ti}.

At every location $\overline{r}$ the vectors $\overline{D}_i(\overline{r})$ and $\overline{K}_i(\overline{r})$ that are being tested result from the integral over S_{bi} of a function involving the two vectors $\overline{f}_{bi}(\overline{r}\,')$ and $\hat{R}$:

$$\overline{D}_i^{(2)}\left\{\overline{f}_{bi}\right\}(\overline{r}) = k_i^2 \int_{S_{bi}} \left[\overline{f}_{bi}(\overline{r}\,') f_{3,i} - \left(\overline{f}_{bi}(\overline{r}\,')\cdot\hat{R}\right)\hat{R}\, f_{3r,i} \right] dS' \tag{179}$$

$$\overline{K}_i^{(2)}\left\{\overline{f}_{bi}\right\}(\overline{r}) = k_i^2 \int_{S_{bi}} \left\{\overline{f}_{bi}(\overline{r}\,')\times\hat{R}\right\} f_{2,i}\, dS' \tag{180}$$

As we chose coplanar S_{bi} and S_{ti} subdomains, $\overline{f}_{bi}(\overline{r}\,')$ and $\hat{R}$ are both coplanar to S_{bi} for every possible position $\overline{r}\,'$. The vector $\overline{D}_i(\overline{r})$ is a linear combination of $\overline{f}_{bi}(\overline{r}\,')$ and $\hat{R}$: it is therefore also coplanar with S_{bi}. As the cross product

between $\bar{f}_{bi}(\bar{r}')$ and $\hat{R}$ is always normal to S_{bi}, the same applies to the vector $\bar{K}_i(\bar{r})$. From the expressions of $f_{3,i}$, $f_{3r,i}$ and $f_{2,i}$, given by equations (77), (78) and (79), we also note that the norm of the complex vectors $\bar{D}_i(\bar{r})$ and $\bar{K}_i(\bar{r})$ are globally decreasing with increasing $\hat{R}$, especially when $k_i R >> 1$.

The vector $\tilde{N}_i(\bar{r})$ originates as the principal value extraction from the nEFIE$_i$ or nMFIE$_i$ integrals at $\bar{r}$. The same applies for $\tilde{T}_i(\bar{r})$ and the tEFIE$_i$ or tMFIE$_i$. Consequently :

- $\tilde{N}_i(\bar{r})$ or $\tilde{T}_i(\bar{r})$ exist only when $\bar{r}$ is inside S_{bi}, where $\bar{f}_{bi}(\bar{r})$ also exists
- $\tilde{N}_i(\bar{r})$ always appear in the nEFIE$_i$ or nMFIE$_i$ in combination with $\bar{D}_i(\bar{r})$, while $\tilde{T}_i(\bar{r})$ is combined with $\bar{K}_i(\bar{r})$ in the tEFIE$_i$ or tMFIE$_i$
- Where they exist, $\tilde{N}_i(\bar{r})$ and $\tilde{T}_i(\bar{r})$ have a magnitude larger than or similar to $\bar{D}_i(\bar{r})$ and $\bar{K}_i(\bar{r})$.

By definition, $\tilde{N}_i(\bar{r})$ is normal to S_{bi} while $\tilde{T}_i(\bar{r})$ is coplanar with S_{bi} and perpendicular to $\bar{f}_{bi}(\bar{r})$.

$$\tilde{N}_i\left\{\bar{f}_{bi}\right\}(\bar{r}) = \frac{j}{k_i}\left\{\nabla_s \cdot \tilde{f}_{bi}(\bar{r})\right\}\hat{n}_i(\bar{r}) \tag{181}$$

$$\tilde{T}_i\left\{\bar{f}_{bi}\right\}(\bar{r}) = \hat{n}_i(\bar{r}) \times \tilde{f}_{bi}(\bar{r}) \tag{182}$$

For the quasi self term $Z_{(t_i,b_i)}$ where S_{ti} and S_{bi} are coplanar, the four vectors $\tilde{N}_i(\bar{r})$, $\tilde{T}_i(\bar{r})$, $\bar{D}_i(\bar{r})$ and $\bar{K}_i(\bar{r})$ are depicted in Figure 27 (p.54) when $\bar{r}$ belongs to S_{bi}, while only $\bar{D}_i(\bar{r})$ and $\bar{K}_i(\bar{r})$ are present when $\bar{r}$ does not belong to S_{bi}. The vectors $\tilde{N}_i(\bar{r})$ and $\bar{D}_i(\bar{r})$ are perpendicular to each other, as well as $\tilde{T}_i(\bar{r})$ and $\bar{K}_i(\bar{r})$, and also $\bar{D}_i(\bar{r})$ and $\bar{K}_i(\bar{r})$.

Considering the orthogonalities between all these vectors, as the nEFIE$_i$ or nMFIE$_i$ must be tested with a vector normal to S_{ti}, while the tEFIE$_i$ or tMFIE$_i$ must be tested with a vector coplanar to S_{ti}, Table 4 summarizes that, regardless of the testing function, self terms, coplanar quasi self terms and more generally all coplanar S_{ti} / S_{bi} situations cannot be tested without discarding the $\bar{D}_i(\bar{r})$ or the $\bar{K}_i(\bar{r})$ vector.

Table 4 : Discarded terms (in red) for coplanar situations

Component	Normal		Tangential	
E (EFIE)	**N-D**	**-K**	**-D**	**T-K**
H (MFIE)	**K**	**N-D**	**K-T**	**-D**
Current density	J	M	J	M

This observation emphasizes the importance of the principal value terms $\tilde{N}_i(\bar{r})$ or $\tilde{T}_i(\bar{r})$ in the four following cases : nEFIE$_i$ or tMFIE$_i$ applied to a PEC structure and nMFIE$_i$ or tEFIE$_i$ applied to a PMC structure. These four cases result in a Z_i

matrix formed by only one of the four cells in Table 4 (p.55), where the discarded term is present. For example, for the tMFIE$_i$ applied to a PEC structure (yellow highlighted in Table 4), the global matrix system of equations (166) reduces to :

$$\left[Z_i^{HJ,t}\right]\left[J_i\right]=\left[V_i^{H,t}\right] \tag{183}$$

In these Z_i matrices, the entries involving overlapping testing and basis function subdomains are located on the main diagonal. A dominant main diagonal leads to a well conditioned matrix. On the other hand, if these diagonal terms are brought down with a wrong testing procedure, the Z_i matrix becomes ill conditioned. In the four cases mentioned above, a wrong testing function is one that also discards or strongly affects the remaining term, $\tilde{N}_i(\bar{r})$ or $\tilde{T}_i(\bar{r})$. Coming back to the example (183) of the tMFIE$_i$ applied to a PEC structure, it cannot be tested with a tangential function aligned with $\bar{f}_{bi}(\bar{r})$, otherwise the main diagonal is nearly reduced to zero[6]. The ideal choice is $\hat{n}_i(\bar{r})\times\bar{f}_{bi}(\bar{r})$, aligned with $\tilde{T}_i(\bar{r})$ at all times, producing a dominant main diagonal. A dual conclusion applies for PMC structures analyzed with tEFIE$_i$. Note that the normal testing of the nEFIE$_i$ or nMFIE$_i$ does not allow such a wrong choice, as the direction of the normal $\hat{n}_i(\bar{r})$ is unique and both $\tilde{N}_i(\bar{r})$ and $\bar{K}_i(\bar{r})$ are aligned with it.

If we analyze a PEC structure with the tEFIE$_i$, only the $\bar{D}_i(\bar{r})$ term will contribute to the main diagonal. Careful observation of (179) shows that $\bar{f}_{bi}(\bar{r})$ is an appropriate testing function, while $\hat{n}_i(\bar{r})\times\bar{f}_{bi}(\bar{r})$ will negatively affect the self term $\bar{D}_i(\bar{r})$, in an average way over S_{bi}. As opposed to the case of tMFIE$_i$ applied to a PEC structure, the main diagonal is not nearly reduced to zero, but sufficiently diminished to render the Z_i matrix ill-conditioned.

To obtain the $\bar{J}$ and $\bar{M}$ current densities flowing at the interface between a dielectric domain D_1 embedded in another dielectric domain D_2 (free-space) we must anticipate on §3.6 and explain that the global Z matrix is a combination of two submatrices Z_1 and Z_2, written independantly in both domains. In the cases of the PMCHWT and the Müller combination schemes based on the tEFIE$_i$ and tMFIE$_i$, this global Z matrix is :

$$\begin{bmatrix} \alpha_1 Z_1^{EJ,t}+\alpha_2 Z_2^{EJ,t} & \alpha_1 Z_1^{EM,t}+\alpha_2 Z_2^{EM,t} \\ \beta_1 Z_1^{HJ,t}+\beta_2 Z_2^{HJ,t} & \beta_1 Z_1^{HM,t}+\beta_2 Z_2^{HM,t} \end{bmatrix}\begin{bmatrix} J \\ M \end{bmatrix}=\begin{bmatrix} \alpha_1 V_1^{E,t}+\alpha_2 V_2^{E,t} \\ \beta_1 V_1^{H,t}+\beta_2 V_2^{H,t} \end{bmatrix} \tag{184}$$

Referring again to Table 4 (p.55), the Z matrix encompasses the four cells indexed with E, H, J and M. The main diagonal is due to the $\bar{D}(\bar{r})$ terms produced by the tEFIE$_i$ and by the tMFIE$_i$. The role of $\tilde{T}_i(\bar{r})$ is therefore of minor importance. In fact, the $\tilde{T}_i(\bar{r})$ term completely disappears with the PMCHWT combination scheme when $\bar{f}_{bi}(\bar{r})$ is the testing function. If we restrict the testing functions to $\bar{f}_{bi}(\bar{r})$ and $\hat{n}_i(\bar{r})\times\bar{f}_{bi}(\bar{r})$, chosen identically in both domains, it is mandatory to use the same testing functions for the tEFIE$_i$ and the tMFIE$_i$. Indeed if we use $\bar{f}_{b1}(\bar{r})$ and $\bar{f}_{b2}(\bar{r})$ for the tEFIE$_1$ and tEFIE$_2$, then $\hat{n}_1(\bar{r})\times\bar{f}_{b1}(\bar{r})$

[6] It is not exactly reduced to zero because RWG span over a pair of triangles. Self terms involve thereby two overlapping and two adjacent triangles.

and $\hat{n}_2(\bar{r})\times\bar{f}_{b2}(\bar{r})$ for the tMFIE$_1$ and tMFIE$_2$, the $\bar{M}$ current density is poorly tested in both the tEFIE$_i$ and both the tMFIE$_i$. Similarly, the $\bar{J}$ current density would be poorly tested if we use $\hat{n}_1(\bar{r})\times\bar{f}_{b1}(\bar{r})$ and $\hat{n}_2(\bar{r})\times\bar{f}_{b2}(\bar{r})$ for the tEFIE$_1$ and tEFIE$_2$, then $\bar{f}_{b1}(\bar{r})$ and $\bar{f}_{b2}(\bar{r})$ for the tMFIE$_1$ and tMFIE$_2$. Using $\bar{f}_{bi}(\bar{r})$ or $\hat{n}_i(\bar{r})\times\bar{f}_{bi}(\bar{r})$ everywhere (called PMCHWT-f-f or PMCHWT-nxf-nxf in this book) eludes the problem. Nevertheless, both $\bar{J}$ and $\bar{M}$ are poorly tested in this case, but one of them in the the tEFIE$_i$ only and the other one in the tMFIE$_i$ only, or oppositely. To ensure proper testing of both $\bar{J}$ and $\bar{M}$ everywhere in the Z_i matrix, some authors have proposed mixed testing schemes, such as for example $\bar{f}_{bi}(\bar{r})+\hat{n}_i(\bar{r})\times\bar{f}_{bi}(\bar{r})$ [31]. We compare in §6.2.5 the excellent results obtained with both the PMCHWT-f-f and the PMCHWT-nxf-nxf. There are no reports in the literature, known to the author, of PMCHWT-nxf-nxf. But there are many examples where PMCHWT-f-f is used, or even presented as the right choice [32][33][34].

Additional detailed information about the Müller combination scheme and appropriate testing functions can be found in [35]. Two examples are treated in §§6.2.5 and 6.8.2 with Müller-f-f and/or Müller-nxf-nxf. We present hereafter three examples of testing schemes, where the testing function is defined on a whole surface (Galerkin), along a line (Razor blade) or at a single point (point matching).

2.3.3 Galerkin testing

The discretized EFIE$_i$ and MFIE$_i$ (120) to (123) contain $N_i^J + N_i^M$ scalar unknowns. If we want to determine them by solving a square matrix system of equations, we must use exactly $N_i^J + N_i^M$ testing functions. As there are $N_i^J + N_i^M$ basis functions, they are natural candidates to construct the testing functions as well. When the testing and basis functions are identical, the procedure is called "Galerkin testing". This is only possible for the tEFIE$_i$ and the tMFIE$_i$. Indeed, the testing functions need to be normal to S_i in the case of the nEFIE$_i$ and the nMFIE$_i$., while the basis functions must lye on S_i.

A linear operator, in this case an integral equation denoted IE, is self adjoint with respect to the inner product defined by (153) if :

$$\int_{S_t} \bar{f}_t \cdot \overline{IE}[\bar{f}_b] = \int_{S_b} \bar{f}_b \cdot \overline{IE}[\bar{f}_t] \tag{185}$$

When Galerkin testing is applied to a self adjoint operator, it produces a symmetric matrix. This property, only fulfilled by the tEFIE$_i$, allows to reduce the matrix fill time by a factor close to two. Many examples where Galerkin testing is used can be found throughout Part II.

2.3.4 Point Matching

The discretized equations (120) to (123) are valid at every possible location $\bar{r}$ on S_i. If we evaluate these equations at $N_i^J + N_i^M$ locations, we can generate $N_i^J + N_i^M$ equations. This sampling process comes down to incorporate a scalar Dirac function in the definition of the testing functions (154) to (157). There are

infinitely many possibilities to choose the $N_i^J + N_i^M$ locations. To obtain a good set of independent equations and a good approximation for the current densities, it seems reasonable to evaluate the discretized equations at the centroid of every element of the mesh, though it is by no means a general rule [36, p.64].

For (122) or (123), this sampling process leads to $N_i^J + N_i^M$ two-dimensional vector equations. To obtain scalar equations the vector equation must be dot multiplied with, or projected onto an "adequate" vector. Some examples of solutions obtained with point matching, which is equivalent to use only one node in the quadrature for the outer integral (see §5.3.2), are presented in §§6.2.1, 6.2.2 and 6.5.1.

2.3.5 Razor blade testing

In the point matching testing scheme the discretized equations are evaluated at a single point, whereas in the Galerkin testing scheme, they are averaged over a surface with a weighting (or testing) function. Halfway between these two extremes a razor blade testing function is defined along a line. In the example of Figure 28 the razor blade testing function is a constant vector defined on a triangle pair, aligned with the dotted line between the centroid of every triangle and the centre of the common edge.

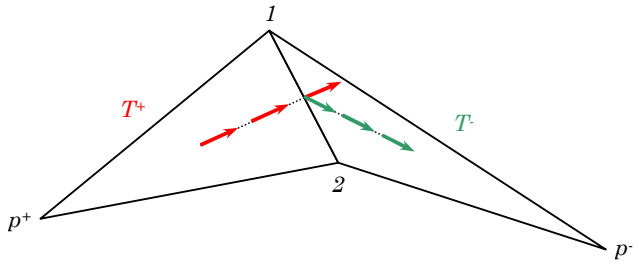

Figure 28 : Example of a razor blade function

This type of testing function has not been used in this book. We refer to [10] for additional details and to [37] for a comparison between Galerkin and razor blade testing.

2.4 Summary

In this chapter the Method of Moments is introduced in a practical way, applied to the electromagnetic scattering problems we aim to solve, described by the canonical expressions presented at the end of the previous chapter. As the choice of the basis and testing functions is very important, we spent quite some time to review their purpose, as well as the properties and (dis)advantages of the many functions available.

Subdomain divergence conforming vector basis functions were recognized as particularly adapted to our situation. In this family, the Rao Wilton Glisson functions have been selected despite some serious drawbacks that have been explained in this chapter and illustrated in chapter 6. The rejection of curl

conforming functions, sometimes encountered in the literature, has also been explained and illustrated.

Regarding the testing functions, they have been introduced in a very general way, in line with the canonical expressions derived in chapter 1 for both the normal and tangential components of the EFIE and MFIE. Some general and original considerations have shown why some choices of testing functions can be disastrous, acceptable or even advantageous.

[1] G.Mie, *Ann. Physik*, 25, 377, 1908.

[2] F. Möglich, "Beugungserscheinungen an Körper von ellipsoidischer Gestalt", *Ann. Phys.*, 83, pp. 601-735, 1927.

[3] Y.-L. Li, J.-Y. Huang, M.-J. Wang, J. T. Zhang, "Scattering Field for the Ellipsoidal Targets Irradiated by an Electromagnetic Wave with Arbitrary Polarizing and Propagating Direction", *Progress In Electromagnetics Research Letters*, Vol. 1, pp. 221-235, 2008.

[4] V.H. Weston, "On Toroidal Wave Functions", *J. Math. Phys.*, Vol. 39, pp. 64-71, 1960.

[5] Y. Nomura and S. Katsura, "Diffraction of electric wave by circular plate and circular hole," *Sci. Rep., Inst., Electr. Comm.*,Tohoku Univ., Vol. 10, pp. 1-26, 1958.

[6] K. Hongo, "Diffraction of Electromagnetic Wave by Disk and Circular Hole in a Perfectly Conducting Plane", *Progress In Electromagnetics Research*, PIER 68, pp. 113-150, 2007.

[7] K.Hongo and H.Serizawa, "Diffraction of Electromagnetic Plane Wave by a Rectangular Plate and a Rectangular Hole in the Conducting Plate", *IEEE Transactions on Antennas and Propagation*, vol. 47, No.6, pp. 1029-1041, June 1999.

[8] R.F.Harrington, *Field Computation by Moment Methods*, IEEE Press Series on Electromagnetic Waves, New York, 1968.

[9] B. M. Kolundžija, "Accurate Solution of Square Scatterer as Benchmark for Validation of Electromagnetic Modeling of Plate Structures", *IEEE Trans. on Antenna and Prop.*, Vol. 46, No.7, pp. 1009-1014, July 1998.

[10] A.F.Peterson, S.L.Ray, R.Mittra, *Computational Methods for Electromagnetics*, 1998.

[11] A. Frenkel, "On entire-domain basis functions with square-root edge singularity," *IEEE Trans. Antennas Propagat.*, vol. 37, pp. 1211–1214, Sep 1989.

[12] R.Garg, *Analytical and Computational Methods in Electromagnetics*, Artech House, Boston, 2008.

[13] S. Wandzura, "Electric Current Basis Functions for Curved Surfaces", *Electromagnetics*, Vol. 12, No.1, pp. 77-91, 1992.

[14] K. Sertel and J. L. Volakis, "Multilevel fast multipole method implementation using parametric surface modeling", *IEEE Antennas and Propagation Society International Symposium,* Vol. 4, pp. 1852-1855, 2000.

[15] V. V. S. Prakash and R. Mittra, "Characteristic basis function method: A new technique for efficient solution of method of moments matrix equation," *Microw. Opt. Technol. Lett.*, Vol. 36, No.2, pp. 95–100, Jan 2003.

[16] L. Matekovits, G. Vecchi, G. Dassano, M. Orefice, "Synthetic function analysis of large printed structures: the solution space sampling approach", *Dig. of 2001 IEEE Antennas and Propag. Society Int'l Symp.*, pp. 568-571, Boston, Massachusetts, July 2001.

[17] F. Vipiana, P. Pirinoli, G. Vecchi, "A multiresolution method of moments for triangular meshes," *IEEE Trans. Antennas Propagation,* vol. 53, pp. 2247–2258, July 2005.

[18] G. Vecchi, "Loop-star decomposition of basis functions in the discretization of the EFIE", *IEEE Trans. Antennas Propagation,* Vol. 57, No.2, pp. 339–346, Feb 1999.

[19] R. Graglia, D. R. Wilton and A. F. Peterson, "Higher order interpolatory vector bases for computational electromagnetics", *IEEE Trans. Antennas Propagation,* Vol. 45, No.3, pp. 329–342, Mar 1997.

[20] B.M. Kolundžija and A.R. Djordjević, *Electromagnetic Modeling of Composite Metallic and Dielectric Structures*, Artech House, Boston, 2002.

[21] G. A. E. Vandenbosch and A. R. Van de Capelle, "Use of subsectional edge expansion functions (SEEFs) to analyse rectangular microstrip antennas with the method of moments," Proc. Inst. Elec. Eng., pt. H, vol. 139, No.2, pp. 159-164, Apr 1992.

[22] E. Bleszynski, M. Bleszynski and T. Jaroszewicz, "AIM Adaptive integral method for solving large-scale electromagnetic scattering and radiation problems", *Radio Science*, Vol. 31, No.5, pp. 1225-1251, Sep-Oct 1996.

[23] F. Vipiana and D. R. Wilton, "Optimized Numerical Evaluation of Singular and Near-Singular Potential Integrals Involving Junction Basis Functions", *IEEE Trans. on Antenna and Prop.*, Vol. 59, No.1, pp. 162-171, Jan 2011.

[24] I. Bogaert and D. De Zutter, "High precision evaluation of the selfpatch integral for linear basis functions on flat triangles", *IEEE Trans. on Antenna and Prop.*, Vol. 58, No.5, pp. 1813-1816, May 2010.

[25] P. Ylä-Oijala and M. Taskinen, "Calculation of CFIE Impedance Matrix Elements With RWG and $n \times$ RWG Functions", *IEEE Trans. on Antenna and Prop.*, Vol. 51, No.8, pp. 1837-1846, August 2003.

[26] P.Silvester, "Construction of triangular finite element universal matrices", *Int. J. Num. Methods Eng.*, Vol. 12, pp. 237-244, 1978.

[27] S.M.Rao, D.R.Wilton and A.W.Glisson, "Electromagnetic scattering by surfaces of arbitrary shape", *IEEE Trans. Antennas Propagat.*, Vol. 30, pp. 409-418, May 1982.

[28] J.Van Bladel, *Singular Electromagnetic Fields and Sources*, IEEE Press, New York, 1991.

[29] A.W.Glisson and D.R.Wilton, "Simple and efficient numerical methods for problems of electromagnetic radiation and scattering from surfaces", *IEEE Trans. Antennas Propagat.*, Vol. 28, No.5, pp. 593-603, Sep 1980.

[30] W.C. Chew, M.S. Tong, B. Hu, *Integral Equation Methods for Electromagnetic and Elastic Waves, Synthesis Lectures on Computational Electromagnetics*, Morgan & Claypool Publishers, 2008.

[31] X. Q. Sheng, J.-M. Jing, J. Song, W. C. Chew and C. C. Lu, "Solution of Combined-Field Integral Equation Using Multilevel Fast Multipole Algorithm for Scattering by Homogeneous Bodies", *IEEE Transactions on Antennas and Propagation*, Vol. 46, No.11, pp. 1718-1726, November 1998.

[32] K. Umashankar, A. Taflove and S. M. Rao, "Electromagnetic Scattering by Arbitrary Shaped Three-Dimensional Homogeneous Lossy Dielectric Objects", *IEEE Trans. Antennas Propagat.*, Vol. 34, No.6, pp. 758-766, June 1986.

[33] J. M. Putnam and L. N. Medgyesi-Mitschang, "Combined Field Integral Equation Formulation for Inhomogeneous Two- and Three-Dimensional Bodies: The Junction Problem", *IEEE Trans. Antennas Propagat.*, Vol. 39, No.5, pp. 67-71, Oct 2005.

[34] S. M. Rao, C.-C. Cha, R. L. Cravey and D. L. Wilkes, "Electromagnetic Scattering from Arbitrary Shaped Conducting Bodies Coated with Lossy Materials of Arbitrary Thickness", *IEEE Trans. Antennas Propagat.*, Vol. 39, No.5, pp. 627-631, May 1991.

[35] P. Ylä-Oijala, M. Taskinen, "Well Conditioned Müller Formulation for Electromagnetic Scattering by Dielectric Objects", *IEEE Trans. Antennas Propagat.*, Vol. 53, No.10, pp. 3316-3323, Oct 2005.

[36] K. F. Warnick, *Numerical Analysis for Electromagnetic Integral Equations*, Artech House, 2008.

[37] E. A. Soliman, G. A. E. Vandenbosch, E. Beyne, "Galerkin versus razor-blade testing in the method of moments formulation for multiconductor transmission lines", *International Journal of RF and Microwave Computer-Aided Engineering*, Vol. 10, No.2, pp. 132-138, Mar 2000.

3 Method of Moments Formulation for Multiple Regions

In chapter 1 the exact integral expressions valid at the inner bounding surface of a volume or on one of the superimposed faces of a sheet have been established. To summarize all possible expressions occurring in a mixed material situation, a new unique notation has been introduced. In chapter 2 the integral equations applicable inside a single domain have been discretized in a general way to allow some discussion about the basis and testing functions. In this chapter a particular choice is made for the discretized equations, they are written in every domain and we incorporate the boundary conditions to solve the entire problem. The original contributions in this process are the definition of a singular edge, a solder line and a sector with its electromagnetic nature and RWG properties, the use of a sector table to organize and visualize the complex filling of the impedance matrix, and the unified presentation of the combination step for both dielectrics and perfect conductors.

3.1 Preamble

Composite structures made of homogeneous PEC and dielectric bodies are of considerable importance in radar scattering, antenna design, microwave engineering. In [1][2][3][4] only composite objects with a symmetry axis are considered. In some other works involving arbitrary three-dimensional objects, either the metallic and dielectric objects are not allowed to be in contact, or the treatment of the junctions is quite complex and not fully developed [5][6][7][8]. To date some quite general approaches have been presented [9][10][11]. In this chapter we make new steps towards a complete treatment. First of all, the PEC bodies are presented along with their PMC dual counterpart. Next, both volumic bodies and sheets are combined in every possible way. The concepts of singular edges, branched bodies and solder line are introduced, and the importance of electrical continuity is emphasized. The essential notion of RWG sectors is identified, for which two important properties are demonstrated. The treatment of composite structures is made very general to allow the use of any testing scheme, coupled to any redundancy reduction scheme. Finally, a new general approach based on the sector property table is proposed. In [12] a systematic approach is described to build the composite Z matrix and V vector corresponding to a collection of linear isotropic homogeneous domains D_i bounded by a closed surface S_i. To explain the additional concepts and properties that are introduced in this book, we illustrate and comment the procedure with a worked example : Figure 29 (p.64) highlights separately the three bodies entering the elementary composite structure : two pyramids (***L*** for *Left* and ***R*** for *Right*) made of two distinct dielectric materials, lossy or not, and one metallic branched plate (***P***), considered to be PEC. These three bounded bodies are embedded in a fourth unbounded one : free space (***O***).

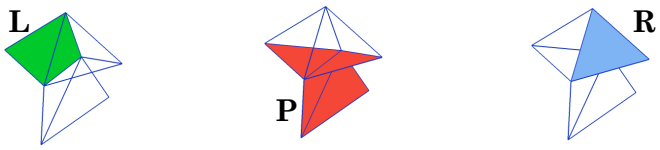

Figure 29 : Two pyramids (L,R) and one branched plate (P)

This elementary structure is meshed with 9 triangles only, and the edge numbers are clearly identified in Figure 30 :

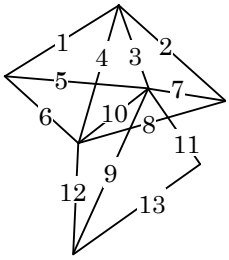

Figure 30 : Edge numbers

In chapter 1 we have established several forms for the three-dimensional EFIE$_i$ and MFIE$_i$ in every domain D_i, as well as their normal and tangential projections on the bounding surfaces S_i. From here on we will restrict ourselves to the tangential projections, called in this book the tEFIE$_i$ and tMFIE$_i$:

$$\hat{n}_i(\bar{r})\times\bar{E}_i^{inc}(\bar{r}) = \hat{n}_i(\bar{r})\times\left\{-\bar{D}_i\left\{Z_i\bar{J}_i\right\}(\bar{r}) + \left[\tilde{T}_i - \bar{K}_i\right]\left\{\bar{M}_i\right\}(\bar{r})\right\} \tag{186}$$

$$\hat{n}_i(\bar{r})\times Z_i\bar{H}_i^{inc}(\bar{r}) = \hat{n}_i(\bar{r})\times\left\{-\left[\tilde{T}_i - \bar{K}_i\right]\left\{Z_i\bar{J}_i\right\}(\bar{r}) - \bar{D}_i\left\{\bar{M}_i\right\}(\bar{r})\right\} \tag{187}$$

The meaning of the $\bar{D}_i$, $\bar{K}_i$ and $\tilde{T}_i$ operators can be found in §1.14, along with their expressions in the first and second form of the integro-differential equations. The vector $\hat{n}_i(\bar{r})$ is the unit normal to S_i at $\bar{r}$, pointing outside D_i. We know that in PEC domains, volumes or sheets, the surface current densities $\bar{J}_i$ and $\bar{M}_i$ are identically zero, but to develop a general scheme, we will omit for a while that domain P is a (PEC) sheet : the index i can therefore be L, R, O or P.

To obtain a numerical MoM solution to the integro-differential equations (186) and (187), we approximate the boundaries S_i with flat triangles and the unknown surface current densities $\bar{J}_i$ and $\bar{M}_i$ with RWG functions (see §2.2.8). For example in domain L where S_L is composed of four triangles :

$$\bar{J}_L(\bar{r}) \cong \sum_{e\in E_L} J_{e,L}\ \bar{f}_{e,L}(\bar{r}) \tag{188}$$

$$\bar{M}_L(\bar{r}) \cong \sum_{e\in E_L} J_{e,L}\ \bar{f}_{e,L}(\bar{r}) \tag{189}$$

where $\bar{f}_{e,L}$ are the RWG_L functions defined all around S_L on the edges $e \in E_L = \{1,3,4,5,6,10\}$ and $J_{e,L}$, $M_{e,L}$ are the unknown coefficients corresponding to every RWG_L defined on S_L inside D_L. As we will show in the next paragraphs, things get a little more complicated inside D_O. To explain clearly how to build the RWG_i in every domain D_i we must first introduce the concepts of singular edges, branches and sectors.

3.2 Singular edges and branches

In the physical world no object has some dimension exactly equal to zero. The thin dielectric substrate supporting a patch antenna, or an even thinner metallic coating both have a finite thickness. Very thin plates have thus a non zero volume delimited by a closed surface made of an upper and a lower face and very thin side faces. Solving electromagnetic problems involving plates with the MoM would require too many elements if the very thin side faces were to be meshed with quasi equilateral triangles. There is one way out for perfectly conducting plates : as soon as the thin dimension of the plate is much smaller than λ, say for example λ/100, it is simply reduced to zero. In this book we already called "sheet" a plate from which the thin dimension has been reduced to zero. This mathematical trick is possible and leads to meaningful solutions thanks to the infinite conductivity of a perfectly conducting sheet. chapter 4 is entirely devoted to the MoM analysis of such sheets. As explained in §1.4.1, a thin dielectric plate cannot be modelled by a dielectric sheet : the latter is simply electromagnetically transparent. For thin dielectric plates, we propose instead to reduce the number of triangles on the thin sides with linearly or logarithmically distributed meshes and elongated triangles (see §§Analytical analysis - very elongated triangles, 6.6, 6.8, 6.9 and 6.10). Other approaches have recently been reported [13][14].

The mesh of a mathematical sheet that can be generated with readily available meshers will be identical for opposite faces and will consist of a unique set of superimposed elements. In this case, every inner edge of a plate is singular : it actually represents two physically distinct edges belonging to the upper and the lower face. A body with two branches left and right of a singular inner edge can be of three types, as depicted in Figure 31 :

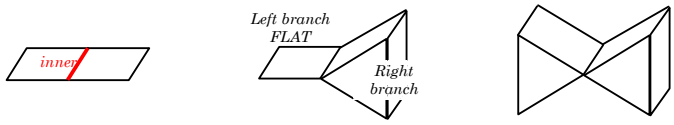

Figure 31 : Bodies with 2 branches

To form a complete linear base for the surface current densities $\bar{J}_i$ and $\bar{M}_i$ the RWG_i functions must completely cover the closed surface S_i enclosing every domain D_i, as depicted in Figure 36 (p.69). On every edge of S_i we must thus define one RWG_i for every pair of triangles belonging to a face of S_i. The homogeneous domain D_G, coloured in green in Figure 32 (p.66), has five branches on edge e. Consequently, five distinct faces of S_G share the edge e. The singular

edge e supports therefore 5 RWGs in domain D_G, as represented in Figure 32. The edge e also supports other RWG$_i$, not represented in Figure 32, for every other domain D_i touching e.

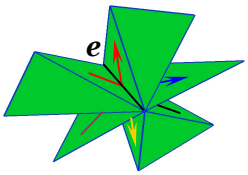

Figure 32 : Homogeneous domain with 5 branches

3.3 RWG scheme on singular edges

3.3.1 Physical Continuity and Sector Concept

On every edge e in the mesh of a composite structure, two or more domains meet. If none of these domains has branches on e (or : they all have one branch) then e supports one group of RWGs. In order to simplify the enforcement of the boundary condition, we choose to orient these RWGs in a tail-arrow sequence from one domain to the other around the edge, as depicted in Figure 33. Note that the sheet has been drawn with a finite thickness to help visualize the RWGs inside and outside it.

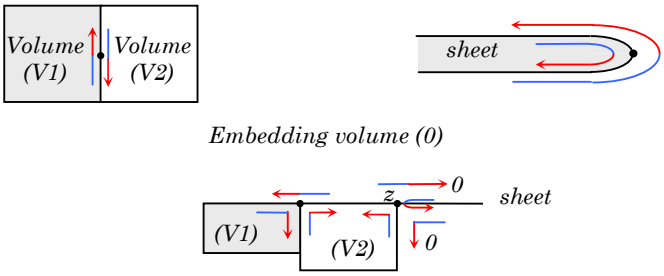

Figure 33 : Edges with no branched domains

Branches are a local property of a homogeneous domain. Domain *V2* and the sheet are NOT two branches of one single homogeneous body on edge z, unless they are made of the same material and soldered together.

If only one of the domains attached to e has b branches on e, then this domain partitions space around the edge in b sectors in which groups of mutually independent RWGs must be defined. Figure 34 (p.67) shows a body with three branches. The singular edge in the mathematical model represents three physical edges, on which the RWGs would be defined as depicted if the physical model was used instead of the mathematical model. To represent correctly the physical reality with the mathematical model, we must maintain the same RWG scheme on the singular edge.

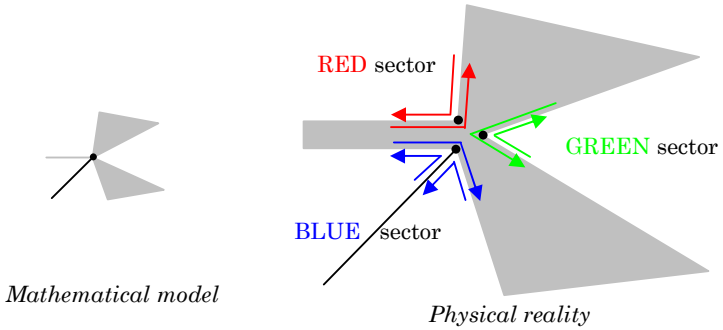

Figure 34 : Edge with one domain having three branches

3.3.2 Solder line

Let us now consider the situations of Figure 35. The singular mathematical model alone makes it impossible to distinguish which homogeneous domain is continuous across the edge. The two only physical possibilities are presented, along with the corresponding RWG scheme : black arrows for the grey domain and blue arrows for the red domain. The important observation here is that the RWGs supporting the current densities on the inner surface of both domains depend on the physical reality, that must be reproduced by the mathematical model.

In our MoM implementation, to eliminate such ambiguities, we have introduced the notion of solder line, represented as a void dot in the middle of the mathematical model in Figure 35. It is a line, as opposed to sheets (=surface) or bodies (=volumes), defined with electromagnetic properties to impose the continuity of only one of the branched domains on a singular edge. An example is given in §6.11.

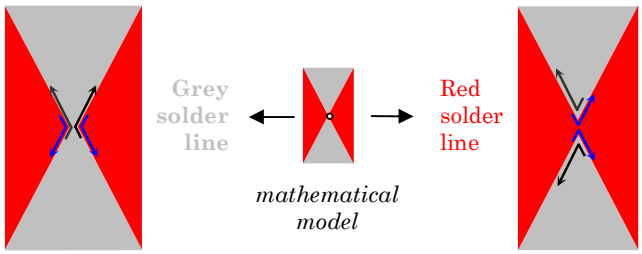

Figure 35 : Homogeneity and continuity

3.3.3 Sector table

It is not physical to have several branched bodies continuous across each other, but it is perfectly possible to imagine several branched bodies on a single edge, aside each other, as depicted in Figure 38 (p.71).

If N domains share an edge e and they all have only one branch, then there is only one sector on e. If only one of the N domains has 2 branches, then there will be 2 sectors on e. If a second domain has also 2 branches on e, then there will be 3 sectors on e (see Figure 38, p.71). In general, if each domain D_i attached to e has b_i branches, then

$$S = 1 + \sum_{i}^{N} (b_i - 1) \tag{190}$$

sectors are created around e, where N is the number of domains D_i on e.

In the example of Figure 29 (p.64), most edges define only one sector, except edge 9 (2 sectors) and edge *10* (3 sectors). This can be derived from (190), considering that only domain P has two branches on edge *9* and only domain P has three branches on edge *10*.

Another important property of sectors is their electromagnetical nature. If at least one domain around an edge within a sector is a PEC (respectively PMC) then the sector is of electric (magnetic) nature and tagged "E" ("M"). If none of the domains around an edge within a sector is a PEC or a PMC, then the sector is of dielectric nature and tagged "D". To be complete, one can also theoretically imagine a sector containing both a PEC and PMC sectors, and tag it as "E+M".

We are now ready to present in Table 5 a summary that will prove very useful in the next paragraphs and chapters.

Table 5 : Sector table

m	Edge	Sector	L	P	R	O	Type	Nature
1	1	1	X			X	I	D
2	2	1			X	X	II	D
3	3	1	X		X	X	III	D
4	4	1	X		X	X	III	D
5	5	1	X	X		X	IV	E
6	6	1	X	X		X	IV	E
7	7	1		X	X	X	V	E
8	8	1		X	X	X	V	E
9	9	1 (L)		X		X	VI	E
10	9	2 (R)		X		X	VI	E
11	10	1 (U)	X	X	X		VII	E
12	10	2 (L)		X		X	VI	E
13	10	3 (R)		X		X	VI	E
14	11	1		X		X	VI	E
15	12	1		X		X	VI	E
16	13	1		X		X	VI	E

The sectors around the singular edges *9* and *10* have been named and numbered and they are attributed a unique number m. The domains contained in every sector m are recorded with a X in the corresponding LPRO column. In the forelast column of Table 5 the 16 sectors are classified in VII types according to the domains they contain : a type I sector contains domains L and O, a type II sector contains domains R and O, and so on. In the last column, mentioning the electromagnetic nature of every sector, we observe that only four sectors are dielectric, those not in contact with the PEC sheet P.

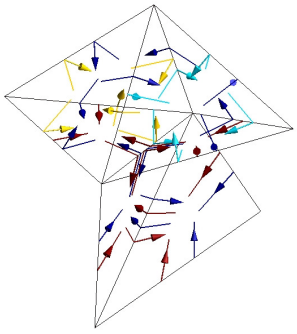

Figure 36 : RWG_i functions in the four domains

In Figure 36 the RWG_i for every domain D_i are depicted as oriented arrows on every edge of S_i. Yellow arrows for L, light blue for R and deep blue for the embedding domain O. As RWGs are purely geometrical functions that can be defined inside every homogeneous domain D_i, red RWGs have also been drawn inside the sheet P. Note in Table 5 (p.68) and in Figure 36 that the embedding domain O has a RWG in every sector, except $m=11$.

3.4 Local ZI=V systems of equations

Having determined every RWG_i functions in every domain D_i, we can discretize the $tEFIE_i$ and $tMFIE_i$. Then, to build a Z_i matrix and V_i vector for every domain D_i, we still have to choose for every sector m and in every domain D_i contained in sector m a tangential testing function $\overline{T}^E_{m,i}(\overline{r}) = \hat{n}_i(\overline{r}) \times \overline{w}^E_{m,i}(\overline{r})$ and $\overline{T}^H_{m,i}(\overline{r}) = \hat{n}_i(\overline{r}) \times \overline{w}^H_{m,i}(\overline{r})$. We refer to §2.3.2 for the choice of testing functions. In this book, in particular for the examples treated in chapter 6, we consider only the following cases :

For "E" sectors :

$$\overline{T}^E_{m,i} = \overline{f}_{m,i} \tag{191}$$

$$\overline{T}^H_{m,i} = \hat{n}_i \times \overline{f}_{m,i} \tag{192}$$

For "D" sectors :

$$\overline{T}^E_{m,i} = \overline{f}_{m,i} = \overline{T}^H_{m,i} \tag{193}$$

$$\overline{T}^E_{m,i} = \hat{n}_i \times \overline{f}_{m,i} = \overline{T}^H_{m,i} \tag{194}$$

where $\overline{f}_{m,i}$ is the RWG_i in sector m and domain D_i and $\hat{n}_i$ is the unit normal to S_i at $\overline{r}$, pointing outside D_i.

It is important to note here that the testing function for the $tMFIE_i$ or tMFIEi depends on the electromagnetic nature of the sector : for example tMFIEi can be tested with $\overline{f}_{m,i}$ or $\hat{n}_i \times \overline{f}_{m,i}$ in "D" sectors, but only with $\hat{n}_i \times \overline{f}_{m,i}$ in "E" sectors.

We obtain, for every domain D_i :

$$\begin{aligned} &\sum_{n\in N_i} Z^{EJ}_{mn,i} J_{n,i} + \sum_{n\in N_i} Z^{EM}_{mn,i} M_{n,i} = V^E_{m,i} \\ &\sum_{n\in N_i} Z^{HJ}_{mn,i} J_{n,i} + \sum_{n\in N_i} Z^{HM}_{mn,i} M_{n,i} = V^H_{m,i} \end{aligned} \qquad (m \in M_i) \tag{195}$$

where :

$$Z^{EJ}_{mn,i} = -Z_i \int_{S_{m,i}} \bar{T}^E_{m,i}(\bar{r}) \cdot \left[\bar{D}_i(\bar{r}) \{ \bar{f}_{n,i} \} \right] dS \tag{196}$$

$$Z^{HJ}_{mn,i} = -Z_i \int_{S_{m,i}} \bar{T}^H_{m,i}(\bar{r}) \cdot \left[\tilde{T}_i - \bar{K}_i \right] \{ \bar{f}_{n,i} \} dS \tag{197}$$

$$Z^{EM}_{mn,i} = \int_{S_{m,i}} \bar{T}^E_{m,i}(\bar{r}) \cdot \left[\tilde{T}_i - \bar{K}_i \right] \{ \bar{f}_{n,i} \} dS \tag{198}$$

$$Z^{HM}_{mn,i} = -\int_{S_{m,i}} \bar{T}^H_{m,i}(\bar{r}) \cdot \left[\bar{D}_i(\bar{r}) \{ \bar{f}_{n,i} \} \right] dS \tag{199}$$

$$V^E_{m,i} = \int_{S_{m,i}} \bar{T}^E_{m,i}(\bar{r}) \cdot \bar{E}^{inc}_i dS \tag{200}$$

$$V^H_{m,i} = Z_i \int_{S_{m,i}} \bar{T}^H_{m,i}(\bar{r}) \cdot \bar{H}^{inc}_i dS \tag{201}$$

The integrals are computed over $S_{m,i}$, the pair of triangles belonging to the discretized closed surface S_i supporting $\bar{f}_{m,i}$.

We can easily determine from Table 5 (p.68) that the set of sectors contained in D_L are $M_L = N_L = \{1,3,4,5,6,11\}$, and similarly for the other domains.

The four local $Z_i I_i = V_i$ systems of equations can be gathered in a single raw global $ZI = V$ system of equations as shown in Figure 37 :

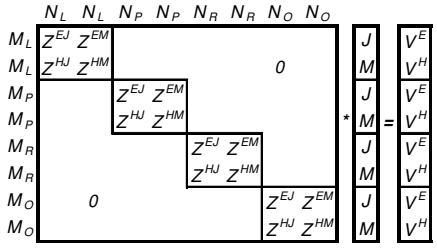

Figure 37 : Local ZI = V system of equations

Still this raw global system of equations does not fully represent the composite structure : the boundary conditions between domains must be accounted for.

In [12], a global system of equations is built from the local $Z_i I_i = V_i$ systems of equations in two additional steps :

- Include the boundary conditions
- Deal with the redundant equations arising from the previous step

In §§3.6 and 3.7 we complete and illustrate this procedure from the practical point of view of the programmer, who favours an efficient and all purpose implementation.

3.5 Two properties of RWG sectors

At this stage a programmer needs to allocate sufficient memory to store the Z matrix and V vector. As every J_i and M_i unknown is attached to one RWG_i, itself defined on one edge, the number of J_i and M_i unknowns in the raw global system of equations is the sum of the J_i and M_i unknowns attached to every edge. Allocating memory based on the size of the raw global system of equations would lead to a huge waste of memory, as we will see.

The two following properties, demonstrated further in this paragraph, provide the optimal answer :

(P1) The J_i and/or M_i unknowns attached to every RWG_i within a sector of an edge are all equal, regardless of the nature of the sector

(P2) If the sector contains a PEC and/or a PMC, then $M_i=0$ and/or $J_i=0$ for this sector

Figure 38 shows an edge common to two bodies having two branches each : the bounded domain *B1* and free space *B2*. They create three sectors : RED is "E", whereas GREEN and BLUE are "D".

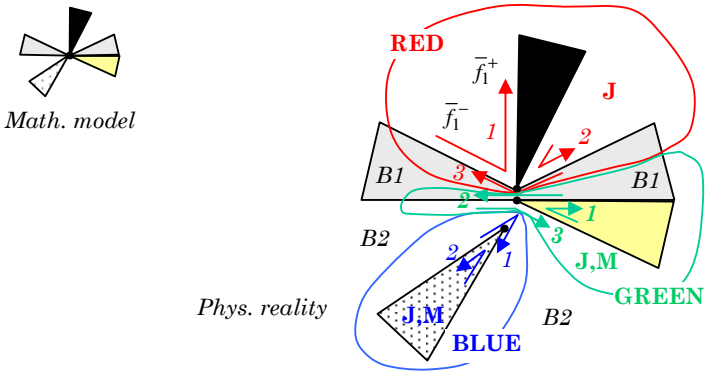

Figure 38 : The two properties of RWG sectors

(P1) allows to write $J_1=J_2=J_3$ and $M_1=M_2=M_3$ in RED, $J_1=J_2$ and $M_1=M_2$ in BLUE, $J_1=J_2=J_3$ and $M_1=M_2=M_3$ in GREEN. If the three sectors were "D", the edge would have $3J$ and $3M$ unknowns. As RED is "E", (P2) adds $M_1=M_2=M_3=0$, eliminating one M unknown.

We demonstrate (P1) in the most complex sector (RED), containing the PEC wedge.

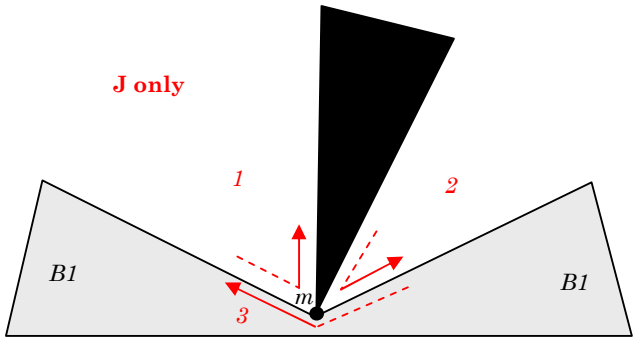

Figure 39 : Demonstration of (P1)

In Figure 39 we have drawn the normal component only of the electric current density across the edge e in sector m, with dotted lines on the T^- triangles and solid line on the T^+ triangles.

Considering the interface between domain *1* and *3*, the boundary conditions (see §1.7) impose that $\bar{J}_1^- + \bar{J}_3^+ = \bar{0}$ anywhere inside the $T_1^- = T_3^+$ triangle. On the edge e, in sector m, we must thus also have for the normal component that $\bar{J}_1^{n-} + \bar{J}_3^{n+} = \bar{0}$.

With RWG functions (see §2.2.8) :

- The electric current density inside the triangle T_i within domain D_i depends only on the three unknowns attached to the three edges of T_i
- The norm of the normal component of the electric current density on the edge e in sector m is continuous across the edge. For example $|\bar{J}_3^{n-}| = |\bar{J}_3^{n+}|$. Note that this is not true for the tangential component, thus also not for the total current density.
- The normal component of the electric current density on the edge e in sector m is also constant all along the edge and depends only on the J_m unknown on this edge. For example, $\bar{J}_3^{n-}$ and $\bar{J}_3^{n+}$ are both determined by the single scalar $J_{m,3}$.

As we have defined the RWGs within a sector in a tail arrow sequence, we can thus write :

$$J_{m,1} = J_{m,3} \tag{202}$$

Applying now the boundary conditions on the interface between domains *2* and *3*, we obtain similarly :

$$J_{m,2} = J_{m,3} \tag{203}$$

If we propagate these equalities from one domain to the next adjacent domain, we deduce that a single unknown J_m needs to be determined in the "E" sector m on edge e.

In a dielectric sector, only one J_m and only one M_m unknown are needed.

To demonstrate (P2) we remember that the boundary condition at the surface of a PEC, for example in domain *1*, states that $\bar{M}_1^+ = \bar{0}$. Similarly, we have in domain *2* that $\bar{M}_2^- = \bar{0}$. Propagating with (P1) the null normal component of the magnetic current density between adjacent domains, we can immediately write in sector m with electromagnetic nature "E" :

$$M_{m,1} = M_{m,2} = M_{m,3} = 0 \tag{204}$$

As a summary, on every edge the number of J unknowns is the sum of the number of "E" and "D" sectors, while the number of M unknowns is the sum of the number of "M" and "D" sectors.

3.6 Global *ZI=V* system of equations

Coming back to the composite structure of Figure 29 (p.64), we continue to ignore that sheet P is perfectly conducting and we derive a full dielectric solution. In Table 5 (p.68) we count m=16 pairs of J_m and M_m unknowns : the size of the global Z matrix is thus 32 x 32.

In the raw *ZI=V* system of equations of Figure 37 (p.70), the forced equality of the unknowns within a sector due to property (P1) results in the collapsing of these unknowns to only one in the I vector and the summing of the corresponding columns of Z. For *m=3* we have J_L=J_R=J_O and M_L=M_R=M_O. Exactly the same scheme applies for *m=4*, the other sector of type III. To contract notations, we will from now on represent sector types instead of the sectors themselves, remembering that a sector type stands for every individual sector of this type. Figure 40 (p.74) shows how property (P1) transforms the raw *ZI=V* system of equations. If a domain does not belong to a given sector type, for example domain L in type II, or domain O in type VII, then the corresponding rows and columns are shaded, meaning a zero value. We obtain a *ZI=V* system of equations that correctly represents the composite full dielectric structure but it is highly redundant : 16x6=96 equations for only 16+16=32 unknowns. The reason of this apparently unphysical situation is quite simple : every row corresponds to an equation created by the testing procedure, as required by the MoM. We have originally chosen to test every EFIE_i and MFIE_i with as many testing functions as there are sectors all around S_i, to obtain square Z_iI_i=V_i local systems of equations, regardless of the boundary conditions between domains. The same way we were free to choose the testing functions , we are now free to select or combine some of the 96 equations to end up with a square *ZI=V* global system of equations.

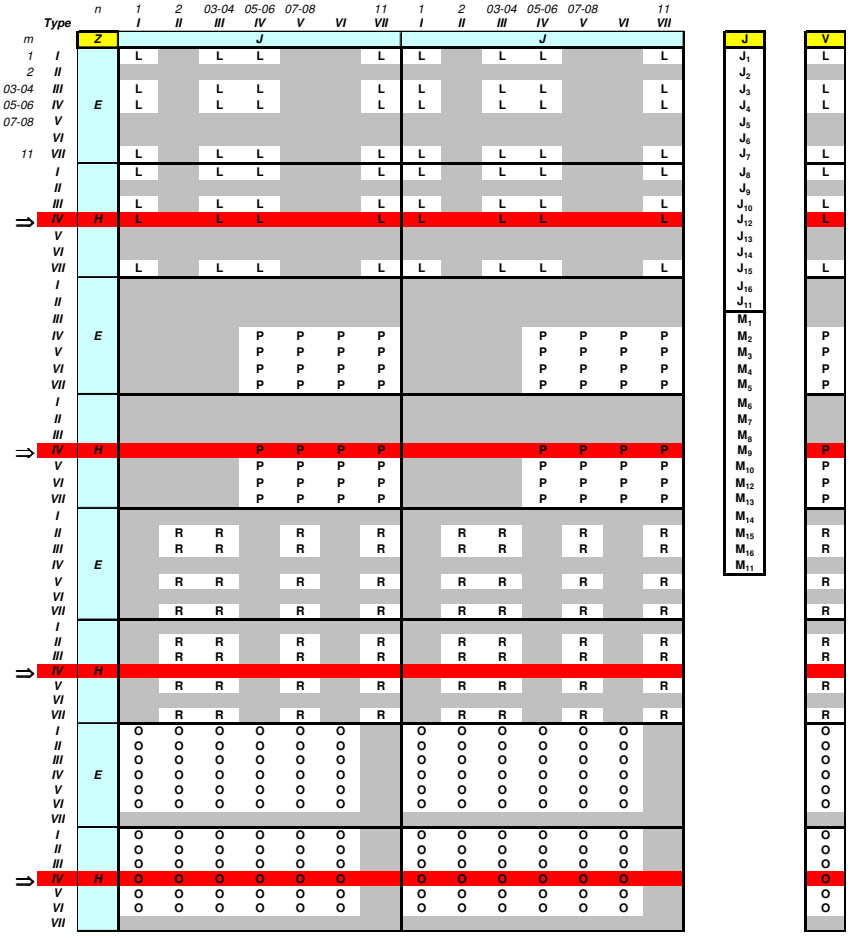

Figure 40 : Redundant *ZI=V* system of equations

Until recently many combination schemes have been analyzed or proposed [15][16], but by far the most widely used combination scheme is PMCHWT [17], named by Mautz and Harrington [18] after Poggio, Miller, Chang, Harrington, Wu and Tsai [19][20]21]. The so-called "Müller" combination scheme [22][23] was recently rediscovered, and presented as a very interesting alternative [24], especially to eliminate the low frequency break-down problem (see §5.2.4). In both combination schemes, the discretized and tested tEFIEi and tMFIEi are combined over every domain D_i. The global result is symbolized in Figure 41 (p.75), where the red row (IV H) results from the combination of the red rows of Figure 40.

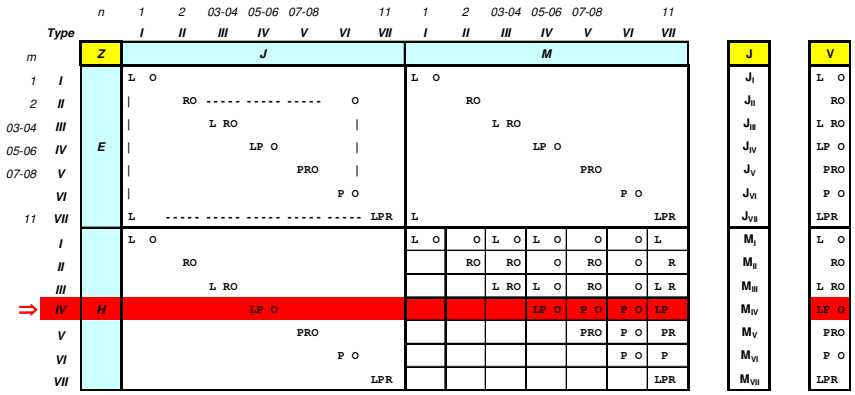

Figure 41 : Full dielectric *ZI=V* system of equations

As an example the entry " P O" at position IV,V in each of the four quadrants means a combination with contribution from the *P* and *O* domains :

$$\sum_{D_i=P,O} \alpha_i Z^{EJ}_{(IV,V),i} \quad \sum_{D_i=P,O} \alpha_i Z^{EM}_{(IV,V),i}$$
$$\sum_{D_i=P,O} \beta_i Z^{HJ}_{(IV,V),i} \quad \sum_{D_i=P,O} \beta_i Z^{HM}_{(IV,V),i} \tag{205}$$

If the RWGs are all oriented in a tail-arrow sequence, as shown in Figure 33 (p.66), then $\alpha_i = 1 = \beta_i$ for PMCHWT, whereas $\alpha_i = \varepsilon_i$ and $\beta_i = \mu_i$ for the Müller scheme [24]. In the particular case of PMCHWT-f-f (the testing function $\overline{T}^E_{m,i} = \overline{f}_{m,i} = \overline{T}^H_{m,i}$), the $\tilde{T}_i$ term in (197) and (198) is discarded. We refer to §2.3.2 for more information about testing schemes.

The PMCHWT is sometimes considered to be unsuitable for the analysis of dielectric bodies with low contrast. In the limit case of a body with $\varepsilon_r = \varepsilon_0$ (see §6.1.4) PMCHWT was reported to yield unstable results [25], while the Müller solution would produce more accurate results [18]. We show in chapter 6 with numerous examples that PMCHWT and Müller can both produce excellent and similar results in this particular case.

From the practical point of view of the programmer, the full dielectric *Z* matrix and *V* vector can be obtained directly from Table 5 (p.68). The *V* vector and the *Z* diagonal entries are combinations on every domain belonging to the sector type. We remind that in the proposed notation a sector type stands for every sector of this type individually. For example position VI,III is actually a *m*x*n* block with $m = \{9,10,12,13,14,15,16\}$ and $n = \{3,4\}$.

3.7 PEC / PMC case

We take now into account the PEC nature of the branched sheet *P*. This introduces 2 additional conditions. Firstly, there are neither $\overline{J}_i$ nor $\overline{M}_i$ current densities inside PEC or PMC domains. This results in the suppression of the whole block indexed *P* in the global raw *ZI=V* system of equations of Figure

37 (p.70). In the full dielectric *ZI=V* system of equations of Figure 41 (p.75), every contribution from domain *P* in the *Z* and *V* combinations disappear.

Secondly, property (P2) results in the suppression of the corresponding columns in *Z*. These two consequences can be visualized below, where the deleted contributions are in red and struckthrough (~~P~~) :

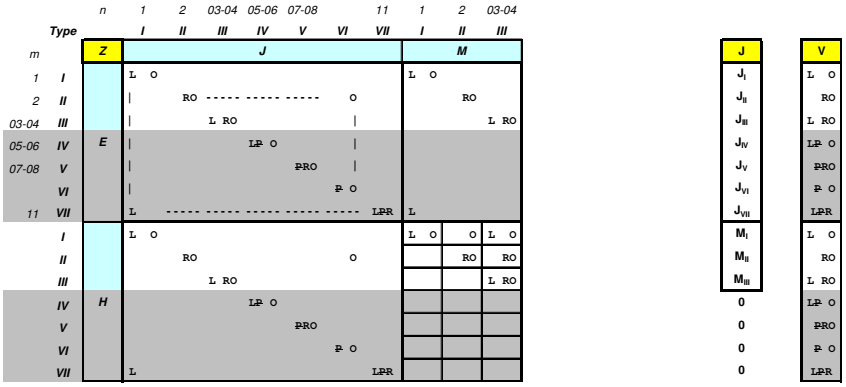

Figure 42 : *ZI=V* system of equations with a PEC

We also remind with (191) to (194) that every sector of nature "E" cannot be tested the same way they would be tested if they were of nature "D".

Again we obtain a redundant system of equations. The usual schemes to obtain a square system of equations are called EFIE (the lower grey zone is dropped), MFIE (the higher grey zone is dropped) or CFIE (both grey zones are combined with some weighting between EFIE and MFIE) [26]. The CFIE (Combined Field Integral Equation) is a possible solution to eliminate the resonances occurring when the EFIE or the MFIE is used to solve volumic bodies (see §5.2.3).

For the embedded parts of a perfectly conducting sheet, the scheme presented in this paragraph fails, as it leads to a singular *Z* matrix. The integro-differential equations relevant for sheets have already been presented in §1.4. Chapter 4 is devoted to the treatment of sheets with the MoM, in particular with a new formulation, the E-MFIE.

3.8 Summary

In this chapter the Method of Moments has been extended to the most general case of multiple linear, homogeneous and isotropic regions. Instead of a purely theoretical approach, we chose to treat a simple but representative example that illustrates the steps allowing to incorporate the boundary conditions to the discretized integral equations, in the case of RWG basis functions.

During this process, several concepts have been introduced : singular edges and branches, electromagnetic sectors around an edge and their properties, summarized in a table, physical continuity and solder line. Some of those

concepts will be reused (singular edge, in chapter 4) or illustrated (solder line, in chapter 6)

The last step of the treatment of multiple regions (combination) has been explained in a general way, presenting PEC or PMC sectors as a special case of dielectric sectors. The most widely used combination schemes for dielectric sectors - PMCHWT and Müller - have been explained, along with less common ones, showing at the same time how infinitely many other combination schemes could be derived.

The special case of embedded sheets, for which the general canvas described in this chapter fails, is treated in chapter Method of Moments for perfectly conducting sheets.

[1] L. N. Medgyesi-Mitschang and J. M. Putnam, "Electromagnetic scattering from axially inhomogeneous bodies of revolution", *IEEE Trans. Antennas Propagat.*, Vol. 32, No.8, pp. 797-806, 1984.

[2] S. Govind, D. R. Wilton and A. W. Glisson, "Scattering from inhomogeneous penetrable bodies of revolution", *IEEE Trans. Antennas Propagat.*, Vol. 32, No.11, pp. 1163-1173, 1984.

[3] P. L. Huddleston, L. N. Medgyesi-Mitschang and J. M. Putnam, "Combined field integral equation formulation for scattering by dielectrically coated conducting bodies", *IEEE Trans. Antennas Propagat.*, Vol. 34, pp. 510-520, April 1986.

[4] P. M. Goggans, A. A. Kishk and A. W. Glisson, "Electromagnetic scattering from objects composed of multiple homogeneous regions using a region-by-region solution", *IEEE Trans. Antennas Propagat.*, Vol. 42, No.6, pp. 865-871, June 1994.

[5] S. M. Rao, C. C. Cha, R. L. Cravey and D. Wilkes, "Electromagnetic scattering from arbitrary shaped conducting bodies coated with lossy materials of arbitrary thickness", *IEEE Trans. Antennas Propagat.*, Vol. 39, No.5, pp. 627-631, May 1991.

[6] Q. Chen and D. R. Wilton "Electromagnetic scattering by three-dimensional arbitrary complex material/conducting bodies", *IEEE AP-S Symposium*, Vol. 2, pp. 590-593, 1990.

[7] E. Arvas, A. Rahhal-Arabi, A. Sadigh and S. M. Rao, "Scattering from multiple conducting and dielectric bodies of arbitrary shape", *IEEE Trans. Antennas Propagat.*, Vol. 33, No.2, pp. 29-36, April 1991.

[8] J. Shin, A. W. Glisson and A. A. Kishk "Analysis of combined conducting and dielectric structures of arbitrary shapes using an E-PMCHW integral equation formulation, *IEEE AP-S Symposium*, Vol. 4, pp. 2282-2285, 2000.

[9] J. M. Putnam and L. N. Medgyesi-Mitschang, "Combined field integral equation for inhomogeneous two- and three-dimensional bodies: the junction problem", *IEEE Trans. Antennas Propagat.*, Vol. 39, No.5, pp. 667-672, May 1991.

[10] Branko M. Kolundžija, "Electromagnetic Modeling of Composite Metallic and Dielectric Structures", *IEEE Transactions on Microwave Theory and Techniques*, Vol. 47, No.7, pp. 1021-1032, July 1999.

[11] B.M. Kolundžija and A.R. Djordjević, *Electromagnetic Modeling of Composite Metallic and Dielectric Structures*, Artech House, Boston, 2002.

[12] P. Ylä-Oijala, M. Taskinen and J. Sarvas "Surface Integral Equation Method for General Composite Metallic and Dielectric Structures with Junctions", *PIER 52*, pp. 81-108, 2005.

[13] I.-Ting Chiang and W. C. Chew, "Thin Dielectric Sheet Simulation by Surface Integral Equation Using Modified RWG and Pulse Bases", *IEEE Transactions on Antennas and Propagation*, Vol. 54, No.7, pp. 1927-1934, July 2006.

[14] I.-Ting Chiang and W. C. Chew, "A Coupled PEC TDS Surface Integral Equation Approach for Electromagnetic Scattering and Radiation From Composite Metallic and Thin Dielectric Objects", *IEEE Transactions on Antennas and Propagation*, Vol. 54, No.11, pp. 3511-3516, Nov 2006.

[15] X. Q. Sheng, J.-M. Jing, J. Song, W. C. Chew and C. C. Lu, "Solution of Combined-Field Integral Equation Using Multilevel Fast Multipole Algorithm for Scattering by Homogeneous Bodies", *IEEE Transactions on Antennas and Propagation*, Vol. 46, No.11, pp. 1718-1726, November 1998.

[16] Ú. C. Resende, F. J. S. Moreira and O. M. C. Pereira-Filho, "EMFIE and MEFIE Formulations for Numerical Solution of Single or Composities Bodies of Revolution", *IEEE Trans. on Antenna and Prop.*, Vol. 53, No.10, pp. 3316-3323, Oct 2005.

[17] Y. Chu, W. C. Chew, J. Zhao, S. Chen, "A surface integral equation formulation for low-frequency scattering from a composite object", *IEEE Trans. Antennas Propagat.*, Vol. 51, No.10, pp. 2837-2844, October 2003.

[18] J. R. Mautz and R. F. Harrington, "Electromagnetic Scattering From a Homogeneous Material Body of Revolution", *Arch. Elek. Ubertragung*, Vol. 33, pp. 71-80, 1979.

[19] A. J. Poggio and E. K. Miller, "Integral equation solutions of three dimensional scattering problems", in *Computer Techniques for Electromagnetics*. Oxford, U.K.: Pergamon, 1973, chap. 4.

[20] Y. Chang and R. F. Harrington, "A Surface Formulation for Characteristic Modes of Material Bodies", *IEEE Trans. Antennas Propagat.*, Vol. 25, No.6, pp. 789-795, November 1977.

[21] T. K. Wu and L. L. Tsai "Scattering from arbitrarily shaped lossy dielectric bodies of revolution", *Radio Sci.*, Vol. 12, No.5, pp. 709-718, 1977.

[22] C. Muller, *Foundations of the Mathematical Theory of Electromagnetic Waves,* Springer-Verlag, Berlin, Germany, 1969.

[23] J. C. Chao, T. L. Liu, F. J. Rizzo, P. A. Martin and L. Udpa "Regularized integral equations and curvilinear boundary elements for electromagnetic wave scattering in three dimensions", *IEEE Trans. on Antenna and Prop.*, Vol. 43, No.12, pp. 1416-1422, Dec 1995.

[24] P. Ylä-Oijala and M. Taskinen "Well Conditioned Müller Formulation for Electromagnetic Scattering by Dielectric Objects", *IEEE Trans. on Antenna and Prop.*, Vol. 53, No.10, pp. 3316-3323, Oct 2005.

[25] T. K. Sarkar, E. Arvas and S. Ponnapalli "Electromagnetic Scattering from Dielectric Bodies", *IEEE Trans. on Antenna and Prop.*, Vol. 37, No.5, pp. 673-676, May 1989.

[26] S. M. Rao and D. R. Wilton "E-Field, H-Field and combined-field solution for arbitrarily shaped three-dimensional dielectric bodies", *Electromagn.*, Vol. 10, No.4, pp. 407-421, 1990.

4 Method of Moments for perfectly conducting sheets

In chapter 3 a unified scheme was proposed to solve numerically with the Method of Moments and RWG basis and testing functions the problem of scattering by any combination of volumes or sheets. It had to be recognized though that this scheme fails in presence of sheets exhibiting embedded edges. In this chapter, the reasons why such edges lead to a singular impedance matrix are explained for the first time in every detail for the most general case of sheets with multiple branches. The severe singularities of the EFIE are pretty well known, and the cure for a simple sheet with two branches became the standard and unique way to solve sheets. The case of the MFIE is far more interesting. In the literature it is everywhere repeated that the MFIE cannot be used to solve sheets, most of the time without any justification and very rarely with a vague or incomplete one. It is not surprising, as the full comprehension requires to use the correct expression of the MFIE for sheets, derived in chapter 1 of this book. This correct expression is also indispensable for the E-MFIE, a novel formulation we introduce in this chapter to fully solve sheets within the unified solving scheme proposed in chapter 3. Finally an efficient implementation of the E-MFIE is also suggested.

4.1 Preamble

In this book we call "sheet" an infinitely thin plate. A sheet can have multiple branches, be twisted and contain holes, as depicted in Figure 43.

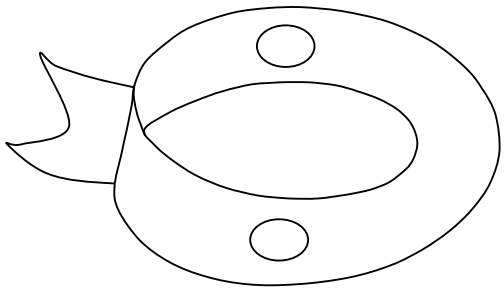

Figure 43 : Moebius-ring sheet, with 2 holes and 1 branch

We consider the scattering by a three-dimensional finite-sized perfectly electric conducting (PEC) sheet of arbitrary shape illuminated by an incident wave. Very few analytical solutions are available for PEC sheets. The most famous examples are the half plane [1], the strip [2], and the quarter plane [3] for infinite sheets, then the circular disc [4] and the square plate [5] for finite-sized sheets. All these solutions allow the determination of the electric current densities on both faces everywhere on the surface of these simple canonical sheets. They show for example that the current density on the face illuminated by the incident plane

wave is intenser than on the shadowed face. To solve for the current densities at the surface of arbitrary-shaped sheets like the one depicted in Figure 43 (p.81), one must resort to a numerical technique, such as the Method of Moments (MoM) described in chapter 2. In the specific case of a zero volume body, namely a sheet it is well known that only the tEFIE can be used, and that it yields only the sum of the current densities on opposite faces. It is also well known that the tMFIE cannot be used (alone) as it depends on both the sum and the difference of the current densities [6][7][8]. If one is interested in the individual current densities on both faces, for example to determine a shielding level or to quantify leakage currents flowing outside an imperfectly shielded enclosure, it is suggested in [6] to incorporate their sum obtained from the tEFIE into the tMFIE, then solve for their difference, and finally extract the individual current densities from their sum and difference. This elegant approach does not say how to cope with the current densities flowing around the sheet borders. Moreover it is not applicable as such for sheets with branches like the ones depicted in Figure 43 and Figure 44. In this chapter we first review in detail the singular behavior of the tEFIE and the tMFIE impedance matrices when applied alone to arbitrary PEC sheets. Next we introduce the E-MFIE, a generalized formulation that yields the individual current densities everywhere on an arbitrary PEC sheet. An efficient implementation of the E-MFIE is then proposed. The E-MFIE is illustrated by an example in §6.9.

4.2 Theory

4.2.1 tEFIE-f and tMFIE-nxf for PEC sheets

The E-MFIE formulation described in this book is based on the tEFIE and tMFIE, the tangential projections of the EFIE and MFIE (see §1.11). It uses RWG basis functions (see §2.2.8), but it naturally extends to rooftop functions (see §2.2.9). For reasons explained in §2.3.2 the tEFIE is tested with the $\overline{RWG}(\bar{r})$ itself, and therefore denoted tEFIE-f. Similarly, the tMFIE is tested with $\hat{n}(\bar{r})\times\overline{RWG}(\bar{r})$ and denoted tMFIE-nxf. The vector $\hat{n}(\bar{r})$ is the unit normal to the triangle pair S_n supporting $\overline{RWG_n}(\bar{r})$ and pointing outside the sheet.

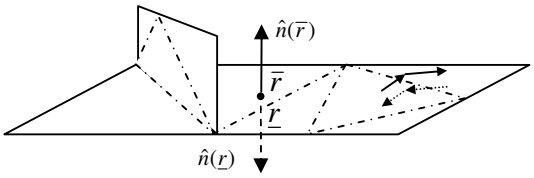

Figure 44 : Opposite faces, inner and border edges of a sheet

Since we are dealing with sheets and not with volumes, it is essential from here on to specify the face where the observation point, $\bar{r}$ or its opposite $\underline{r}$ (see Figure 44), is situated as it determines the orientation of the unit normal to that face, $\hat{n}(\bar{r})$ or $\hat{n}(\underline{r})$.

The first step in the MoM is to create a mesh made of adjacent non-overlapping triangles and to define the basis functions. In the case of sheets, it is customary to generate only one unique mesh for every pair of opposite faces. One could imagine creating two different meshes for every pair of opposite faces. Such meshes are beyond the scope of this book as they would require careful treatment of singularities that appear in the interactions between partly overlapping triangles on opposite faces.

PEC sheets meshed uniquely for every pair of opposite faces have at first sight two types of edges. The border edges surrounding the sheet and supporting only one RWG, folded around the edge. The inner edges separate the space all around them in two or more electrically isolated sectors in which independent current densities are flowing (see §3.3). Consequently, they support one RWG in every sector. In Figure 44 (p.82) the inner edges are represented as dotted lines while border edges are solid lines. Actually, every edge can be regarded as defining p sectors, where $p=1$ for border edges and $p \geq 2$ for inner edges. We call p-edge an edge supporting p sectors. We further qualify a p-edge as "embedded" if all its p sectors belong to the same homogenous domain, for example free space, or any other dielectric medium. As there are no fields and currents inside a PEC structure, we remind that the tEFIE and tMFIE are written inside dielectric domains only. Every part of the sheet can be individually in contact with only one or several dielectric domains.

In the worked example of Figure 45 (p.84) there are seven border edges defining sectors 1 to 7, one *2*-edge defining sectors 8 and 9 and one *3*-edge defining sectors 10, 11 and 12. It is straightforward but important to note here that for every border edge b (for example $b = 5$ in Figure 45*b*) :

$$\overline{RWG}_b^+(\bar{r}) = -\overline{RWG}_b^-(\bar{r}) \tag{206}$$

where the superscripts + and – indicate the positive and negative triangles supporting the RWG.

Conventionally we will orient the RWG's all around every inner edge i in a tail-arrow sequence, as depicted in Figure 45 (p.84) for the 2-edge (sectors 8,9) and for the 3-edge (sectors 10,11,12). This choice, proposed in [9] and elaborated in §3.3, will ease the discussion that follows as it permits to generalize (206) to p-edges. For example in sectors 10, 11 and 12 of Figure 45b (p.84) :

$$\begin{aligned} \overline{RWG}_{10}^+(\bar{r}) &= -\overline{RWG}_{11}^-(\bar{r}) \\ \overline{RWG}_{11}^+(\bar{r}) &= -\overline{RWG}_{12}^-(\bar{r}) \\ \overline{RWG}_{12}^+(\bar{r}) &= -\overline{RWG}_{10}^-(\bar{r}) \end{aligned} \tag{207}$$

With every RWG properly defined, the vector electric current density at any point $\bar{r}$ on any face of any part of the sheet can now be linearly approximated by :

$$\bar{J}(\bar{r}) \approx \sum_n^N J_n \overline{RWG}_n(\bar{r}) \tag{208}$$

where J_n is the complex scalar unknown linked to the $\overline{RWG}_n(\bar{r})$ defined on one edge in one sector. The total number N of J_n unknowns is equal to the total number of all sectors around every edge of the mesh. If N_p is the number of p-edges, then $N=\Sigma[p.N_p]$. In the case of Figure 45, $N_1=7$, $N_2=1$ and $N_3=1$ so that $N=12$.

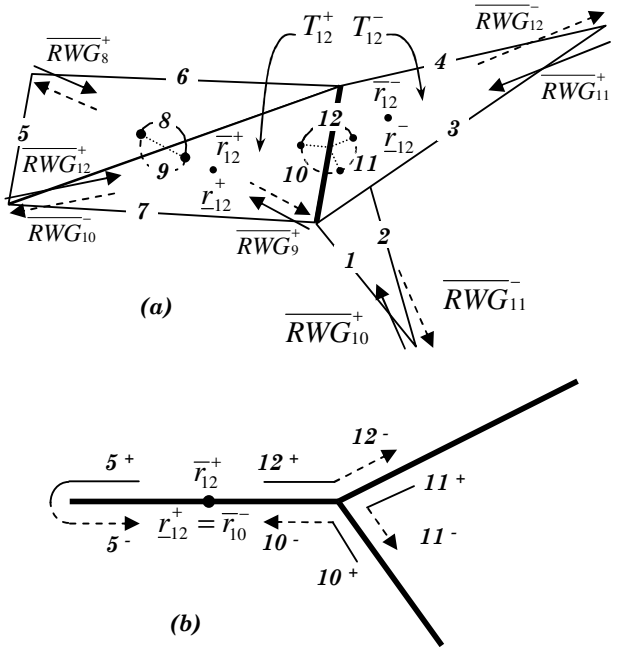

Figure 45 : Elementary Sheet with 1- 2- and 3-edges and 12 sectors
(a) : 3D view , (b) : 2D projection

These J_n unknowns can be determined by solving a NxN system of equations $ZI=V$ that will be established in §§4.2.2 and 4.2.3. Including (208) in the general expressions for the EFIE and MFIE for PEC sheets given in §1.12, we hereafter discretize the tangential component of the EFIE (called tEFIE in this book) and of the MFIE (called tMFIE in this book). Then we dot multiply the discretized equations with the appropriate weighting function $\overline{w}(\bar{r})$. As an example, let us consider with reference to Figure 45 that the observation point $\bar{r}=\overline{r}_{12}^+$, then $\overline{r}_{12}^-$, is running on triangles T_{12}^+, then T_{12}^-, in sector 12. For the tMFIE-nxf, developed in §4.2.3, we also need to consider $\underline{r}_{12}^+$, the point opposite to $\overline{r}_{12}^+$ from the perspective of sector 12 (then $\underline{r}_{12}^-$, the opposite of $\overline{r}_{12}^-$). It is recognized that $\underline{r}_{12}^+=\overline{r}_{10}^-$ ($\underline{r}_{12}^-=\overline{r}_{11}^+$) and $T_{12}^+=T_{10}^-$ ($T_{12}^-=T_{11}^+$), as illustrated in Figure 45. To maintain general expressions in what follows, we use m or n to refer to sectors and N for the total number of unknowns and equations.

4.2.2 tEFIE-f applied to PEC sheets

From (122) the discretized tEFIE at $\bar{r} = \bar{r}_m^+$ on the triangle T_m^+ reads :

$$-\hat{n}(\bar{r}_m^+) \times \sum_{n=1}^{N} Z_n \bar{D}_n(\bar{r}_m^+)[J_n] = \hat{n}(\bar{r}_m^+) \times \bar{E}_m^{inc}(\bar{r}_m^+) \tag{209}$$

with the expression on the triangle pair $S_n = T_n^+ + T_n^-$, choosing for example the first form (110) for $\bar{D}_n$:

$$\begin{aligned} \bar{D}_n^{(1)}(\bar{r}_m^+) = & \ \bar{D}_n^{(1)+}(\bar{r}_m^+) + \bar{D}_n^{(1)-}(\bar{r}_m^+) \\ = & \frac{j}{k_n} \int_{T_n^+} \left\{ k_n^2 G_n \, \overline{RWG}_n^+(\bar{r}') - \nabla_s' \cdot \overline{RWG}_n^+ \bar{\nabla}' G_n(\bar{r}_m^+ - \bar{r}') \right\} dS' \\ & + \frac{j}{k_n} \int_{T_n^-} \left\{ k_n^2 G_n \, \overline{RWG}_n^-(\bar{r}') - \nabla_s' \cdot \overline{RWG}_n^- \bar{\nabla}' G_n(\bar{r}_m^+ - \bar{r}') \right\} dS' \end{aligned} \tag{210}$$

where G_n is the free-space Green's function in sector n.

Due to (206), we have for every triangle pair S_b where b is a (border) *1*-edge, and for any observation point $\bar{r}$:

$$\bar{D}_b^+(\bar{r}) = -\bar{D}_b^-(\bar{r}) \quad \Rightarrow \quad \bar{D}_b(\bar{r}) = \bar{0} \tag{211}$$

With (207) this property generalizes to embedded p-edges. For example in sectors 10, 11 and 12 of Figure 45 (p.84) :

$$\left.\begin{aligned} \bar{D}_{10}^+(\bar{r}) &= -\bar{D}_{11}^-(\bar{r}) \\ \bar{D}_{11}^+(\bar{r}) &= -\bar{D}_{12}^-(\bar{r}) \\ \bar{D}_{12}^+(\bar{r}) &= -\bar{D}_{10}^-(\bar{r}) \end{aligned}\right\} \Rightarrow \begin{aligned} & \left(\bar{D}_{10} + \bar{D}_{11} + \bar{D}_{12}\right)(\bar{r}) = \bar{0} \\ & \textit{in general}: \ \sum_{n=1}^{p} \bar{D}_n(\bar{r}) = \bar{0} \end{aligned} \tag{212}$$

If all p sectors around a p-edge do not belong to the same domain, then the corresponding opposite equalities in (212) are not true anymore. Indeed the electromagnetic properties ε_n and μ_n differ in these sectors, thus also k_n and G_n. Dot multiplying the discretized tEFIE by $\hat{n}_m^+(\bar{r}_m^+) \times \overline{RWG}_m^+(\bar{r}_m^+)$, integrating over T_m^+ , we obtain after elimination of the $\hat{n}_m^+ \times$ term :

$$\sum_{n=1}^{N} \underbrace{Z_n \int_{T_m^+} -\overline{RWG}_m^+(\bar{r}_m^+) \cdot \bar{D}_n(\bar{r}_m^+) \ dS}_{z_{mn}^{E+}} J_n = \underbrace{\int_{T_m^+} \overline{RWG}_m^+(\bar{r}_m^+) \cdot \bar{E}_m^{inc}(\bar{r}_m^+) \ dS}_{v_m^{E+}} \tag{213}$$

Adding the contribution of T_m^- , we obtain the complete $Z^E I = V^E$ system of equations for the tEFIE-f ($m=1..N$) :

$$\sum_{n=1}^{N} J_n z_{mn}^E = \sum_{n=1}^{N} J_n \left(z_{mn}^{E+} + z_{mn}^{E-} \right) = v_m^{E+} + v_m^{E-} = v_m^E \tag{214}$$

4.2.3 tMFIE-nxf applied to PEC sheets

The tMFIE for a PEC sheet, written for an observation point on the sheet where both faces are embedded in a single domain, includes a principal value term containing the difference between the current densities on opposite faces (see §1.12). On T_m^+ and T_m^- respectively :

$$\frac{1}{2}\left\{ \bar{J}(\bar{r}_m^+) - \bar{J}(\underline{r}_m^+) \right\} + \hat{n}_m^+(\bar{r}_m^+) \times \int_S \left\{ \bar{J}(\bar{r}\,') \times \bar{\nabla}' G_n\left(\bar{r}_m^+ - \bar{r}\,'\right) \right\} dS' = \hat{n}_m^+(\bar{r}_m^+) \times \bar{H}_i(\bar{r}_m^+) \quad (215)$$

$$\frac{1}{2}\left\{ \bar{J}(\bar{r}_m^-) - \bar{J}(\underline{r}_m^-) \right\} + \hat{n}_m^-(\bar{r}_m^-) \times \int_S \left\{ \bar{J}(\bar{r}\,') \times \bar{\nabla}' G_n\left(\bar{r}_m^- - \bar{r}\,'\right) \right\} dS' = \hat{n}_m^-(\bar{r}_m^-) \times \bar{H}_i(\bar{r}_m^-) \quad (216)$$

where S is the total surface of the sheet, including both faces everywhere. If the domains are different on both faces of the PEC sheet at the observation point, then the principal value term only contains the current density in the domain in which the tMFIE is written, while S is restricted to the surface of the sheet in contact with the domain containing the observation point (see §1.4.2).

After discretization of (215) with (208), we obtain :

$$\frac{1}{2}\sum_{n=1}^{N} J_n \left\{ \overline{RWG}_n(\bar{r}_m^+) - \overline{RWG}_n(\underline{r}_m^+) \right\} + \hat{n}_m^+(\bar{r}_m^+) \times \sum_{n=1}^{N} J_n \bar{K}_n(\bar{r}_m^+) = \hat{n}_m^+(\bar{r}_m^+) \times \bar{H}_i(\bar{r}_m^+) \quad (217)$$

with :

$$\begin{aligned} \bar{K}_n(\bar{r}_m^+) &= \bar{K}_n^+(\bar{r}_m^+) + \bar{K}_n^-(\bar{r}_m^+) \\ &= \int_{T_n^+} \left\{ \overline{RWG}_n^+(\bar{r}\,') \times \bar{\nabla}' G_n(\bar{r}_m^+ - \bar{r}\,') \right\} dS' \\ &+ \int_{T_n^-} \left\{ \overline{RWG}_n^-(\bar{r}\,') \times \bar{\nabla}' G_n(\bar{r}_m^+ - \bar{r}\,') \right\} dS' \end{aligned} \quad (218)$$

Similarly to (211) and (212), we have the properties at any observation point $\bar{r}$ for border edges b and for embedded p-edges, for example in sectors 10, 11 and 12 of Figure 45 (p.84) :

$$\bar{K}_b^+(\bar{r}) = -\bar{K}_b^-(\bar{r}) \quad \Rightarrow \quad \bar{K}_b(\bar{r}) = \bar{0} \quad (219)$$

$$\left.\begin{aligned} \bar{K}_{10}^+(\bar{r}) &= -\bar{K}_{11}^-(\bar{r}) \\ \bar{K}_{11}^+(\bar{r}) &= -\bar{K}_{12}^-(\bar{r}) \\ \bar{K}_{12}^+(\bar{r}) &= -\bar{K}_{10}^-(\bar{r}) \end{aligned}\right\} \Rightarrow \begin{aligned} &\bar{K}_{10} + \bar{K}_{11} + \bar{K}_{12}(\bar{r}) = \bar{0} \\ &\textit{in general}: \ \sum_{n=1}^{p} \bar{K}_n(\bar{r}) = \bar{0} \end{aligned} \quad (220)$$

Note that exactly three RWG_n do contribute to each principal value term in (217). For instance, on T_{12}^+ :

$$\bar{J}(\bar{r}_{12}^{+}) = J_7 \overline{RWG}_7(\bar{r}_{12}^{+}) + J_8 \overline{RWG}_8(\bar{r}_{12}^{+}) + J_{12} \overline{RWG}_{10}(\bar{r}_{12}^{+}) \tag{221}$$

$$\bar{J}(\bar{r}_{12}^{+}) = J_7 \overline{RWG}_7(\bar{r}_{12}^{+}) + J_8 \overline{RWG}_8(\bar{r}_{12}^{+}) + J_{12} \overline{RWG}_{10}(\bar{r}_{12}^{+}) \tag{222}$$

Before proceeding, we replace these $\overline{RWG}_n(\bar{r})$ in the principal value term by the equivalent $-\hat{n}(\bar{r})\times\hat{n}(\bar{r})\times\overline{RWG}_n(\bar{r})$. Next we dot multiply the discretized tMFIE by $\overline{RWG}_m$, integrate over T_m^+, redistribute the dot and cross products to obtain :

$$\begin{aligned}\sum_{n=1}^{N} J_n \underbrace{\int_{T_m^+} \hat{n}(\bar{r}_m^+)\times\overline{RWG}_m^+(\bar{r}_m^+)\cdot\left\{\bar{I}_n(\underline{\bar{r}}_m^+) + \bar{K}_n(\bar{r}_m^+)\right\}\, dS}_{z_{mn}^{H+}} \\ = \underbrace{\int_{T_m^+} \hat{n}(\bar{r}_m^+)\times\overline{RWG}_m^+(\bar{r}_m^+)\cdot\left\{\bar{H}_i(\bar{r}_m^+)\right\}\, dS}_{v_m^{H+}}\end{aligned} \tag{223}$$

where :

$$\bar{I}_n(\underline{\bar{r}}_m^+) = \frac{-1}{2}\left\{\hat{n}(\bar{r}_m^+)\times\overline{RWG}_n(\bar{r}_m^+) + \hat{n}(\underline{r}_m^+)\times\overline{RWG}_n(\underline{r}_m^+)\right\} \tag{224}$$

$$\hat{n}(\bar{r}_m^+) = -\hat{n}(\underline{r}_m^+) \tag{225}$$

As opposed to the operators $\bar{D}$ in (211), (212) and $\bar{K}$ in (219), (220), the principal value term $\bar{I}$ in (224) has a different property, this time for any *pair of* opposite observation points $\bar{r}$ and $\underline{r}$ denoted by $\underline{\bar{r}}$. Taking again the example of sectors 10, 11 and 12, if $\underline{\bar{r}}$ belongs to one of the triangles attached to the *3*-edge, then :

$$\sum_{n=10}^{12} \bar{I}_n(\underline{\bar{r}}) \neq \bar{0} \tag{226}$$

If $\underline{\bar{r}}$ does not belong to one of the triangles attached to the *3*-edge, this sum is identically zero.

Adding also the contribution from T_m^-, we finally obtain the complete $Z^M I = V^M$ system of equations for the tMFIE-nxf ($m=1..N$) :

$$\sum_{n=1}^{N} J_n z_{mn}^{M} = \sum_{n=1}^{N} J_n \left(z_{mn}^{M+} + z_{mn}^{M-}\right) = v_m^{M+} + v_m^{M-} = v_m^{M} \tag{227}$$

4.3 Singularities arising with PEC sheets

4.3.1 Singularity of Z^E obtained with the tEFIE-f

Considering the properties (206) and (207) for $\overline{RWG}_m$ in the equation (213) it is easy to derive, in the example of Figure 45 (p.84), that for any (column) n of Z^E :

$$\begin{array}{lll} z_{mn}^{E+} = -z_{mn}^{E-} & & (m = 1..7) \\ z_{8n}^{E+} = -z_{9n}^{E-} & z_{9n}^{E+} = -z_{8n}^{E-} & \\ z_{10n}^{E+} = -z_{11n}^{E-} & z_{11n}^{E+} = -z_{12n}^{E-} & z_{12n}^{E+} = -z_{10n}^{E-} \end{array} \tag{228}$$

These relationships show that the sum of the p rows of Z^E corresponding to all p sectors around an embedded p-edge are identically zero, for example :

$$\left(z_{10n}^{E+} + z_{10n}^{E-}\right) + \left(z_{11n}^{E+} + z_{11n}^{E-}\right) + \left(z_{12n}^{E+} + z_{12n}^{E-}\right) = 0 \quad for \quad all \quad n \tag{229}$$

Border edges yield rows filled with zeros, while inner edges yield linearly dependent rows, making Z^E singular. The classical way [9] to circumvent the singularity of the tEFIE-f system of equations and solve sheets anyway is to remove for every embedded edge one RWG in one sector. Indeed (212) in (213) and (214) ensures that :

$$\sum_p z_{mp}^E = 0 \qquad for \quad all \quad m \tag{230}$$

Considering (229) and (230), the rows and columns of Z^E involving the embedded *3*-edge defining sectors 10, 11 and 12 in Figure 45 (p.84) look like :

$$\begin{pmatrix} \left(Z_{1..9,1..9}^E\right) & \left(z_{1..9,10}^E\right) & \left(z_{1..9,11}^E\right) & -\left(\sum_{n=10}^{11} z_{1..9,n}^E\right) \\ \left(z_{10,1..9}^E\right) & z_{10,10}^E & z_{10,11}^E & -\sum_{n=10}^{11} z_{10,n}^E \\ \left(z_{11,1..9}^E\right) & z_{11,10}^E & z_{11,11}^E & -\sum_{n=10}^{11} z_{11,n}^E \\ -\left(\sum_{m=10}^{11} z_{m,1..9}^E\right) & -\sum_{m=10}^{11} z_{m,10}^E & -\sum_{m=10}^{11} z_{m,11}^E & -\sum_{m=10}^{11} z_{m,12}^E \end{pmatrix} \begin{pmatrix} \left(J_{1..9}\right) \\ J_{10} \\ J_{11} \\ J_{12} \end{pmatrix} = \begin{pmatrix} \left(v_{1..9}^E\right) \\ v_{10}^E \\ v_{11}^E \\ -\sum_{m=10}^{11} v_m^E \end{pmatrix} \tag{231}$$

where the parentheses enclose a (sub)vector or a (sub)matrix spanning over rows and/or columns 1 to 9. Adding rows 10 and 11 to row 12 and adding columns 10 and 11 to column 12 leads to a 11×11 system of equations surrounded by zeros that can be uniquely solved for J_1 to J_9, J_{10}-J_{12} and J_{11}-J_{12} , but not for J_{10}, J_{11} or J_{12} individually :

$$\begin{pmatrix} \left(Z_{1..9,1..9}^E\right) & \left(z_{1..9,10}^E\right) & \left(z_{1..9,11}^E\right) & 0 \\ \left(z_{10,1..9}^E\right) & z_{10,10}^E & z_{10,11}^E & 0 \\ \left(z_{11,1..9}^E\right) & z_{11,10}^E & z_{11,11}^E & 0 \\ 0 & 0 & 0 & 0 \end{pmatrix} \begin{pmatrix} \left(J_{1..9}\right) \\ J_{10} - J_{12} \\ J_{11} - J_{12} \\ J_{12} \end{pmatrix} = \begin{pmatrix} \left(v_{1..9}^E\right) \\ v_{10}^E \\ v_{11}^E \\ 0 \end{pmatrix} \tag{232}$$

This process must be repeated for every embedded edge to extract from $Z^E I = V^E$ a regular and thus solvable subsystem. In the most common case of an embedded *2*-edge, considering that opposite directions have been chosen for the RWGs in the two sectors (see Figure 45, p.84), a solution is obtained for the sum of the

current densities in both sectors. Considering again the example of Figure 45 (p.84), row and column 8 must be removed from (232) and a solution is obtained for J_7-J_8. Removing one RWG in every sector also implies that border edges, having only one sector, are completely discarded. Fortunately, the sum of the normal components of the current densities around the border edge b is known to be zero [10][11, p. 653]. Since it is entirely determined by the unknown J_b, this unknown does not need to be calculated and the corresponding rows and columns can be discarded. In the example of Figure 45 (p.84), rows and columns 1 to 7 must also be removed from (232).

4.3.2 Singularity of Z^M obtained with the tMFIE-nxf

Considering the properties (206), (207) and (225), it is easy to derive from equation (223), based on the example of Figure 45 (p.84), that for any (column) n of Z^M :

$$\begin{aligned} &z_{mn}^{M+} = z_{mn}^{M-} && (m=1..7) \\ &z_{8n}^{M+} = z_{9n}^{M-} \quad z_{9n}^{M+} = z_{8n}^{M-} && \\ &z_{10n}^{M+} = z_{11n}^{M-} \quad z_{11n}^{M+} = z_{12n}^{M-} \quad z_{12n}^{M+} = z_{10n}^{M-} && \end{aligned} \tag{233}$$

With (227), the two first relationships in (233) show that, for any (column) n :

$$\begin{aligned} &z_{mn}^{M} \neq 0 && (m=1..7) \\ &z_{8n}^{M} - z_{9n}^{M} = 0 && \end{aligned} \tag{234}$$

To generalize (234) we now show that only embedded p-edges with an even number of sectors (p=2,4,6,…) yield linearly dependent rows and columns. If we consider an embedded *3*-edge and an embedded *4*-edge, equation (233) means that the p elements $z_{1..p,n}$ can be schematically expressed as depicted in Figure 46 :

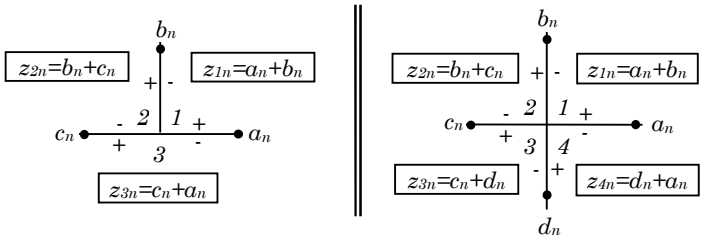

Figure 46 : tMFIE-nxf z_{mn} elements around a p-edge

where, for example, b_n represents $z_{1n}^{M-} = z_{2n}^{M+}$.

To obtain a null row by combining rows m=*1..p*, considering that a_n, b_n, ... are all independent and all appear twice around the p-edge to form the p elements $z_{1..p,n}$, the only way is to successively subtract and add the first *p-1* adjacent rows and compare with the p^{th} row. If the number of rows is even, for example *p=4*, one obtains $a_n+b_n-(b_n+c_n)+(c_n+d_n)=a_n+d_n$ which is identical to row 4, meaning linear

dependence. If the number of rows is odd, for example $p=3$, one obtains $a_n+b_n-(b_n+c_n)=a_n-c_n$ while row 3 contains a_n+c_n, meaning linear independence. It is straightforward to generalize this reasoning to any value of p, even or odd.

Unfortunately, though the tMFIE-nxf is less singular than the tEFIE-f when applied to PEC sheets, the simple combination of rows and columns to obtain J_1-J_p, J_2-J_p … J_{p-1}-J_p for every p-edges is not possible with the tMFIE-nxf. Such a unique solution to the rank deficient system of equations (232) could indeed be obtained because not only the rows but also the columns of Z^E are linearly dependent. This is ensured by (230), stemming from (212). As shown by (223), the elements of Z^M contain two terms : $\overline{K}$ and $\overline{I}$. The integral term $\overline{K}$ satisfies property (220), similar to (212). But the principal value term $\overline{I}$ does not, in view of property (226). As a consequence, the columns of Z^M are not linearly dependent and cannot be combined to allow the unique solution J_1-J_p, J_2-J_p … J_{p-1}-J_p, as for the tEFIE-f.

This impossibility to obtain a unique solution can be related to the fact that the tMFIE-nxf depends on both the sum of the current densities on both faces of a sheet, through the $\overline{K}$ term, but also on their difference, through the $\overline{I}$ term. On the other hand, the tEFIE-f depends only on the sum of the current densities on both faces of a sheet, through the $\overline{D}$ term in (210).

4.4 E-MFIE for PEC sheets

4.4.1 The E-MFIE formulation

Instead of removing rows and combining columns, we now propose to maintain all RWGs on every edge and sector, and mix tEFIE-f and tMFIE-nxf rows to construct a regular Z matrix. For the border edges, only the tMFIE-nxf can be used, since the tEFIE-f rows are identically zero. For 2-edges, we use the tEFIE-f on one face and the tMFIE-nxf on the other face. Note that the choice of the tEFIE-f and tMFIE-nxf faces is local to every edge, entirely arbitrary and there is no need to maintain the same choice for adjacent edges. For p-edges, we are free to select q tEFIE-f and p-q tMFIE-nxf among the p sectors. If p is even, q must be greater than 0 and smaller than p. If p is odd, we are free to choose the tMFIE-nxf exclusively ($q=0$). For example, (235) is one possible $ZI=V$ system of equations that can be assembled with the E-MFIE for the elementary structure in Figure 45 (p.84).

This very simple E-MFIE scheme has the advantage of being universal : regardless of the presence of volumes or sheets made of various materials, there is only one procedure to generate the mesh and the RWGs everywhere. The E-MFIE needs to be used only on every embedded p-edge of sheets, and the individual current densities are obtained everywhere directly from the one-step resolution of a global $ZI=V$ system of equations. Note also that the E-MFIE provides the current densities flowing around border edges. The ease of implementation of the E-MFIE scheme is particularly advantageous in presence of p-edges with $p \geq 3$ and partly embedded sheets. In such cases indeed, the derivation of the current densities on opposite faces of sheets becomes less

straightforward than described in [6] for a simple PEC sheet embedded in free space, as will be shown in §4.4.2.

$$\begin{pmatrix} z^M_{1,1} & \cdots & z^M_{1,n} & \cdots & z^M_{1,12} \\ \cdots & \cdots & \cdots & \cdots & \cdots \\ z^M_{7,1} & \cdots & z^M_{7,n} & \cdots & z^M_{7,12} \\ z^M_{8,1} & \cdots & z^M_{8,n} & \cdots & z^M_{8,12} \\ z^E_{9,1} & \cdots & z^E_{9,n} & \cdots & z^E_{9,12} \\ z^E_{10,1} & \cdots & z^E_{10,n} & \cdots & z^E_{10,12} \\ z^M_{11,1} & \cdots & z^M_{11,n} & \cdots & z^M_{11,12} \\ z^M_{12,1} & \cdots & z^M_{12,n} & \cdots & z^M_{12,12} \end{pmatrix} \begin{pmatrix} J_1 \\ \cdots \\ J_n \\ \cdots \\ J_{12} \end{pmatrix} = \begin{pmatrix} v^M_1 \\ \cdots \\ v^M_7 \\ v^M_8 \\ v^E_9 \\ v^E_{10} \\ v^M_{11} \\ v^M_{12} \end{pmatrix} \tag{235}$$

However the E-MFIE has the disadvantage to require a Z matrix of dimension $N=\Sigma[p.N_p]$ whereas a tEFIE-f solution with elimination of one unknown per embedded edge (see §4.3.1) requires a Z matrix of dimension $N_E=\Sigma[(p-1).N_p]$. For regular sheet shapes, where the number of border edges is small as compared to the number of inner edges, N is somewhat larger than $2N_E$. For fractal sheets, or sheets containing many holes, the ratio between border edges and inner edges increases and N can become closer to $3N_E$. The memory required to store a Z matrix of size NxN is proportional to N^2, while the CPU time to solve the $ZI=V$ system of equations rates as N^2 with an efficient iterative solver or as N^3, with a direct LU solver. Considering a ratio N/N_E comprised between 2 and 3 and a direct LU solver (or an efficient iterative solver), the E-MFIE solution is 8 to 27 (respectively 4 to 9) times slower to obtain than the classical tEFIE-f solution. This significant increase in required CPU time is the price to pay to access the current densities on both faces of the sheet in one step only. If this price is not acceptable, we propose hereafter an efficient implementation of the E-MFIE, at the expense of a multi-step resolution scheme.

4.4.2 Efficient implementation of the E-MFIE

For a sheet containing p-edges with $p \geq 3$, several E-MFIE matrices can be constructed, depending on the number of tEFIE-f and tMFIE-nxf rows that are chosen. Since the efficient implementation of the E-MFIE is based on the separate resolution of the tEFIE-f and tMFIE-nxf portions of the E-MFIE system of equations, it requires that a maximum of tEFIE-f rows be chosen. For the example of Figure 45 (p.84) we must select the tMFIE-nxf for every 1-edge, only one tEFIE-f for the 2-edge (sector 9) and two tEFIE-f for the 3-edge (sectors 11 and 12). The resulting $ZI=V$ system of equations is depicted in Figure 47 (p.92), where the m,n indices denote the sectors.

In the Z matrix, blank cells correspond to zero values and identical symbols are used for identical values. We can make three observations.

Firstly we consider the z_{mn} terms where n is a border edge (1 to 7 in this example). Due to (211) the corresponding tEFIE-f submatrix is zero. Due to (219),

(220) and (226) the corresponding tMFIE-nxf submatrix is very sparse, and purely real as it is entirely determined by the principal terms (224).

Secondly, the square tMFIE-nxf submatrix Z_{mn} where both m an n are border edges is symmetric, and can therefore be filled faster.

		1	2	3	4	5	6	7	8	9	10	11	12				
	9								-A	A	-B-C	B	C		J1		
EFIE	11								-D	D	-E-F	E	F		J2		VE
	12								-G	G	-H-I	H	I		J3		
	1	AA	HH						-a	a	aa	bb	cc		J4		
	2	HH	BB						-b	b	dd	ee	ff		J5		
	3			CC	JJ				-c	c	gg	hh	ii	*	J6	=	
	4			JJ	DD				-d	d	jj	kk	ll		J7		
MFIE	5					EE	KK		e	f	-vv-uu	vv	ww		J8		VH
	6					KK	FF		g	h	-xx-yy	xx	yy		J9		
	7							GG	j	k	mm	nn	oo		J10		
	8					LL	MM		l	m	pp	qq	rr		J11		
	10	NN	PP					QQ	n	p	ss	tt	uu		J12		
		Real							Complex								

Figure 47 : E-MFIE matrix for the example of Figure 45

Thirdly we consider in the tMFIE-nxf portion the $z_{m(1..p)}$ interaction terms between a triangle pair S_m and the p triangle pairs $S_1 \ldots S_p$ around a p-edge. If no triangles in the pair S_m superimposes to one of the triangles in $S_1 \ldots S_p$, then the sum $z_{m(1)}+\ldots+z_{m(p)}=0$. Otherwise, this sum is a real value obtained from the sum of the principal terms only, which are far easier and faster to compute than the integral terms (218). These properties stem from (220) and (226). The interaction terms for which the above sum is zero are grey-shaded in Figure 47. In the tEFIE-f portion of the E-MFIE matrix, the same sum $z_{m(1)}+\ldots+z_{m(p)}=0$ at all times, due to (212).

We can thus transform the original $ZI=V$ system of equations into that shown in Figure 48 :

		1	2	3	4	5	6	7	8+9	10+11+12	9	11	12				
	9										A	B	C		J1		
EFIE	11										D	E	F		J2		VE
	12										G	H	I		J3		
	1	AA	HH							aa+bb+cc	a	bb	cc		J4		
	2	HH	BB							dd+ee+ff	b	ee	ff		J5		
	3			CC	JJ					gg+hh+ii	c	hh	ii	*	J6	=	
	4			JJ	DD					jj+kk+ll	d	kk	ll		J7		
MFIE	5					EE	KK		e+f		f	vv	ww		J8		VH
	6					KK	FF		g+h		h	xx	yy		J10		
	7							GG	j+k	mm+nn+oo	k	nn	oo		J9-J8		
	8					LL	MM		l+m	pp+qq+rr	m	qq	rr		J11-J10		
	10	NN	PP					QQ	n+p	ss+tt+uu	p	tt	uu		J12-J10		
		Real									Complex						

Figure 48 : Efficient E-MFIE system of equations

This system of equations can now be solved through the following steps. With V_E, the 3x3 tEFIE submatrix provides J_9-J_8, J_{11}-J_{10} and J_{12}-J_{10}. Next we subtract from V_H the 9x3 complex part of the MFIE portion multiplied by the 3x1 vector $[J_9\text{-}J_8;J_{11}\text{-}J_{10};J_{12}\text{-}J_{10}]$, to form V_H'. The 9 remaining unknowns J_1 to J_8 and J_{10} can

now be obtained from V_H' and the real sub-block of the 9x9 MFIE submatrix. Finally J_9, J_{11} and J_{12} are derived in an obvious way from the previous results.

The increased implementation complexity of this procedure as compared to the simple one-step E-MFIE procedure described in §4.4.1 is worth it only if the size N_E of the tEFIE-f submatrix is a significant portion of N, the size of the E-MFIE matrix. In the example of Figure 45 (p.84), $N/N_E=4$. As mentioned at the end of §4.4.1, N/N_E should be comprised between 2 and 3 for realistic sheets. In such cases, a computing time reduction by a factor between 3 and 4 can be expected if a direct LU solver is used. A sparse solver can also be used to speed up the resolution of the tMFIE-nxf submatrix system of equations [12].

4.5 Summary

This chapter was devoted to embedded sheets, as it was recognized that this case only didn't fit in the general canvas described in chapter 3 to treat any combination of linear, homogeneous and isotropic bodies.

In the first place, the singularities associated with the impedance matrices of both the tEFIE and tMFIE are analyzed in great details, starting from the correct three-dimensional vector expressions valid for sheets established in chapter 1.

The tEFIE analysis is not entirely new, excep the generalization to *p*-edges, for which a detailed explanation of the singular behaviors as well as the widely used cure are paralleled to the explanations given afterwards for the tMFIE.

In the case of the tMFIE, a much less singular behavior is revealed, especially for embedded edges supporting an odd number of sectors. Despite this milder singularity, it is fully demonstrated why there is no cure available, as for the tEFIE, closing once for all the nebulous debate about the mysterious inability of the tMFIE to deal with so-called "open surfaces".

Additionally, a new formulation is proposed – the E-MFIE – that allows to fully solve arbitrary perfectly conducting sheets according to the general canvas described in chapter 3. Moreover, this new formulation yields a richer solution than the one obtained with the cured tEFIE : the current densities on both faces and around every edge are revealed instead of only their sum. The E-MFIE is illustrated in chapter 6.

Fitting to the general canvas of chapter 3 with an easy implementation has a price : a larger impedance matrix. If the generality and ease of implementation is deemed less important than the resource needed to obtain the richer solution, then an efficient implementation of the E-MFIE is proposed.

[1] A. Sommerfeld, *Math. Anal.*, No. 47, pp. 317, 1896.

[2] G.A. Grinberg, "A New Method for Solving Problems Related to the Diffraction of Electromagnetic Waves by a Plane with an Unbounded Straight Slit", *Zh. Tekhn. Fiz.*, 27, pp. 2410-2419, 1957.

[3] J.Radlow, "Diffraction by a quarter-plane", *Arch. Rational Mech. Anal.*, Vol. 8, No. 1, pp. 139-158, 1961.

[4] Y. Nomura and S. Katsura, "Diffraction of Electromagnetic Waves by Circular Plate and Circular Hole", *J. Phys. Soc. Japan*, Vol. 10, No. 4, pp. 285-304, 1955.

[5] K.Hongo and H.Serizawa, "Diffraction of Electromagnetic Plane Wave by a Rectangular Plate and a Rectangular Hole in the Conducting Plate", *IEEE Transactions on Antennas and Propagation*, Vol. 47, No. 6, pp. 1029-1041, June 1999.

[6] B.M. Kolundzija and A.R. Djordjević, *Electromagnetic Modeling of Composite Metallic and Dielectric Structures*, Artech House, Boston, 2002.

[7] D. R. Wilton, "Computational Methods, Scattering: Scattering and Inverse Scatter-ing" in *Pure and Applied Science*, E. R. Pike and P. C. Sabatier, Eds., AcademicPress / Elsevier: Amsterdam, Netherlands, vol. 1, chap. 1.5.5, pp. 316-365, 2002.

[8] D.B.Davidson *Computational Electromagnetics for RF and Microwave Engineering*, Cambridge University Press, 2005.

[9] P. Ylä-Oijala, M. Taskinen and J. Sarvas "Surface Integral Equation Method for General Composite Metallic and Dielectric Structures with Junctions", *PIER 52*, pp. 81-108, 2005.

[10] K.Barkeshli J.L.Volakis, "EM Scattering From Thin Strips - Part I Analytical Solutions for Wide and Narrow Strips", *IEEE Trans. on Education*, Vol. 47, No. 1, pp. 100-106, February 2004.

[11] M. Born, E. Wolf, *Principles of Optics*, 7th (expanded) edition, Cambridge University Press, London, 1999.

[12] K. Kourtis, G. I. Goumas, and N. Koziris, "Optimizing sparse matrix-vector multiplication using index and value compression", in *Conf. Computing Frontiers*, pp. 87–96, 2008.

5 Accuracy of the Method of Moments

The Method of Moments is expected to yield an accurate approximation of the unknown exact solution. In this chapter we first review the various types of errors that can be encountered and we explain how they can be controlled or avoided. Next we concentrate on the numerical integration errors, especially those occurring in the evaluation of singular integrals. The many ways to cope with these problematic integrals are reviewed, with their advantages and disadvantages. In line with our objective of generality, we choose the integration strategy that offers the greatest versatility : high efficiency polynomial quadratures. But to quantify how well the main objective of accuracy is also met with this choice, we propose an original detailed three-level analysis. First the accuracy of the numerical integration is measured with the help of self derived exact solutions for the interaction between two adjacent triangles, regular and elongated. Secondly we verify our observations at system level on a canonical elementary body. Finally, in §6.12 at the end of chapter 6, we confirm our conclusions with a double pyramid made of mixed material and meshed with regular triangles, and with the challenging case of a very thin dielectric plate containing elongated triangles.

5.1 Approximations introduced by the Method of Moments

The Method of Moments is a numerical technique where a set of exact integro-differential equations are being discretized. In Electromagnetics, these integro-differential equations are derived from Maxwell's equations. For problems involving only homogeneous and isotropic domains, they can be expressed in function of two unknown surface current densities $\bar{J}$ and $\bar{M}$. After discretization, these integro-differential equations become a $ZI=V$ matrix system of equations, where the vector I contains all coefficients to determine an approximation for $\bar{J}$ and $\bar{M}$. This was the topic of chapters 2, 3 and 4.

The integro-differential equations involve two or more domains delimited by closed surfaces. Except in a few specific cases where entire domain basis functions can be used (see §2.2.3), the boundaries of these domains must be partitioned into subdomains. When a rounded surface is replaced by a series of flat facets, or when an exponential flaring is replaced by a spline fitting, a small but sometimes non negligible *geometrical error* is introduced, illustrated by Figure 70 (p.143) and quantified in Table 17 (p.153).

When subdomain basis functions (see §2.2.4) are used to represent the equivalent current densities, the exact solution is generally replaced by a constant, piecewise linear or higher order polynomial function. The *physical error*, due to the approximation of the physical magnitudes of interest, is inherent to the numerical method. As such it is unavoidable, but this error is expected to tend towards zero if the polynomial order of the approximating functions is increased, and/or if the size of the subdomains is reduced [1, p.70]. The influence of the

mesh density is shown in §§6.2.4 and 6.7. However this convergent behavior can only be expected if some conditions are fulfilled :

- the basis functions must possess sufficient derivability with regard to the integro-differential operator applied to them. For example, using pulse basis functions (§2.2.6) to represent the equivalent surface current densities as constant over every mesh element in a discretized equation where the surface divergence of these current densities is present will not guarantee a better approximation if the size of the subdomains is reduced [2, p.51].
- the basis functions must be able to represent the actual physical behavior of the surface current densities.
  - On some edges and corners, depending on the geometry and electromagnetic properties of the domains as well as on the incident fields, the surface current densities can be infinite, while their growth towards infinity close to such edges and corners is usually very slow. Any attempt to represent this specific behavior with a linear, or even a higher order polynomial function, will always suffer from a large absolute error in the close vicinity of the edges and corners, regardless of the fineness of the mesh.
  - As explained in §2.2.5 and illustrated in §6.6.2, basis functions must not impose tangential continuity between subdomains to model equivalent surface densities around edges and corners of a dielectric body.

In this book, we also explained and illustrated another aspect of the *physical error*, appearing for example with RWG (§2.2.8) and rooftop (§2.2.9) basis functions, because they are defined as incomplete linear expansions over a pair of adjacent subdomains, imposing that the normal component of the surface current densities be constant along every edge of the subdomains. Therefore surface current densities showing a strong transverse gradient cannot be modelled and lead to unphysical zigzagging (see for example Figure 68, p.141 - top left - and Figure 138, p.215). In cases where the normal component of the surface current densities must vary significantly along an edge, very distorted patterns result (see Figure 116, p.192 and Figure 129, p.205).

As a result of the geometrical and physical approximations, the Method of Moments produces a $ZI=V$ matrix system of equations. The errors on the surface current densities $\bar{J}$ and $\bar{M}$ are directly proportional to $I=Z^{-1}V$, thus also strongly dependent on the accuracy of the elements of the impedance matrix Z and the source vector V. Theses elements are obtained through numerical integrations, called quadratures (§5.3.1). The elements of V are easy to obtain with a very high accuracy, but in the formulations containing the $1/R^3$ singularity (§5.3.3), some crucial elements of Z require much more care. Poorly or wrongly estimated z_{ij} and/or v_i elements can induce moderate to high errors on some I_j elements, that can be greatly amplified if the Z matrix exhibits a large condition number (§5.2.2). The *quadrature errors* are covered extensively in §§5.4 and 5.5.

5.2 Numerical issues and limitations

5.2.1 Problem size – CPU time limitation

If linear RWG basis functions are used over quasi equilateral triangles, their edges a should be at most $\lambda/10$ long. The average surface of such triangles is $a^2\sqrt{3}/4$. A sphere of diameter $D=n\lambda$ has a surface πD^2 . Approximately $(400\pi/\sqrt{3})n^2 \approx 725n^2$ quasi equilateral triangles are required to mesh it. For a cube of dimensions DxDxD, using rectangular triangles with the same average surface necessitates approximately $924n^2$ triangles. For a PEC structure, the number of complex elements in the Z matrix is NxN, where N is the number of (triangle) edges. For a dielectric structure, the size of Z is $2N$x$2N$. A closed surface completely meshed with T triangles counts exactly $1{,}5T$ edges. The number of bytes required to represent complex numbers in double precision is compiler dependant. Considering the ANSI-C minimum of 16bytes, mostly encountered, the largest value of n for a PEC or dielectric sphere, and for a PEC or dielectric cube that can be solved within 2GBytes of RAM memory in double precision is reported in Table 6. If triangles smaller than $\lambda/10$ are used, for example to improve the overall accuracy, or when the structure presents details possibly much smaller than $\lambda/10$, the maximum dimensions of the total surface that can be analyzed diminishes.

Table 6 : Largest size in $n\lambda$ units that fits within 2GBytes

	PEC	Dielectric
Sphere (diameter = $n\lambda$)	$n \leq 3{,}26$	$n \leq 2{,}31$
Cube (side = $n\lambda$)	$n \leq 2{,}89$	$n \leq 2{,}04$

It is clear from Table 6 that the classical Method of Moments cannot be used on a single 32-bits laptop for structures stretching across many wavelengths, or even for subwavelength structures containing too many dielectrics and very fine details.

There are variations and improvements of the original MoM to handle these situations, such as the use of macro basis functions [3], or aggregate synthetic functions [4], and the multilevel fast multipole algorithm [5][6], but they are beyond the scope of this book. Indeed in chapter 6 we analyzed only structures small enough to allow global or local mesh refinements while keeping all problems solvable within 2GBytes of RAM with the classical Method of Moments explained in chapters 2, 3 and 4.

Nevertheless, a novelty has been introduced for the fine analysis of the surface current densities close to edges or corners, and along the sides of very thin PEC or dielectric plates : *lin-* and *log-distributed meshes*. These meshes use very elongated triangles instead of quasi equilateral triangles, reducing thereby drastically the number of unknowns and the size of the Z matrix. A detailed analysis of the accuracy that can be obtained with such elongated triangles and

meshes can be found in §§5.5.3, 6.2.5, 6.6, 6.8, 6.9 and 6.10, along with the impact on the condition number (see §5.2.2).

5.2.2 Condition number

The Method of Moments leads to a $ZI=V$ system of equations. It can be solved for I either with a direct solver (such as LU, or QR decomposition) or with an iterative solver (for example : Conjugate gradient method). For iterative solvers, the speed of convergence to an accurate enough solution, or even the convergence itself, can be jeopardized if the condition number of the matrix Z becomes too large. Much work has been done during the last decennia to develop efficient preconditioners and reduce the condition number of Z. This area is a whole field in itself and will not be addressed in this book, where only direct solving has been considered.

Direct solvers do not suffer from poor or lack of convergence, but they can suffer from an excessively high condition number, especially if the elements of Z and/or V are poorly estimated, as explained hereafter. Even if those elements are well estimated, an excessively high condition number favours the propagation of roundoff errors during the direct solving phases. This problem is further enhanced for large matrices, and/or if single precision is used instead of double precision. Our experience, in particular with very thin plates and elongated triangles, shows that condition numbers in excess of 10^{12} start to cause such problems when double precision is used.

In the field of numerical analysis, the condition number of a function with respect to an argument measures how much the function can change in proportion to small changes in the argument. The "function" is the solution of a problem and the "arguments" are the data in the problem. A problem with a low condition number is said to be well-conditioned, while a problem with a high condition number is said to be ill-conditioned. For example, the condition number associated with the linear equation :

$$ZI = V \tag{236}$$

gives a bound on how inaccurate the solution I will be if there is an error on the elements of Z or those of V. Considering also the perturbed equation :

$$Z(I + \Delta_V I) = V + \Delta V \tag{237}$$

one can apply the Schwarz inequality to both (236) and (237) :

$$\|V\| \le \|Z\| \|I\| \tag{238}$$

$$\|\Delta_V I\| \le \left\|Z^{-1}\right\| \|\Delta V\| \tag{239}$$

where any vector and matrix norms can be used. The most common is the Euclidian 2-norm :

$$\|V\| = \sqrt{V^* V} = \sqrt{\sum_i |V_i|^2} \tag{240}$$

$$\|Z\| = \sqrt{\sum_i \sum_j |Z_{ij}|^2} \tag{241}$$

Combining (238) and (239), we conclude that :

$$\frac{\|\Delta_V I\|}{\|I\|} \le \kappa(Z) \frac{\|\Delta V\|}{\|V\|} \tag{242}$$

where the condition number $\kappa(Z)$ is given by :

$$\kappa(Z) = \|Z\| \|Z^{-1}\| \tag{243}$$

Considering now the perturbed equation :

$$(Z + \Delta Z)(I + \Delta_Z I) = V \tag{244}$$

one obtains :

$$\frac{\|\Delta_Z I\|}{\|I + \Delta_Z I\|} \le \kappa(Z) \frac{\|\Delta Z\|}{\|Z\|} \tag{245}$$

When the Euclidian 2-norm is used for (243), it can be shown that the condition number is equal to the ratio of the largest to the smallest singular value σ of Z :

$$\kappa(Z) = \frac{|\sigma(Z)|_{\max}}{|\sigma(Z)|_{\min}} \tag{246}$$

The identity matrix has a condition number equal to 1, while a singular matrix has at least one null eigenvalue and therefore an infinite condition number.

Equations (242) and (245) show that small relative errors introduced in the estimation of Z and/or V can be amplified by the condition number κ(Z). These errors are down-limited by the finite machine precision, especially when 8-digits numbers (float) are used instead of 16-digits (double). They can become much worse than the machine-precision limit when the elements of Z are evaluated with low order or inappropriate quadratures (see §5.5).

When the Method of Moments is applied to two dielectric domains (e.g. a finite-size dielectric body embedded in free space), the global matrix system of equations is obtained after a combination of the local matrix system of equations written in each domain D_1 and D_2 :

$$\begin{bmatrix} \alpha_1 Z_1^{EJ,t} + \alpha_2 Z_2^{EJ,t} & \alpha_1 Z_1^{EM,t} + \alpha_2 Z_2^{EM,t} \\ \beta_1 Z_1^{HJ,t} + \beta_2 Z_2^{HJ,t} & \beta_1 Z_1^{HM,t} + \beta_2 Z_2^{HM,t} \end{bmatrix} \begin{bmatrix} J \\ M \end{bmatrix} = \begin{bmatrix} \alpha_1 V_1^{E,t} + \alpha_2 V_2^{E,t} \\ \beta_1 V_1^{H,t} + \beta_2 V_2^{H,t} \end{bmatrix} \tag{247}$$

As explained in §2.3.1, this combination is only possible if the impedance Z_i of each domain D_i is incorporated in the z_{ij} terms belonging to the $Z_i^{EJ,t}$ and $Z_i^{HJ,t}$

subblocks, while the I vector contains J and not $Z_i J$. Doing so, those terms in Z lose their adimensionality (see §§1.14 and 2.2.7). In the PMCHWT combination scheme (see §3.6), as $\alpha_i = 1 = \beta_i$ those terms become in the average approximately Z_0 times larger than in the remainder of the Z matrix, where $Z_0 \approx 120\pi$ is the impedance of free space. Modifying the whole system of equations as shown in (247) makes the whole Z matrix adimensional and rescales the elements of Z and I to a similar order of magnitude. The condition number of the rescaled Z is thereby approximately reduced by a factor Z_0.

$$\begin{bmatrix} Z^{EJ,t}/Z_0 & Z^{EM,t} \\ Z^{HJ,t}/Z_0 & Z^{HM,t} \end{bmatrix} \begin{bmatrix} Z_0 J \\ M \end{bmatrix} = \begin{bmatrix} V^{E,t} \\ V^{H,t} \end{bmatrix} \tag{248}$$

In the Müller combination scheme (see §3.6), as $\alpha_i = \varepsilon_i$ and $\beta_i = \mu_i$, the global Z matrix can be made adimensional if the following rescaling is applied :

$$\begin{bmatrix} Z^{EJ,t}/(\varepsilon_0 Z_0) & Z^{EM,t}/\varepsilon_0 \\ Z^{HJ,t}/(\mu_0 Z_0) & Z^{HM,t}/\mu_0 \end{bmatrix} \begin{bmatrix} Z_0 J \\ M \end{bmatrix} = \begin{bmatrix} V^{E,t}/\varepsilon_0 \\ V^{H,t}/\mu_0 \end{bmatrix} \tag{249}$$

The E-MFIE matrices (see §4.4) contain both a $Z^{EJ,t}$ and a $Z^{HJ,t}$ subblock that are both applied to the whole vector J. Dividing both subblocks by Z_0 as in (248) has no effect on the condition number as the whole matrix is divided by a unique value.

As the condition number can be greatly improved by the above described operations, it becomes meaningless to make comparisons of condition numbers from one problem to another unless a reference configuration for Z is adopted. In the literature, condition numbers are very often reported, but without any clear mention of eventual manipulations on Z.

To conclude this paragraph, we list below a series of observations revealed by the examples treated in chapter 6. In these examples, when available, the condition number (CN) has always been computed for the adimensional versions of Z described by (248) or (249) with the built-in function '*cond*' available in Matlab 7.1™.

- The CN of the tEFIE$^{\nabla_f}$-f and tEFIE$^{\nabla_G}$-f are always quasi identical. We refer hereafter to any of them as tEFIE-f.
- The CN of the tMFIE-nxf is always 100 to 1000 lower than for the tEFIE-f.
- For homogeneous or regular meshes, the CN for the tMFIE-nxf is fairly independent on the mesh characteristic length h, while it increases approximately with $1/h$ for the tEFIE-f.
- The CN of both the tEFIE-f and the tMFIE-nxf increase if an irregular mesh (with elongated triangles) is used instead of a regular one, but the increase is more important for the tEFIE-f.
- For a very thin PEC plate of thickness t and with 90° edges the CN increases proportionally to $(1/t)^2$, for both the tEFIE-f and the tMFIE-nxf.

- For a given structure, the CN of the PMCHWT-f-f in the dielectric case is fairly identical to the CN of the tEFIE-f in the PEC case.
- The CN of the PMCHWT-nxf-nxf and Müller-nxf-nxf is much lower than the CN of the PMCHWT-f-f and Müller-f-f.
- The CN of a dielectric sphere improves for higher permittivities ε_r with the PMCHWT-f-f and the Müller-f-f combinations, but it degrades with the PMCHWT-nxf-nxf and the Müller-nxf-nxf combinations.

5.2.3 Resonance

In 1949, when he derived the two alternative integral equations later named EFIE and MFIE [7] for a volume enclosed in a bounding surface *S*, Maue already noted the non-uniqueness of the exterior solution at interior cavity resonance frequencies [8]. In the case of the EFIE applied to a PEC volume, the existence of such internal resonances causing high spurious radiated fields can easily be proved and understood from a physical and numerical viewpoint. They appear because the boundary condition $\hat{n}\times\overline{E}=\overline{0}$ imposed only on the outside surface *S* of the PEC volume does not guarantee zero surface current densities, at the resonant frequencies determined by the geometry of *S*, inside the PEC volume. Mathematically, these spurious surface current densities do not radiate outside the PEC volume. But the geometrical and numerical approximations involved in the MoM induce some leakage that will contribute to a possibly large error in the scattered fields [9]. The physical explanation for the even larger spurious fields caused by the MFIE applied to the same PEC volume is less obvious [10]. At the MFIE resonance frequencies, identical to the EFIE ones, non zero $\hat{n}\times\overline{E}$ are allowed on *S* equal to the current densities of the interior cavity modes. We refer to [11, §4.3.2] for a physical explanation of the resonances that can also occur in presence of dielectric scatterers when either the EFIE or the MFIE alone is used. Again, the resonance frequencies are identical to those encountered if the dielectric object would be a PEC object solved with the EFIE or MFIE alone.

For a spherical cavity of diameter *D* filled with air, the lowest resonance frequency is produced by the TM_{101} mode. It corresponds to a wavelength $\lambda_0=D/1.145$. Otherwise stated, there is no resonance if $D<1.145\lambda_0$. For a cubical cavity *D*x*D*x*D*, the lowest resonance frequencies of the TE_{110}, TM_{101} and TM_{011} modes are identical and correspond to $D<0.7071\lambda_0$. If the cubical or spherical cavities are filled with a dielectric of relative permittivity ε_r, then λ_0 must be replaced by $\lambda=\lambda_0/\sqrt{\varepsilon_r}$ in the above formulas [12, Chap4].

For dielectric structures, the widespread use of PMCHWT or Müller formulation (see §3.6), where both the EFIE and MFIE coexist, eliminates the resonances. For PEC structures, many cures have been proposed, such as :

- inserting of a lossy object inside the region [13]. The resonance frequencies become complex and are damped, but not completely suppressed. Moreover, the number of unknowns and the complexity of the problem are increased.

- inserting of shorts in the resonance cavity to push the resonance frequencies of the resonant modes higher [14].
- searching for a minimum norm solution of the EFIE [15]. A disadvantage of this method is that it requires to choose weights for the least-squares error and the norms that need to be formed.
- augmenting the EFIE or MFIE with the boundary conditions for the normal component of the fields on S [16]. This method increases the number of unknowns and leads to an overdetermined system of equations, that must be solved for example with a least-squares error procedure.
- combining the EFIE and MFIE into a Combined Field Integral Equation (CFIE). This last method is by far the most popular and will be shortly explained hereafter.

The CFIE is based on various works [17][7][18] and was first established under the following form :

$$\text{CFIE} = a \;\; \text{tEFIE-f} + b \;\; \text{tMFIE-nxf} \tag{250}$$

where $a = \alpha$, $b = Z_0(1-\alpha)$, $0 < \alpha < 1$ and $Z_0 \approx 120\pi$ is the impedance of vacuum. The proof of the uniqueness of the CFIE solution has been given [18], but only partial assertions have been published about its connection with the cavity problem [19]. Several variants have been proposed [20][21][22], but it is beyond the scope of this book to enter into more details. Instead, for all examples treated in chapter 6 we took care to properly dimension the PEC objects to avoid this phenomenon. Resonance problems are also avoided in all dielectric cases with the use of either PMCHWT or Müller combination schemes.

5.2.4 Low frequency breakdown

If a PEC structure is solved with the tEFIE-f, it can suffer from the so-called low frequency breakdown problem [23][24]. If the frequency is very low, or if the mesh density is very high compared to the wavelength, the Z matrix becomes very to extremely ill-conditioned. No clear limit is mentioned in the abundant literature to quantify “very low” or “very high”. In fact, the condition number degrades progressively with decreasing frequency or increasing mesh density. The limit to an acceptable highest value for the condition number is implementation dependent (single or double precision, direct or iterative solving,…), and probably also problem dependent (single PEC volume, multiple dielectric domains,…). We refer to §5.2.2 for a detailed discussion on condition numbers.

The low frequency breakdown problem has also been reported for dielectric scatterers solved with PMCHWT-f-f [25]. On the other hand, it has been proved that tMFIE-nxf doesn not suffer from low frequency breakdown [26].

It is not within the scope of this book to address this specific problem, but we mention the three main cures that have been proposed during the last decennias : the loop-tree or loop-star decomposition [23][27][28][29], the

stabilization of the EFIE [30][31], or the use of an appropriate Müller formulation [32].

In the examples treated in chapter 6, the low frequency breakdown has been avoided by choosing objects and meshes with a ratio *characteristic dimension* $/\lambda$ large enough to ensure acceptable condition numbers.

5.3 Numerical integration

In §2.3.1 we have presented very general expressions for the discretized integro-differential equations and the possible testing schemes. In §3.4 and for the remainder of this book, we have restricted ourselves to the first form of the tangential integro-differential equations (see §1.9), RWG basis functions $\overline{f}_{n,i}(\overline{r}')$ (see §2.2.8) and RWG or nxRWG testing functions $\overline{T}_{m,i}(\overline{r})$. In every domain D_i, the elements of the local Z_i matrix that we have to compute are double surface integrals over $S_{m,i}$ and $S_{n,i}$, the domains of definition of $\overline{f}_{n,i}(\overline{r}')$ and $\overline{T}_{m,i}(\overline{r})$. They have the form :

$$Z_{mn,i}^{EJ} = -Z_i \int_{S_{m,i}} \overline{T}_{m,i}(\overline{r}) \cdot \left[\overline{D}_i(\overline{r}) \left\{ \overline{f}_{n,i} \right\} \right] dS \tag{251}$$

$$Z_{mn,i}^{HJ} = \int_{S_{m,i}} \overline{T}_{m,i}(\overline{r}) \cdot \left[\overline{K}_i(\overline{r}) \left\{ \overline{f}_{n,i} \right\} - \frac{\hat{n}_{m,i}(\overline{r}) \times \overline{f}_{n,i}(\overline{r})}{2} \right] dS \tag{252}$$

with :

$$\overline{D}_i^{(1)} \left\{ \overline{f}_{n,i} \right\} (\overline{r}) = \frac{j}{k_i} \int_{S_{n,i}} \left\{ k_i^2 G_i \overline{f}_{n,i} - \nabla'_s \cdot \overline{f}_{n,i} \;\; \overline{\nabla}' G_i \right\} dS' \tag{253}$$

$$\overline{K}_i^{(1)} \left\{ \overline{f}_{n,i} \right\} (\overline{r}) = \int_{S_{n,i}} \left\{ \overline{f}_{n,i} \times \overline{\nabla}' G_i \right\} dS' \tag{254}$$

The free-space Green's function G_i, the impedance Z_i and the wavenumber k_i inside domain D_i are defined with (56), (68) and (69). $\hat{n}_{m,i}(\overline{r})$ is the unit normal to $S_{m,i}$.

In the next paragraphs, we examine in detail the non trivial problem of accurately evaluating these integrals.

5.3.1 Quadratures over triangles

The double surface integrals (251) and (252) have no close form analytical solution, they must be evaluated numerically. It was not long after the invention of infinitesimal calculus by Isaac Newton and Gottfried Leibniz, during the seventeenth century, that numerical quadratures for one-dimensional domains have been developed. Just to name two of them, the Newton-Cotes formulas and Simpson's rules. Until recently, many variations and improvements to these early methods have been proposed, but it was not before the mid twentieth century that the first quadrature over triangles has been published [33]. Three quadrature strategies have been reported : polynomial moment fitting, Duffy's transformation, and extrapolation [34].

The extrapolation technique, based on the work of Richardson [35], was first exploited by Romberg for one-dimensional integrations [36] to improve the convergence rate of the trapezoidal integration rule. It was then easily extended to the integration over a square by several authors during the 1960s. In the next decade, it required much more effort to transpose this theory from the square to regularly shaped triangles [37][38][39], then more recently to arbitrary triangles [40].

With Duffy's transformation [41], the two-dimensional integration over a triangle is transformed into an integration over a square, that can be performed as the product of two one-dimensional integrals. In principle, any pairs of one-dimensional quadrature rules can be used, such as for example the Gauss-Legendre or Gauss-Jacobi rules [42].

In the polynomial moment fitting method, the integral over the domain S_i bis replaced y a weighted sum on a set of nodes :

$$\int_{S_i} f_i(x,y)\,dxdy \cong \sum_n^N w_n f_i(x_n,y_n) S_i \tag{255}$$

A quadrature is thus defined by the coordinates (x_n,y_n) of N nodes and their associated weights (w_n), for example :

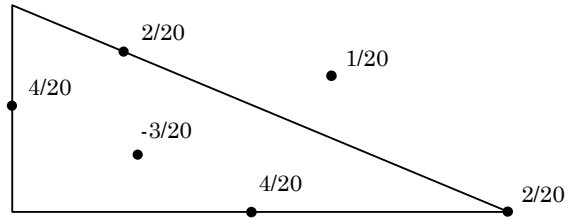

Figure 49 : 5 nodes quadrature

The number of nodes N, their location and weights are determined such that the integral is exactly identical to the sum in (255) when the integrand $f_i(x,y)$ is any polynom in the two variables x and y up to a degree d. A quadrature rule is said to be minimal when its number of nodes N reaches the lower bound determined by the following results [43] :

$$\begin{aligned} N &\geq \frac{(d+2)(d+4)}{8} && \text{if } d \text{ is even} \\ N &\geq \frac{(d+1)(d+3)}{8} + \frac{(d+1)}{4} && \text{if } d \text{ is odd} \end{aligned} \tag{256}$$

Long after the seven-points and fifth degree quadrature of Radon [33], a minimal formula of degree 4 with all positive weights was constructed by Schmid [44]. Exploiting for the first time the symmetry groups of the triangle, Lyness and Jespersen developed symmetric quadrature rules up to a degree 11 [45], later on extended up to a degree 20 by Dunavant [46] and up to a degree 30 by Wandzura

and Xiao [47]. These quadratures are given with 16 significant digits. Some of them, but not all, are minimal.

In the fictive example shown in Figure 49 (p.104) :

- the sum of the weights equals 1/2 and not 1. This supposes using $2S_i$ instead of S_i in the summation (255). This is common practice for quadratures over triangular domains, for which the norm of the cross product of any two sides of the triangle equals $2S$.
- the nodes are irregularly located inside the triangle, on its edges and vertices
- some nodes are located outside the triangle
- the weigths are positive or negative

The two last properties are undesirable. A *good* quadrature should have all its nodes inside the integration domain (to avoid extrapolation of the integrand outside the domain) and positive weights (to improve convergence and stability) [34]. Quadratures where the nodes respect the symmetry groups of the triangle are also regarded as preferable, but not indispensable.

In this book, we have restricted ourselves to polynomial quadratures. For reasons that will be explained in §5.3.3, their nodes will be distributed strictly inside the triangle, and not on their edges or vertices.

5.3.2 Practical integration within the MoM

Before investigating in detail the possible inaccuracies due to the quadratures, we explain concretely how the numerical integration of the double surface integrals must be performed to approximate (251) or (252) with a polynomial quadrature. RWG functions span over a pair of adjacent triangles, as illustrated by Figure 50 :

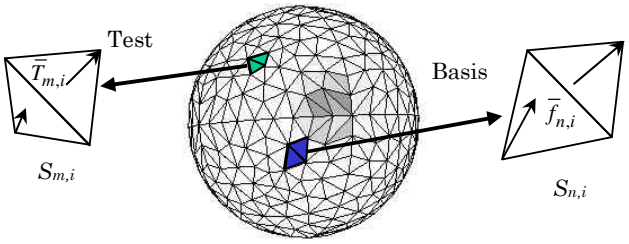

Figure 50 : Test and Basis RWG

The double integrals involving the test triangle pair $S_{m,i} = T^+_{m,i} \cup T^-_{m,i}$ and the basis triangle pair $S_{n,i} = T^+_{n,i} \cup T^-_{n,i}$ will thus be decomposed in four separate integrals :

$$\int_{S_{m,i}}\int_{S_{n,i}} = \int_{T^+_{m,i}}\int_{T^+_{n,i}} - \int_{T^+_{m,i}}\int_{T^-_{n,i}} - \int_{T^-_{m,i}}\int_{T^+_{n,i}} + \int_{T^-_{m,i}}\int_{T^-_{n,i}} \tag{257}$$

Considering the example shown in Figure 51, the part of the analytical double surface integral in (252), involving $T^+_{m,i}$ and $T^-_{n,i}$ and the vector function $\bar{K}^{(1)}_i$, will be approximated by the following nested summation if the testing function $\bar{T}^+_{m,i} = \bar{f}^+_{m,i}$:

$$\begin{aligned} &\int_{T^+_{m,i}} \bar{f}^+_{m,i} \cdot \left(\int_{T^-_{n,i}} \left(\bar{f}^-_{n,i} \times \bar{\nabla}' G_i \right) dS' \right) dS \\ &\cong \sum_{p=1}^{P=3} \bar{f}^+_{m,i}(\bar{r}_p) \cdot \left[\sum_{q=1}^{Q=4} \bar{f}^-_{n,i}(\bar{r}'_q) \times \left[\bar{\nabla}' G_i(\bar{r}_p - \bar{r}'_q) \right] (w_i S^-_{n,i}) \right] (w_j S^+_{m,i}) \end{aligned} \tag{258}$$

Note that the number of nodes does not need to be the same, or even from the same type of quadrature, for the inner (*basis*) and outer (*test*) surface integral.

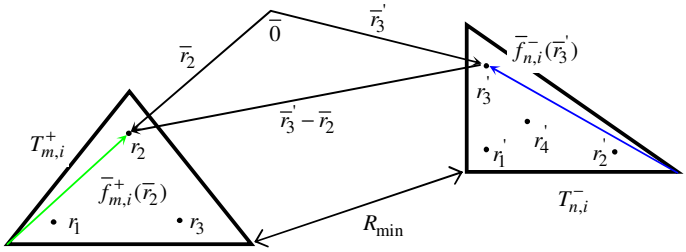

Figure 51 : Numerical integration of a double surface integral

Any numerical integration scheme introduces an additional error in the application of the MoM : the quadrature error. For a given quadrature type, the accuracy required in the evaluation of every integral will dictate the required number of nodes for this integral. On the other hand, the time needed to perform all the nested integrations will increase as *P*x*Q*, if *P* and *Q* are respectively the number of nodes for the outer and inner integrals. The tradeoff is clearly to use as few nodes as possible while guaranteeing the desired accuracy in the final result.

Polynomial quadratures are very performant with integrands that can accurately be approximated with polynomial expansions. Unfortunately, the free-space Green's function and especially its gradient introduce complications when the test and basis domains $S_{m,i}$ and $S_{n,i}$ are very close to each other, or even overlap. The resulting $Z_{mn,i}$ terms have been called (quasi) self terms in §2.3.2, and were shown to be dominant in the Z matrix. As such, they require special care and must be evaluated with sufficient accuracy.

5.3.3 *1/R* and *1/R³* singularities

Equations (251) and (252) contain the free-space Green's function and/or its gradient. When the observation point $\bar{r}$ in the test element $S_{m,i}$ also belongs to

the basis element $S_{n,i}$, the distance $R = |\bar{r} - \bar{r}'|$ can become zero in the integration process. As can be seen in its Taylor's polynomial expansion (259), the free-space Green's function then goes to infinity as $1/R$. The gradient of the free-space Green's function (260) is even more singular, going to infinity as $1/R^3$.

$$\begin{aligned} G_i &= \frac{e^{-jk_iR}}{4\pi R} \\ &= \frac{1}{4\pi R}\left[1 + (-jk_iR) + \frac{(-jk_iR)^2}{2} + \frac{(-jk_iR)^3}{6} + \frac{(-jk_iR)^4}{24} + \ldots\right] \\ &= \frac{k_i}{4\pi}\left[\frac{1}{k_iR} - j - \frac{k_iR}{2} + j\frac{(k_iR)^2}{6} + O(k_iR)^3\right] \end{aligned} \tag{259}$$

$$\begin{aligned} \bar{\nabla}' G_i &= \frac{1 + jk_iR}{4\pi R^3} e^{-jk_iR}\ \bar{R} \\ &= \frac{1 + jk_iR}{4\pi R^3}\left[1 + (-jk_iR) + \frac{(-jk_iR)^2}{2} + \frac{(-jk_iR)^3}{6} + \frac{(-jk_iR)^4}{24} + \ldots\right]\bar{R} \\ &= \frac{k_i^3}{4\pi}\left(\frac{1}{(k_iR)^3} + \frac{1}{2(k_iR)} - j\frac{1}{3} - \frac{(k_iR)}{8} + O(k_iR)^2\right)\bar{R} \end{aligned} \tag{260}$$

With an integrand exhibiting such a behavior, the inner integrals cannot be well approximated by a polynomial function of moderate order in the vicinity of the singularity $R=0$. As shown in Figure 55, Figure 56 and Figure 57 (pp.115 to 117) the accuracy of polynomial quadratures becomes extremely poor in such a situation, even with a high number of nodes.

There are several strategies to cope with these singularities. The two last ones actually avoid the singularities by eliminating them.

- A few specialized quadratures are available to handle singular integrals over triangles [48][49]. Unfortunately they are tailored for specific singular behaviors which are not those encountered here.
- The extrapolation integration technique mentioned in §5.3.1 has been extended to deal with several types of singular integrands, belonging to the class of homogeneous functions [50][51].
- Adaptive quadrature schemes have been developed, mainly to accommodate integration domains other than squares, circles or triangles. Based on successive decompositions of the integration domain in affine subdomains, they ensure convergence for regular and singular integrands. Being general purpose in essence, they require a very large number of nodes to obtain several exact significant digits, typically many hundreds [52].
- For integrand functions having a $1/R$ singularity on a vertex, Duffy's transformation naturally eliminates it by projecting the vertex on one edge of a square [41]. Despite its mathematical elegance, this method has some disadvantages. Firstly, it requires manipulations to accommodate

singularities occurring all along an edge and not on a vertex only. Secondly, it is not efficient for $1/R^n$ singularities where n is not equal to 1 [53]. Thirdly it has been shown to be accurate only on sufficiently regular triangles [54], a drawback we cannot afford as we intend to make extensive use of elongated triangles.

– In this book, we have considered the singularity extraction technique [55][56], explained in §5.4.

5.4 Extraction of the $1/R$ and $1/R^3$ singularities for the free-space Green's function

To explain in detail the extraction process for the $1/R$ and $1/R^3$ singularities, we repeat hereunder the two types of terms entering the Z_i matrix that contain double integrals of the free-space Green's function and/or its gradient. We will omit from here on the subscript i, but remember that every element Z_{mn} in the global Z matrix is a combination of elements $Z_{mn,i}$ from local Z_i matrices originating from domains D_i (see §3.6).

$$Z_{mn}^{EJ} = -\frac{jZ}{k}\int_{S_m} \bar{T}_m(\bar{r})\cdot\left[\int_{S_n}\left\{k^2 G(R)\bar{f}_n(\bar{r}') - \nabla'_s\cdot\bar{f}(\bar{r}')\ \bar{\nabla}'G(R)\right\}dS'\right]dS \tag{261}$$

$$Z_{mn}^{HJ} = \int_{S_m} \bar{T}_m(\bar{r})\cdot\left[-\frac{\hat{n}_m(\bar{r})\times\bar{f}_n(\bar{r})}{2} + \int_{S_n}\left\{\bar{f}_n(\bar{r}')\times\bar{\nabla}'G(R)\right\}dS'\right]dS \tag{262}$$

As explained with (257), the integrals on S_m and S_n in (261) and (262) are a sum of integrals on the triangles T_m^+, T_m^- and T_n^+, T_n^- : $Z_{mn} = Z_{mn}^{++} + Z_{mn}^{+-} + Z_{mn}^{-+} + Z_{mn}^{--}$. The expressions of the RWG basis functions on the triangles T_n^+ and T_n^- are given by (262), where $A_n^\pm$ is the area of the triangle $T_n^\pm$ and L_n is the length of the edge common to T_n^+ and T_n^-.

$$\bar{f}_n^\pm(\bar{r}') = \pm\frac{L_n}{2A_n^\pm}(\bar{r}' - \bar{p}_n^\pm) = \pm C_n^\pm(-\bar{R}\ +\ \bar{r} - \bar{p}_n^\pm) \tag{263}$$

The functions $\bar{f}_m^-/C_m^-$ and $\bar{f}_n^+/C_n^+$ are illustrated in Figure 52.

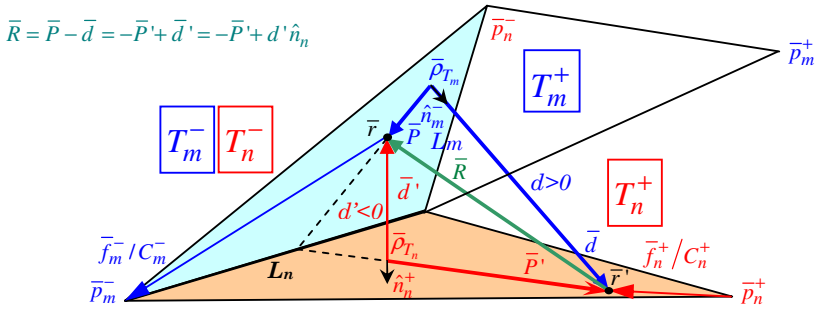

Figure 52 : Vectors involved in the two nested integrals

When $T_m^{\pm}$ and $T_n^{\pm}$ share common points, R can go to *0*, making the inner integrand in (261) and (262) infinite by virtue of the $1/R^3$ and $1/R$ terms revealed in (259) and (260).

5.4.1 Singularity associated with Z^{HJ}

Let us consider first (262), containing only the gradient of the free-space Green's function. For self terms situations, the tangential testing function $\overline{T}_m(\overline{r})$ is perpendicular to $\overline{f}_n(\overline{r}')\times\overline{\nabla}'G(R)$ and the tested inner integral reduces to its principal value term (see also §2.3.2). For example the integral involving $T_n^- = T_m^-$ writes :

$$Z_{mn}^{HJ--} = -\iint_{T_m^-} \overline{T}_m^-(\overline{r})\cdot\left(\frac{1}{2}\hat{n}_m^-(\overline{r})\times\overline{f}_n^-(\overline{r})\right)dS \tag{264}$$

This integral presents no singularity and can be integrated analytically or numerically. Details are given in Appendix D, and show that numerical integration can be performed exactly with only 1 point for $\overline{T}_m^-(\overline{r}) = \overline{f}_m^-(\overline{r})$ but requires 3 points for $\overline{T}_m^-(\overline{r}) = \hat{n}_m^-(\overline{r})\times\overline{f}_m^-(\overline{r})$.

If $T_m^{\pm} \neq T_n^{\pm}$, the principal value term in (262) is identically zero and only the surface integral remains in the inner integrand. For example :

$$Z_{mn}^{HJ-+} = \int_{T_m^-} \overline{T}_m^-(\overline{r})\cdot\left[\int_{T_n^+}\left\{\overline{f}_n^+(\overline{r}')\times\overline{\nabla}'G(R)\right\}dS'\right]dS \tag{265}$$

For coplanar triangles, like T_m^+ and T_n^- , the three vectors involved in the dot and cross product in (262) cancel the integral. For example :

$$Z_{mn}^{HJ+-} = 0 \tag{266}$$

If the triangles share a common edge (T_m^- and T_n^+) or a common vertex (T_m^+ and T_n^+) without being coplanar as in Figure 52 (p.108), the extraction of both the $1/R^3$ and $1/R$ singularities decomposes (262) into the sum of three integrals. For example, for Z_{mn}^{HJ-+} :

$$\iint_{T_m^-} \overline{T}_m^-(\overline{r})\cdot\left(\iint_{T_n^+}\left[\overline{f}_n^+(\overline{r}')\times\overline{R}\left(\frac{jkR+1}{4\pi R^3}e^{-jkR} - \frac{1}{4\pi R^3} - \frac{k^2}{8\pi R}\right)\right]dS'\right)dS \tag{267}$$

$$\iint_{T_m^-} \overline{T}_m^-(\overline{r})\cdot\left(\iint_{T_n^+}\left[\overline{f}_n^+(\overline{r}')\times\overline{R}\left(\frac{k^2}{8\pi R}\right)\right]dS'\right)dS \tag{268}$$

$$\iint_{T_m^-} \overline{T}_m^-(\overline{r})\cdot\left(\iint_{T_n^+}\left[\overline{f}_n^+(\overline{r}')\times\overline{R}\left(\frac{1}{4\pi R^3}\right)\right]dS'\right)dS \tag{269}$$

From here on in this paragraph indices (^+_n) or superscript (') will both be used to refer to magnitudes related to T_n^+ , thus depending on the variable $\overline{r}'$, and not on the variable $\overline{r}$.

Using (263), valid for a triangular domain, and the fact that $\overline{R}\times\overline{R}=\overline{0}$, (268) and (269) can now be rewritten as :

$$+C_n^+\iint_{T_m^-}\overline{T}_m^-(\overline{r})\cdot(\overline{r}-\overline{p}_n^+)\times\frac{k^2}{8\pi}\left(\iint_{T_n^+}\frac{\overline{R}}{R}dS'\right)dS \tag{270}$$

$$+C_n^+\iint_{T_m^-}\overline{T}_m^-(\overline{r})\cdot(\overline{r}-\overline{p}_n^+)\times\frac{1}{4\pi}\left(\iint_{T_n^+}\frac{\overline{R}}{R^3}dS'\right)dS \tag{271}$$

The integrand of (267) is bounded everywhere on T_n^+. As shown in Figure 56 and Figure 57 (p.117), this regular inner integral can be evaluated quite accurately with polynomial quadratures, even with a limited number of nodes.

The evaluation of (270) and (271), having singular integrands on T_n^+, can be performed as follows : analytical closed form solution for the inner integral, then numerical evaluation of the outer integral.

These analytical closed form solutions are expressed in function of local coordinates and distances for the pair formed by the observation point $\overline{r}$ and the triangle T_n^+, explained hereafter and illustrated in Figure 53.

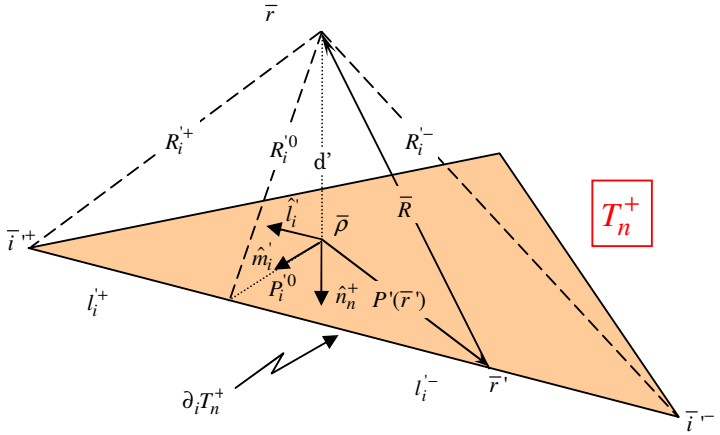

Figure 53 : Coordinates and distances involved in the inner integral

The unit normal to the triangle T_n^+ is $\hat{n}_n^+$. The orientation of $\hat{n}_n^+$ depends on the global closed surface S_i and on the domain D_i the triangle T_n^+ belongs to, as well as on the convention adopted for the orientation of the normal to S_i (outwards or inwards D_i). The normal projection $\overline{\rho}$ of $\overline{r}$ on T_n^+ determines the origin of a local orthonormal coordinate system for all three edges $\partial_i T_n^+$. The unit vector $\hat{m}_i'$ is normal to the edge $\partial_i T_n^+$ and pointing outwards T_n^+, in the plane of T_n^+. Finally, the unit vector $\hat{l}_i' = \hat{n}_n^+ \times \hat{m}_i'$ determines the sense of integration for line integrals on every edge $\partial_i T_n^+$ on the contour ∂T_n^+.

The *signed* values d', $P_i'^0$, $l_i'^-$ and $l_i'^+$ are the coordinates in the $\hat{m}_i', \hat{l}_i', \hat{n}_n^+$ basis respectively of $\bar{r}$, $\bar{i}_i'^-$ and $\bar{i}_i'^+$, that can be obtained from $\bar{R}_i'^- = \bar{r} - \bar{i}'^-$ and $\bar{R}_i'^+ = \bar{r} - \bar{i}'^+$ as :

$$d' = \bar{R}_i'^- \cdot \hat{n}_n^+ = \bar{R}_i'^+ \cdot \hat{n}_n^+ \tag{272}$$

$$P_i'^0 = -\bar{R}_i'^- \cdot \hat{m}_i' = -\bar{R}_i'^+ \cdot \hat{m}_i' \tag{273}$$

$$l_i'^\pm = -\bar{R}_i'^\pm \cdot \hat{m}_i' \tag{274}$$

In Figure 53 (p.110) : $d' < 0$, $l_i'^- < 0$, $l_i'^+ > 0$ and $P_i'^0 > 0$. The positive values $R_i'^-$ (resp. $R_i'^+$) are the distances between $\bar{r}$ and $\bar{i}'^-$ (resp. $\bar{i}'^+$).

Finally, the vector $\bar{R}$ is decomposed into a surface component $-\bar{P}'(\bar{r}')$ lying in the triangle T_n^+ and depending on the integration variable $\bar{r}'$, and a normal component $\bar{d}' = d' \cdot \hat{n}_n^+$, independent of the integration variable $\bar{r}'$.

The integral (270) contains the $1/R$ singularity. The analytical solution for the inner integral is fully derived in Appendix E.3. The final result is given hereafter :

$$\iint_{T_n^+} \frac{\bar{R}}{R} dS' = \iint_{T_n^+} \frac{-\bar{P}'}{R} dS' + \iint_{T_n^+} \frac{\bar{d}'}{R} dS' = -\sum_i \hat{m}_i' I_i'^{+1} + \bar{d}' K'^{-1} \tag{275}$$

with :

$$K'^{-1} = \sum_i P_i'^0 \ln\left(\frac{l_i'^+ + R_i'^+}{l_i'^- + R_i'^-}\right) - |d'| \sum_i \left[\tan^{-1} \frac{l_i'^+ P_i'^0}{\left(R_i'^0\right)^2 + |d'| R_i'^+} - \tan^{-1} \frac{l_i'^- P_i'^0}{\left(R_i'^0\right)^2 + |d'| R_i'^-} \right] \tag{276}$$

$$I_i'^{+1} = \frac{1}{2} \left\{ l_i'^+ R_i'^+ - l_i'^- R_i'^- + \left(R_i'^0\right)^2 \ln\left(\frac{l_i'^+ + R_i'^+}{l_i'^- + R_i'^-}\right) \right\} \tag{277}$$

For any observation point $\bar{r}$, (275) is finite and continuously differentiable. It can therefore be integrated numerically on T_m^- in (270) with great accuracy.

The integral (271) contains the $1/R^3$ singularity. We observe from (260) that the contribution of (271) to the real part of (265) becomes dominant as soon as $2/(kR)^3 > 1/(kR)$, or approximatively $R < \lambda/5$. This is always the case for adjacent triangles in a MoM mesh, as their characteristic dimension should never exceed λ/10 (see §2.2.4). It is therefore important to evaluate (271) with enough accuracy.

The analytical solution for the inner integral is fully derived in Appendix E.3 :

$$\iint_{T_n^+} \frac{\bar{R}}{R^3} dS' = -\iint_{T_n^+} \frac{\bar{P}'}{R^3} dS' + \bar{d}' \iint_{T_n^+} \frac{1}{R^3} dS' = (s) + (n) \tag{278}$$

If $\bar{r}$ is located anywhere in the plane containing T_n^+, including inside T_n^+ or on its boundary (*d'=0*), then (278) reduces to the surface component *(s)* only. In this case indeed the vector $\bar{R}$ is at all times coplanar with T_n^+ during the integration over T_n^+, hence the vector resulting from this integration cannot have a component normal to T_n^+. This important remark solves the problem due to the discontinuity of the normal component *(n)* across T_n^+, mentioned hereafter.

The analytical closed form solution for *(n)* is a vector directed along $\hat{n}_n^+$ with norm $\Omega(\bar{r})$, the signed solid angle from which the triangle T_n^+ is seen from the point $\bar{r}$ [57]. The norm of this vector is thus bounded between -2π and +2π. The analytical expression of *(n)* is fully derived in Appedix E.3 and the final result is given hereafter :

$$(n) = \iint_{T_n^+} \frac{\bar{d}'}{R^3} dS' = \hat{n}_n^+ \cdot \begin{cases} \dfrac{d'}{|d'|} \displaystyle\sum_{i=1}^{3} \left(\tan^{-1} \frac{P_i'^0 l_i'^+}{\left(R_i'^0\right)^2 + |d'| R_i'^+} - \tan^{-1} \frac{P_i'^0 l_i'^-}{\left(R_i'^0\right)^2 + |d'| R_i'^-} \right) & (d' \neq 0) \\ 0 & (d' = 0) \end{cases} \tag{279}$$

It is important to note here that *(n)* is a continuous function everywhere in space except on T_n^+, including its boundaries $\partial_i T_n^+$ for *i = 1,2,3*. Indeed, if we consider a trajectory passing through the triangle, the function *(n)* tends to 2π on the side where $\hat{n}_n^+$ is pointing to and to -2π on the other side. There is thus a 4π discontinuity across every inner point of the triangle T_n^+. For a trajectory that would cross the plane of T_n^+ via a point belonging to one of the three edges, *(n)* tends to +π or -π depending from which side of $\hat{n}_n^+$ we are approaching the edge. Finally, on the three vertices, the function *(n)* is equal to the opening angle of T_n^+ as seen from this vertex, again with a + or – sign depending on the approach side. For all points coplanar with, and outside T_n^+, the function *(n)* equals zero. We can generalize this in (279) by choosing that *(n)=0* for all points coplanar to T_n^+, including inside T_n^+ where *(n)* undergoes everywhere a jump with mean value zero between both sides of T_n^+. This choice is consistent with the remark made earlier as a comment to (278), stating that *(n)* should be equal to zero when *d'=0*.

The analytical solution of *(s)* is also fully derived in Appendix E.3 :

$$(s) = \iint_{T_n} \frac{-\bar{P}'}{R^3} dS' = \sum_i \hat{m}_i' \int_{\partial_i T_n} \frac{dl'}{R} = \sum_i \hat{m}_i' \ln \left[\frac{R_i'^+(\vec{r}) + l_i'^+(\vec{r})}{R_i'^-(\vec{r}) + l_i'^-(\vec{r})} \right] \tag{280}$$

It is easy to see that *(s)* is not bounded everywhere on T_m^- [57][56], as opposed to *(n)* : if $\bar{r}$ is located anywhere on the edge common to T_n^+ and T_m^- then (280) becomes infinite, as $R_i'^-(\bar{r}) + l_i'^-(\bar{r}) = 0$. In this case the outer integral in (269) possesses at its turn a singular integrand, with logarithmic behavior.

A very elegant solution to avoid this logarithmic singularity in the outer integral, resulting from the $1/R^3$ singularity in the inner integral, has been proposed in [54], but it introduces some programming complexity : line integrals appear aside the surface integrals, but above all the order of integration on T_m^- and T_n^+ must be inverted, as can be seen in the two expressions below in the case $\overline{T}_m^-(\overline{r}) = \overline{f}_m^-(\overline{r})$ and $\overline{T}_m^-(\overline{r}) = \hat{n}_m^-(\overline{r}) \times \overline{f}_m^-(\overline{r})$:

$$\begin{aligned} &+C_n^+ \iint_{T_m^-} \overline{f}_m^-(\overline{r}) \cdot (\overline{r} - \overline{p}_n^+) \times \frac{1}{4\pi} \left(\iint_{T_n^+} \frac{-\overline{P}}{R^3} dS' \right) dS \\ &\qquad = -C_n^+ C_m^- \oint_{\partial T_n^+} (\overline{p}_m^- - \overline{p}_n^+) \times \hat{m}_n^+(\overline{r}') \cdot \left(\iint_{T_m^-} \frac{(\overline{r} - \overline{p}_m^-)}{4\pi R} dS \right) dl \end{aligned} \tag{281}$$

$$\begin{aligned} &+C_n^+ \iint_{T_m^-} \left(\hat{n}_m^-(\overline{r}) \times \overline{f}_m^-(\overline{r}) \right) \cdot (\overline{r} - \overline{p}_n^+) \times \frac{1}{4\pi} \left(\iint_{T_n^+} \frac{-\overline{P}}{R^3} dS' \right) dS \\ &\qquad = C_n^+ C_m^- \oint_{\partial T_n^+} \hat{m}_n^+(\overline{r}') \cdot \hat{n}_m^-(\overline{r}) \left(\iint_{T_m^-} \frac{\left| \overline{r} - \overline{p}_m^- \right|^2}{4\pi R} dS \right) dl' \\ &\qquad + C_n^+ C_m^- \oint_{\partial T_n^+} (\overline{p}_m^- - \overline{p}_n^+) \times \hat{m}_n^+(\overline{r}') \cdot \left(\hat{n}_m^-(\overline{r}) \times \iint_{T_m^-} \frac{(\overline{r} - \overline{p}_m^-)}{4\pi R} dS \right) dl' \end{aligned} \tag{282}$$

It is further shown in [54] how the two surface integrals over T_m^- can be reduced to integrals of R^n and $\overline{R}R^n$ ($n \geq -1$), for which closed form solutions are presented in Appendix E.

A very general iterative and adaptative numerical integration scheme is proposed in [52] to cope with singular integrands, but it is far more complex to implement than Gaussian quadratures and requires a lot of nodes, typically several hundreds, to obtain three or more exact significant digits. Such a number of nodes is acceptable to compute isolated integrals, but it becomes prohibitive if used repeatedly to fill the complete Z matrix.

We also mention an original proposal where the logarithmic singularity is extracted at its turn from the outer integral [58]. We have analyzed this technique and concluded that it provides the announced superior performances only in the case of quasi equilateral triangles. The results of this study are not reported in this book.

Instead of those solutions, that are either tailored for specific (testing) situations, or require ad hoc modifications to the MoM code, we chose to investigate the possibility to use the high efficiency polynomial quadratures having only inner nodes described in [46] and [47]. To assess the ability or not for these quadratures to evaluate correctly the logarithmic singularity with a limited number of nodes, we derived several analytical solutions in a canonical case, presented in §5.5.

5.4.2 Singularities associated with Z^{EJ}

The integro-differential expression (261), contains both the free-space Green's function and its gradient. Classically, when $\overline{T}_m = \overline{f}_m = RWG$, the derivative on the free-space Green's function is transferred to the test function. We show in Appendix F how (261) then becomes :

$$Z_{mn}^{EJ} = -\frac{jZ}{k}\int_{S_m}\int_{S_n}\left\{ k^2 \overline{f}_m(\overline{r})\cdot\overline{f}_n(\overline{r}') + \nabla_s\cdot\overline{f}_m\nabla'_s\cdot\overline{f}_n\right\}G(R)dS'dS \tag{283}$$

Doing so, Z_{mn}^{EJ} does not contain the $1/R^3$ singularity anymore, but only the $1/R$ singularity from the free-space Green's function. We will call tEFIE$^{\nabla f}$-f the alternate form (283), valid only when $\overline{T}_m = \overline{f}_m = RWG$ and tEFIE$^{\nabla G}$-f the general form (261), valid for any testing function $\overline{T}_m$.

If we consider Z_{mn}^{EJ-+} , the extraction scheme leads to the following decomposition :

$$\int_{T_m^-}\int_{T_n^+}\left\{ k^2 \overline{f}_m^-(\overline{r})\cdot\overline{f}_n^+(\overline{r}') + \nabla_s\cdot\overline{f}_m^-\nabla'_s\cdot\overline{f}_n^+\right\}\left(\frac{e^{-jkR}}{4\pi R}-\frac{1}{4\pi R}\right)dS'dS \tag{284}$$

$$\int_{T_m^-}\int_{T_n^+}\left\{ k^2 \overline{f}_m^-(\overline{r})\cdot\overline{f}_n^+(\overline{r}') + \nabla_s\cdot\overline{f}_m^-\nabla'_s\cdot\overline{f}_n^+\right\}\frac{1}{4\pi R}dS'dS \tag{285}$$

The singular term (285) can be integrated analytically on T_n^+ , then numerically on T_m^- , as follows :

$$\begin{aligned}
&\frac{k^2}{4\pi}\int_{T_m^-}\overline{f}_m^-(\overline{r})\cdot\int_{T_n^+}\overline{f}_n^+(\overline{r}')\frac{1}{R}dS'dS \\
&= \frac{k^2}{4\pi}C_n^+\int_{T_m^-}\overline{f}_m^-(\overline{r})\cdot\int_{T_n^+}\left(\overline{r}-\overline{p}_n^+-\overline{R}\right)\frac{1}{R}dS'dS \\
&= \frac{k^2}{4\pi}C_n^+\int_{T_m^-}\overline{f}_m^-(\overline{r})\cdot\left[\left(\overline{r}-\overline{p}_n^+\right)\int_{T_n^+}\frac{1}{R}dS' - \int_{T_n^+}\frac{\overline{R}}{R}dS'\right]dS
\end{aligned} \tag{286}$$

$$\int_{T_m^-}\int_{T_n^+}\nabla_s\cdot\overline{f}_m^-\nabla'_s\cdot\overline{f}_n^+\frac{1}{4\pi R}dS'dS = \frac{1}{4\pi}\int_{T_m^-}\nabla_s\cdot\overline{f}_m^-\nabla'_s\cdot\overline{f}_n^+\int_{T_n^+}\frac{1}{R}dS'dS \tag{287}$$

Both (286) and (287) contain the integral of $1/R$ and/or $\overline{R}/R$, that both have been treated with (275). The first term (284) is bounded everywhere on T_n^+ and can therefore be integrated numerically. In [54], it is observed that the first derivative of the integrand is not continuous, what limits the accuracy of polynomial quadratures. The extraction of a second term, responsible for the discontinuity of the first derivative of the integrand, is therefore suggested :

$$G(R) = \left(\frac{e^{-jkR}}{4\pi R}-\frac{1}{4\pi R}+\frac{k^2}{8\pi}R\right)+\frac{1}{4\pi R}-\frac{k^2}{8\pi}R \tag{288}$$

A summary of the accuracy that can be obtained without or with extraction of one or two terms and integration with high efficiency quadratures [46][47] is given in Figure 55 (p.115). The computed integral is :

$$\iint_T G(R)\,dS' \tag{289}$$

The triangles T and the observation point $\bar{r}$ are in the xy plane, as depicted in Figure 54. We consider three triangles T : one is right-angled and isosceles when $Y=\lambda/10$ and two are (very) elongated when $Y=\lambda/10^3$ ($Y=\lambda/10^5$).

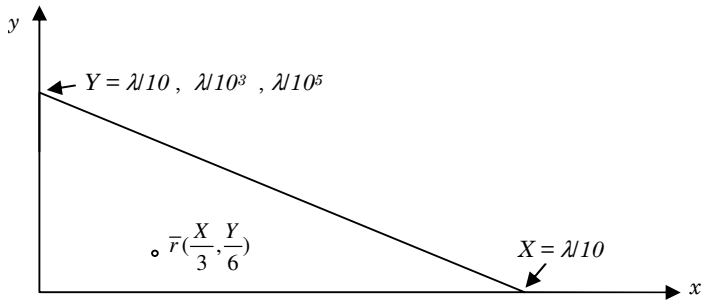

Figure 54 : Triangles T for the integral (289)

The relative errors presented in Figure 55 are related to the real part of (289) only, as the imaginary part does not suffer from any singularity. Expression (289) has been computed without any singularity extraction (blue lines), with one term extracted (red lines) and finally two terms (green lines). As the exact solution to (289) is not known, we use as reference value to determine the relative error the solution obtained with 73 nodes and two terms extracted.

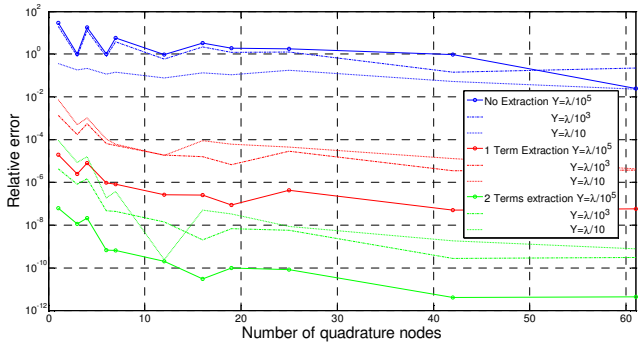

Figure 55 : Relative error on (289)

It is made clear that for all triangles, from $X/Y=10$ to 10^5 :

- Singularity extraction is indispensable when R can be equal to 0
- The extraction of only one term allows to compute (289) with 4 to 5 exact significant digits
- The extraction of two terms allows to compute (289) with 7 to 8 exact significant digits

In this book we have extracted only one term in singular integrals involving the free-space Green's function.

When $\overline{T}_m = \hat{n}_m \times \overline{f}_m = \hat{n}_m \times RWG$ the $1/R^3$ singularity due to the gradient of the free-space Green's function can also be eliminated thanks to the Gauss divergence theorem [54], but as the test function is not divergence conforming the surface integral over T_m^- and T_m^+ turns into a contour integral. For example, for the part of the integral involving $\overline{\nabla}'G(R)$ and T_m^- in (261) :

$$\begin{aligned}&\iint_{T_m^-}\left(\hat{n}_m^-(\overline{r})\times\overline{f}_m^-(\overline{r})\right)\cdot\left(\iint_{S_n}\nabla'_s\cdot\overline{f}_n(\overline{r}')\ \ \overline{\nabla}'G(R)\,dS'\right)dS\\&\quad=\oint_{\partial T_m^-}\hat{m}_m^-(\overline{r})\cdot\left(\hat{n}_m^-(\overline{r})\times\overline{f}_m^-(\overline{r})\right)\left(\iint_{S_n}G(R)\nabla'_s\cdot\overline{f}_n(\overline{r}')\ \,dS'\right)dl\end{aligned}\tag{290}$$

In this book, we have not used the transformation (290). Instead we have used the high efficiency polynomial quadratures having only inner nodes described in [46] and [47] to integrate either (283) when $\overline{T}_m = \overline{f}_m = RWG$ or the general form (261) for both $\overline{T}_m = \overline{f}_m$ or $\overline{T}_m = \hat{n}_m \times \overline{f}_m$.

In this latter very general case (261), the extraction scheme leads to the following decomposition, for example for Z_{mn}^{EJ-+} :

$$\int_{T_m^-}\overline{T}_m^-(\overline{r})\cdot\int_{T_n^+}\frac{1}{4\pi}\left\{\begin{array}{l}k^2\overline{f}_n^+(\overline{r}')\left(\dfrac{e^{-jkR}}{R}-\dfrac{1}{R}\right)\\\qquad+\nabla_s\cdot\overline{f}_n^+\left(\dfrac{jkR+1}{R^3}e^{-jkR}-\dfrac{1}{R^3}+\dfrac{k^2}{2R}\right)\overline{R}\end{array}\right\}dS'dS\tag{291}$$

$$\int_{T_m^-}\overline{T}_m^-(\overline{r})\cdot\int_{T_n^+}\frac{1}{4\pi}\left\{\begin{array}{l}k^2\overline{f}_n^+(\overline{r}')\left(\dfrac{1}{R}\right)\\\qquad+\nabla_s\cdot\overline{f}_n^+\left(\dfrac{\overline{R}}{R^3}-\dfrac{k^2}{2}\dfrac{\overline{R}}{R}\right)\end{array}\right\}dS'dS\tag{292}$$

We have seen with (275) and (278) how to integrate (292).

The first term (291) is bounded everywhere on T_n^+ and can therefore be integrated numerically. Figure 55 (p.115) shows how accurate this numerical integration can be for the first part of this integral, related to *G(R)*. We now present a similar accuracy study for the second part, related to $\overline{\nabla}G(R)$. The computed integral is now :

$$\iint_T\overline{\nabla}G(R)dS'\tag{293}$$

The triangles T and the observation point $\overline{r}$ are those depicted in Figure 54 (p.115). The integral (293) is complex and vector valued, having components in the *x* and *y* directions. Only the real part is affected by singularities. The relative error on the real part of the *x* and *y* component is presented in Figure 56 and Figure 57 (p.117). Expression (293) has been computed without any singularity extraction (blue lines) and with two terms (green lines). As the exact solution to

(293) is not known, we use as reference value to determine the relative error the solution obtained with 73 nodes and two terms extracted.

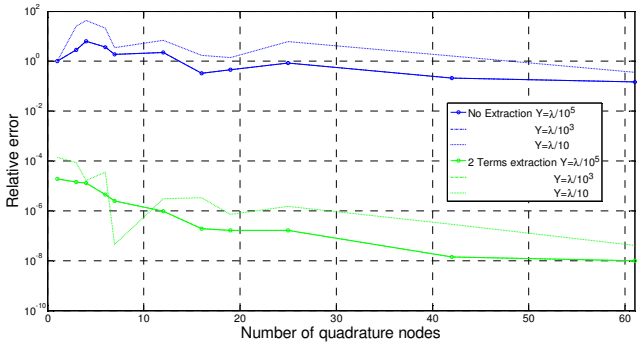

Figure 56 : Integral of $\bar{\nabla}G_x$

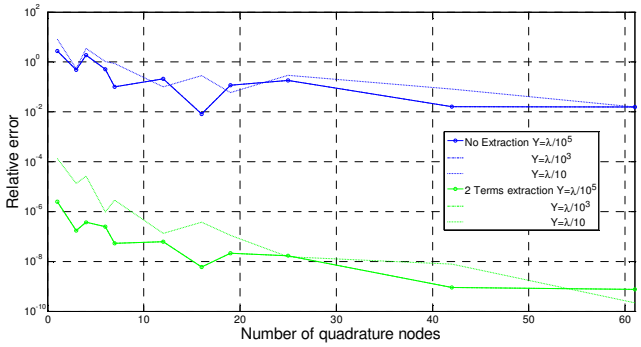

Figure 57 : Integral of $\bar{\nabla}G_y$

Again, singularity extraction proves indispensable. With as few as 7 nodes, integral (293) can be computed with at least 5 exact significant digits.

5.5 High efficiency quadratures and $1/R^3$ singularity

5.5.1 Analytical analysis – regular triangles

To quantify the accuracy that can be obtained with high efficiency polynomial quadratures in the evaluation of (271), containing the logarithmic singularity (280) in the outer integrand, exact analytical expressions have been derived with the aid of [59] for the following integral :

$$I = +\frac{C'}{4\pi}\iint_T \bar{T}(\bar{r})\cdot(\bar{r}-\bar{p}')\times\left(\iint_{T'}\frac{-\bar{P}'}{R^3}dS'\right)dS \tag{294}$$

The integral I has been calculated in the canonical situation depicted in Figure 58 for both weighting function $\overline{T} = \overline{f} = RWG$ and $\overline{T} = \hat{n} \times \overline{f}$, but only for α = 90°. It has also been computed numerically, and the two solutions are compared.

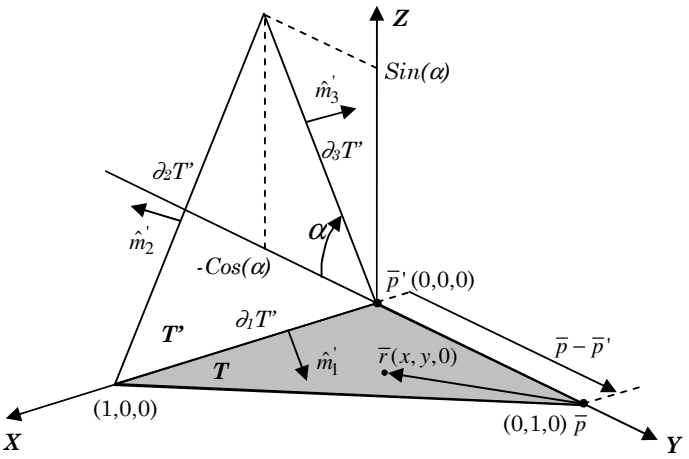

Figure 58 : Geometry of the canonical case solved analytically

All details are given in Appendix G, and summarized hereafter. When α = 90°, (294) reduces to :

$$I = \frac{\sqrt{2}}{4\pi}\left(I_1 - I_2\right) = \frac{\sqrt{2}}{4\pi}\left(\left[I_1^+ - I_1^-\right] - \left[I_2^+ - I_2^-\right]\right) \tag{295}$$

with :

$$I_1 = \begin{Bmatrix} \int_0^1 \int_0^{1-y} P(x,y) \ln\left[\sqrt{(1-x)^2 + y^2} + (1-x)\right] dxdy \\ -\int_0^1 \int_0^{1-x} P(x,y) \ln\left[\sqrt{x^2 + y^2} - x\right] dydx \end{Bmatrix} = I_1^+ - I_1^- \tag{296}$$

$$I_2 = \frac{1}{\sqrt{2}} \begin{Bmatrix} \int_0^1 \int_0^{1-y} P(x,y) \ln\left[\sqrt{x^2 + y^2 + 1} + \frac{x+1}{\sqrt{2}}\right] dxdy \\ -\int_0^1 \int_0^{1-x} P(x,y) \ln\left[\sqrt{(1-x)^2 + y^2} + \frac{x-1}{\sqrt{2}}\right] dxdy \end{Bmatrix} = I_2^+ - I_2^- \tag{297}$$

and :

$$P_{\overline{T}=\overline{f}}(x,y) = -x \tag{298}$$

$$P_{\overline{T}=\hat{n}\times\overline{f}}(x,y) = x^2 + y^2 - y \tag{299}$$

No analytical solution could be found for I_2^+ . As this integral is regular (the integrand is bounded everywhere on T), it can be evaluated very accurately with the high efficiency polynomial quadratures, as shown in Table 7 (p.119). In the absence of analytical solution for I_2^+ , the numerical solution obtained with 73

nodes is used as a reference to measure the relative error when less nodes are used. Table 7 shows that the relative error improves very quickly, in a way similar to the inner integral (293) summarized in Figure 56 and Figure 57 (p.117).

Table 7 : Numerical integration of I_2^+

#	$I_{2,f}^+$: Numerical	|Rel error|	$I_{2,n\times f}^+$: Numerical	|Rel error|
1	-0.08450337367004	0.11e-0	-0.028167791223347	4.90e-0
3	**-0.094**612293851424	1.37e-3	**+0.007**012501289788	21.4e-3
4	**-0.094**697637869101	2.28e-3	+0.006604208568921	78.4e-3
6	**-0.09448**3384173796	10.3e-6	**+0.00715**7053742892	1.20e-3
7	**-0.094**478779228638	38.5e-6	**+0.00717**151008889	0.81e-3
12	**-0.094482**452578854	0.42e-6	**+0.007165**729119605	1.30e-6
16	**-0.094482**394759082	0.20e-6	**+0.007165**750921513	4.40e-6
19	**-0.094482**408305059	54.9e-9	**+0.007165**727125872	1.05e-6
25	**-0.0944824136**91372	2.09e-9	**+0.0071657193**31997	34.6e-9
42	**-0.0944824134965**51	28.7e-12	**+0.00716571957**576	0.56e-9
61	**-0.0944824134937**93	0.47e-12	**+0.0071657195798**58	7.82e-12
73	-0.094482413493837	Ref	+0.007165719579802	Ref

The exact analytical expressions for I_1^-, I_1^+ and I_2^- are :

Table 8 : Exact solutions

	$\bar{T}=\bar{f}=RWG$	$\bar{T}=\hat{n}\times\bar{f}$
I_1^-	$\left[11+9\sqrt{2}\ln\left(\sqrt{2}+1\right)\right]/36$	$\left[-2-\sqrt{2}\ln\left(\sqrt{2}+1\right)\right]/16$
I_1^+	$\left[11-12\ln\left(\sqrt{2}+1\right)\right]/36$	$\left[2-3\sqrt{2}+\ln\left(\sqrt{2}+1\right)\right]/24$
I_2^-	$\dfrac{11+3\sqrt{2}\left(\ln(\sqrt{2}+1)-\pi/2\right)+3\ln 2}{36\sqrt{2}}$	$\dfrac{1+\ln(\sqrt{2}-1)+\sqrt{2}\left(\pi/8-1\right)}{12\sqrt{2}}$

The singular integrands in I_1^+, I_1^- and I_2^- become infinite only on the edge $\partial_t T'$ with a smooth logarithmic behavior. The relative error obtained with the high efficiency polynomial quadratures in the evaluation of the total terms I_f and I_{nxf} given by equation (294) is presented in Table 9 (p.120).

The relative error is now improving much slower with the number of quadrature nodes. Surprisingly enough, the 16 and 42 nodes quadratures outperform all the other choices for both $\bar{T}=\bar{f}$ and $\bar{T}=\hat{n}\times\bar{f}$, still showing a relative error around 0,3% and 0,07% with 16 nodes. Table 7 shows that 3 (respectively 7) nodes are

necessary and sufficient to obtain a similar accuracy with the non singular integral $I^{+}_{2,f}$ ($I^{+}_{2,n\times f}$).

Table 9 : Relative error on I

# nodes	I_f = -0,03505		$I_{n\times f}$ = 0,01074	
	Numerical	Rel error	Numerical	Rel error
1	-0,01693	-0,52	-0,00564	-1,53
3	-0,02545	-0,27	+0,00384	-0,63
4	-0,02613	-0,25	+0,00384	-0,64
6	-0,02969	-0,15	+0,00685	-0,36
7	-0,03102	-0,12	+0,00775	-0,28
12	-0,03217	-0,082	+0,00868	-0,19
16	**-0,03517**	**+0,0033**	**+0,01074**	**+0,0007**
19	-0,03341	-0,047	+0,00954	-0,11
25	-0,03420	-0,024	+0,01026	-0,044
42	**-0,03510**	**+0,0012**	**+0,01088**	**+0,0136**
61	-0,03450	-0,016	+0,01034	-0,037
73	-0,03481	-0,007	+0,01056	-0,017

Even with 16 or 42 nodes, the relative error on the $1/R^3$ singular term (294) is quite moderate. We must remember though that (294) is only a part of the total element $Z_{mn} = Z^{++}_{mn} + Z^{+-}_{mn} + Z^{-+}_{mn} + Z^{--}_{mn}$ entering the Z matrix, for example Z^{++}_{mn}. Also the main term (267) and the $1/R$ singularity (268) must be added to (294) to obtain Z^{++}_{mn}. To quantify the global impact of the $1/R^3$ singularity, integrated numerically with polynomial quadratures, an elementary numerical example is analyzed in §5.5.2.

5.5.2 Numerical example

The four faces PEC pyramid depicted in Figure 59 is 1m x 1m x 1m and illuminated by a 10 MHz plane wave polarized along *X* and travelling from –*Z* to +*Z*. The six edges are numbered from 1 to 6.

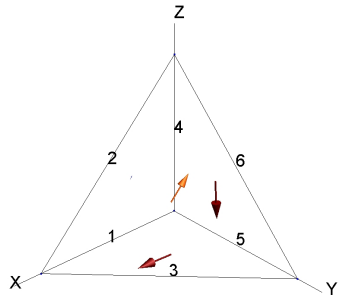

Figure 59 : Canonical PEC pyramid

The electric current densities in the middle of each of the four faces obtained with the tMFIE-nxf are depicted with arrows, showing a strong *X*-*Z* orientation, as expected.

In Figure 60 we see the influence of the number of quadrature nodes in the evaluation of two singular terms : firstly Z_{12}, the interaction between the RWGs defined on edges *1* and *2*, then Z_{33}, the self interaction on edge *3*. For both elements it is apparent that the 16 and 42 nodes quadratures lead quicker to the correct value for these two elements. With the pyramid Z_{12}^{++} corresponds to the analytical example of Figure 58 (p.118). The total value for Z_{12}^{++}, computed for the pyramid with 16 nodes, equals 0,01076. In Table 9 (p.120) we read that the exact analytical value of the part of Z_{12}^{++} due to the $1/R^3$ singularity equals 0,01074, showing that the $1/R^3$ term is highly dominant in Z_{12}^{++}. On the other hand, Z_{12}^{++} is only approximately 8 times smaller than Z_{12}, for which the value computed with 16 nodes is close to 0,0849. The relative error on Z_{12} is therefore approximately 8 times smaller than the relative error on Z_{12}^{++} reported in Table 9 (p.120).

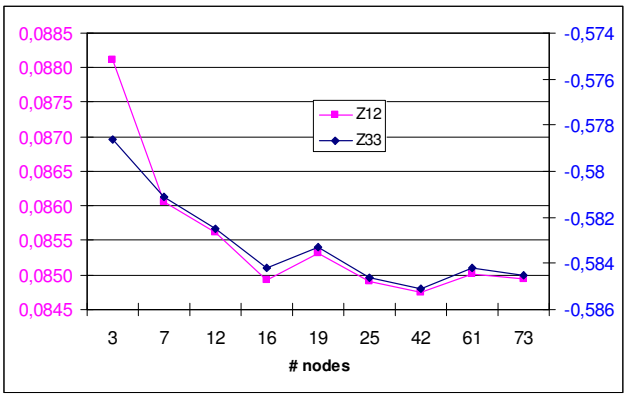

Figure 60 : Numerical integration of two singular terms

In Figure 61 we show the real part of J_3 and J_5, the coefficients of the RWGs defined on edge *3* and *5*, contributing to the strongest electric current densities present on the pyramid.

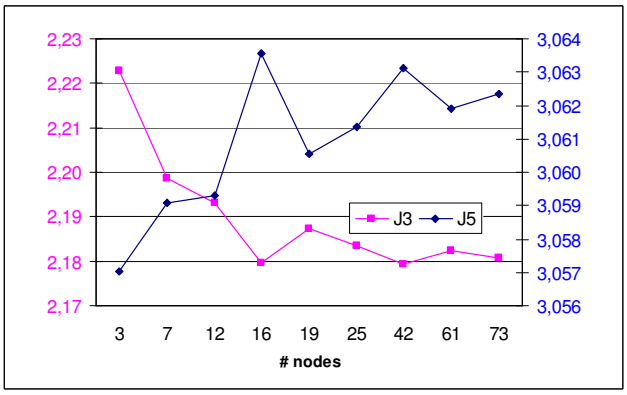

Figure 61 : Values of J_3 and J_5 on the pyramid of Figure 59

Both curves show a convergent behavior with higher number of nodes, from which we can roughly extrapolate the limit value for J_3 (~2,18±0,01) and J_5 (~3,063±0,001). Again it is clear that the 16 and 42 nodes quadratures lead much quicker to the extrapolated limit value.

5.5.3 Analytical analysis - very elongated triangles

This canonical case represented in Figure 58 (p.118) and Figure 59 (p.120) is only representative of meshes where quasi equilateral triangles are used. In some instances though, as will be shown in §§6.5 and 6.7, (very) elongated triangles are useful to greatly diminish the total number of triangles in the mesh, thus the size of the Z matrix, equal to the number of triangle edges for PEC bodies, and twice this number for dielectric bodies embedded in free space. To this end, we generalize for arbitrary S, T and Z the analytical solution already presented in §5.5.1 and we examine again the ability of the 16 and 42 nodes quadratures to integrate (294) over very elongated triangles.

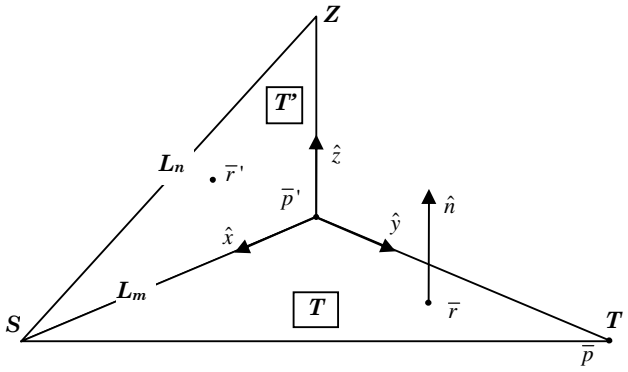

Figure 62 : Elongated triangles

This analysis provides quantitative arguments to the warning expressed in [60, p.34] regarding Gaussian integration rules on elongated triangles.

The many symbolic integral expressions involved towards the final exact solution presented hereafter are given in Appendix H. They are so complex and lengthy that they have been calculated for the $\overline{T} = \hat{n} \times \overline{f}$ case only, with the aid of [59]. This testing function occurs for example when the tMFIE-nxf is applied to PEC bodies (see §2.3.2). It is also advised if the Müller scheme is applied to dielectrics [32].

For the situation depicted in Figure 62, the integral (294) reduces to :

$$\mathrm{I} = \frac{\sqrt{S^2 + Z^2}}{4\pi STZ} \left\{ \underbrace{(I_1^+ - I_1^-)}_{I_1} - \underbrace{(I_2^+ - I_2^-)}_{I_2} \right\} \tag{300}$$

where :

$$I^{+}_{1,n\times f} = \int_0^T \int_0^{S(1-y/T)} \left(x^2 + y^2 - yT\right) \ln\left[S - x + \sqrt{(S-x)^2 + y^2}\right] dxdy$$

$$= \frac{ST}{144} \begin{bmatrix} 12(S^2 - T^2)\ln\left[S + \sqrt{S^2 + T^2}\right] \\ -18S\sqrt{S^2 + T^2} \\ +6\frac{S^3}{T}\ln\left[T/S + \sqrt{(T/S)^2 + 1}\right] \\ -S^2 + 13T^2 \end{bmatrix} \tag{301}$$

$$I^{-}_{1,n\times f} = \int_0^T \int_0^{S(1-y/T)} \left(x^2 + y^2 - yT\right) \ln\left[\sqrt{x^2 + y^2} - x\right] dxdy$$

$$= \frac{ST}{144} \begin{bmatrix} \frac{-43S^4 + 12S^3T - 36S^2T^2 + 18ST^3 + 13T^4}{(S^2 + T^2)} \\ +\frac{6S^3(2S^2 + T^2)}{(S^2 + T^2)^{3/2}} \ln\left[\frac{\sqrt{(S/T)^2 + 1} - S/T}{\sqrt{(T/S)^2 + 1} + T/S}\right] \\ +12(S^2 - T^2)\ln T \end{bmatrix} \tag{302}$$

$$I^{-}_{2,n\times f} = \frac{S}{\sqrt{S^2 + Z^2}} \int_0^S \int_0^{T(1-x/S)} \left(\underbrace{x^2}_{(1)} + \underbrace{y^2}_{(2)} - \underbrace{yT}_{(3)}\right) \ln\left[\sqrt{(S-x)^2 + y^2} - \frac{S(S-x)}{\sqrt{S^2 + Z^2}}\right] dydx \tag{303}$$

with :

$$
\begin{aligned}
(1) &= \frac{S^3 T}{144}\left[+12\ln S - 13 + 12C_{x^2}\right]\frac{S}{\sqrt{S^2+Z^2}} \\
(2) &= \frac{ST^3}{144}\left[+12\ln S - 3 + 12C_{y^2}\right]\frac{S}{\sqrt{S^2+Z^2}} \\
(3) &= \frac{ST^3}{144}\left[-24\ln S + 8 + 12C_{yT}\right]\frac{S}{\sqrt{S^2+Z^2}}
\end{aligned}
\tag{304}
$$

$$
\begin{aligned}
C_{x^2} = {} & \ln\left[\sqrt{1+(T/S)^2} - \frac{1}{\sqrt{1+(Z/S)^2}}\right] \\
& + \frac{S/T}{\sqrt{1+(S/Z)^2}}\left(\tan^{-1}\left[T/S\sqrt{1+(S/Z)^2}\right] + \tan^{-1}\left[\frac{T/Z}{\sqrt{1+(T/S)^2}}\right]\right) \\
& - \frac{S/T}{\sqrt{1+(Z/S)^2}}\ln\left[T/S + \sqrt{1+(T/S)^2}\right] - 1
\end{aligned}
\tag{305}
$$

$$
\begin{aligned}
C_{y^2} = {} & \ln\left[\sqrt{1+(T/S)^2} - \frac{1}{\sqrt{1+(Z/S)^2}}\right] + \frac{(S/T)^2}{1+(S/Z)^2} - \frac{1}{3} \\
& - \frac{(S/T)^3}{\left[1+(S/Z)^2\right]^{3/2}}\left(\tan^{-1}\left[T/S\sqrt{1+(S/Z)^2}\right] + \tan^{-1}\left[\frac{T/Z}{\sqrt{1+(T/S)^2}}\right]\right) \\
& + \frac{(S/T)^3\left[1+3(Z/S)^2\right]}{2\left[1+(Z/S)^2\right]^{3/2}}\ln\left[T/S + \sqrt{1+(T/S)^2}\right] - \frac{(S/T)\sqrt{1+(S/T)^2}}{2\sqrt{1+(Z/S)^2}}
\end{aligned}
\tag{306}
$$

$$
\begin{aligned}
C_{yT} = {} & 2\left(\frac{S}{T}\right)^2\ln\left[1 - \frac{1}{\sqrt{1+(Z/S)^2}}\right] + 2\left(\frac{S}{T}\right)^2\frac{\sqrt{1+(T/S)^2}-1}{\sqrt{1+(Z/S)^2}} \\
& + \left[\frac{(S/T)^2}{1+(Z/S)^2}\right]\ln\left[1+\left(\frac{T}{Z}\right)^2+\left(\frac{T}{S}\right)^2\right] \\
& - \ln\left[\frac{\sqrt{1+(T/S)^2}\sqrt{1+(Z/S)^2}+1}{\sqrt{1+(T/S)^2}\sqrt{1+(Z/S)^2}-1}\bullet\frac{\sqrt{1+(Z/S)^2}-1}{\sqrt{1+(Z/S)^2}+1}\right] \\
& - 2\left[1+\left(\frac{S}{T}\right)^2\right]\ln\left[\sqrt{1+(T/S)^2} - \frac{1}{\sqrt{1+(Z/S)^2}}\right] + 1
\end{aligned}
\tag{307}
$$

Again the last integral $I^{+}_{2,n\times f}$ could not be solved analytically, but it is bounded everywhere on T, as can be deduced from its expression :

$$I^{+}_{2,n\times f} = \frac{S}{\sqrt{S^2+Z^2}} \int_0^T \int_0^{S(1-y/T)} \left(x^2+y^2-yT\right) \ln\left[\begin{array}{l} \sqrt{x^2+y^2+Z^2} \\ + \dfrac{S\,x+Z^2}{\sqrt{S^2+Z^2}} \end{array} \right] dxdy \tag{308}$$

This regular integral will be integrated very accurately with the same high efficiency polynomial quadratures that will be used in the evaluation of the singular $I^{-}_{1,n\times f}$, $I^{+}_{1,n\times f}$ and $I^{-}_{2,n\times f}$ [46][47].

Figure 63 to Figure 65 show the relative error committed on (300), the total term *I*, in function of the number of quadrature nodes for fixed values of *S*, *T* and/or *Z* and across a wide variation range of *S*, *T* and/or *Z*. We define :¨

$$\text{Relative error in \% = 100*Abs(Numerical/Exact-1)} \tag{309}$$

where :

$$\text{“Exact”} = I^{+}_{1,Exact} - I^{-}_{1,Exact} - (I^{+}_{2,Numerical\ 73nodes} - I^{-}_{2,Exact}) \tag{310}$$

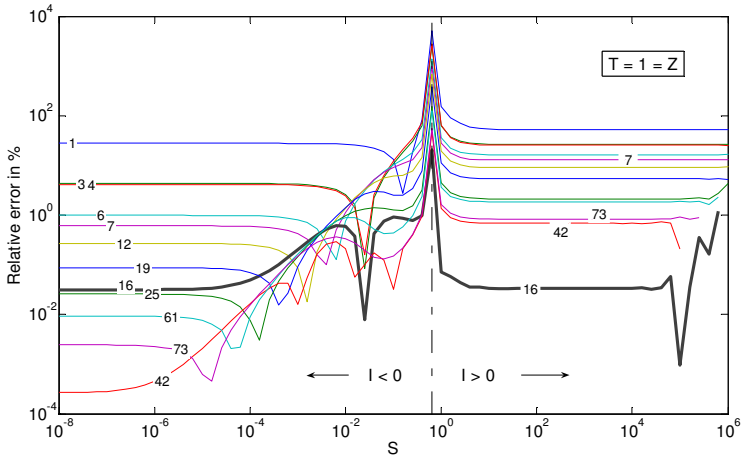

Figure 63 : Relative error as a function of *S* for *T=1=Z*

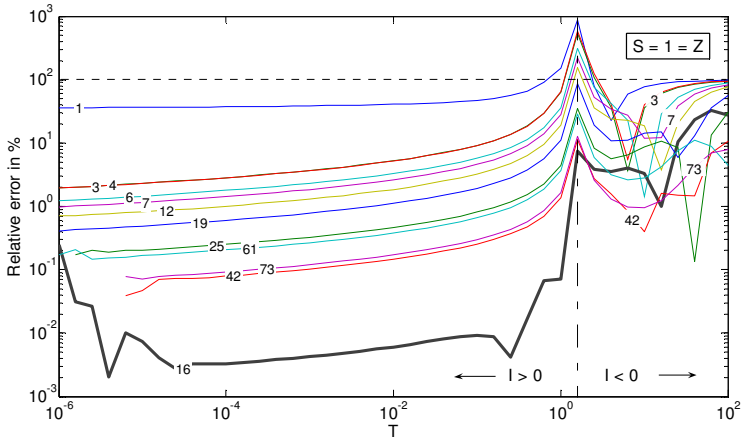

Figure 64 : Relative error in function of T for $S=1=Z$

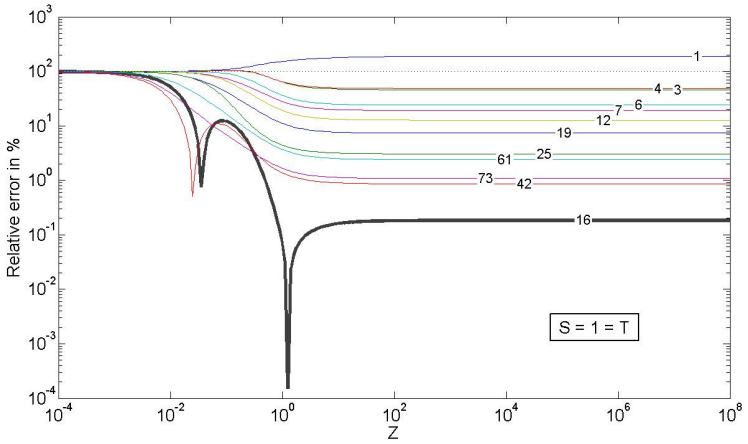

Figure 65 : Relative error in function of Z for $S=1=T$

The 16 nodes quadrature does not always show the best relative error performance across the wide range of variation of S, T and Z , but it clearly provides the best overall relative error, nearly always better than 1%, sometimes close to 0,1% but sometimes as high as 10%. The peak areas on the vertical dotted line correspond to $I=0$, a region where the relative error grows artificially high due to its definition (309). One also observes, in Figure 64 and Figure 65, that when the ratio Z/T becomes smaller than 0.01, the twelve available high efficiency polynomial quadratures fail. $I_{numerical}$ tends to zero and the relative error converges to 100 %. A detailed analysis shows that the twelve quadratures still perform well and estimate the three terms I_1^- , I_1^+ , I_2^- with their respective accuracy (say for example 0.1% with 16 nodes and 10% with 3 nodes). The problem is that when Z/T becomes small(er than 0.01) the final result I is a

small number to be obtained from the difference of much bigger numbers I_1 and I_2. As can be seen in Table 10, when $Z/T = 10^{-4}$ the relative error requested on I_1 and I_2 must be lower than 0.01% to estimate $I = I_1 - I_2$. with at least one exact digit. Such an accuracy on I_1 and I_2 is not attainable, even with the 16 nodes quadrature.

Table 10 : I_1 and I_2 when Z/T becomes smaller than 0.01

			Exact			Numerical (16 nodes)		
S	T	Z	I_1	I_2	I	I_1	I_2	I
1	1	10^{-4}	**0.1461**837	**0.1461**574	0.0208581	0.1459128	0.1459126	0.0001108
1	1	10^{-3}	"	0.1459238	0.0206738	"	0.1458989	0.0011058
1	1	10^{-2}	"	0.1436958	0.0197986	"	0.1447217	0.0094784
1	1	10^{-1}	"	0.1260032	0.0161391	"	0.1232675	0.0181104
1	1	1	"	0.0507840	0.0107362	"	0.0504452	0.0107438

It should be remembered though that the singular integral I is only a fraction of the total Z_{mn} element entering the Z matrix, sometimes negligible but not always. One could also argue that the vast majority of the Z matrix elements are related to non adjacent triangles. These elements do not lead to a singular integral such as (263) and can be computed very accurately. But on the other hand the few elements in Z related to adjacent or overlapping triangles should be the largest ones. In many cases, a poor estimation of the singular I elements has no significant impact on the final solution J and M. Still, as shown in §6.12, we have identified situations where the accuracy provided by the 16 nodes quadrature is essential for a good solution.

As a conclusion, it is probably a safe idea to avoid the $1/R^3$ singularity with the transformation of the double integrals proposed in [54], but as will be shown in chapter 6, an efficient integration scheme including a 16 nodes quadrature only where needed is a good and moderately costly alternative, but without guarantee to work in any situation.

5.6 Summary

In the previous chapters new expressions, theorems and formulations have been presented, with an often repeated objective of generality. In this chapter we focused on another important objective of this book : ensuring the accuracy of the approximate result delivered by the Method of Moments.

Before concentrating on the error produced by the numerical integrations occurring during the filling of the impedance matrix, we first reviewed the many numerical issues and limitations inherent to the application of the Method of Moments to electromagnetic problems : laptop resource limitations, high condition number, resonance and low frequency breakdown. In the examples treated in chapter 6, we deliberately chose to avoid those well-known pitfalls to make sure we isolated the numerical integration issue, if present.

Numerical integration can be performed with several techniques, many of them being very accurate, but sometimes at the expense of complex programming. After reviewing most of these techniques, we justified our choice (high efficiency

polynomial quadratures) with the desire to maintain an easy and very general implementation. We also assessed the validity of this choice, especially in the integration of the singular integrals, that appeared to yield the main elements of the impedance matrix. To this end, extensive analytical effort has been put in the derivation of exact expressions for the singular interactions between two orthogonal triangles, regular and elongated. A direct comparison between analytical and numerical results has permitted to observe that two quadratures provided a much higher accuracy in the singular case : the 16 and 42 nodes ones. This observation was further supported at system level with the example of a simple canonical pyramid, then confirmed in chapter 6 with two large examples showing that the accuracy provided by the 16 and 42 nodes quadratures is necessary in some cases.

These observations and confirmations do not form a complete and definitive demonstration though. The overall superiority of the 16 and 42 nodes quadratures have only been demonstrated in some cases, but not at all in general. Moreover, this superiority is limited : the absolute accuracy provided by those two quadratures remain quite modest as compared to the accuracy provided by the same family of high efficiency quadratures in the regular cases. As it is not at all guaranteed that some examples could be found where even the 16 and 42 nodes quadrature would fail as well, we recommend for example to select an alternative where the $1/R^3$ singularity is eliminated, but at the expense of generality.

[1] K. F. Warnick, *Numerical Analysis for Electromagnetic Integral Equations*, Artech House, 2008.

[2] A. F. Peterson, S. L. Ray, R. Mittra, *Computational Methods for Electromagnetics*, 1998.

[3] V. V. S. Prakash and R. Mittra, "Characteristic basis function method: A new technique for efficient solution of method of moments matrix equation," *Microw. Opt. Technol. Lett.*, Vol. 36, No.2, pp. 95-100, Jan 2003.

[4] L. Matekovits, G. Vecchi, G. Dassano, M. Orefice, "Synthetic function analysis of large printed structures: the solution space sampling approach", *Dig. of 2001 IEEE Antennas and Propag. Society Int'l Symp.*, pp. 568-571, Boston, Massachusetts, July 2001.

[5] C. C. Lu and W. C. Chew, "A multilevel algorithm for solving boundary integral equations of wave scattering", *Microwave Opt. Tech. Lett.*, Vol. 7, No.10, pp. 466-470, 1994.

[6] J. M. Song, C. C. Lu and W. C. Chew, "MLFMA for electromagnetic scattering by large complex objects", *IEEE Trans. on Antenna and Prop.*, Vol. 45, pp. 1488-1493, Oct 1997.

[7] A. J. Poggio and E. K. Miller, "Integral equation solutions of three dimensional scattering problems", in *Computer Techniques for Electromagnetics*. Oxford, U.K.: Pergamon, 1973, chap. 4.

[8] A.W. Maue, "The formulation of a general diffraction problem by an integral equation", *Zeitschrift für Physik.*, Bd. 126, pp. 601-618, 1949.

[9] J. M. Song, W. W. Chu and W. C. Chew, "Numerical resonances in method of moments", *IEEE APS Int. Symp. Dig.*, Honolulu, Hawaii, pp. 4861-4864, Jun 2007.

[10] W. C. Chew and J. M. Song, "Gedanken experiments to understand the internal resonance problems of electromagnetic scattering", *Electromagn.*, Vol. 27, No.8, pp. 457-472, Nov-Dec 2007.

[11] W.C. Chew, M.S. Tong, B. Hu, *Integral Equation Methods for Electromagnetic and Elastic Waves*, Synthesis Lectures on Computational Electromagnetics, Morgan & Claypool Publishers, 2008.

[12] A.Ishimaru, *Electromagnetic Wave Propagation, Radiation and Scattering*, Prentice Hall Inc., 1991.

[13] J. C. Monson and N. J. Damaskos, "A Scheme for Eliminating Internal Resonances: The Parasitic Body Technique", *IEEE Trans. on Antenna and Prop.*, Vol. 42, No.8, pp. 1089-1096, Nov 1982.

[14] A. F. Peterson, "The interior resonance problem associated withsurface integral equations of electromagnetics: numerical consequences and a survey of remedies", *Electromagn.*, Vol. 10, pp. 293-312, 1990.

[15] T. K. Sarkar and S. M. Rao, "A Simple Technique for Solving E-Field Integral Equations for Conducting Bodies at Internal Resonances", *IEEE Trans. on Antenna and Prop.*, Vol. 30, No.6, pp. 1250-1254, Nov 1982.

[16] A. D. Yaghjian, "Augmented Electric- and Magnetic-Field Integral Equations", *Radio Sci.,* Vol. 16, pp. 987-1001, Nov 2001.

[17] F. K. Oshiro and K. M. Mitzner, "Digital Computer Solution of Three-Dimensional Scattering Problem" , *Digest of IEEE Int. Antennas. Prop. Symp.,* Ann Arbor, MI, pp. 257-263, Oct 1967.

[18] J. R. Mautz and R. F. Harrington, "H-Field, E-Field and Combined-Field Solutions for Conducting Bodies of Revolution", *Arch. Elek. Ubertragung*, Vol. 32, No.4, pp. 157-164, 1978.

[19] W.C. Chew, J. M. Jin, E. Michielssen and J. M. Song, *Fast and Efficient Algorithms in Computational Electromagnetics*, Boston: Artech House, 2001.

[20] B. M. Kolundzija, "Generalized combined field integral equation", *Proc. IEEE AP-S Int. Symp.*, Baltimore, pp. 852-855, June 1996.

[21] X. Q. Sheng, J.-M. Jing, J. Song, W. C. Chew and C. C. Lu, "Solution of Combined-Field Integral Equation Using Multilevel Fast Multipole Algorithm for Scattering by Homogeneous Bodies", *IEEE Transactions on Antennas and Propagation*, Vol. 46, No.11, pp. 1718-1726, November 1998.

[22] P. Ylä-Oijala and M. Taskinen "Application of Combined Field Integral Equation for Electromagnetic Scattering Problems", *Proc. XXVIIth URSI General Assembly*, Maastricht, 2002.

[23] D. R. Wilton and A. W. Glisson, "On improving the electric field integral equation at low frequencies", in *Proc. URSI Radio Science Meeting*, Los Angeles, CA, p. 24, Jun 1981.

[24] J.-S. Zhao and W. C. Chew, "Integral equation solution of Maxwell's equations from zero frequency to microwave frequencies", *IEEE Trans. on Antenna and Prop.*, Vol. 48, pp. 1635-1645, Oct 2000.

[25] S. Y. Chen, W. C. Chew, J. M. Song and J.-S. Zhao, "Analysis of low-frequency scattering from penetrable scatterers", *IEEE Trans. on Remote Sensing*, Vol. 39, pp. 726-735, Apr 2001.

[26] Y. Zhang, T. C. Cui, W. C. Chew and J.-S. Zhao, "Magnetic field integral equation at very low frequencies", *IEEE Trans. on Antenna and Prop.*, Vol. 51, No.8, pp. 1864-1871, Aug 2003.

[27] J. S. Lim, S. M. Rao and D. R. Wilton, "A novel technique to calculate the electromagnetic scattering by surfaces of arbitrary shape", in *Proc. URSI Radio Science Meeting Dig.*, p. 322, 1993.

[28] G. Vecchi, "Loop-star decomposition of basis functions in the discretization of the EFIE", *IEEE Trans. on Antenna and Prop.*, Vol. 47, No.2, pp. 339-346, Feb 1999.

[29] Y. Chu, W. C. Chew, J. Zhao and S. Chen, "A surface integral equation formulation for low-frequency scattering from a composite object", *IEEE Trans. on Antenna and Prop.*, Vol. 51, No.10, pp. 2837-2844, Oct 2003.

[30] R. J. Adams and G. S. Brown, "Stabilation procedure for electric field integral equation", *Electron. Lett.*, Vol. 35, No.25, pp. 2015-2016, 1999.

[31] H. Contopanagos, B. Dembart, M. Epton, J. J. Ottusch, V. Rokhlin, J. L. Fischer and S. M. Wandzura, "Well-conditioned boundary integral equations for three-dimensional electromagnetic scattering", *IEEE Trans. on Antenna and Prop.*, Vol. 50, No.12, pp. 1824-1830, Dec 2002.

[32] P. Ylä-Oijala and M. Taskinen "Well Conditioned Müller Formulation for Electromagnetic Scattering by Dielectric Objects", *IEEE Trans. on Antenna and Prop.*, Vol. 53, No.10, pp. 3316-3323, Oct 2005.

[33] J. Radon, "Zur mechanischen Kubatur", *Monatsch. Math.*, Vol. 52, pp. 286-300, 1948.

[34] J. N. Lyness and R. Cools, "A Survey of Numerical Cubatures over Triangles", *Proceedings of Symposia in Applied Mathematics*, 1994.

[35] L. F. Richardson, "The deferred approach to the limit", *Trans. Phil. Roy. Soc.*, Vol. 226, pp. 261-299, 1927.

[36] W. Romberg, "Vereinfachte numerische Integration", *Det Kongelige Norske Videnskabers Selskab Forhandlinger* (Trondheim), Vol. 28, No.7, pp. 30-36, 1955.

[37] J. N. Lyness and K. K. Puri, "The Euler Maclaurin expansion for the simplex", *Math. Comp.*, Vol. 27, pp. 273-293, 1973.

[38] J. N. Lyness, "Quadrature over a Simplex", *SIAM J. Numer. Anal.*, Vol. 15, pp. 122-133 and 870-877, 1978.

[39] E. de Doncker, "New Euler Maclaurin Expansions and Their Application to Quadrature Over the s-Dimensional Simplex", *Math. Comp.*, Vol. 33, pp. 1003-1018, 1979.

[40] G. Walz, "Romberg type quadrature over arbitrary triangles", *Mannheimer Mathem. Manuskripte*, Nr. 225,. Mannheim, 1997.

[41] M. G. Duffy, "Quadrature over a pyramid or cube of integrands with a singularity at a vertex", *SIAM J. Numer. Anal.*, Vol. 19, pp. 1260-1262, Dec 1982.

[42] A. H. Stroud and D. Secrest, *Gaussian Quadrature Formulas*, Prentice-Hall, Englewoods Cliffs, N. J., 1966.

[43] G. G. Rasputin, "On the construction of cubature formulas containing preassigned knots", *Metody Vychisl.*, Vol. 13, pp. 122-128, 1983 (Russian).

[44] H. J. Schmid, "Interpolatorische Kubaturformeln", *Dissertationes Math.*, Vol. CCXX, 1983.

[45] J. N. Lyness and D. Jespersen, "Moderate degree symmetric quadrature rules for the triangle", *J. Inst. Maht. Appl.*, Vol. 15, pp. 19-32, 1975.

[46] D. A. Dunavant, "High Degree Efficient Symmetrical Gaussian Quadrature Rules For the Triangle", *International Journal for Numerical Methods in Engineering*, Vol. 21, pp. 1129-1148, 1985.

[47] S. Wandzura and H. Xiao, "Symmetric Quadrature Rules on a Triangle," *Computers and Mathematics with Applications*, Vol. 45, No.12, pp. 1829-1840, June 2003.

[48] C. Schwab and W. L. Wendland, "On numerical cubatures of singular surface integrals in boundary elements ", *Numerische Mathematik*, Vol. 62, No.1, pp. 343-369, October 1992.

[49] R. Klees, "Numerical calculation of weakly singular surface integrals ", *Journal of Geodesy*, Vol. 70, No.11, pp. 781-797, 1996.

[50] J. N. Lyness and G. Monegato, "Quadrature error functional expansion for the simplex when the integrand has singularities at vertices", *Math. Comp.*, Vol. 34, pp. 213-225, 1980.

[51] A. Sidi, "Euler-Maclaurin expansions for integrals over triangles and squares of functions having algebraic/logarithmic singularities along an edge", *J. Approx. Theory*, Vol. 39, No.1, pp. 39-53, 1983.

[52] R. Cools and A. Haegemans, "Cubpack. A Package for Automatic Cubature; Framework Description", *ACM Trans. On Mathematical Software*, Vol. 29, No.3, pp. 287-296, September 2003.

[53] D. J. Taylor, "Accurate and Efficient Numerical Integration of Weakly Singular Integrals in Galerkin EFIE Solutions", *IEEE Trans. on Antenna and Prop.*, Vol. 51, No.7, pp. 1630-1637, July 2003.

[54] P. Ylä-Oijala and M. Taskinen "Calculation of CFIE Impedance Matrix Elements With RWG and $n \times$ RWG Functions", *IEEE Trans. on Antenna and Prop.*, Vol. 51, No.8, pp. 1837-1846, August 2003.

[55] S.M.Rao, D.R.Wilton and A.W.Glisson, "Electromagnetic scattering by surfaces of arbitrary shape", *IEEE Trans. on Antenna and Prop.*, Vol. 30, pp. 409-418, May 1982.

[56] R. E. Hodges, Y.Rahmat-Samii, "The Evaluation of MFIE Integrals with the use of Vector Triangle Basis Functions", *Microwave and Optical Technology Letters*, Vol. 14, No.1, January 1997.

[57] R. D. Graglia, "On the Numerical Integration of the Linear Shape Functions Times the 3-D Green's Function or its Gradient on a Plane Triangle", *IEEE Transactions on Antenna and Prop.*, Vol. 41, No.10, pp. 1448-1454, October 1993.

[58] L.Gürel and Ö.Ergül, "Singularity of the Magnetic-Field Integral Equation and its extraction", *IEEE Antennas and Wireless Prop. Lett.*, Vol. 4, pp. 229-232, 2005.

[59] Wolfram Research, Inc. Online 2009:h*ttp://integrals.wolfram.com/*

[60] D. R. Wilton, "*Computational Methods, Scattering: Scattering and Inverse Scatter-ing in Pure and Applied Science*", E. R. Pike and P. C. Sabatier, Eds., AcademicPress / Elsevier: Amsterdam, Netherlands, Vol. 1, 2002.

Part II

6 Numerical examples

Part II of this book is entirely devoted to a large series of examples. Our originality and contribution resides in the analysis down to current density level. We believe that many of the observations and conclusions made in Part II are not accessible to whom only compares magnitudes resulting from the integration of those current densities, such as far fields or scattering coefficients.

The examples have been selected and are presented in an evolutive sequence to serve several purposes.

First of all, they illustrate and compare many concepts elaborated in Part I. Extensive cross-referencing is provided between Part I and Part II to help the reader either to find the example(s) illustrating a theory, or to refer to the theory supporting the observations or conclusions related to a given example.

The second objective is to show and quantify the accuracy of the MoM in the interesting and useful case of a PEC sheet deposited on a very thin dielectric substrate. To reach this goal, we make extensive use of the reference solution described in §6.1.4, but we also start from the sphere and progressively deform it into a rounded cube, then a cube and finally a very thin plate. In the almost unique case of the sphere, the analytical solution is available for both the PEC and dielectric case. Moreover, the absence of sharp edges eliminates high gradients of surface current densities, what proves to yield the best accuracy for all tested formulations, as well as an excellent match between the tMFIE-nxf and the two tEFIE-f formulations. The sphere also offers a unique opportunity to precisely measure the flat facet error, due to the approximation of the curved surface with flat triangles. Armed with the solid and rich accuracy references provided by the sphere, we can measure the progressive degradation of the accuracy throughout all the above mentioned transitional geometries, until the very thin dielectric plate with a PEC coating.

The third objective is to support with two full-scale geometries the conclusions drawn in chapter 5 : the superiority, or even the necessity, of the 16 and 42 nodes quadratures if our general and versatile integration strategy is chosen among the others, presented in chapter 5.

The fourth objective is to extensively compare the two tEFIE-f and the tMFIE-nxf solutions for various PEC objects, and verify when or where both formulations provide convergent independent solutions.

Great attention has been paid to provide every details necessary to reproduce all the results. Those details include the numerical integration parameters, as they play an essential part in this book.

6.1 Introduction

6.1.1 Parameters common to all examples

Except in §6.12 the incident field is always a plane wave with wavelength λ_0 in free space (λ is the wavelength in dielectrics). The incoming electric field has unitary amplitude $|E^{inc}| = 1$ V/m, whereby the incoming magnetic field has an amplitude $|H^{inc}| = 2.653$ mA/m $\approx 1/Z_0$. The zero phase reference of the plane wave is located at *(x,y,z) = (0,0,0)*.

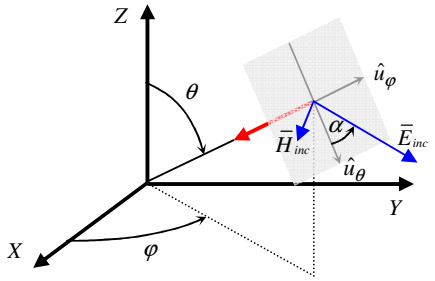

Figure 66 : Angles definition for the incident plane wave

As an example, the angles (θ, φ, α) defining a wave coming from -*Z* going to +*Z* and polarized along *X* are θ = 180° and φ - α = 180°.

The first form of the integro-differential equations has been used (§1.9), along with the tangential projection of the integro-differential equations : tEFIE or tMFIE (see §1.11).

The mesh, made of flat triangles, is unique for every interface between adjacent domains, and also for both faces of perfectly conducting sheets. The length of any edge in the mesh is always smaller than or equal to λ/9. The basis functions are always RWG, for both the electric and magnetic surface current densities (see §2.2.8).

The E-MFIE used for sheets is always based on tEFIE$^{\nabla G}$-f (see §5.4.2) and the tMFIE-nxf.

Every element of *Z*, *V* and *I* has been generated, stored and used in double precision, with 16 significant digits. The *ZI*=*V* system of equations is solved with a direct LU decomposition.

6.1.2 Variable parameters

For PEC sectors (see §3.2), we can choose among :

– tEFIE$^{\nabla f}$-f or tEFIE$^{\nabla G}$-f (see §5.4.2)

– tMFIE-nxf

– E-MFIE for embedded edges

For Dielectric sectors, we can choose a PMCHWT or a Müller combination (see §3.6) of either :

– tEFIE-f ($^{\nabla f}$ or $^{\nabla G}$) and tMFIE-f or

– tEFIE$^{\nabla G}$-nxf and tMFIE-nxf

For PEC and dielectric sectors, more insight about the testing functions (denoted with the subscript -f or -nxf) is given in §2.3.2.

To compute every $z_{mn,i}$ elements entering the Z matrix, the distance R_{min} between the triangle pairs $S_{m,i}$ and $S_{n,i}$ is first determined. Singularity extraction (see §5.4) is applied only if $R_{min} < \lambda/10$. When $R_{min} = 0$, it is also detected individually for the four interactions between the two pairs of triangles which interactions are self terms, as they require a special treatment. For example, self terms reduce to the principal value in the tMFIE-nxf (see §2.3.2), but not in the tEFIE-f. The number of nodes used in the outer and inner integrals is different, and varies with R_{min}.

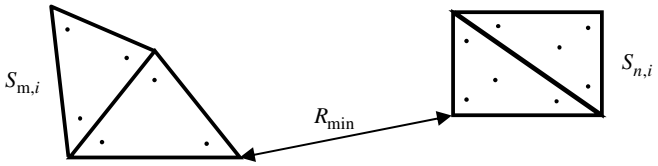

Figure 67 : Geometry to determine the number of quadrature nodes

An example is given in Table 11, including also the number of nodes used in the numerical computation of the elements $v_{m,i}$ of the source vector V.

Table 11 : Example of a scheme for the number of integration nodes

	Self Term	$R_{min} < \lambda/100$	$R_{min} \in [\lambda/100; \lambda/10]$	$R_{min} > \lambda/10$	V
Inner	3	3	3	3	--
Outer	42	16	7	3	3

6.1.3 Presentation of the results

After solving $I=Z^{-1}V$, the vector I is used to compute the electric and magnetic current densities in the middle of every triangle inside every dielectric domain, as shown in §2.2.8 with (147) and (148). As we have used the harmonic version of Maxwell's equations, the surface current densities we obtain are complex valued. We refer to (12) in §1.2 to relate these complex surface current densities to the physical surface current densities varying with time at frequency $f = \omega/(2\pi)$.

The electric and magnetic surface current densities are normalized respectively to $|H^{inc}|$ and $|E^{inc}|$. The resulting magnitudes are thereby adimensional and vary in a limited range of values that is similar for $J/|H^{inc}|$ and $M/|E^{inc}|$, easing comparisons between them.

For a visual and qualitative representation, the real and imaginary parts of the surface current densities are represented as oriented arrows, superimposed on the (meshed) geometry. Their length and color both indicate the amplitude of the surface current density. When the amplitude variation of the surface current densities is large, for example close to sharp edges, a logarithmic scale is used. Otherwise, a linear scale is used.

We refer to §6.2.1 for a complete description of the quantitative analyses that are performed on every component of the current densities.

The condition number of Z is computed with the function '*cond*' in Matlab™ 7.1 and denoted CN. For dielectric domains, CN is computed for the appropriate adimensional version of Z, as explained in §5.2.2.

6.1.4 The $\varepsilon_r = 1$ reference solution

One can imagine a body V with arbitrary bounding surface S, filled with a dielectric of relative permittivity $\varepsilon_r \approx 1$, or even equal to one. To show that such a situation is not a trivial mathematical exercise, we give in Table 12 the relative permittivity of some gases.

The solution for the scattering by a volume filled with a linear, isotropic and homogeneous dielectric with relative permittivity equal to one is very simple : the surface current densities anywhere on S inside free space are given by :

$$\bar{J}_0 = +\hat{n}_0 \times \bar{H}_{inc} \tag{311}$$

$$\bar{M}_0 = -\hat{n}_0 \times \bar{E}_{inc} \tag{312}$$

The surface current densities on S inside the dielectric body are identical but with opposite sign. We will make extensive use of this simple reference solution throughout this chapter to assess the accuracy of several MoM formulations for various structures.

Such a void body can also be combined with another non trivial body, PEC or dielectric. The void body can be loose from the other body, touch it or even completely embed it. The solution for the electric and magnetic current densities on the surface of the non trivial body should not be altered by the presence of the void body, independently of the shape, size and location of this void body. We will also make use of this property to examine the behavior of the MoM solutions in presence of more than one dielectric or PEC body (§§6.3.1 and 6.10.1).

Table 12 : Relative permittivity of some gases

Gas name	ε_r
Air 0°C	1,00059
40 atm	1,0218
80 atm	1,0439
CO2, 0°C	1,000985
H2, 0°C	1,000264
Water vapor, 145°C	1,00705

6.2 Sphere

A sphere with radius $\lambda_0/6$ is illuminated by a plane wave travelling in free space from *-Z* to *+Z* and polarized along *X*. The incoming electric field has unitary amplitude $|E^{inc}| = 1$ V/m. The zero phase reference of the plane wave is located at *(x,y,z) = (0,0,0)*.

To illustrate how the electric and magnetic current densities look like, a first very accurate solution obtained with the MoM on a 748 triangles mesh is presented. The longest edge among all triangles has a length of $\lambda_0/20$ when $\varepsilon_r = 1$ and $\lambda/10$ of it when $\varepsilon_r = 4$. The magnetic current density being identically zero on the PEC sphere, it is not represented.

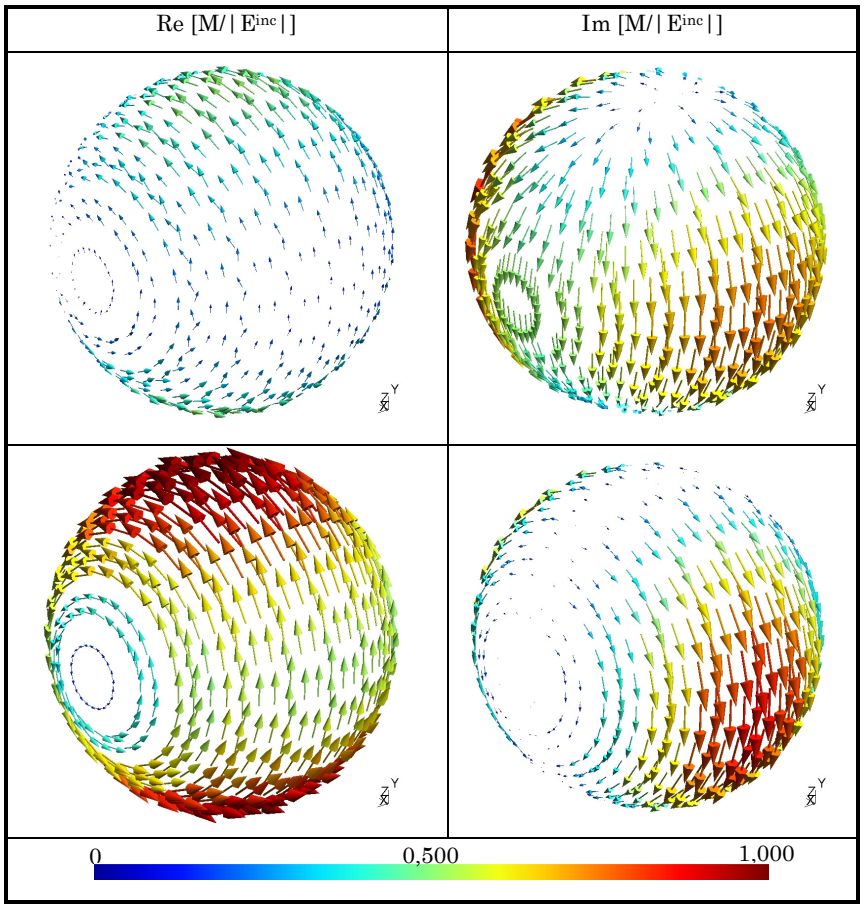

Figure 68 : $M/|E^{inc}|$: $\varepsilon_r = 4$ (Top) / $\varepsilon_r = 1$ (Bottom)

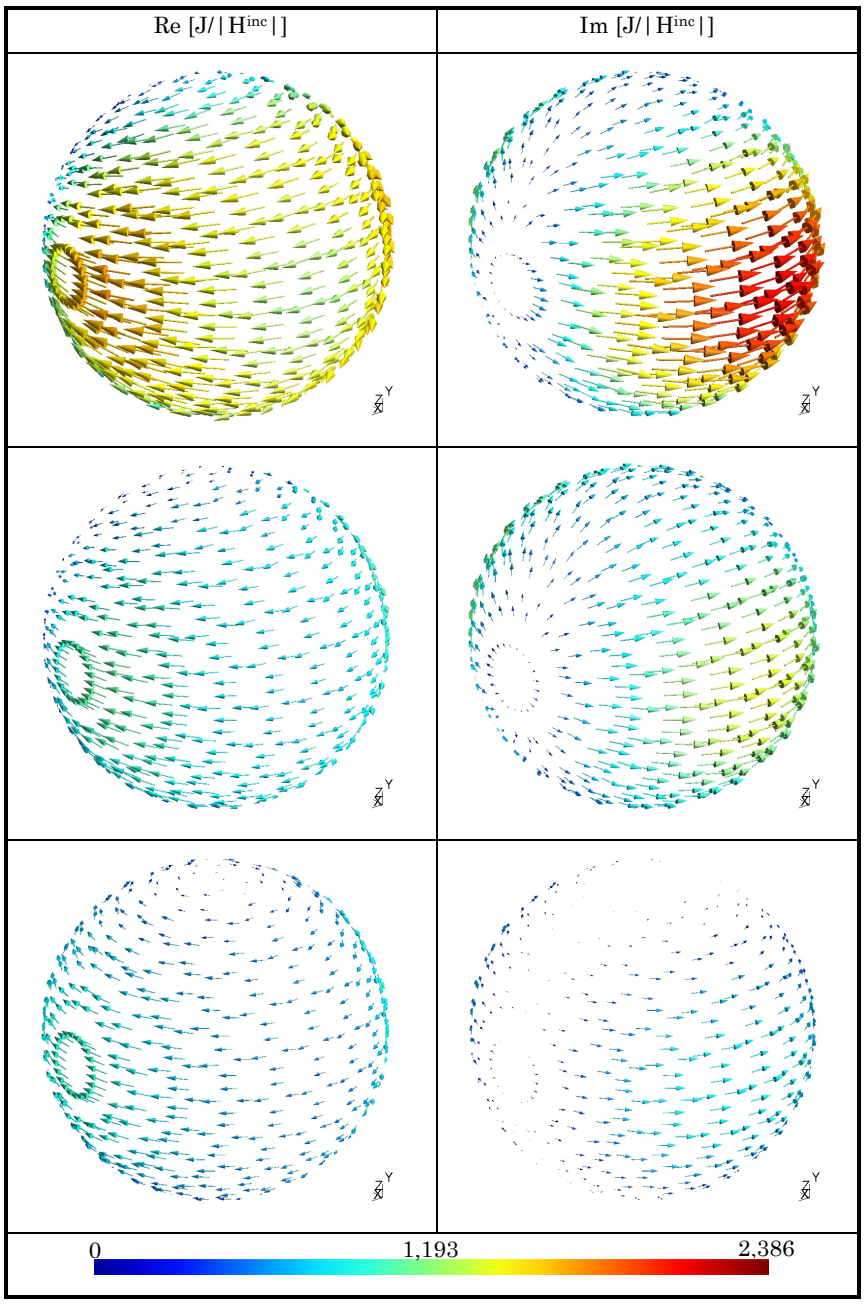

Figure 69 : $J/|H^{inc}|$: PEC (Top) / $\varepsilon_r = 4$ (Middle) / $\varepsilon_r = 1$ (Bottom)

The electric surface current density is the highest on the PEC sphere, and decreases with ε_r on the dielectric sphere (Figure 69, p.142), while the opposite is true for the magnetic surface current density (Figure 68, p.141). Table 13 shows the largest amplitude of the surface current density *J* and *M* on the sphere :

Table 13 : Maximum values of the surface current densities

	$Max(J/\lvert H^{inc}\rvert)$	$Max(M/\lvert E^{inc}\rvert)$
PEC	2,386	0
$\varepsilon_r = 4$	1,523	0,937
$\varepsilon_r = 1$	1,000	1,000

6.2.1 tEFIE-f

To quantify the accuracy of the $tEFIE^{\nabla f}$-f and the $tEFIE^{\nabla G}$-f (see §5.4.2) for several integration schemes, we compare the MoM solutions for the surface current density computed at every triangle centroid with the exact Mie solution [1] computed, with at least 6 correct significant digits, on the sphere at the same spherical coordinate as the triangle centroid. As illustrated in Figure 70, the flat facet mesh introduces an unavoidable geometrical error.

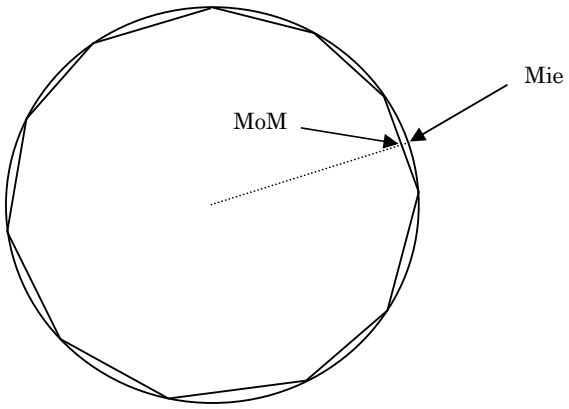

Figure 70 : Mesh error on the sphere

We use the mesh of Figure 71 (p.144), containing 608 quasi equilateral triangles. The largest triangle edge has a length of $\lambda_0/19$.

EFIE resonances are excluded as the sphere diameter is smaller than $1.145\lambda_0$ (see §5.2.3).

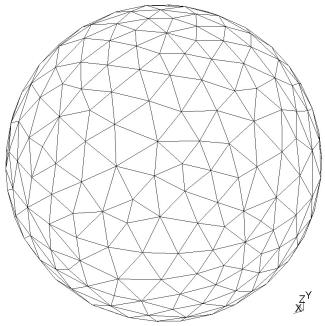

Figure 71 : Regular $\lambda_0/19$ mesh of a sphere with radius $\lambda_0/6$

The absolute error is computed separately for every component of the real and imaginary part of $\bar{J}$, namely $Re(J_x)$, $Re(J_y)$, $Re(J_z)$ and $Im(J_x)$, $Im(J_y)$, $Im(J_z)$. To obtain relative errors in percent, these absolute errors are then multiplied by 100 and divided by MaxJ, where :

$$MaxJ_{(Mie\ Solution)} = \max\begin{Bmatrix} \max(\mathrm{Re}\,J_x), \max(\mathrm{Re}\,J_y), \max(\mathrm{Re}\,J_z), \\ \max(\mathrm{Im}\,J_x), \max(\mathrm{Im}\,J_y), \max(\mathrm{Im}\,J_z) \end{Bmatrix} \tag{313}$$

These relative errors, calculated at the spherical coordinate of every triangle centroid, are represented by a blue dot in Figure 72 (p.145). For all six components of $\bar{J}$, the average and the standard deviation of every relative error are indicated, and the average is also illustrated by a red horizontal line. The *X* axis of every subplot is the Mie solution, scaled between $-MaxJ/|H^{inc}|$ and $+MaxJ/|H^{inc}|$.

We compare hereafter the $tEFIE^{\nabla_f}$-f and $tEFIE^{\nabla_G}$-f solutions for the eleven integration schemes listed in Table 14. In the 1 node integration scheme, all integrations are performed with only one node. In all other integration schemes, one or three nodes are used for the inner integrals and outer integrals for which $R_{min} > \lambda/100$.

Table 14 : Eleven integration schemes with tEFIE-f for the sphere

	Self Term	$R_{min} < \lambda/100$	$R_{min} \in [\lambda/100; \lambda/10]$	$R_{min} > \lambda/10$	V
Inner	1		1	1	--
Outer	1		1	1	1
Inner	3		3	3	--
Outer	3, 6, 7, 12, 16, 19, 25, 42, 61, 73		3	1	3

A comparison between the $tEFIE^{\nabla_f}$-f and $tEFIE^{\nabla_G}$-f solutions obtained with the 16 nodes quadrature can be found in Figure 72 (p.145). For the other integration schemes listed in Table 14, only the average relative error is reported in Table

15. For both the tEFIE$^{\nabla f}$-f and the tEFIE$^{\nabla G}$-f, the distribution of the relative errors on the 608 triangles is quite similar but also very good, with an average around 1% for all six components of J, and a maximum below 5%. The condition number of both Z matrices is quasi identical (500 and 515).

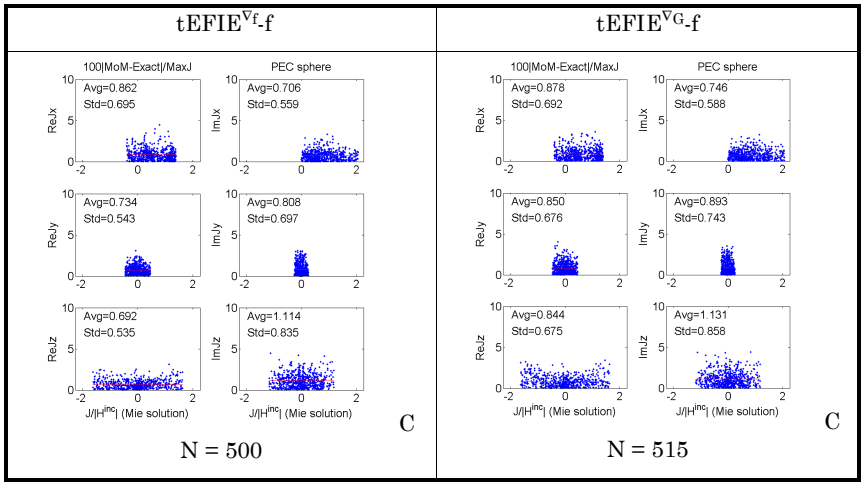

Figure 72 : Relative errors and CN (tEFIE-f, 16 nodes quadrature)

Table 15 : Average relative error with tEFIE-f on PEC sphere in function of the number of integration nodes

	tEFIE$^{\nabla f}$-f						tEFIE$^{\nabla G}$-f					
	Re			Im			Re			Im		
	J_x	J_y	J_z	J_x	J_y	J_z	J_x	J_y	J_z	J_x	J_y	J_z
1	0,93	0,75	0,74	0,76	0,83	1,11	2,93	1,70	1,94	1,68	1,26	1,62
3	0,87	0,74	0,69	0,72	0,81	1,11	1,07	0,94	1,02	0,97	0,93	1,23
6	0,86	0,73	0,69	0,71	0,81	1,11	0,89	0,92	0,96	0,87	0,95	1,18
7	0,86	0,73	0,69	0,71	0,81	1,11	0,85	0,89	0,92	0,84	0,94	1,17
12	0,86	0,73	0,69	0,71	0,81	1,11	0,83	0,87	0,88	0,81	0,92	1,16
16	0,86	0,73	0,69	0,71	0,81	1,11	0,88	0,85	0,84	0,75	0,89	1,13
19	0,86	0,73	0,69	0,71	0,81	1,11	0,84	0,86	0,86	0,78	0,91	1,15
25	0,86	0,73	0,69	0,71	0,81	1,11	0,85	0,86	0,85	0,76	0,90	1,14
42	0,86	0,73	0,69	0,71	0,81	1,11	0,88	0,85	0,85	0,75	0,89	1,13
61	0,86	0,73	0,69	0,71	0,81	1,11	0,86	0,85	0,85	0,76	0,90	1,14
73	0,86	0,73	0,69	0,71	0,81	1,11	0,87	0,85	0,85	0,75	0,90	1,13

The tEFIE$^{\nabla f}$-f contains only the $1/R$ singularity. After its extraction from the inner integral, the outer integral is never singular and can be integrated very accurately with only a few nodes. There is indeed no significant accuracy improvement if more than 6 nodes are used in the outer integral when $R_{min} < \lambda/100$. Even an integration with only 1 node everywhere already yields an accuracy quite similar to the best one obtained with more nodes. The difference

between a 1 node and a 16 nodes integration is so tiny that is not perceptible in Figure 73.

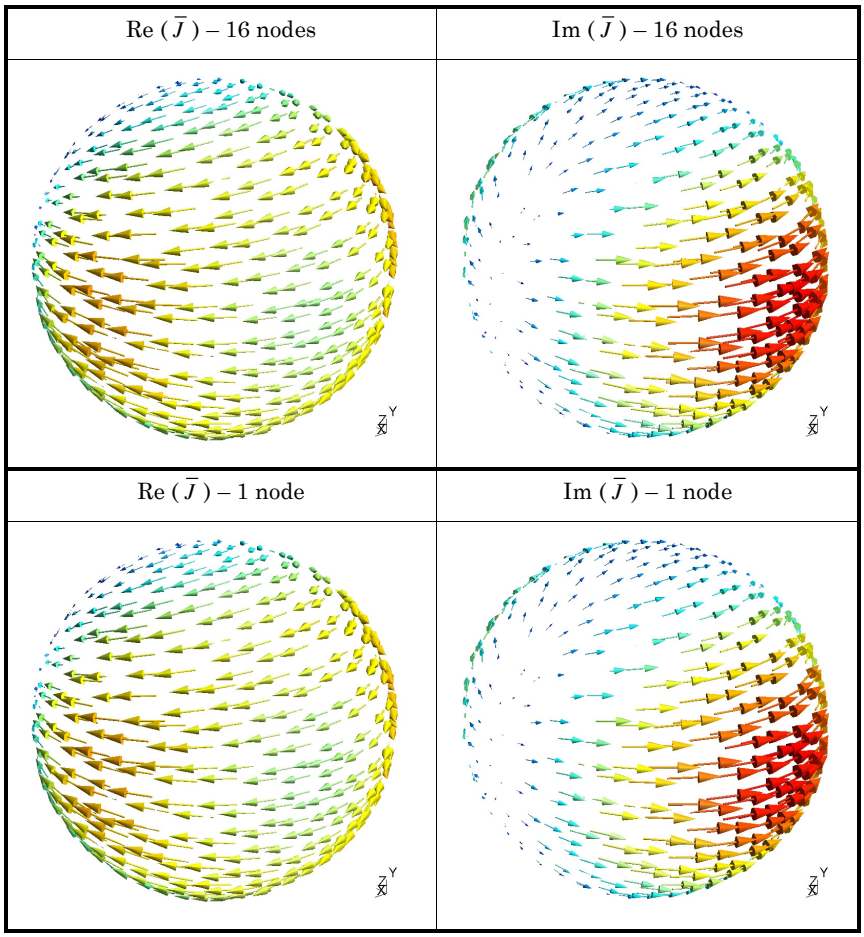

Figure 73 : tEFIE$^{\nabla f}$-f with only 1 or 16 integration nodes

The tEFIE$^{\nabla G}$-f contains a $1/R$ and a $1/R^3$ singularity. After their extraction, the $1/R^3$ singularity leaves a logarithmic singularity in the outer integral. As shown in §5.5 a higher number of nodes might be necessary to obtain acceptable accuracy, while the 16 and 42 nodes quadratures outperform the others, at least in the analyzed canonical cases. Table 15 (p.145) shows indeed an extremely small advantage of the 16 and 42 nodes quadratures, but this effect will be more convincing with other examples (§6.12). On the other hand, as can be seen in detail in Figure 74 (p.147), the relative error pattern with the 1-node integration scheme is visibly worse than the others, though still surprisingly acceptable.

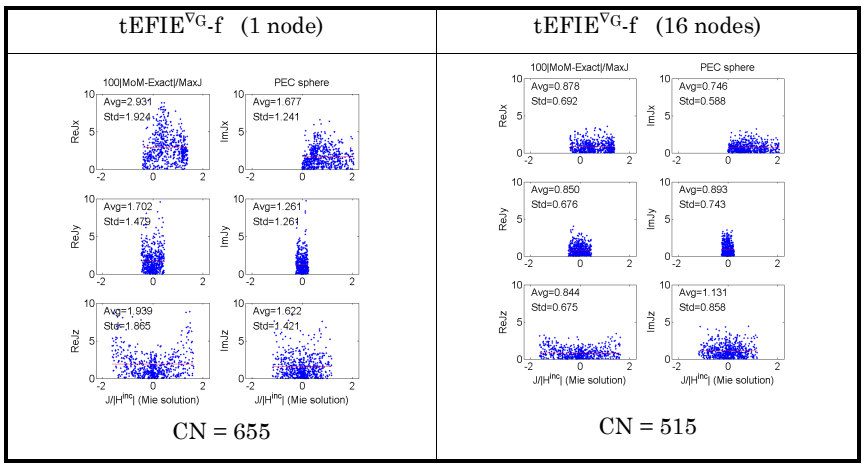

Figure 74 : Relative error with tEFIE$^{\nabla G}$-f and 16 nodes quadrature

6.2.2 tMFIE-nxf

We solve now exactly the same sphere scattering problem as in §6.2.1, but with the tMFIE-nxf. In this way we can measure the accuracy of this solution with the help of the exact Mie solution, and then compare the tMFIE-nxf solution to the tEFIE$^{\nabla G}$-f solution, both containing the $1/R^3$ singularity. Table 16 shows that the evolution of the average relative error with regard to the exact Mie solution, as a function of the number of integration nodes chosen for the outer integral when $R_{min} < \lambda/100$, is quite similar for both solutions. A detailed comparison, presented in Figure 75 (p.148), shows that the tMFIE-nxf performs slightly better than the tEFIE$^{\nabla G}$-f, especially for the 1-node integration scheme. MFIE resonances are excluded as the sphere diameter is smaller than $1.145\lambda_0$ (see §5.2.3).

Table 16 : Average relative error with tMFIE-nxf and tEFIE$^{\nabla G}$-f

	tMFIE-nxf						tEFIE$^{\nabla G}$-f					
	Re			Im			Re			Im		
	J_x	J_y	J_z	J_x	J_y	J_z	J_x	J_y	J_z	J_x	J_y	J_z
1	2,41	1,01	1,16	0,99	0,72	1,06	2,93	1,70	1,94	1,68	1,26	1,62
3	1,44	0,81	0,83	0,77	0,80	1,07	1,07	0,94	1,02	0,97	0,93	1,23
6	1,15	0,76	0,75	0,75	0,80	1,06	0,89	0,92	0,96	0,87	0,95	1,18
7	1,10	0,75	0,73	0,75	0,81	1,06	0,85	0,89	0,92	0,84	0,94	1,17
12	1,03	0,74	0,72	0,75	0,81	1,06	0,83	0,87	0,88	0,81	0,92	1,16
16	0,83	0,72	0,68	0,77	0,82	1,06	0,88	0,85	0,84	0,75	0,89	1,13
19	0,97	0,73	0,70	0,75	0,81	1,06	0,84	0,86	0,86	0,78	0,91	1,15
25	0,94	0,73	0,69	0,75	0,81	1,06	0,85	0,86	0,85	0,76	0,90	1,14
42	0,91	0,72	0,68	0,76	0,81	1,06	0,88	0,85	0,85	0,75	0,89	1,13
61	1,07	0,75	0,74	0,76	0,79	1,05	0,86	0,85	0,85	0,76	0,90	1,14
73	0,92	0,73	0,69	0,76	0,81	1,06	0,87	0,85	0,85	0,75	0,90	1,13

Both solutions, when integrated with 16 nodes, show a maximum relative error with regard to the exact solution of less than 5%. If we compare directly the tMFIE-nxf and tEFIE$^{\nabla G}$-f at every 608 triangle centroid, we find that the maximum difference between the two solutions is less than 3%, as shown in Figure 76 (p.149).

The condition number is two orders of magnitude better with tMFIE-nxf than with tEFIE$^{\nabla G}$-f in the 16 nodes case. It is only 6 times lower in the 1 node case.

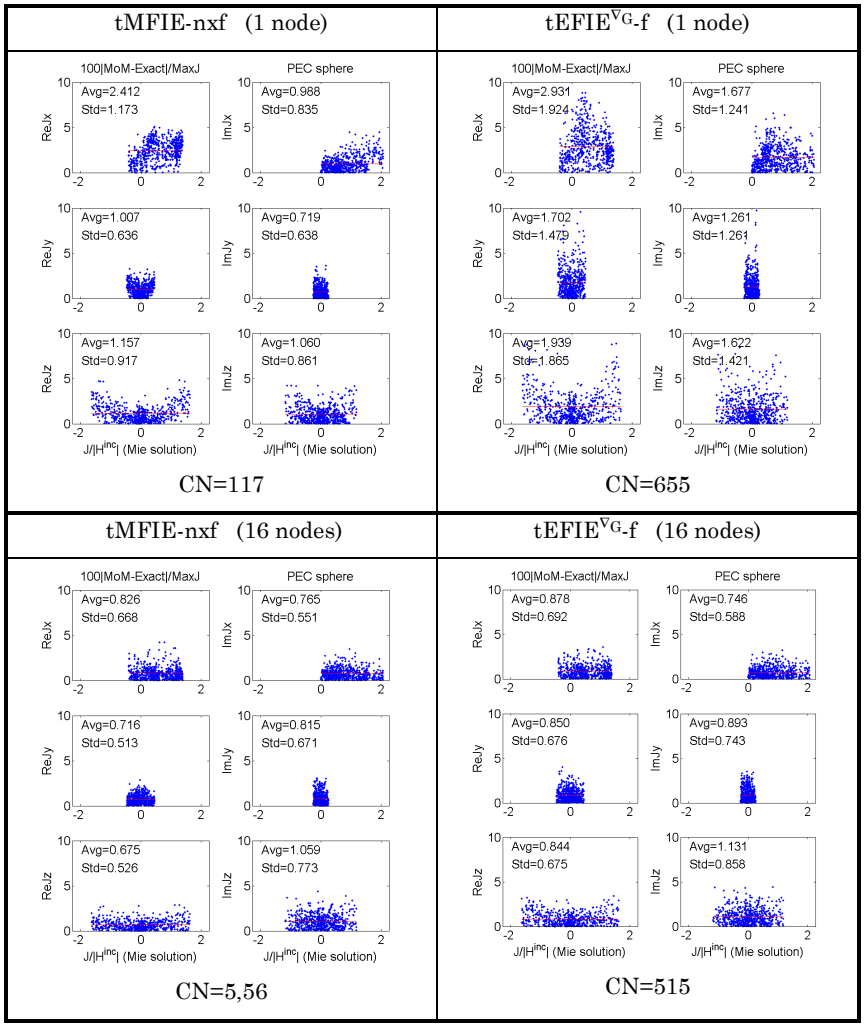

Figure 75 : tMFIE-nxf and tEFIE$^{\nabla G}$-f relative errors for a PEC sphere

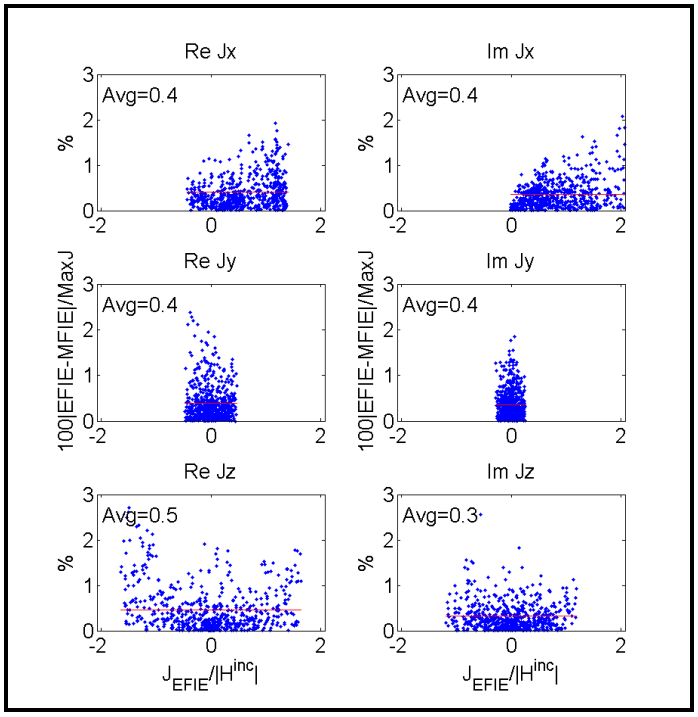

Figure 76 : Direct comparison tMFIE-nxf / tEFIE$^{\nabla G}$-f for a PEC sphere

6.2.3 Homogeneous and inhomogeneous mesh

We compare in Figure 77 (p.150) the relative errors obtained with tEFIE$^{\nabla G}$-f and tMFIE-nxf with a uniform and with a less uniform mesh, both having a comparable number of similarly sized triangles.

We use the following integration scheme :

	Self Term	$R_{min} < \lambda/100$	$R_{min} \in [\lambda/100; \lambda/10]$	$R_{min} > \lambda/10$	V
Inner	3		3	3	--
Outer	16		7	3	3

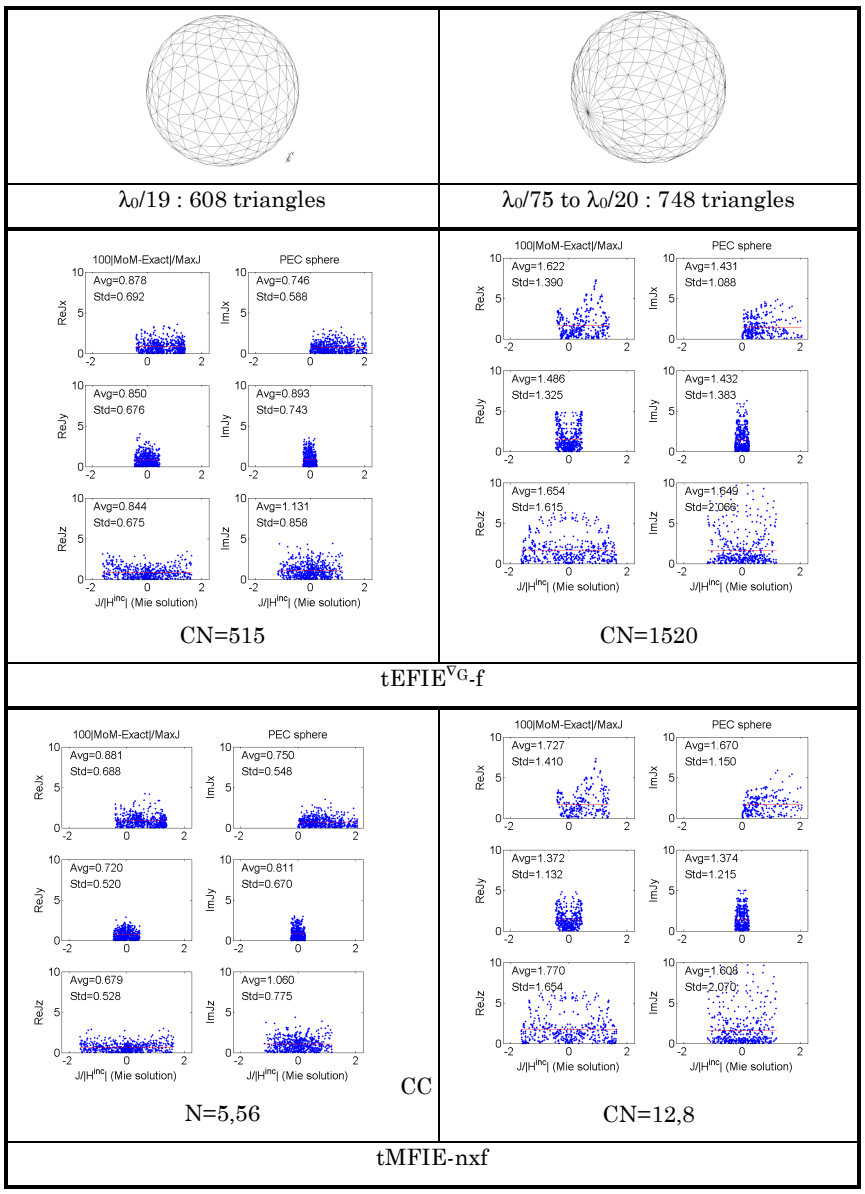

Figure 77 : Relative errors on a (non) uniform mesh of a PEC sphere

The tEFIE$^{\nabla G}$-f and tMFIE-nxf solutions obtained with the uniform mesh are twice better than the solutions obtained with a mesh containing triangles moderately stretched around the -*X* and +*X* poles. The condition number follows a similar trends for both the tEFIE$^{\nabla G}$-f and the tMFIE-nxf, while being much lower in the tMFIE-nxf case.

6.2.4 Mesh density

In Figure 79 (p.152) we compare the relative errors of the solutions obtained with the tEFIE$^{\nabla_f}$-f for the PEC sphere meshed uniformly with finer and finer meshes presented in Figure 78. The maximum dimension of the triangle sides in each of the four meshes ranges from $\lambda_0/11$ to $\lambda_0/51$.

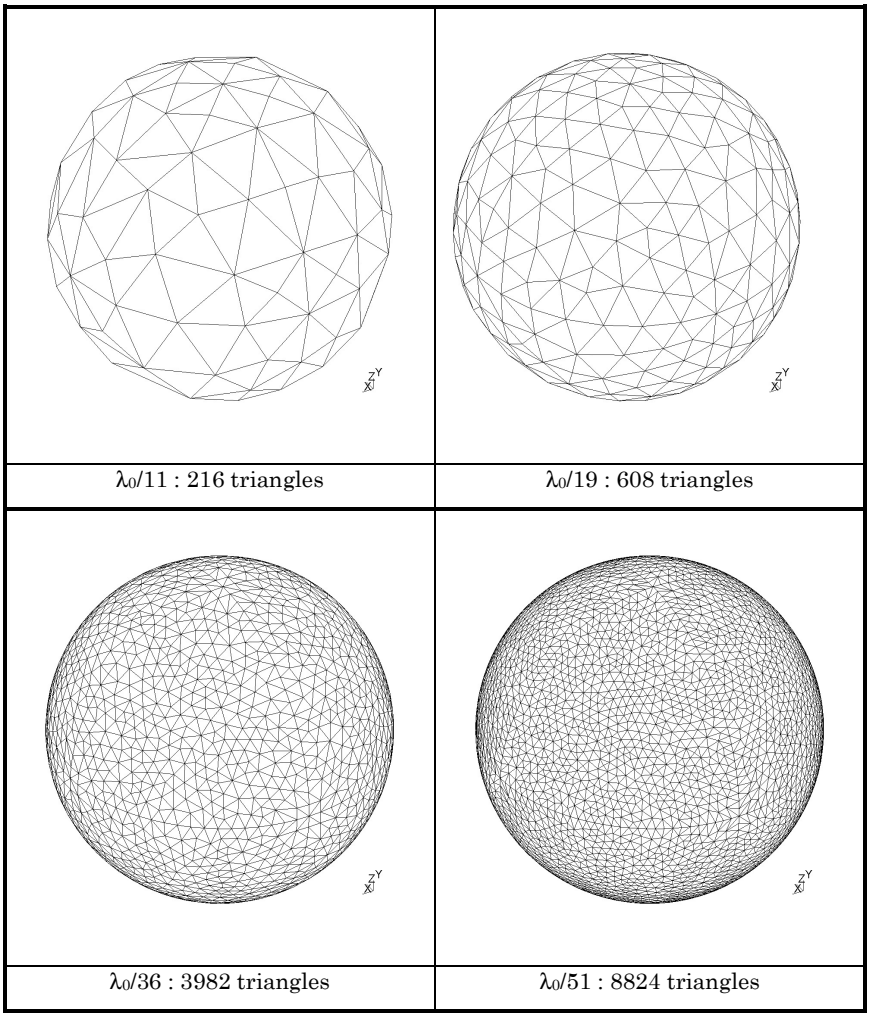

$\lambda_0/11$: 216 triangles	$\lambda_0/19$: 608 triangles
$\lambda_0/36$: 3982 triangles	$\lambda_0/51$: 8824 triangles

Figure 78 : Four uniform meshes of a sphere

The number of rows and columns of the Z matrix for the PEC sphere embedded in free space is $N \times N$ where $N=1,5T$ is the number of mesh edges and T is the number of triangles in the mesh, mentioned in Figure 78.

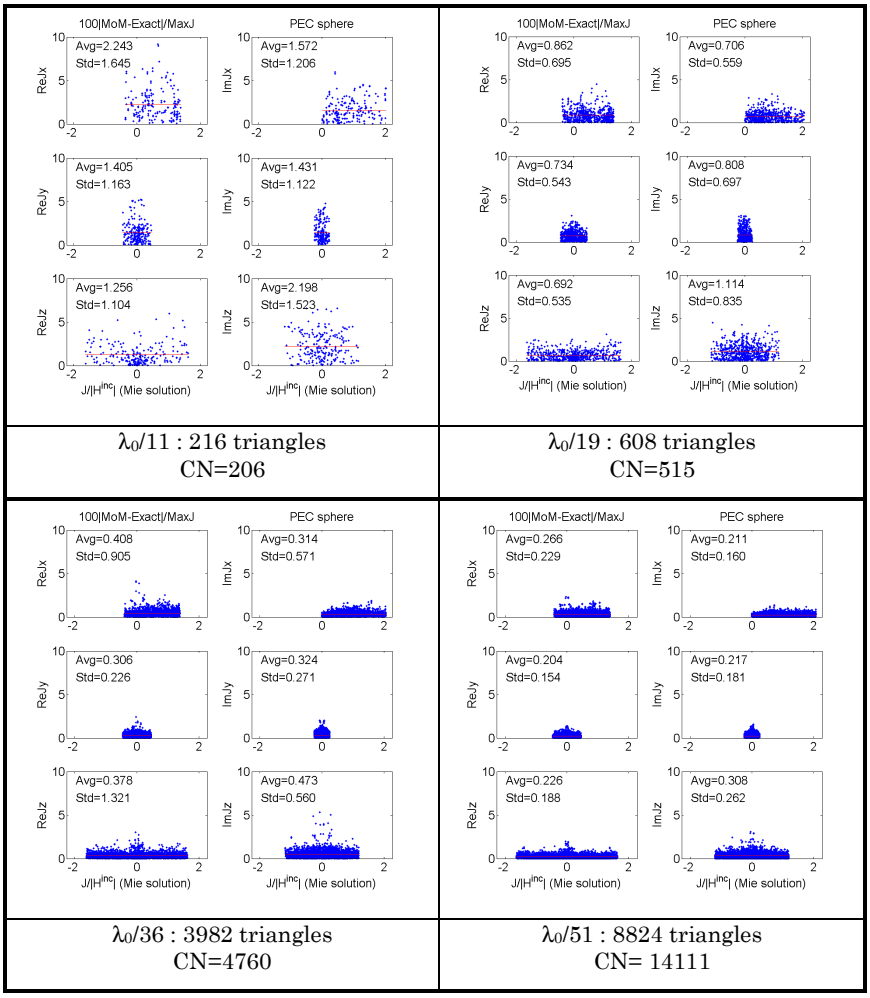

$\lambda_0/11$: 216 triangles CN=206	$\lambda_0/19$: 608 triangles CN=515
$\lambda_0/36$: 3982 triangles CN=4760	$\lambda_0/51$: 8824 triangles CN= 14111

Figure 79 : Relative error of the tEFIE$^{\nabla_f}$-f with four meshes

The relative errors do improve when the mesh is refined, proportionally to $1/h$, where h is the mesh characteristic dimension [2]. This linear improvement is quite slow in comparison with the huge increase in solving resources : the required memory and the fill time of the Z matrix is proportional to N^2, while the solving time is proportional to N^3 with a direct solver and to kN^2 with an iterative solver.

6.2.5 Dielectric sphere

Next we analyse the dielectric sphere, for which a solution is sought with the PMCHWT and the Müller combination schemes, where the $tEFIE^{\nabla G}$ and tMFIE are both tested either with -f or -nxf. The inhomogeneous mesh contains 748 triangles and is shown in Figure 77 (p.150). The length of the edge of every triangle is comprised between $\lambda_0/75$ and $\lambda_0/20$. On a dielectric sphere, not only an electric but also a magnetic surface current density is present. Both surface current densities will be considered in the comparisons.

We use the following integration scheme :

	Self Term	$R_{min} < \lambda/100$	$R_{min} \in [\lambda/100; \lambda/10]$	$R_{min} > \lambda/10$	V
Inner	1		1	1	--
Outer	16		7	3	3

The first analysis concerns a dielectric sphere with $\varepsilon_r = 1$.

In this specific case, we can use two different reference solutions :

– the "Mie" solution, computed on the sphere (see Figure 70, p.143)

– the exact analytical solution (see §6.1.4), computed exactly at the triangles centroids, called hereafter "Facet" solution.

Note that for $\varepsilon_r = 1 = \mu_r$, the PMCHWT and Müller combination schemes (§3.6) are identical.

Table 17 : Average relative errors for a dielectric sphere with $\varepsilon_r = 1$

		Re J			Im J			Re M			Im M		
		x	y	z	x	y	z	x	y	z	x	y	z
PMCHWT-f-f	**Ref = Mie**	3,0	0,7	3,2	2,1	1,1	2,0	0,5	3,3	2,9	0,9	1,7	2,5
PMCHWT-nxf-nxf	**Ref = Mie**	3,1	0,5	3,3	2,2	1,0	2,1	0,4	3,3	2,9	0,7	1,8	2,5
PMCHWT-f-f	**Ref = Facet**	0,6	0,6	0,6	0,8	1,0	1,1	0,5	0,5	0,6	0,9	0,8	0,9
PMCHWT-nxf-nxf	**Ref = Facet**	0,4	0,5	0,5	0,8	1,0	1,1	0,4	0,5	0,4	0,8	0,8	0,9

Table 17 shows that the average relative errors of the MoM solutions, relatively to the "Mie" solution (2 to 3%), are a factor 3 to 6 higher than the average error of the MoM against the Facet solution (0,4 to 1,1%). This was expected, and it reveals that the main contribution to the errors measured for the PEC sphere in the previous paragraphs is due to the flat facet approximation of the curved surface of the sphere (see Figure 70, p.143).

In the second analysis, we compare the condition number and the average relative errors on various MoM solutions against the "Mie" reference solution for dielectric spheres with a relative permittivity ranging between $\varepsilon_r = 1$ and $\varepsilon_r = 4$.

Table 18 : Average relative error and condition number for dielectric spheres

				Re J			Im J			Re M			Im M		
			CN	x	y	z	x	y	z	x	y	z	x	y	z
$\varepsilon_r = 1$	PMCHWT	f-f	1500	3,0	0,7	3,2	2,1	1,1	2,0	0,5	3,3	2,9	0,9	1,7	2,5
		nxf-nxf	13	3,1	0,5	3,3	2,2	1,0	2,1	0,4	3,3	2,9	0,7	1,8	2,5
$\varepsilon_r = 2$	PMCHWT	f-f	1486	2,7	0,7	2,8	2,3	1,2	2,2	0,8	3,5	2,9	0,6	2,0	2,6
		nxf-nxf	36	2,7	0,6	2,8	2,3	1,2	2,3	0,8	3,7	3,2	0,5	2,2	2,8
	Muller	f-f	993	2,7	0,7	2,8	2,3	1,2	2,2	0,8	3,5	2,9	0,6	2,0	2,6
		nxf-nxf	19	2,7	0,6	2,8	2,3	1,2	2,3	0,7	3,5	2,9	0,5	2,0	2,7
$\varepsilon_r = 4$	PMCHWT	f-f	1471	2,6	1,0	2,3	2,2	1,3	2,2	1,1	2,6	2,0	1,0	2,4	2,6
		nxf-nxf	59	2,6	1,0	2,3	2,2	1,3	2,2	1,5	3,2	2,9	1,3	2,8	3,0
	Muller	f-f	590	2,6	1,0	2,3	2,2	1,3	2,2	1,1	2,6	2,0	1,0	2,4	2,6
		nxf-nxf	32	2,6	1,0	2,3	2,2	1,3	2,2	1,0	2,6	1,9	1,0	2,4	2,6

This comparison summarized in Table 18 shows that :

- The average relative errors on ReJ, ImJ, ReM and ImM do not vary significantly when ε_r increases from 1 to 4.
- All combination and testing schemes perform evenly, but PMCHWT-nxf-nxf shows a slightly higher average relative error for higher ε_r.
- The condition number for the PMCHWT-f-f is the highest. It slightly decreases with increasing ε_r.
- The PMCHWT-nxf-nxf and Müller-nxf-nxf schemes exhibit a very low condition number, that seems to increase proportionally to ε_r.

In the third and last analysis, we compare the two meshes of Figure 80, the first one containing 748 triangles, the second one 1748.

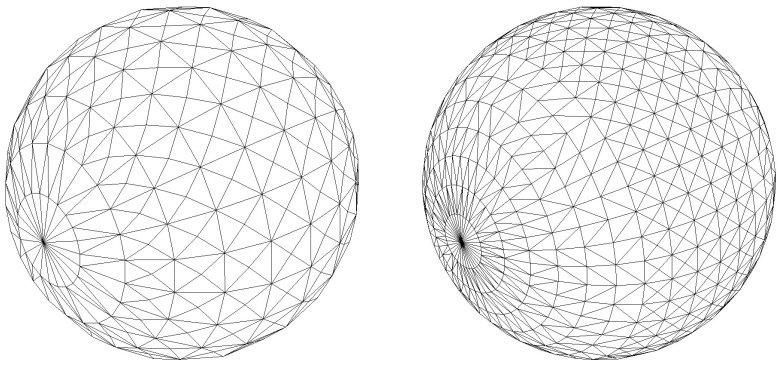

Figure 80 : Two meshes for a sphere

For the 748 triangles sphere, the longest triangle edge has a length of $\lambda_0/20$ when $\varepsilon_r = 1$ and $\lambda/10$ when $\varepsilon_r = 4$. For the 1748 triangles sphere, the longest triangle edge has a length of $\lambda_0/27$ when $\varepsilon_r = 1$ and $\lambda/13$ when $\varepsilon_r = 4$.

Table 19 : Influence of the mesh size
on the average relative error and the condition number

				Re J			Im J			Re M			Im M		
			CN	x	y	z	x	y	z	x	y	z	x	y	z
$\varepsilon_r = 4$	Ref = Mie	748	1471	2,6	1,0	2,3	2,2	1,3	2,2	1,1	2,6	2,0	1,0	2,4	2,6
		1748	17861	1,3	0,6	1,2	1,0	0,8	1,3	0,4	1,0	0,6	0,5	1,0	1,3
$\varepsilon_r = 1$	Ref = Mie	748	1500	3,0	0,7	3,2	2,1	1,1	2,0	0,5	3,3	2,9	0,9	1,7	2,5
		1748	18062	1,7	0,4	1,8	1,1	0,7	1,4	0,3	1,7	1,4	0,6	1,0	1,5
	Ref = Facet	748		0,60	0,60	0,60	0,80	1,00	1,10	0,50	0,50	0,60	0,90	0,80	0,90
		1748		0,34	0,43	0,44	0,57	0,72	0,75	0,33	0,36	0,36	0,58	0,52	0,65

As we observed with the PEC sphere, the average relative errors improve approximately as $1/h$, if we define a characteristic length h in these inhomogeneous meshes as :

$$h = \sqrt{\frac{S_{sphere}}{Number\ of\ triangles}} \tag{314}$$

In the case $\varepsilon_r = 1$ the same quantitative observation is true for both the Mie-MoM and the Facet-MoM comparison.

The condition number is multiplied by more than a factor 12 between the inhomogeneous mesh with 748 and the one containing 1748 triangles. In comparison, the condition numbers computed in §6.2.4 with four homogeneous meshes increase much slower with higher mesh density.

6.3 Sphere in a half spherical shell

We analyze now the mixed material body presented in Figure 81. The mesh has edges that are at most $\lambda_0/19$ long, and the global Z matrix counts 1726 J unknowns and 796 M unkowns.

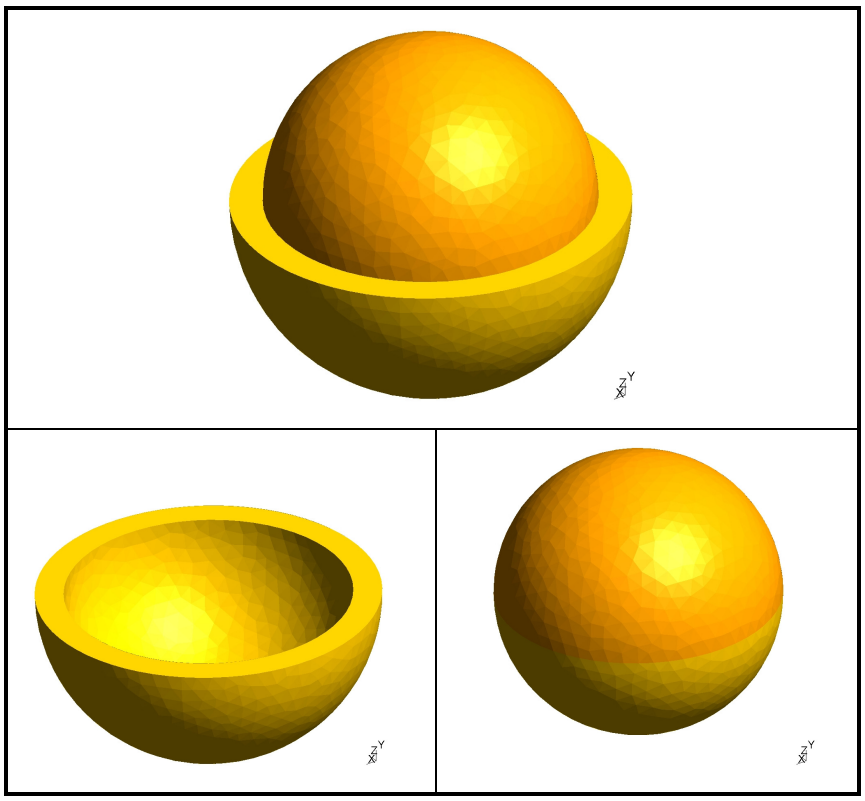

Figure 81 : Sphere in a half spherical shell

We use the following integration scheme :

	Self Term	$R_{min} < \lambda/100$	$R_{min} \in [\lambda/100; \lambda/10]$	$R_{min} > \lambda/10$	V
Inner	3		3	3	--
Outer	16		3	1	3

6.3.1 PEC sphere inside a $\varepsilon_r = 1$ shell

We begin with a PEC sphere and a $\varepsilon_r = 1$ shell. The electric current density on the sphere should not be altered by the presence of a $\varepsilon_r = 1$ shell. This is confirmed by

Figure 82, where we compare the Mie and MoM solutions for J on the PEC sphere, with or without the $\varepsilon_r = 1$ shell.

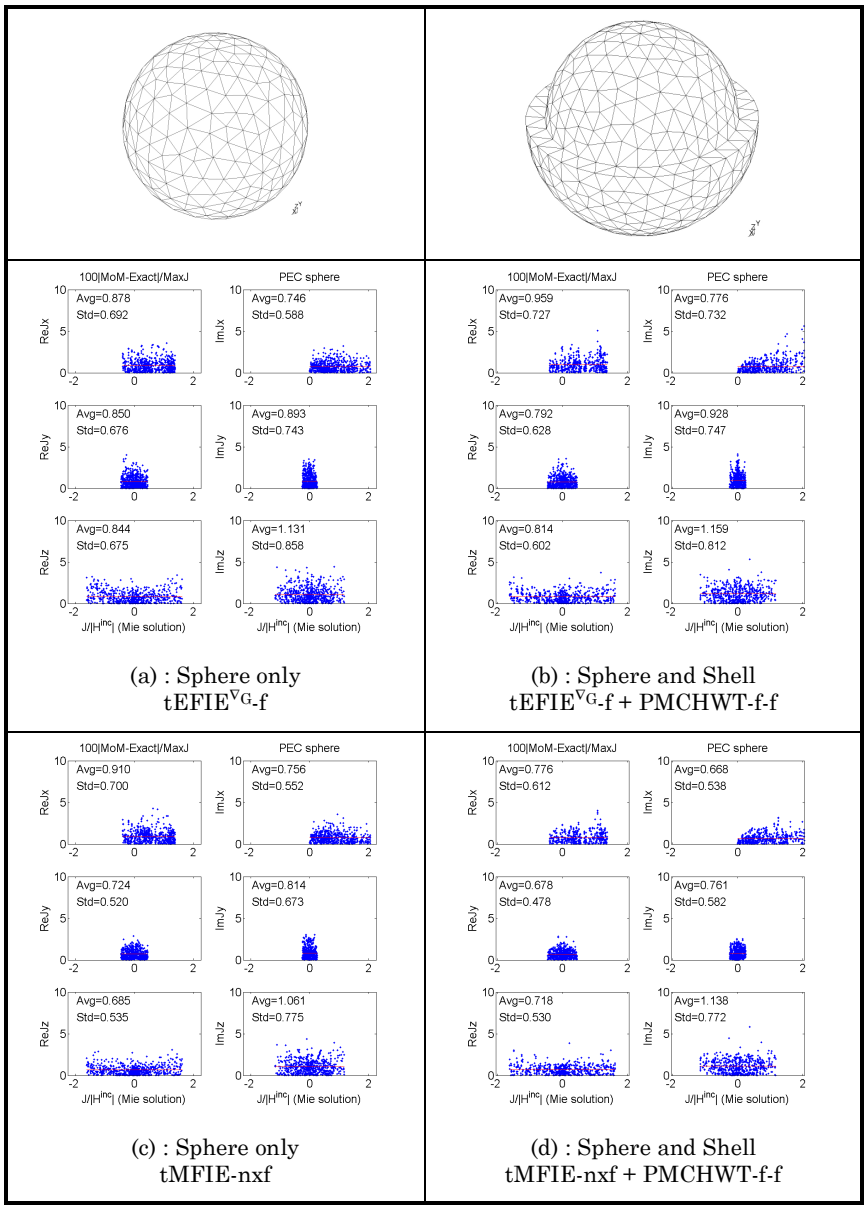

Figure 82 : Relative error on a PEC sphere, with and without $\varepsilon_r = 1$ shell

As opposed to the current density on the PEC sphere, the current density on the $\varepsilon_r = 1$ shell is not the same as what it would be without the presence of the PEC sphere.

On the inside part of the shell :

- the magnetic current density is identically zero, because this part of the shell is in contact with a PEC body
- the electric current density is the one expected on the bottom half of the PEC sphere if it were alone fully embedded in free space.

On the outside part of the shell, as suggested in Figure 83, the electric and magnetic current densities must produce everywhere in space the same electric and magnetic fields that would be scattered by the electric current density on the hidden bottom part of the PEC sphere.

On the thin annular part of the shell :

- the electric current density must be zero, because in the plane of the annular ring the incident and scattered magnetic fields are both lying in the *XZ* plane
- the magnetic current density is expected to be quite high as the total electric field is the highest close to the PEC sphere and lies in the plane of the annular ring

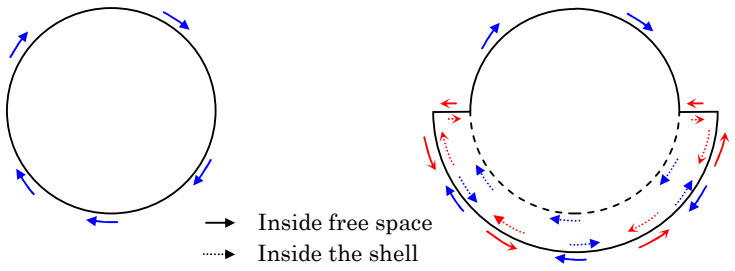

Figure 83 : Equivalent radiating electric and magnetic current densities

On the outer spherical part of the shell :

- the magnetic current density is expected to be very small as the total electric field is quasi radial at close distance from the sphere (it is exactly radial everywhere on the sphere)
- the electric current density is expected to be very similar in shape, but somewhat lower in amplitude than the electric current density on the bottom half of the PEC sphere.

All the observations made are confirmed by Figure 84 (p.159), where we present successively the current densities around the isolated sphere, in free space surrounding the half sphere and its shell, and in the shell alone :

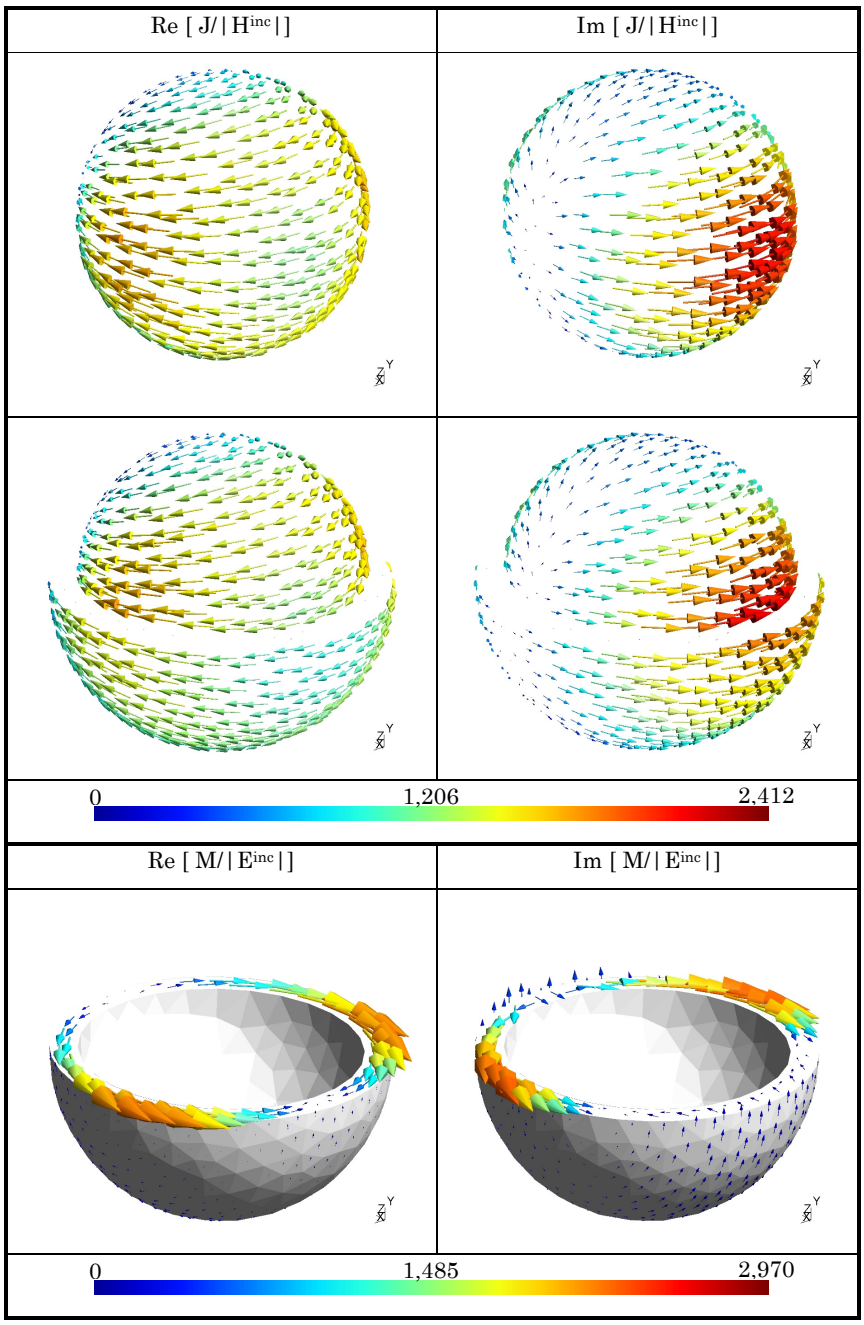

Figure 84 : J and M on the $\varepsilon_r = 1$ shell and on the isolated PEC sphere

6.3.2 PEC sphere inside a $\varepsilon_r = 9$ shell

In Figure 85 we compare the electric and magnetic current densities on a $\varepsilon_r = 1$ and a $\varepsilon_r = 9$ shell, partly embedding the same PEC sphere as in §6.3.1. To make sure that all triangle edges are at most $\lambda/9$ long when $\varepsilon_r = 9$, a mesh is used where the triangle edges are twice smaller than in §6.3.1. The size of the global Z matrix is 10212x10212. The tEFIE$^{\nabla_f}$-f is used for PEC sectors and with tMFIE-f in dielectric sectors in the PMCHWT-f-f scheme.

As in Table 13 (p.143), the electric surface current density gets higher in a dielectric with high permittivity : max[$J/|H^{inc}|$]=2,896 in the $\varepsilon_r = 9$ shell and 2,412 in the $\varepsilon_r = 1$ shell (see Figure 84, p.159).

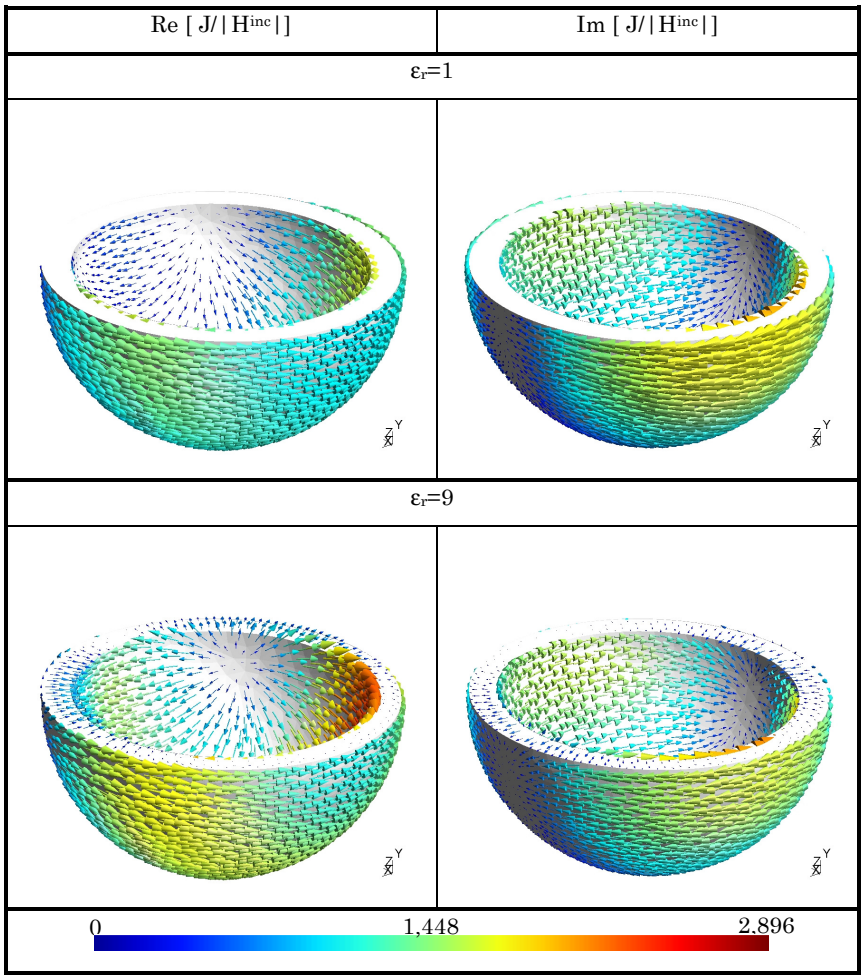

Figure 85 : J on a $\varepsilon_r = 1$ and a $\varepsilon_r = 9$ shell

We have also seen with Table 13 (p.119) that the magnetic current density decreases on a dielectric with high permittivity. While max[$M/|E^{inc}|$] = 3,150 in the $\varepsilon_r = 1$ shell, it is only 0,850 in the $\varepsilon_r = 9$ shell.

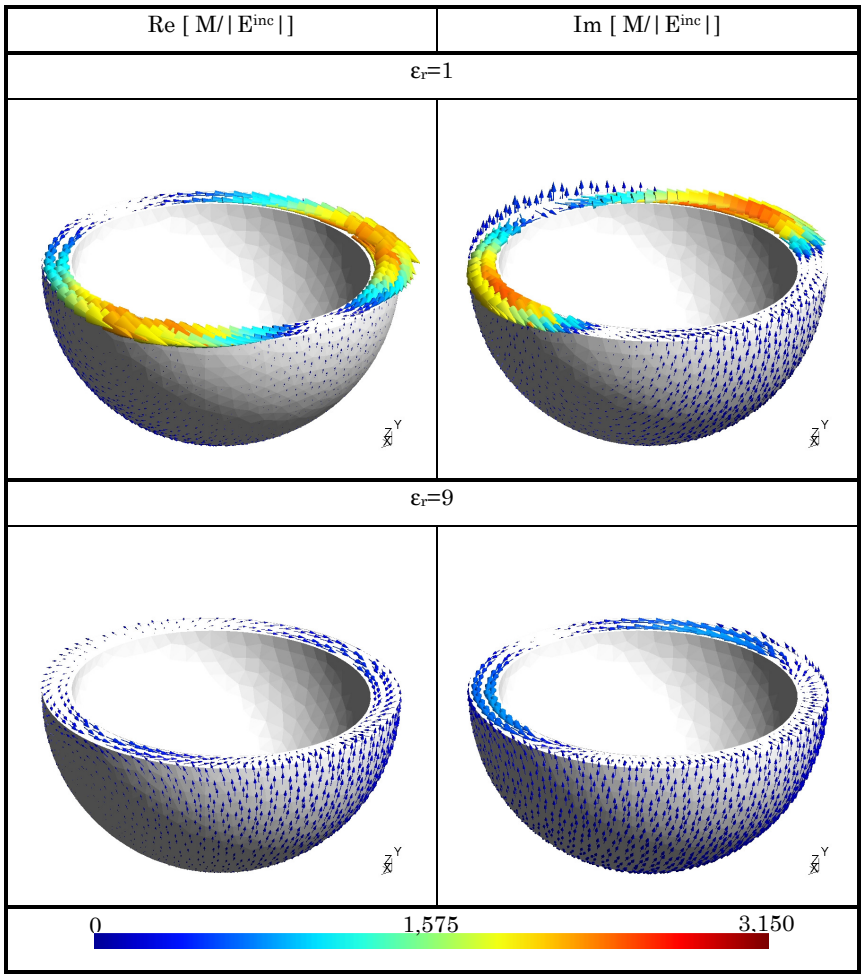

Figure 86 : M on a $\varepsilon_r = 1$ and a $\varepsilon_r = 9$ shell

6.4 Rounded cube

Halfway between the perfect shape of the sphere and the more challenging case of a cube, we analyze the cube with rounded edges and corners shown in Figure 87.

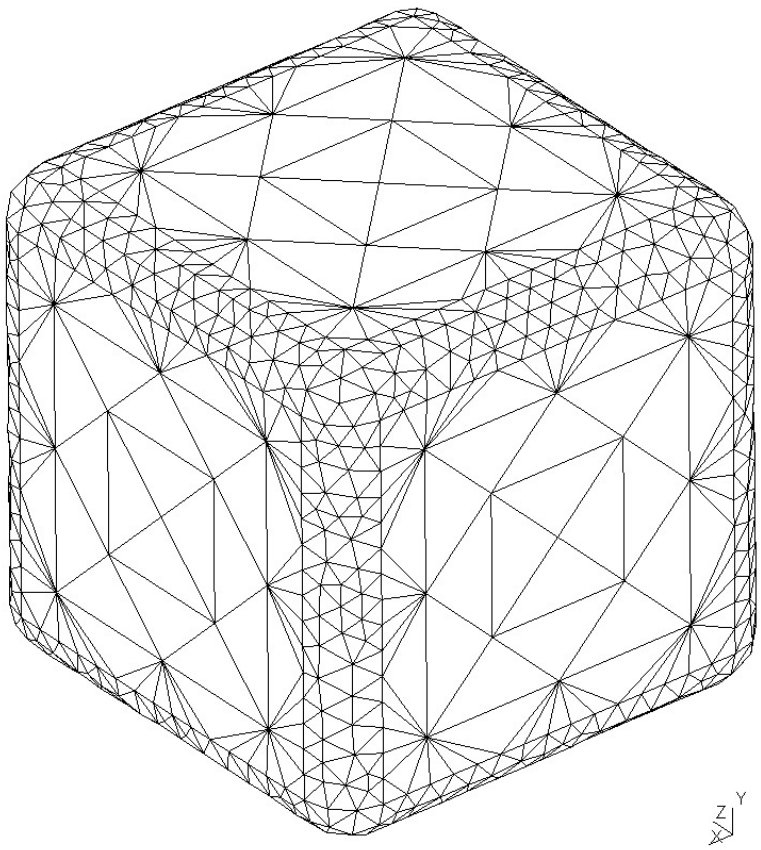

Figure 87 : Mesh of a cube with rounded edges and corners

The length of the sides of the cube is $\lambda_0/4$ and the radius of the rounded edges and corners is $\lambda_0/40$. It is illuminated with the same plane wave used in §6.2 and §6.3, a plane wave travelling from *-Z* to *+Z* and polarized along *X*. The incoming electric field has a unitary amplitude $|E^{inc}| = 1$ V/m and its phase is zero at the centre of the cube. The mesh contains 1866 triangles of various sizes and shapes. The largest triangles, in the middle of the flat faces, have edges not exceeding $\lambda_0/13$, while the smallest are $\lambda_0/127$.

6.4.1 Dielectric rounded cube

The only exact solution available for the rounded cube is the case $\varepsilon_r = 1$ (see §6.1.4). This reference solution will allow to quantify the accuracy of the MoM, and compare it with the accuracy obtained with the sphere. Note that there is no flat facet approximation error : the current densities J and M are calculated at the same location with the MoM solution and with the exact solution, namely at every triangle centroid.

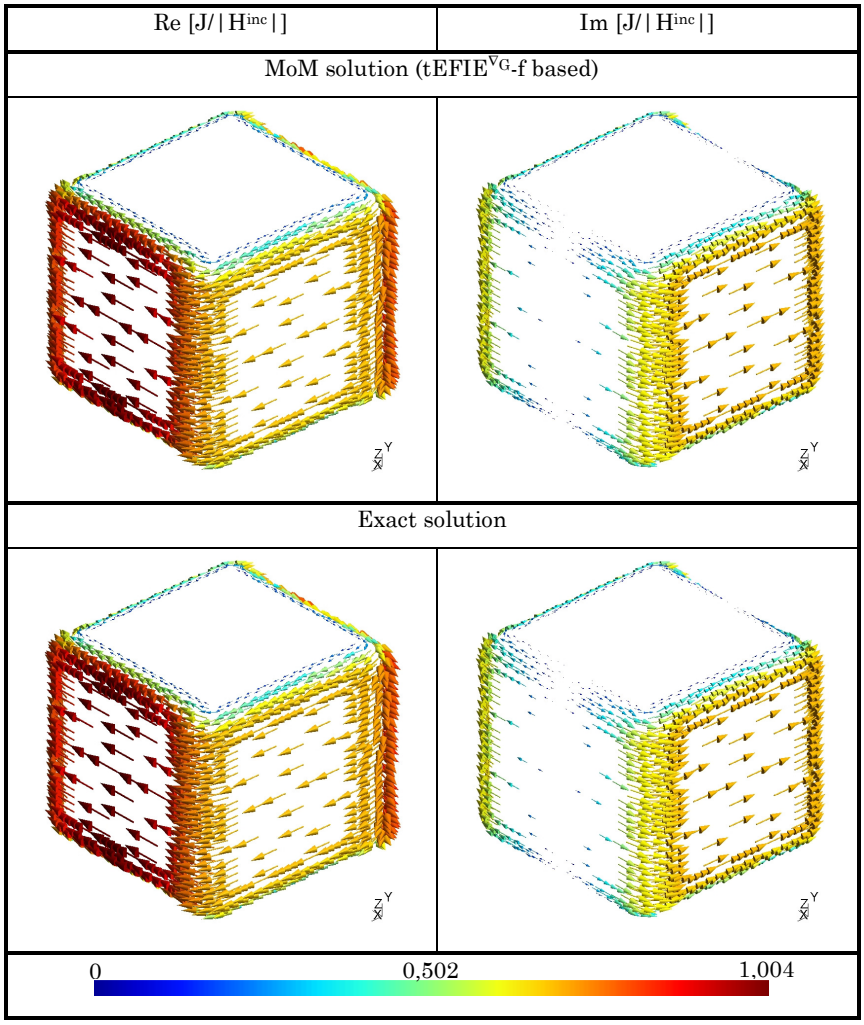

Figure 88 : $J/|H^{inc}|$ on the $\varepsilon_r = 1$ rounded cube

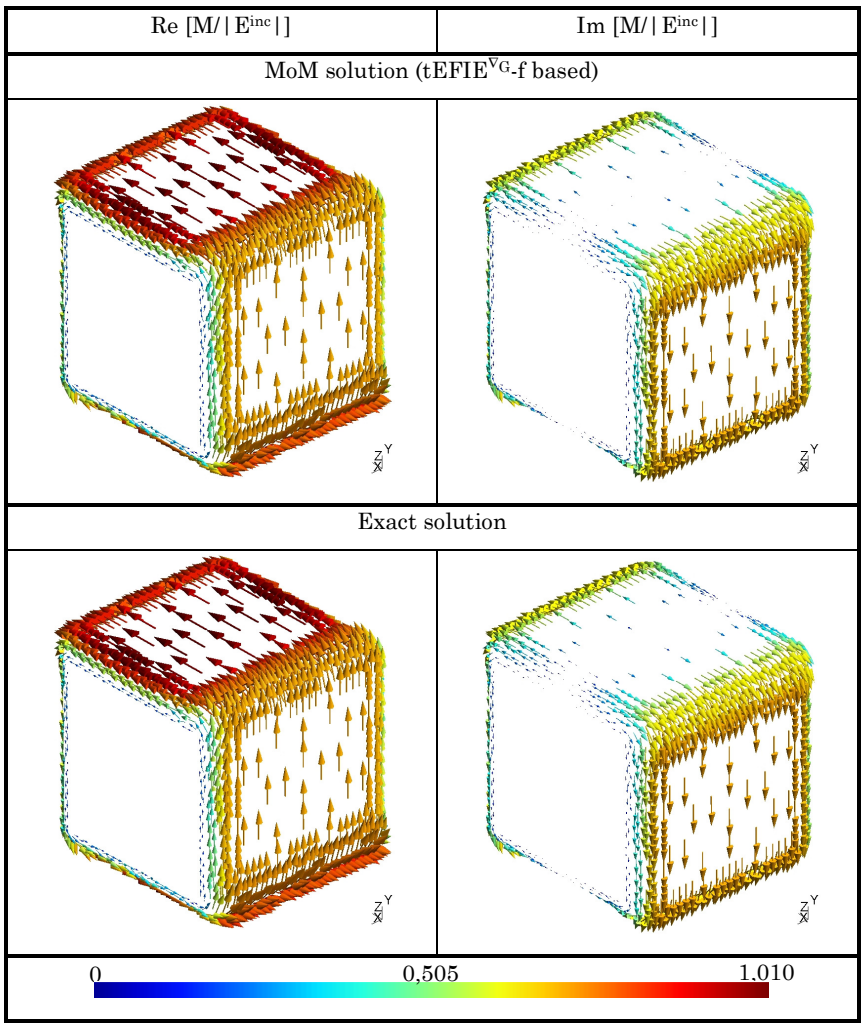

Figure 89 : $M/|E^{inc}|$ on the $\varepsilon_r = 1$ rounded cube

Visually, there is no difference between the MoM and the exact solution. A quantitative comparison is given in Figure 90 (p.165).

Two solutions have been obtained with the PMCHWT-f-f, based on the tMFIE-f and either tEFIE$^{\nabla f}$-f or tEFIE$^{\nabla G}$-f. The following integration scheme has been used :

	Self Term	$R_{min} < \lambda/100$	$R_{min} \in [\lambda/100; \lambda/10]$	$R_{min} > \lambda/10$	V
Inner	3		3	3	--
Outer	16		16	3	3

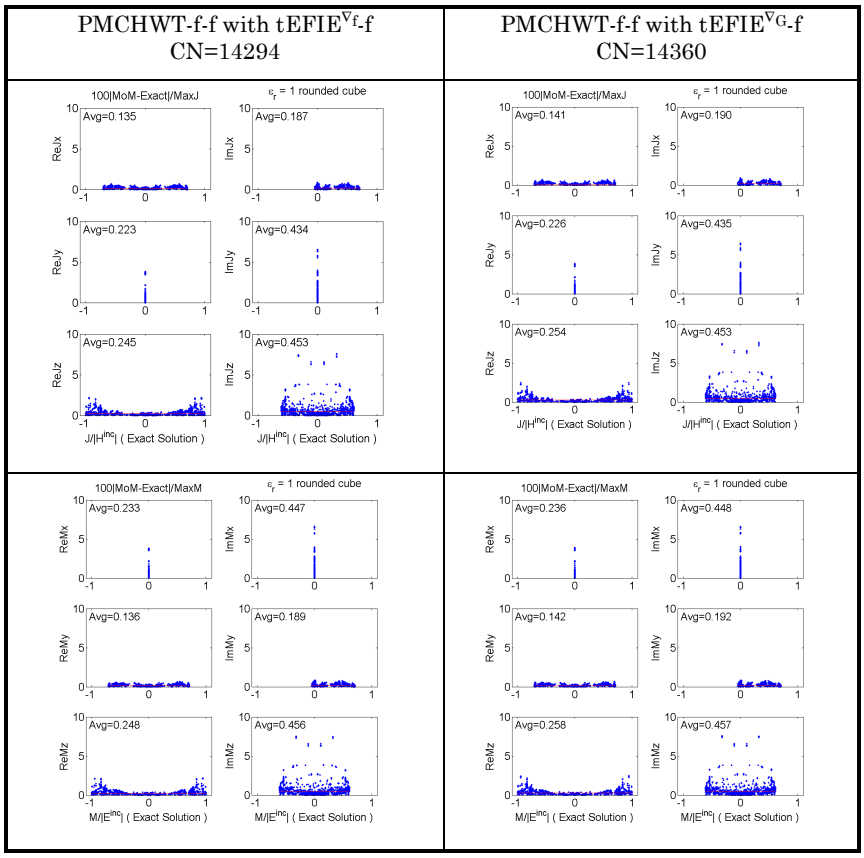

Figure 90 : Relative error for the $\varepsilon_r = 1$ rounded cube

The observed relative errors are comparable to those already reported for the $\varepsilon_r = 1$ sphere in Table 17 (p.153). Extrapolating the conclusions of Table 18 (p.154), we can expect similar relative errors for the $\varepsilon_r = 2$ and $\varepsilon_r = 4$ rounded cube, for which no exact solution is available. The condition numbers are similar to those already reported in Table 19 (p.155) for the sphere meshed with a mix of 1748 regular and stretched triangles.

6.4.2 PEC rounded cube

No analytical solution is available for the PEC rounded cube. But we can construct and compare two independent numerical solutions, for example with the tEFIE$^{\nabla G}$-f and the tMFIE-nxf.

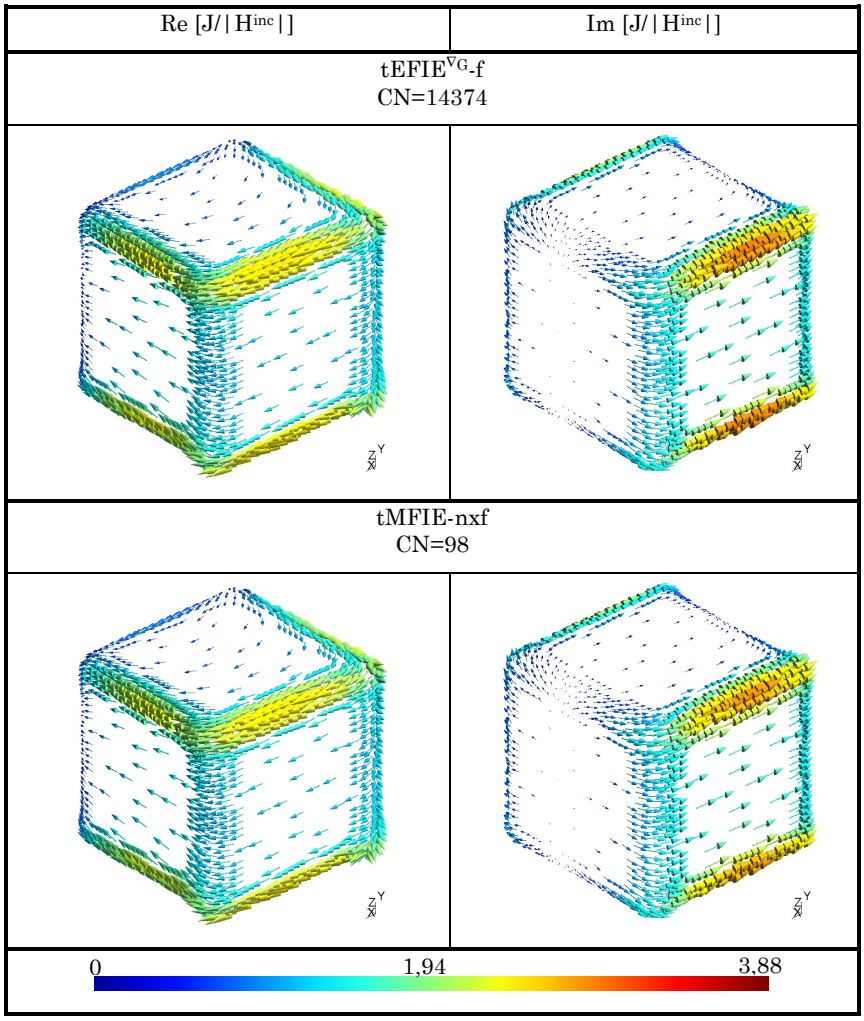

Figure 91 : tEFIE$^{\nabla G}$-f and tMFIE-nxf solutions (PEC rounded cube)

As already observed in §6.2.2, the condition number of the tMFIE-nxf is significantly lower than the tEFIE$^{\nabla G}$-f one.

The following integration scheme has been used :

	Self Term	$R_{min} < \lambda/100$	$R_{min} \in [\lambda/100; \lambda/10]$	$R_{min} > \lambda/10$	V
Inner	3		3	3	--
Outer	16		16	3	3

We have seen in §6.2 with the PEC sphere that both integro-differential equations yield very accurate solutions, when compared to the exact Mie solution, and both are very similar when compared against each other (see Figure 76, p.149). As both integro-differential equations also produce similar solutions for the rounded cube, and as both solutions are sound from a physical point of view, we can reasonably assume that these two MoM solutions are accurate within their differences.

As can be seen in Figure 92, the difference between tEFIE$^{\nabla G}$-f and tMFIE-nxf is somewhat larger for the rounded cube than for the sphere. This is especially true for the largest current densities, namely those flowing along the horizontal rounded edges. A closer look at Figure 91 (p.166) reveals that these highest current densities are somewhat intenser in the tEFIE$^{\nabla G}$-f solution. This behavior will be amplified with the upcoming examples, where sharp edges will be present.

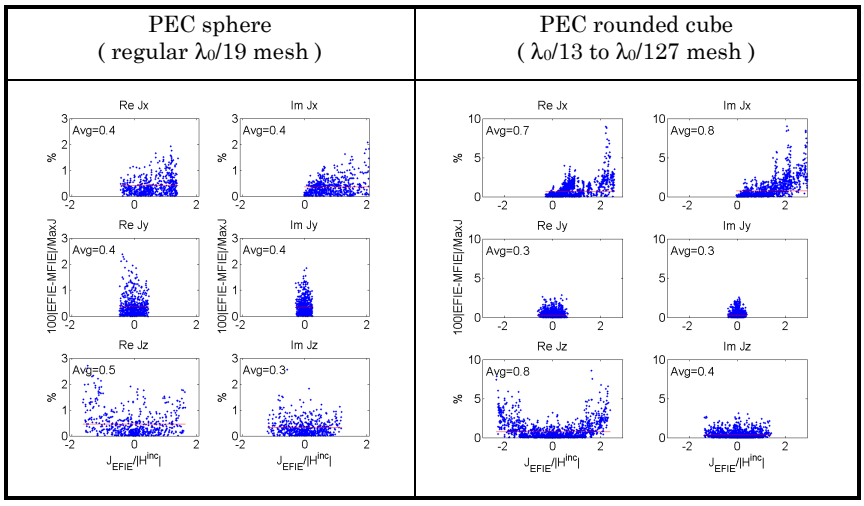

Figure 92 : Comparison tEFIE$^{\nabla G}$-f and tMFIE-nxf for the PEC sphere and for the rounded cube

6.5 Cube : regular meshes

The cube with rounded edges is modified to become a cube with sharp edges. To allow direct comparisons with the cube with rounded edges and corners, the dimensions of the cube remain identical ($\lambda_0/4 \times \lambda_0/4 \times \lambda_0/4$) as well as the incoming plane wave (travelling from *-Z* to *+Z*, polarized along *X*, the incoming electric field has unitary amplitude $|E^{inc}| = 1$ V/m and zero phase at the centre of the cube).

We analyze the solutions obtained for two uniform meshes, with characteristic length $\lambda_0/11$ and $\lambda_0/25$, where the characteristic length is the largest side of any triangle in the mesh.

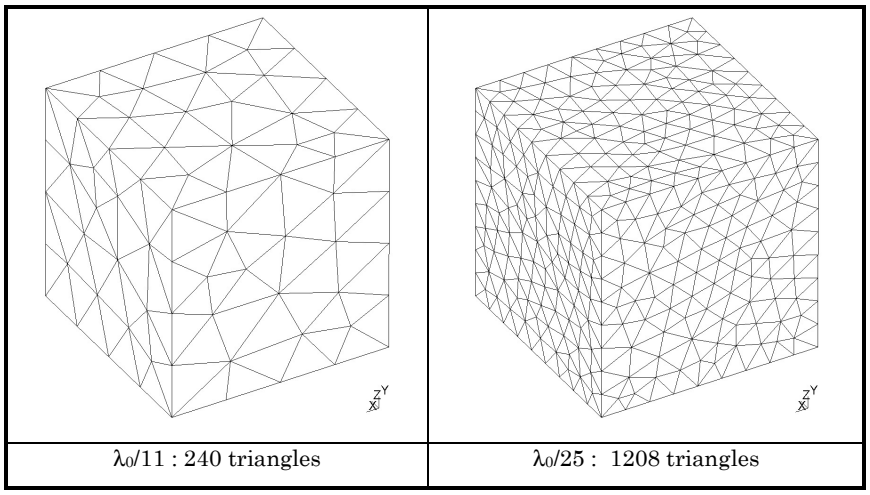

$\lambda_0/11$: 240 triangles	$\lambda_0/25$: 1208 triangles

Figure 93 : Two uniform meshes for a cube with side $\lambda_0/4$

6.5.1 Dielectric cube

In Figure 94 (p.169) and Figure 95 (p.170) and we superimpose the MoM and Exact solutions for $\varepsilon_r = 1$, for both the electric and magnetic current density. This qualitative comparison shows only distinguishable differences close to the vertical edges. The quantitative comparison reveals that :

- The maximum relative error is in the order of 3 to 6% while the average relative errors are around or below 1%
- The mesh refinement by a factor somewhat larger than 2 induces a reduction in both the maximum and average relative errors by a similar factor.

The condition numbers are respectively 167 and 1014 for the $\lambda_0/11$ and $\lambda_0/25$ meshes.

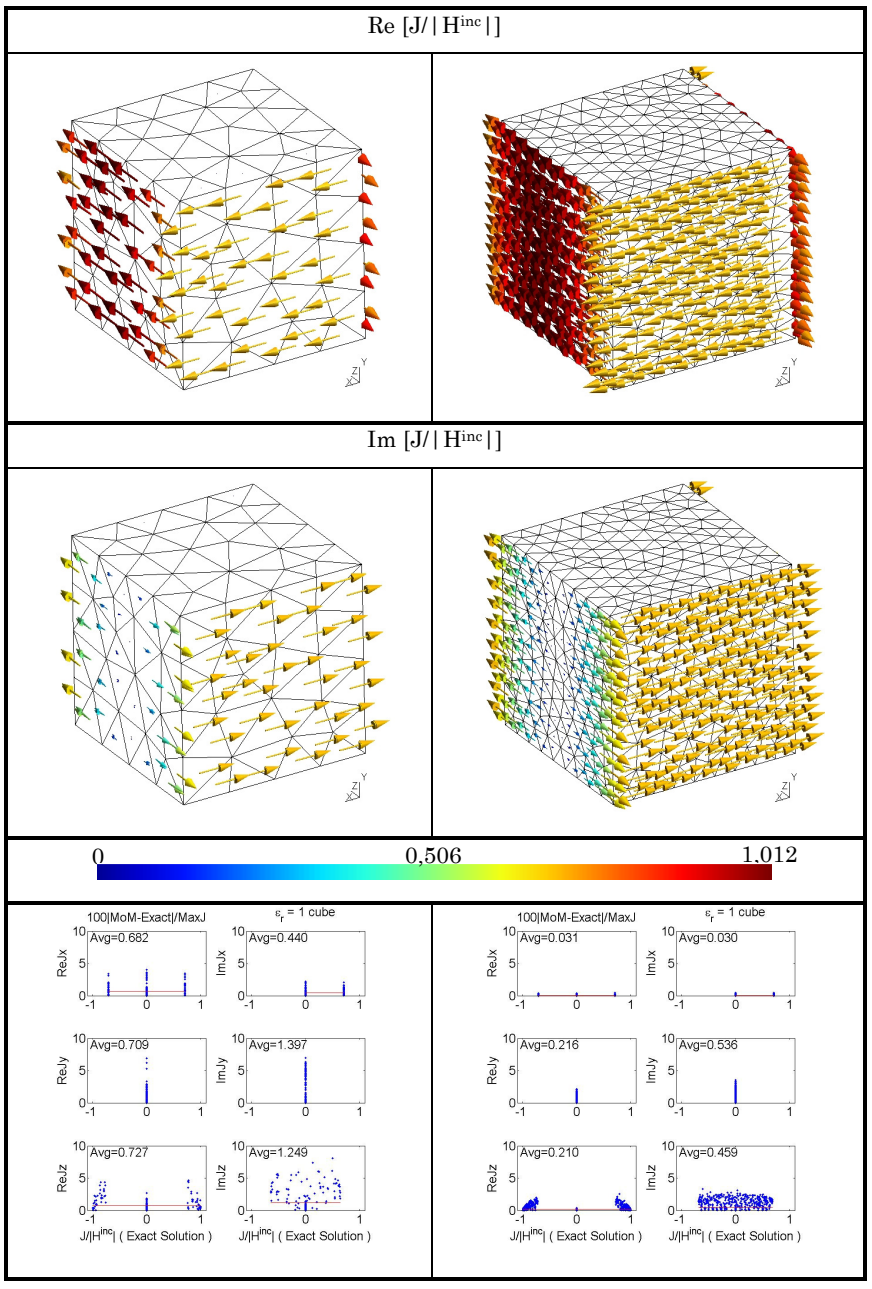

Figure 94 : J current density on a $\varepsilon_r = 1$ cube

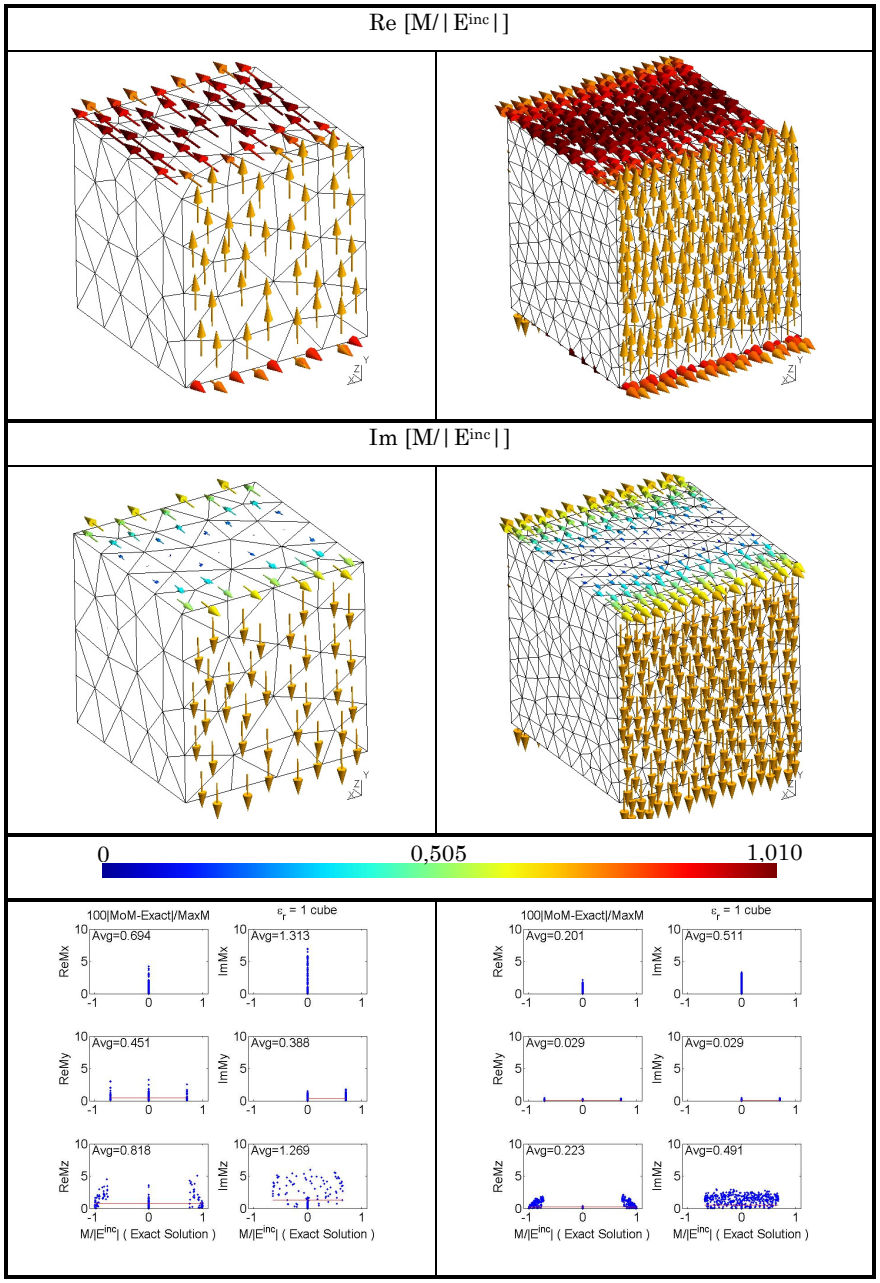

Figure 95 : M current density on a $\varepsilon_r = 1$ cube

The above solutions have been obtained with the PMCHWT-f-f, combining the tEFIE$^{\nabla G}$-f and the tMFIE-f.

The following integration scheme has been used :

	Self Term	$R_{min} < \lambda/100$	$R_{min} \in [\lambda/100; \lambda/10]$	$R_{min} > \lambda/10$	V
Inner	3		3	3	--
Outer	16		3	1	3

The average relative errors obtained when reducing or increasing the number of nodes in the outer integral when $R_{min} < \lambda/100$ are listed in Table 20, and illustrated in Figure 96 for the highest surface current densities components. The advantage of the 16 nodes quadrature is visible, though very limited.

Table 20 : Average relative error on the $\lambda_0/11$ cube ($\varepsilon_r = 1$), PMCHWT-f-f

	Re			Im			Re			Im		
	J_x	J_y	J_z	J_x	J_y	J_z	J_x	J_y	J_z	J_x	J_y	J_z
1	1,58	1,13	3,54	1,86	1,57	2,13	1,39	1,56	3,35	1,69	1,71	2,11
3	0,72	0,71	1,79	0,53	1,42	1,48	0,70	0,60	1,74	1,34	0,53	1,63
6	0,76	0,70	1,12	0,46	1,40	1,34	0,69	0,53	1,08	1,31	0,41	1,39
7	0,74	0,69	1,00	0,45	1,40	1,32	0,68	0,51	0,97	1,30	0,39	1,36
12	0,71	0,69	0,87	0,43	1,39	1,29	0,68	0,48	0,87	1,30	0,38	1,33
16	0,68	0,71	0,73	0,44	1,40	1,25	0,69	0,45	0,82	1,31	0,39	1,27
19	0,69	0,70	0,77	0,43	1,39	1,27	0,68	0,46	0,82	1,31	0,38	1,30
25	0,68	0,70	0,74	0,43	1,40	1,26	0,69	0,45	0,80	1,31	0,38	1,28
42	0,68	0,71	0,73	0,44	1,40	1,25	0,70	0,45	0,82	1,31	0,39	1,27
61	0,68	0,71	0,73	0,43	1,40	1,25	0,69	0,45	0,81	1,31	0,38	1,28
73	0,68	0,71	0,73	0,43	1,40	1,25	0,69	0,45	0,81	1,31	0,39	1,27

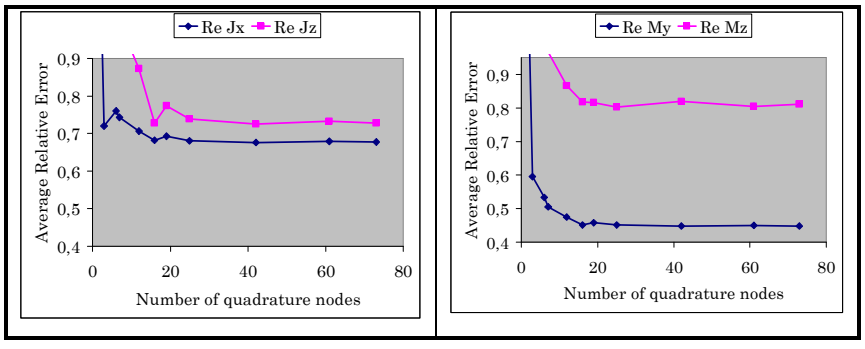

Figure 96 : Relative error in function of the number of quadrature nodes

6.5.2 PEC cube

There is no exact solution for the scattering by a PEC cube. As for the rounded cube (§6.4.2), we assess the accuracy of the MoM by comparing the tEFIE$^{\nabla G}$-f and tMFIE-nxf solutions. In Figure 97 and Figure 98 we show the real and imaginary part of the electric current density for two uniform meshes with characteristic length $h = \lambda_0/11$ and $h = \lambda_0/25$.

EFIE and MFIE resonances are excluded as the cube side is smaller than $0{,}7071\,\lambda_0$ (see §5.2.3). The condition number (CN) is much lower for the tMFIE-nxf, and nearly independent of h. It increases much faster than $1/h$ for the tEFIE$^{\nabla G}$-f.

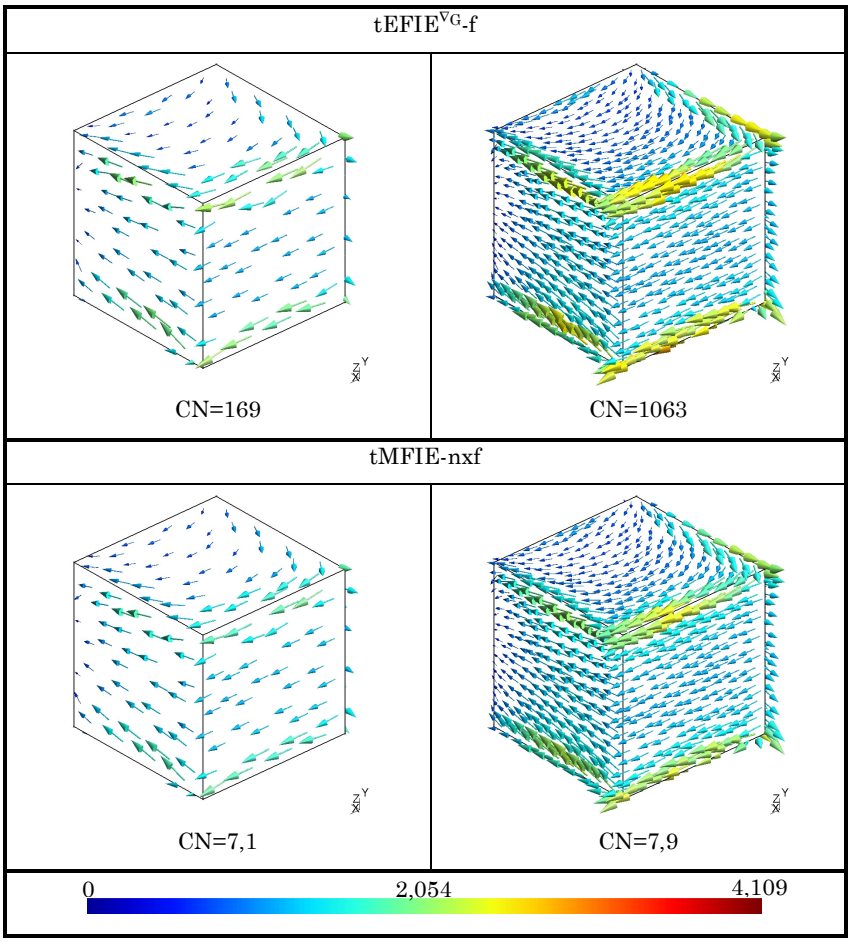

Figure 97 : Re[J/|H^{inc}|] with tEFIE$^{\nabla G}$-f and tMFIE-nxf (PEC cube)

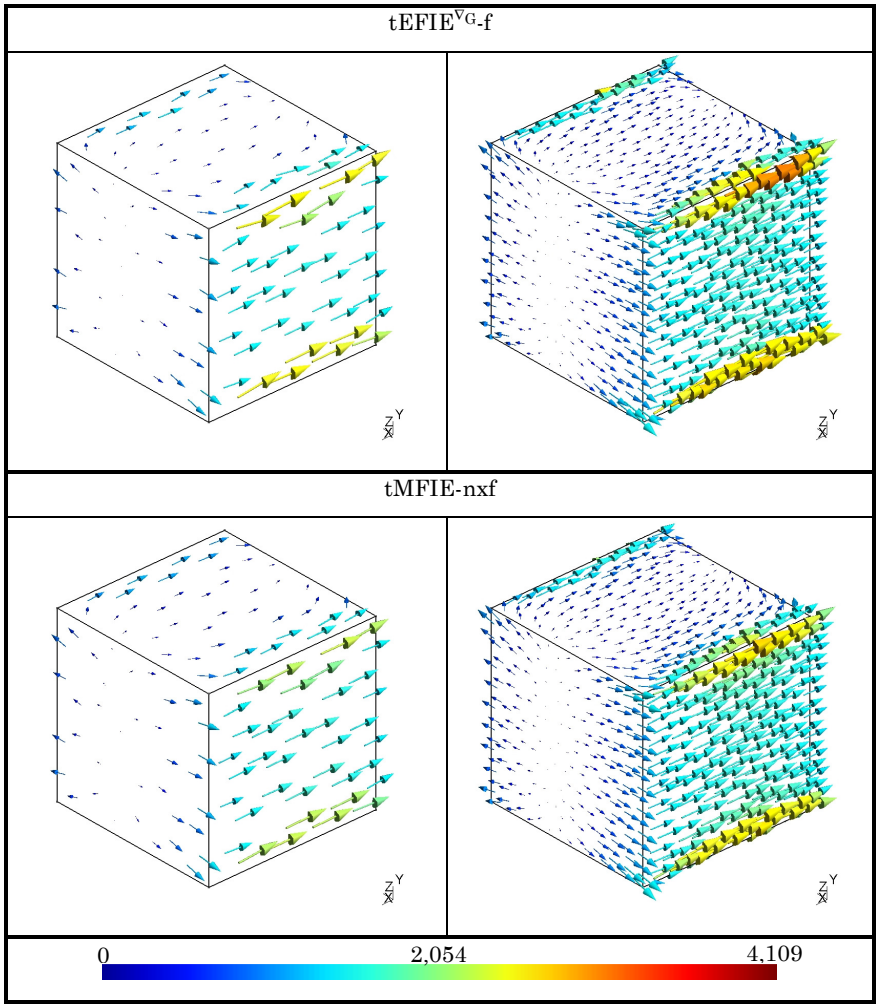

Figure 98 : Im[J/|H^{inc}|] with tEFIE$^{\nabla G}$-f and tMFIE-nxf (PEC cube)

To allow direct visual comparison, every current density patterns in Figure 97 and Figure 98 have been scaled to 4,109. We give in Table 21 the actual maximum electric current densities for every case :

Table 21 : Max [J /|H^{inc}|]

	tEFIE$^{\nabla G}$-f	tMFIE-nxf
λ_0/11 mesh	3,306	2,930
λ_0/25 mesh	4,109	3,687

In Figure 99 we present a summary of the differences between tEFIE$^{\nabla G}$-f and tMFIE-nxf solutions for the PEC sphere, the PEC rounded cube and the two PEC cubes analyzed in §6.2, 6.4.2 and 6.5.2.

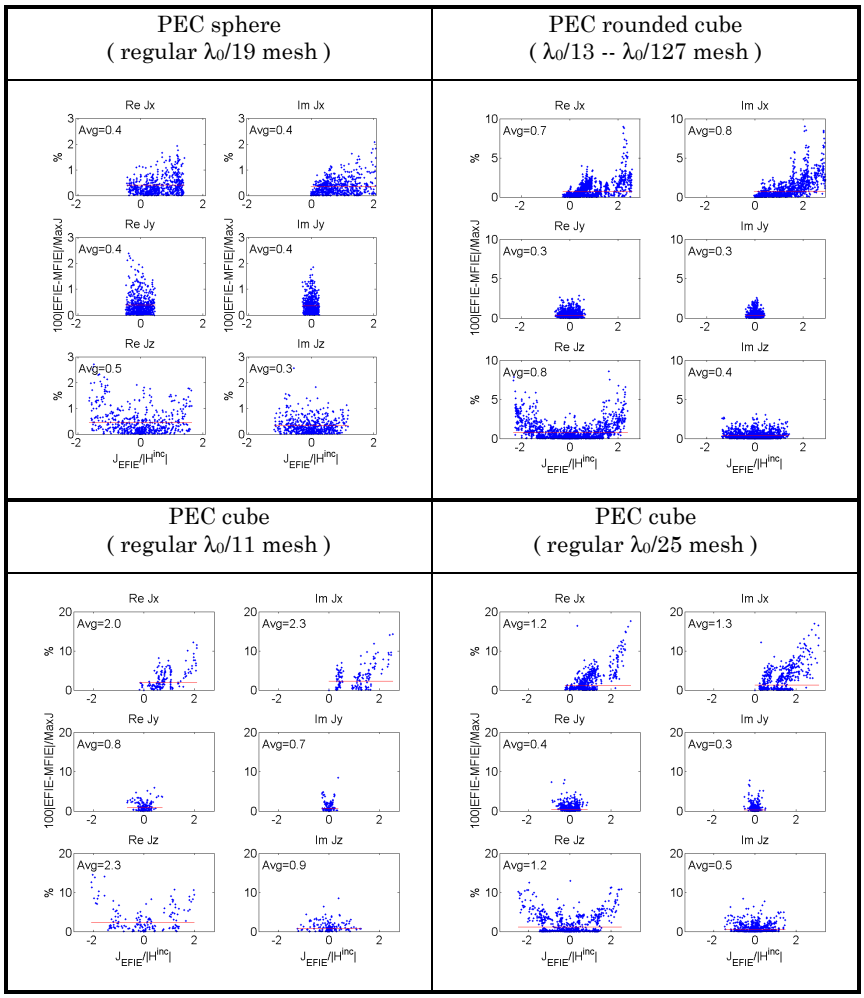

Figure 99 : Comparison tEFIE$^{\nabla G}$-f and tMFIE-nxf for several PEC bodies

With the PEC rounded cube, the largest differences between tEFIE$^{\nabla G}$-f and tMFIE-nxf were found to be due to the high current densities flowing close to the horizontal edges. This pattern is further enhanced with the PEC cube, and clearly visible in Figure 97 (p.172) and Figure 98 (p.173).

6.6 Cube : Log-distributed meshes

To better capture the high current densities flowing along the horizontal edges, we introduce log-distributed meshes. As can be seen in Figure 100 the triangles of such a mesh are constrained in a multi level square grid. In a local *XY* coordinate system centered at every face the coordinates of the *X* and *Y* straight lines forming the three-level grid in Figure 100 are [-1 -0,99 -0,9 +0,9 +0,99 +1]*C/2* where *C* is the length of the side of the cube. This mesh is called log-distributed as the coordinates of the grid follow a logarithmic distribution and not a linear one. This distribution allows to compute the current densities very close to the edges and corners ($\lambda_0/800$) with only 1238 triangles at the expense of reasonably stretched triangles. In comparison, meshing this $C = \lambda_0/4$ cube with only right-angled "$\lambda_0/800$" triangles would require $6x2x200^2$=480.000 triangles. The largest triangles, in the middle of the flat faces, have edges not exceeding $\lambda_0/13$, while the smallest edges of the triangles located in the eight corners are as small as $\lambda_0/1131$. The triangles adjacent to these smallest triangles as well as those defined all along the 12 cube edges are stretched with a largest to smallest edge ratio of 10:1.

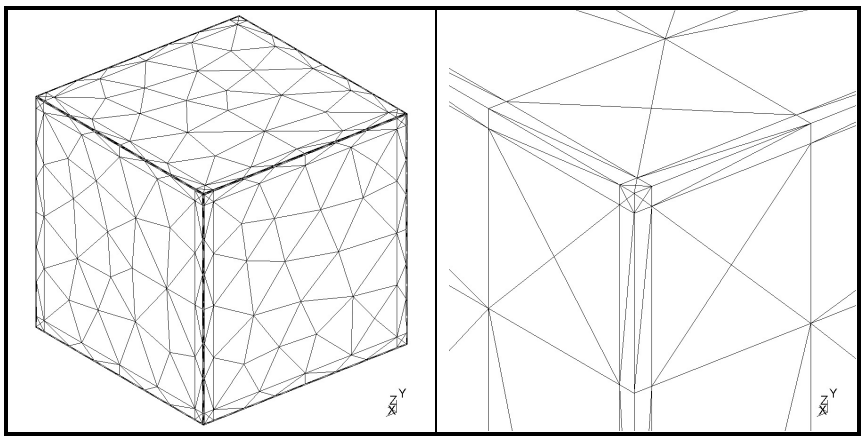

Figure 100 : Log-distributed mesh of the $\lambda_0/4$ cube

6.6.1 Dielectric cube : $\varepsilon_r = 1$

In this paragraph we quantify the accuracy of the MoM solution with a log-distributed mesh by comparing it to the exact solution in the case $\varepsilon_r = 1$. Two solutions are obtained with PMCHWT-f-f, using tMFIE-f and either tEFIE$^{\nabla_f}$-f or tEFIE$^{\nabla_G}$-f.

The following integration scheme has been used :

	Self Term	$R_{min} < \lambda/100$	$R_{min} \in [\lambda/100; \lambda/10]$	$R_{min} > \lambda/10$	V
Inner	3		3	3	--
Outer	16		16	3	3

In Figure 101 (p.177) and Figure 102 (p.178) the same amplitude and color scaling is used for the Exact and the MoM solutions, to allow direct visual comparison between the current densities.

We give in Table 22 the actual maximum electric current densities for every case :

Table 22 : Max [J /| H^{inc} |] and Max [M /| E^{inc} |]

		tEFIE$^{\nabla_f}$-f	tEFIE$^{\nabla_G}$-f
Max [J /| H^{inc} |]	$\varepsilon_r = 1$	1,101	1,052
	$\varepsilon_r = 2$	1,252	1,223
Max [M /| E^{inc} |]	$\varepsilon_r = 1$	1,10	1,05
	$\varepsilon_r = 2$	1,24	1,21

The exact solution in the case $\varepsilon_r = 1$ gives maximum normalized current densities J/| H^{inc} | and M/| E^{inc} | equal to 1 (see §6.1.4). The MoM solutions in this case overestimate these maximum current densities by 5 or 10%.

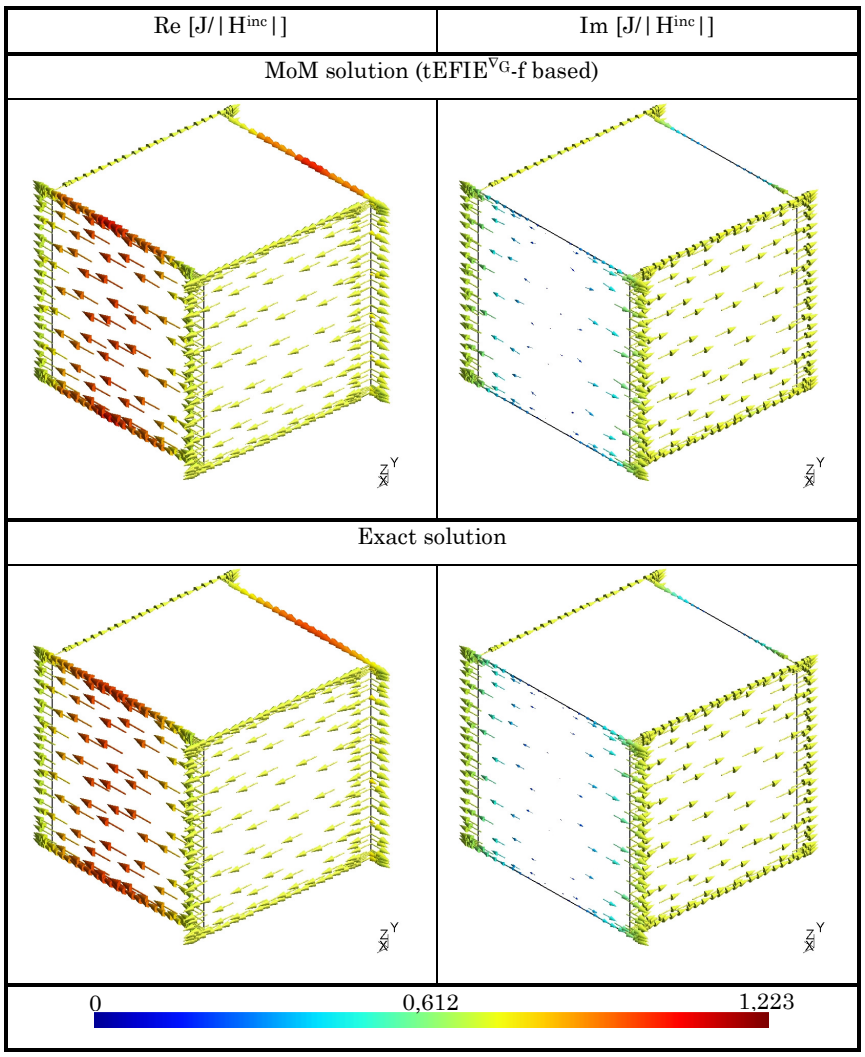

Figure 101 : $J/|H^{inc}|$ on the $\varepsilon_r = 1$ cube

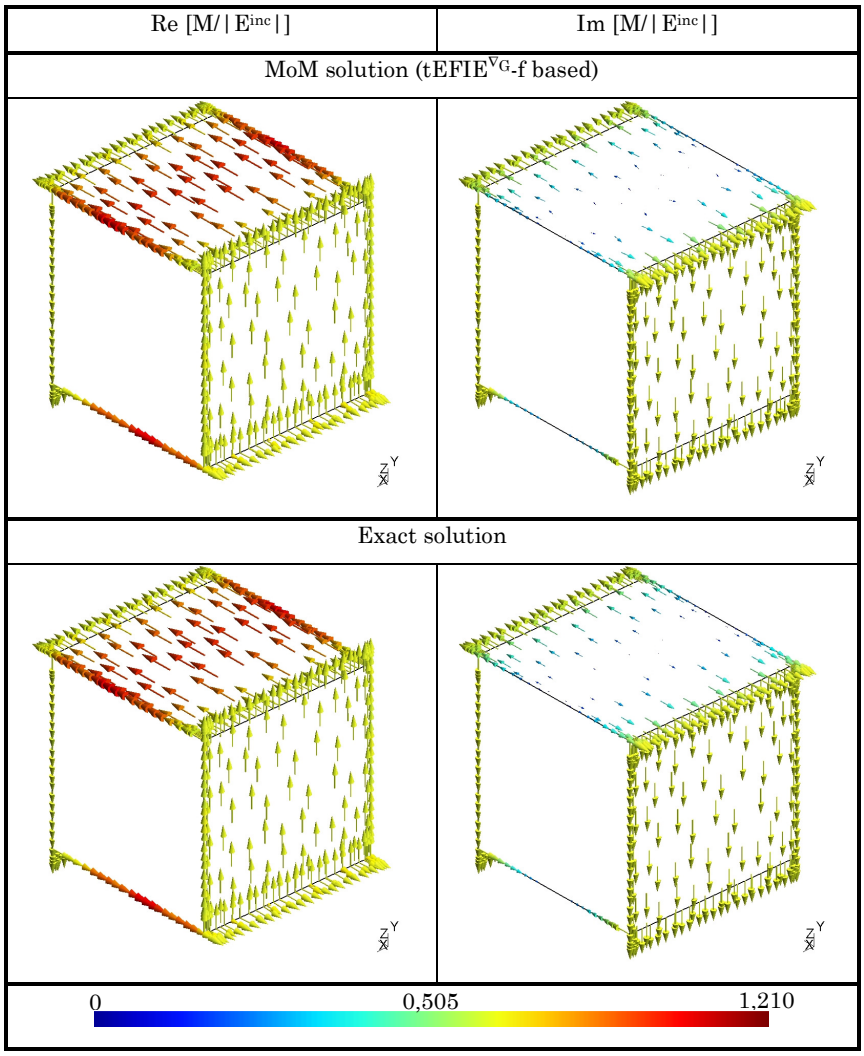

Figure 102 : $M/|E^{inc}|$ on the $\varepsilon_r = 1$ cube

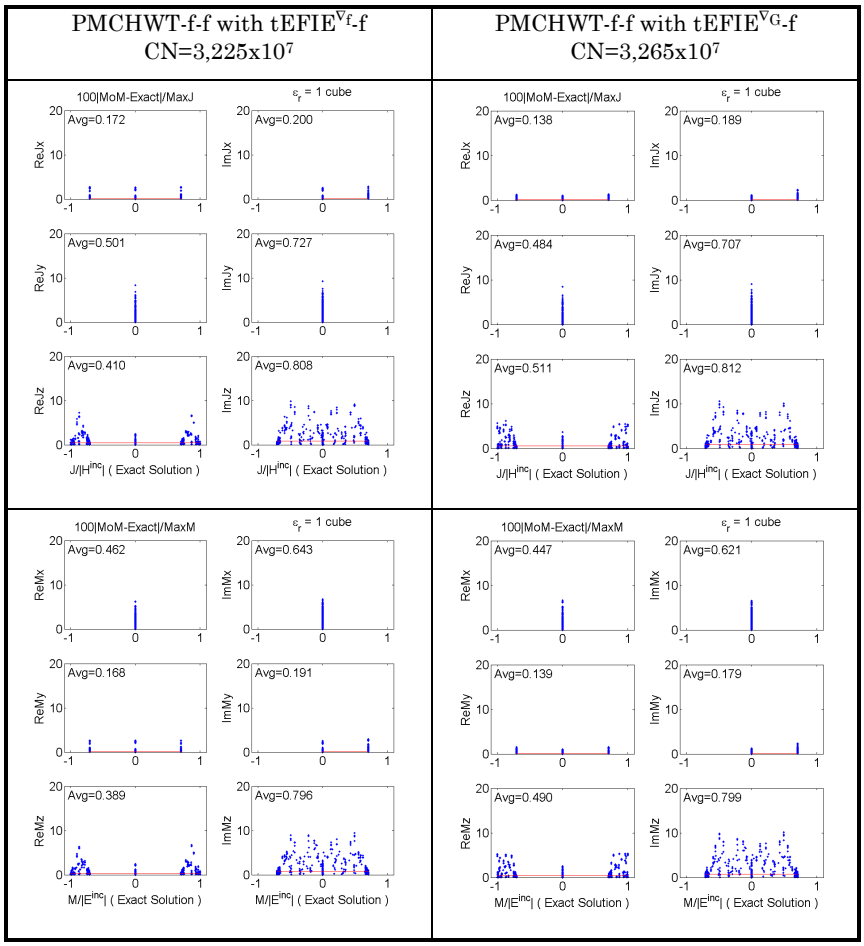

Figure 103 : Relative error for the $\varepsilon_r = 1$ cube

The electric current density *J* obtained with the MoM differs from the exact solution by as much as 12%. In comparison, the relative error was only 4% in the case of the rounded cube (Figure 90, p.165) and 3 to 6% for the uniformly meshed cube (Figure 94, p.169).

The magnetic current density *M* obtained with the MoM differs from the exact solution by at most 14%. In comparison, the relative error was only 4% in the case of the cube with rounded edges and corners (Figure 90, p.165) and 3 to 6% for the uniformly meshed cube (Figure 95, p.170).

The PMCHWT-f-f solution based on the tEFIE$^{\nabla f}$-f and on the tEFIE$^{\nabla G}$-f give comparable solutions with very similar relative errors. Also the condition numbers are quite similar, and both very high as compared to the homogeneous mesh of §6.5.1.

6.6.2 Dielectric cube : $\varepsilon_r = 2$

There is no analytical solution for the dielectric cube, and we do not have two independent MoM solutions that we can compare against each other, such as the tEFIE-f and tMFIE-nxf for the PEC cube. In Figure 104 we present the solution obtained with PMCHWT-f-f (tEFIE$^{\nabla_f}$-f+tMFIE-f) for the $\lambda_0/4$ cube with $\varepsilon_r = 2$.

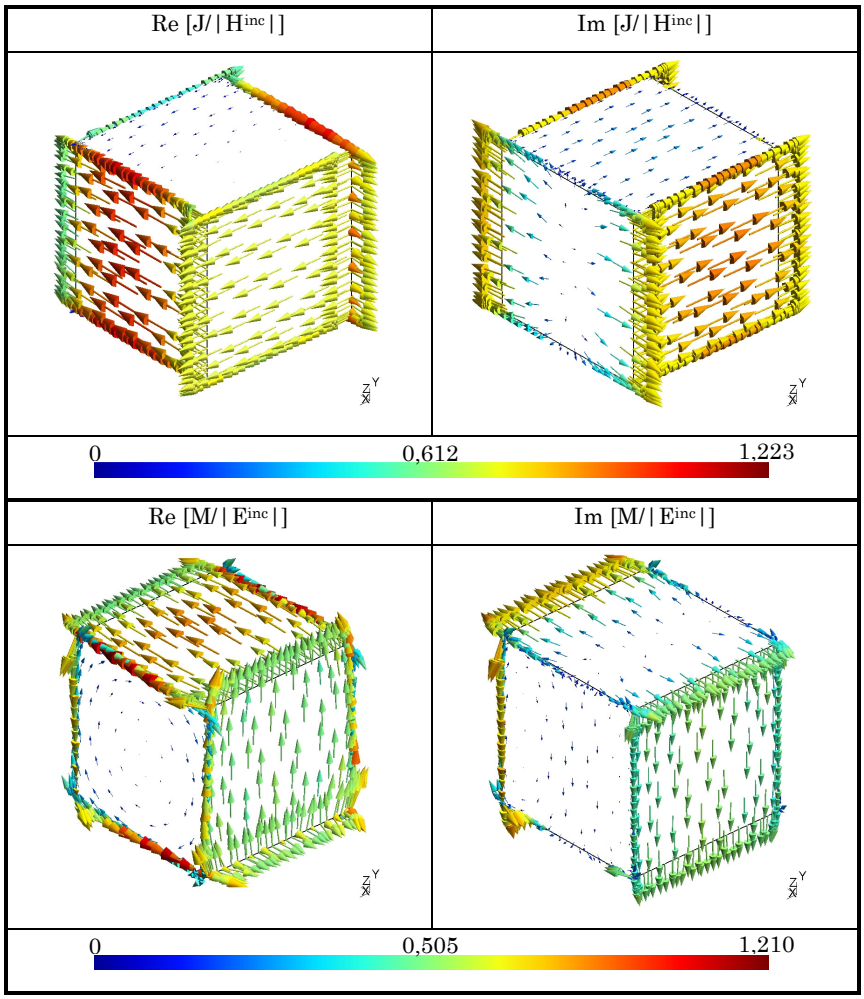

Figure 104 : J and M current density on a $\lambda_0/4$ cube with $\varepsilon_r = 2$

We expect the $\varepsilon_r = 2$ solution to be a smooth evolution away from the $\varepsilon_r = 1$ solution. This is the case if we compare Figure 101 (p.177) and Figure 102 (p.178) to Figure 104 (p.180). Remember that we have scaled the current densities identically for the $\varepsilon_r = 1$ and $\varepsilon_r = 2$ cases in all these figures; the actual maximum

amplitudes, reported in Table 22 (p.176), show that the maximum current densities when $\varepsilon_r = 2$ are 20 to 25% higher than when $\varepsilon_r = 1$.

A closer look to the upper front corner (*C/2; C/2; -C/2*) and surrounding edges shows a surprising behavior. In Figure 105 we see that the magnetic current density loops around the corner. This creates a sheer discontinuity in the tangential component of $\bar{M}$ across the edges : near the corner the magnetic current density bends to flow in opposite directions on every face. Another sheer behavior can be observed close to corner (*C/2; C/2; C/2*) with the electric current density.

To understand these sheer behaviors, one has to think of the exact solution for a $\varepsilon_r = 1$ cube illuminated by a plane wave where the incident electric field $\bar{E}_{inc}$ is neither normal nor parallel to any of the faces and compute the magnetic current density $\bar{M} = \bar{n} \times \bar{E}_{inc}$ on every face around a corner. Due to the abrupt change of orientation of the normals to the faces, the same sheer behavior is observed for $\bar{M}$.

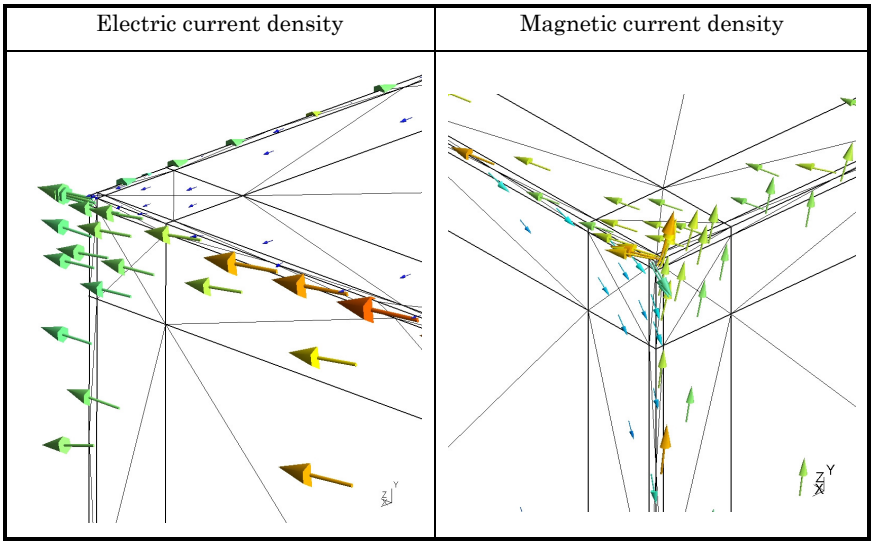

Figure 105 : Sheer current density on the edges of a dielectric

It is possible to model these sheer tangential discontinuities with RWG functions, but it would not be possible with curl conforming functions (see §2.2.5).

The condition number is $3{,}216 \times 10^7$, slightly lower than the $\varepsilon_r = 1$ case in §6.6.1.

6.6.3 PEC cube

Again we present a comparison between the tEFIE-f and tMFIE-nxf solutions, as previously for the PEC sphere and (rounded) cube. The following integration scheme has been used :

	Self Term	$R_{min} < \lambda/100$	$R_{min} \in [\lambda/100; \lambda/10]$	$R_{min} > \lambda/10$	V
Inner	3		3	3	--
Outer	16 or 42		16 or 42	3	3

To allow direct visual comparison, all current density patterns in Figure 107 (p.183) have been scaled to 10,48. We give in Table 23 the actual maximum electric current densities for every case :

Table 23 : Max [J / | H^{inc} |]

tEFIE$^{\nabla G}$-f	10,48
tEFIE$^{\nabla f}$-f	10,41
tMFIE-nxf	9,24

A quantitative comparison between both tEFIE-f solutions shows in Figure 106 that they differ by less than a fraction of a percent in the average, but by up to 30% for some current densities. A closer look to the data reveals that these high differences are located near the eight corners, as can be seen in Figure 107 (p.183). Using 42 nodes instead of 16 in the tEFIE$^{\nabla G}$-f brings the maximum differences between both tEFIE-f down below 10%.

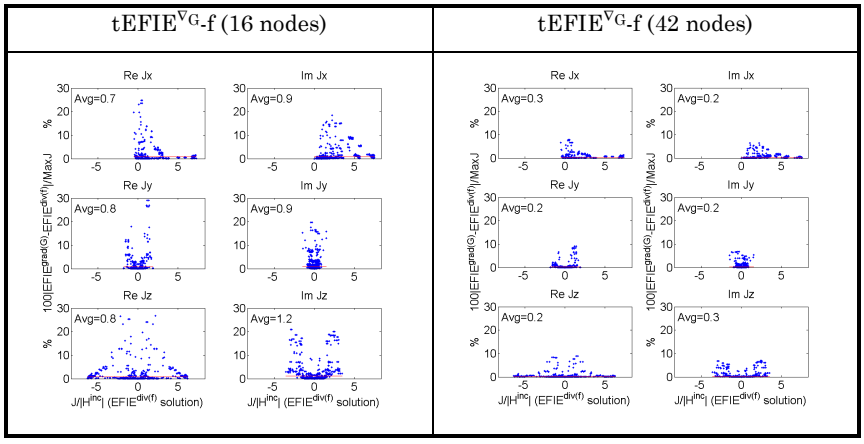

Figure 106 : Comparison tEFIE$^{\nabla f}$-f and tEFIE$^{\nabla G}$-f

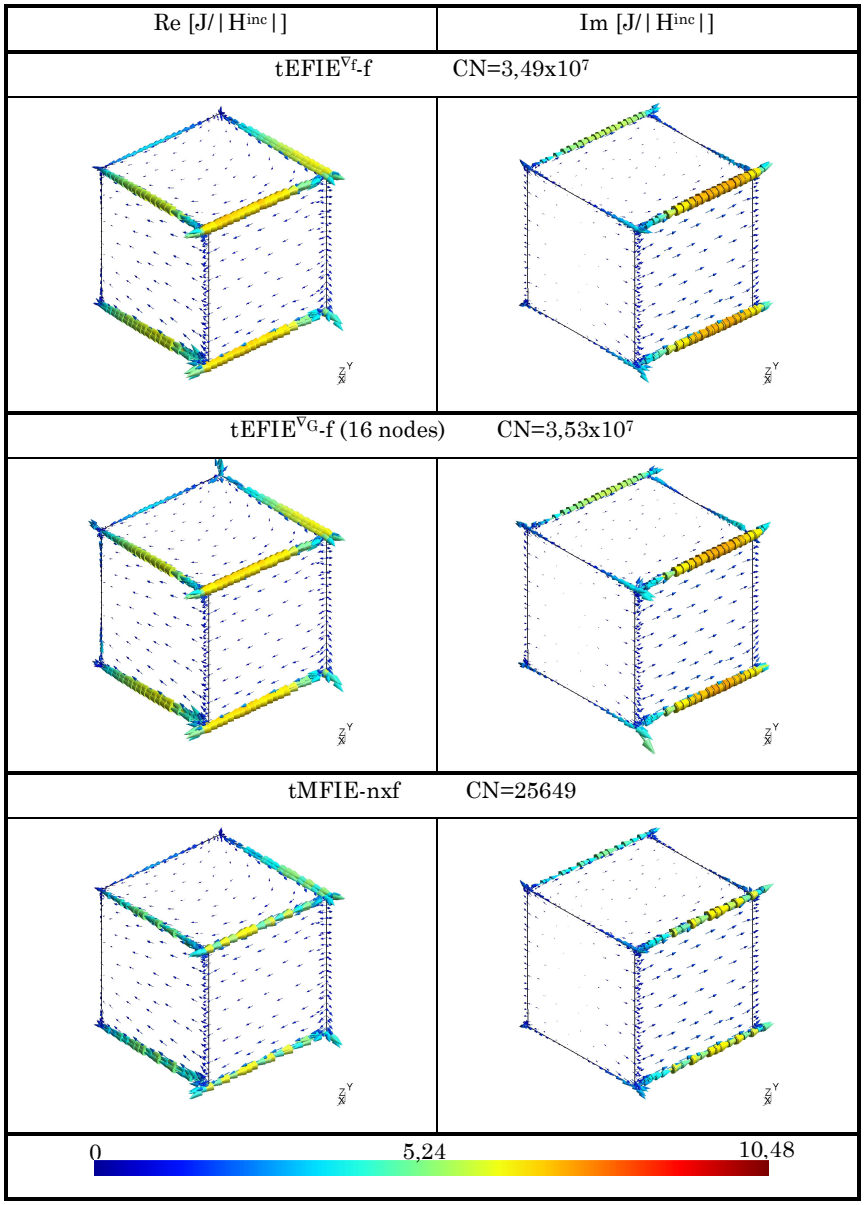

Figure 107 : tEFIE-f and tMFIE-nxf solutions for the PEC cube

The condition numbers are quasi identical for the tEFIE$^{\nabla f}$-f and tEFIE$^{\nabla G}$-f, and 1300 times higher than the condition number of the tMFIE-nxf.

EFIE and MFIE resonances are excluded as the cube side is smaller than $0{,}7071\lambda_0$ (see §5.2.3).

A quantitative comparison between the tEFIE$^{\nabla f}$-f and the tMFIE-nxf solutions shows in Figure 108 that both solutions differ for the PEC cube with 3-levels log-distributed mesh by up to 35%. To ease direct comparisons, we reproduce the differences between tEFIE$^{\nabla f}$-f and tMFIE-nxf already measured for other PEC bodies (Figure 99, p.174). A closer look reveals that the electric current densities away from edges and corners obtained with the tEFIE$^{\nabla f}$-f and the tMFIE-nxf differ by 5 to 10% only. Only the current densities computed on the elongated triangles along the edges differ significantly, the tEFIE$^{\nabla f}$-f surface current density being always higher than the tMFIE-nxf surface current density. This cannot be attributed to the elongated triangles, as the same relative difference between tEFIE$^{\nabla f}$-f and tMFIE-nxf is observed with regularly shaped triangles (see Figure 99, p.174).

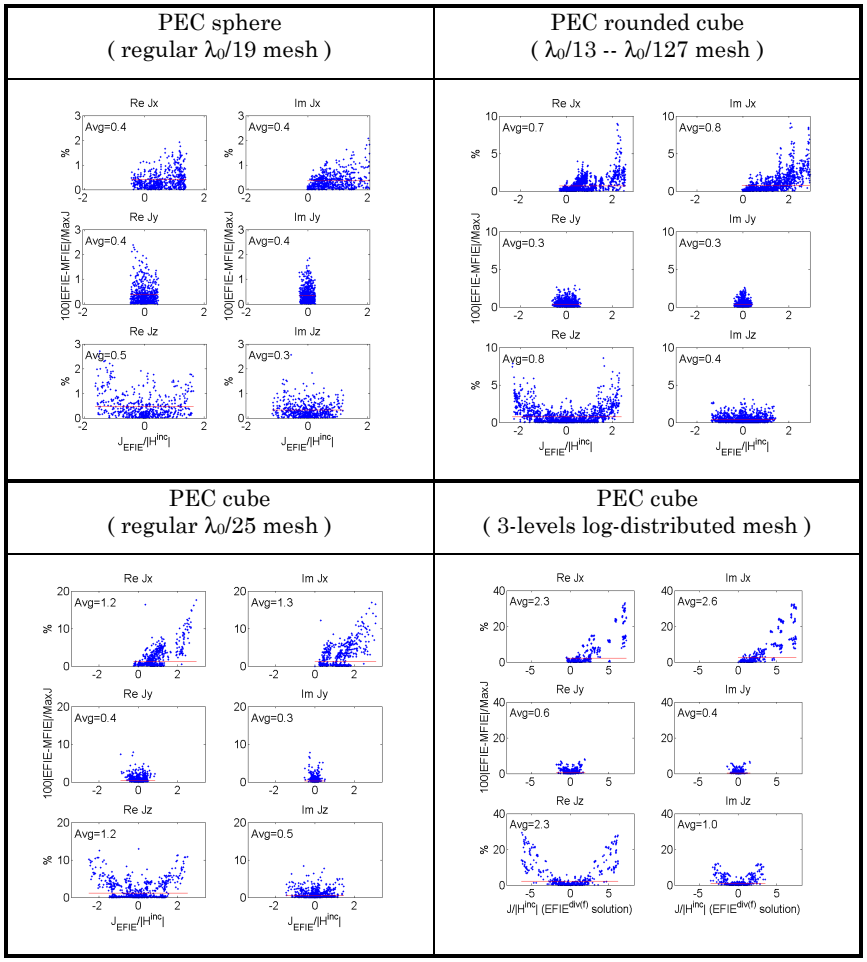

Figure 108 : Comparison tEFIE$^{\nabla f}$-f / tMFIE-nxf for several PEC bodies

A closer look to the electric current density near the edges and corners shows that there is no sheer behavior on the PEC cube, as observed on the dielectric cube (see Figure 105, p.181). We can also observe in Figure 109 that the tEFIE$^{\nabla_f}$-f and tMFIE-nxf current densities are visually quite similar except very close to the horizontal edges.

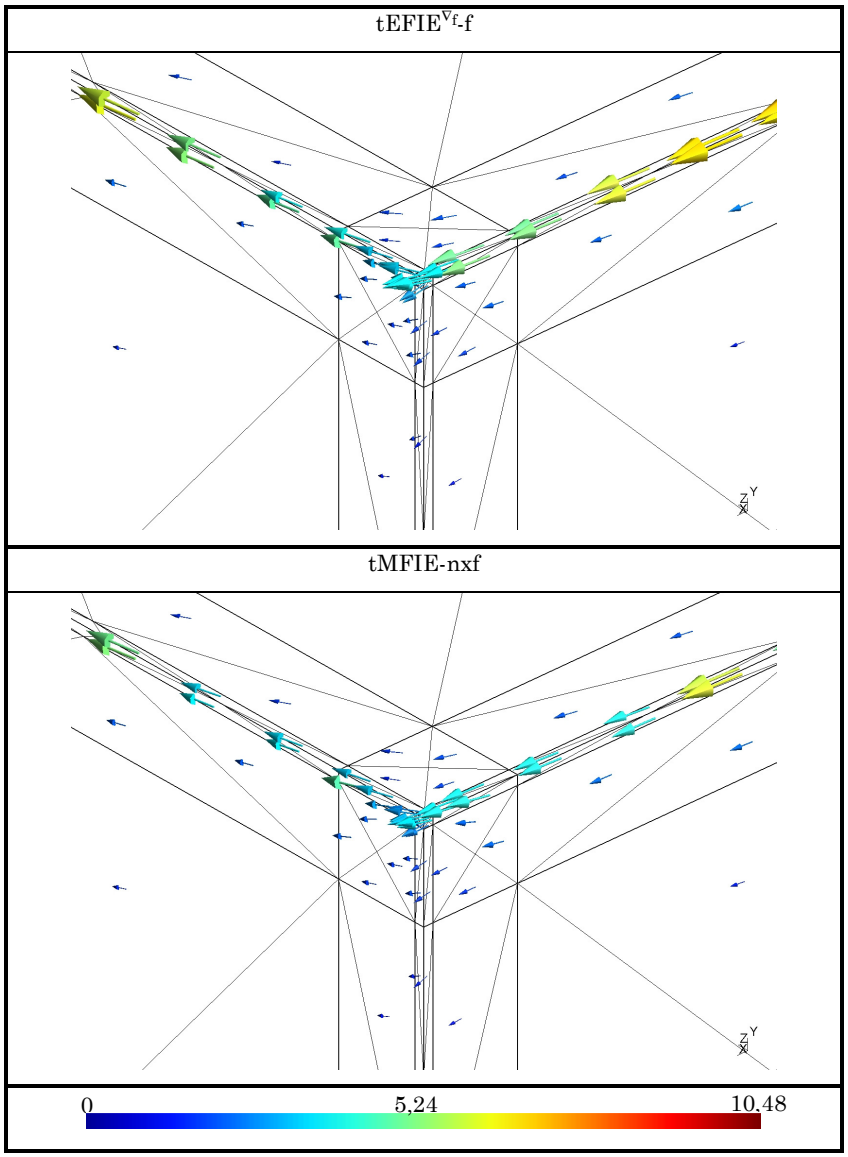

Figure 109 : J/|H^{inc}| close to edges and corners of a PEC cube

6.7 Thin plates : regular meshes

We reduce one dimension of the $\lambda_0/4$ cube analyzed in §§6.5 and 6.6 to obtain a plate of thickness $\lambda_0/100$. In this paragraph we analyze the solutions obtained with four "uniform" meshes with higher and higher densities. We will also use four different log-distributed meshes in §6.8.

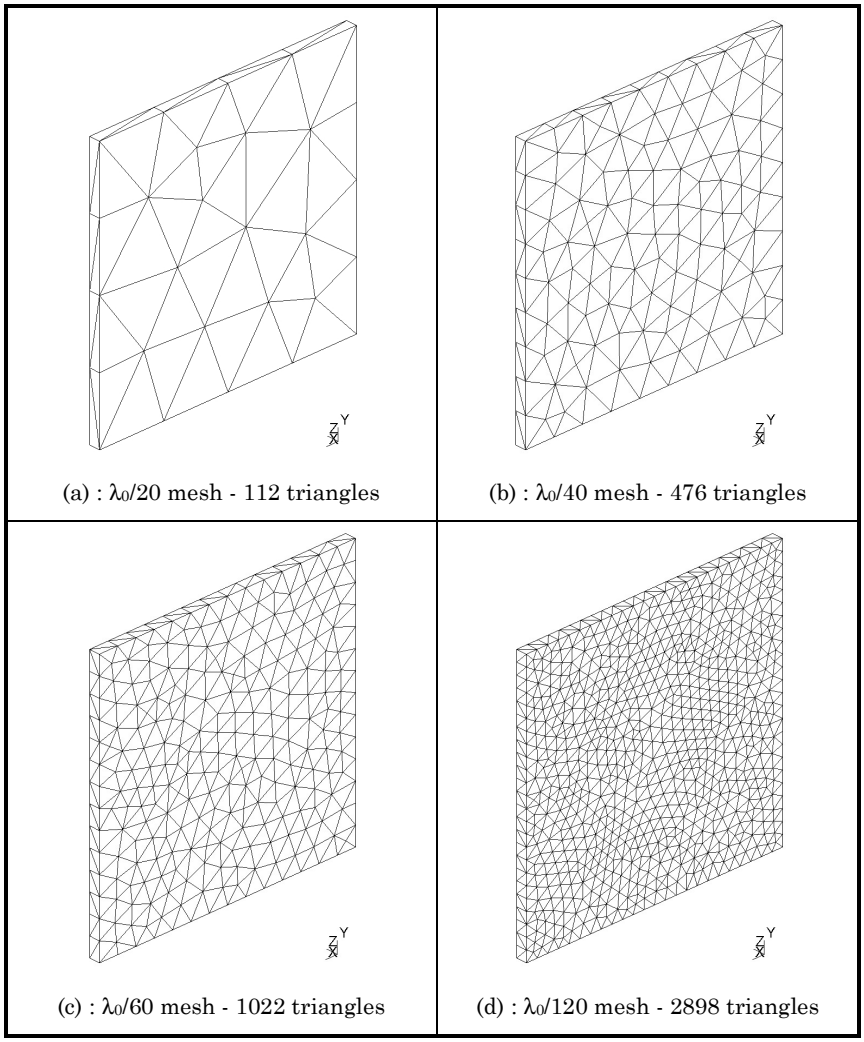

(a) : $\lambda_0/20$ mesh - 112 triangles

(b) : $\lambda_0/40$ mesh - 476 triangles

(c) : $\lambda_0/60$ mesh - 1022 triangles

(d) : $\lambda_0/120$ mesh - 2898 triangles

Figure 110 : Four meshes for a plate $\lambda_0/4$ x $\lambda_0/4$ x $\lambda_0/100$

The sizes of the meshes indicated in Figure 110 (p.186) correspond here to the maximum radius of the circumscribed circle enclosing any triangle.

The correspondence with the previous characteristic length definition, based on the largest triangle edge, is given in Table 24 :

Table 24 : mesh characteristic length

Radius of circumscribed circle	Largest edge
$\lambda_0/20$	$\lambda_0/12$
$\lambda_0/40$	$\lambda_0/26$
$\lambda_0/60$	$\lambda_0/40$
$\lambda_0/120$	$\lambda_0/69$

6.7.1 Dielectric plate : $\varepsilon_r = 1$

We first quantify the accuracy of the MoM solution by comparing it to the exact solution in the case $\varepsilon_r = 1$. The solutions are obtained with PMCHWT-f-f (tEFIE$^{\nabla f}$-f + tMFIE-f). The following integration scheme has been used :

	Self Term	$R_{min} < \lambda/100$	$R_{min} \in [\lambda/100; \lambda/10]$	$R_{min} > \lambda/10$	V
Inner	3		3	3	--
Outer	16		16	3	3

In Figure 112 (p.189), Figure 114 (p.191) and Figure 115 (p.192) the same amplitude and color scaling is used for the Exact and the MoM solutions, to allow direct visual comparison between the current densities. The exact solution in the case $\varepsilon_r = 1$ gives maximum normalized current densities $J / |H^{inc}|$ and $M / |E^{inc}|$ equal to 1 (see §6.1.4). The MoM solutions for the maximum normalized J and M current densities are also equal to 1,00 with an accuracy better than 1%.

The condition numbers are given in Table 25. They are quite similar to those reported in Table 27 (p.197) for the same structures filled with PEC material instead of dielectric, and analyzed with tEFIE$^{\nabla f}$-f.

Table 25 : Condition number versus characteristic length (CL)

Mesh CL	$\lambda_0/20$	$\lambda_0/40$	$\lambda_0/60$	$\lambda_0/120$
CN	1347	1948	2842	7813

In Figure 111 we summarize the relative errors measured on the electric current density with the four meshes. Note that the relative errors on the real parts range from 0 to 1%, while they range from 0 to 10% for the imaginary parts. The average and maximum relative errors diminish with a finer mesh. They are extremely small for the large current densities ($\mathrm{Re}[\,J/|H^{inc}|\,] \sim 1$) but they are much higher for the smallest current densities ($\mathrm{Im}[\,J/|H^{inc}|\,] < 0{,}05$). In Figure 112 (p.189) the length scale of the ImJ arrows are magnified 20 times : it reveals that even the low current densities are very accurate everywhere, except on the two vertical thin sides. Similar observations and conclusions are made for the magnetic current density in Figure 113 (p.190) and Figure 114 (p.191). Additional comments are given in Figure 116 (p.192).

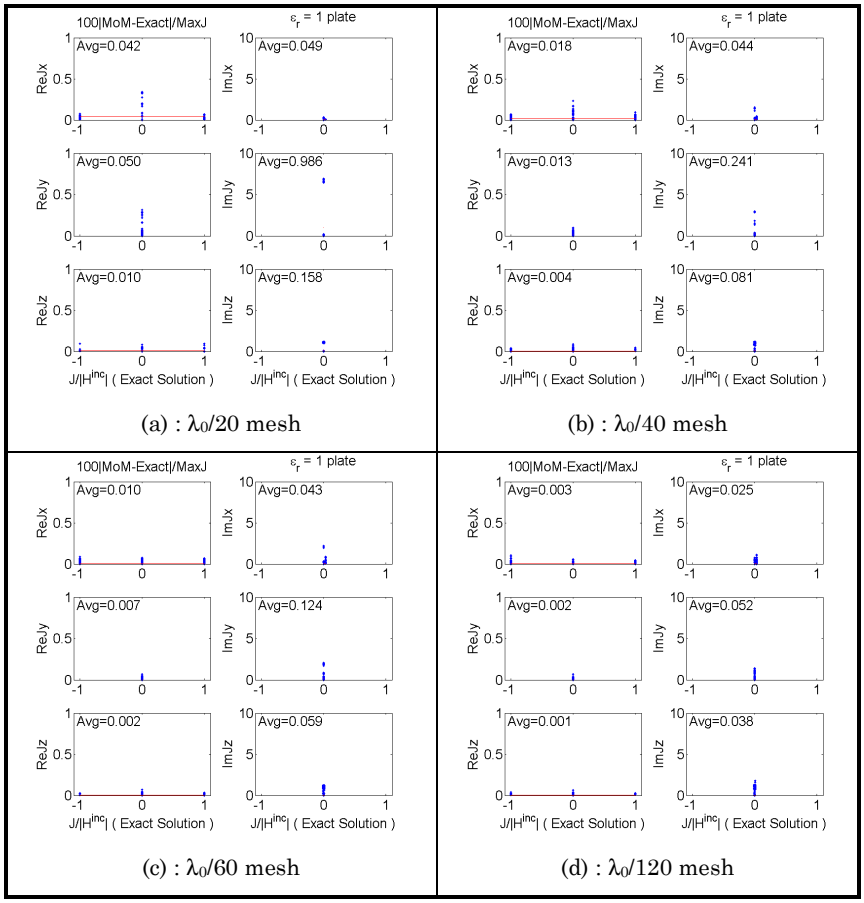

(a) : $\lambda_0/20$ mesh

(b) : $\lambda_0/40$ mesh

(c) : $\lambda_0/60$ mesh

(d) : $\lambda_0/120$ mesh

Figure 111 : Relative error on the J current density for the $\varepsilon_r = 1$ plate

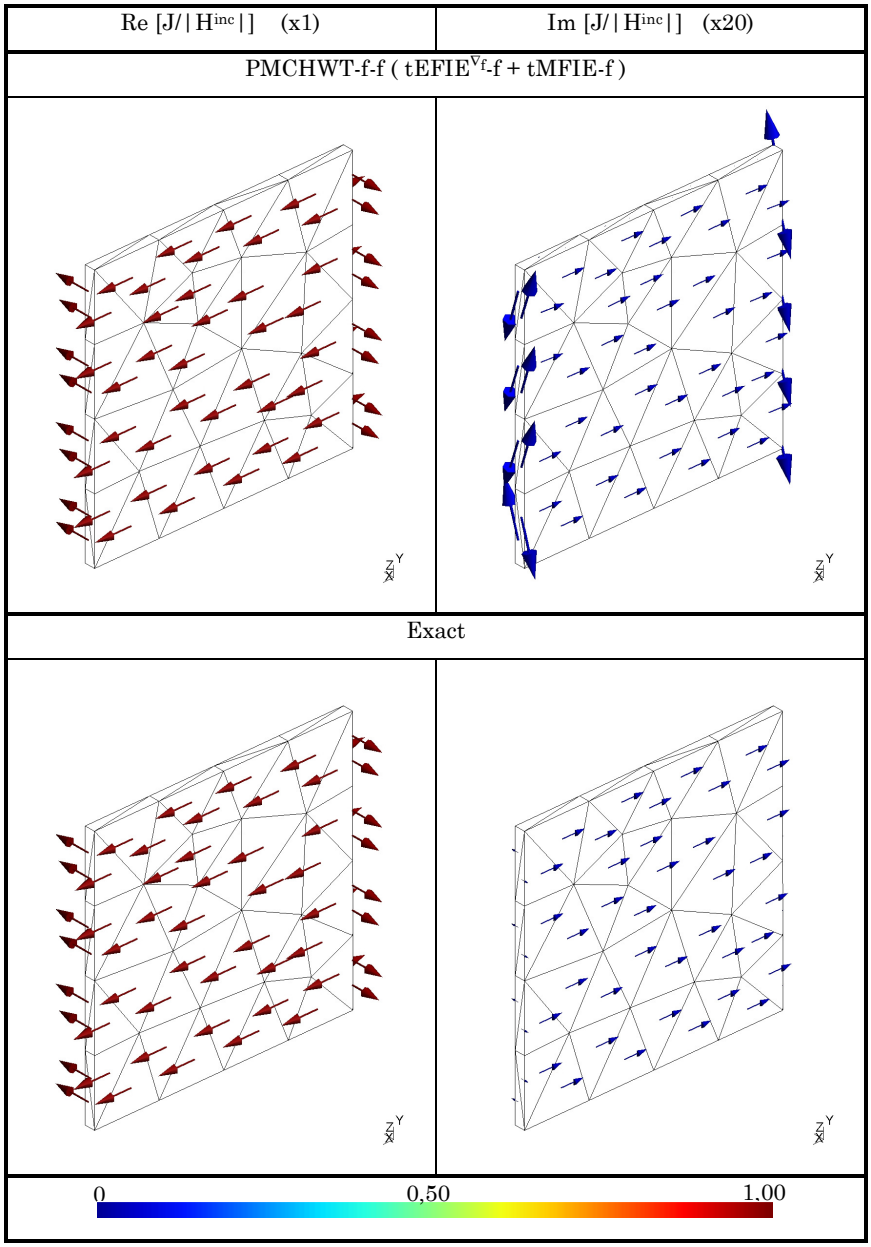

Figure 112 : $J/|H^{inc}|$ for the $\varepsilon_r = 1$ plate with $\lambda_0/20$ mesh

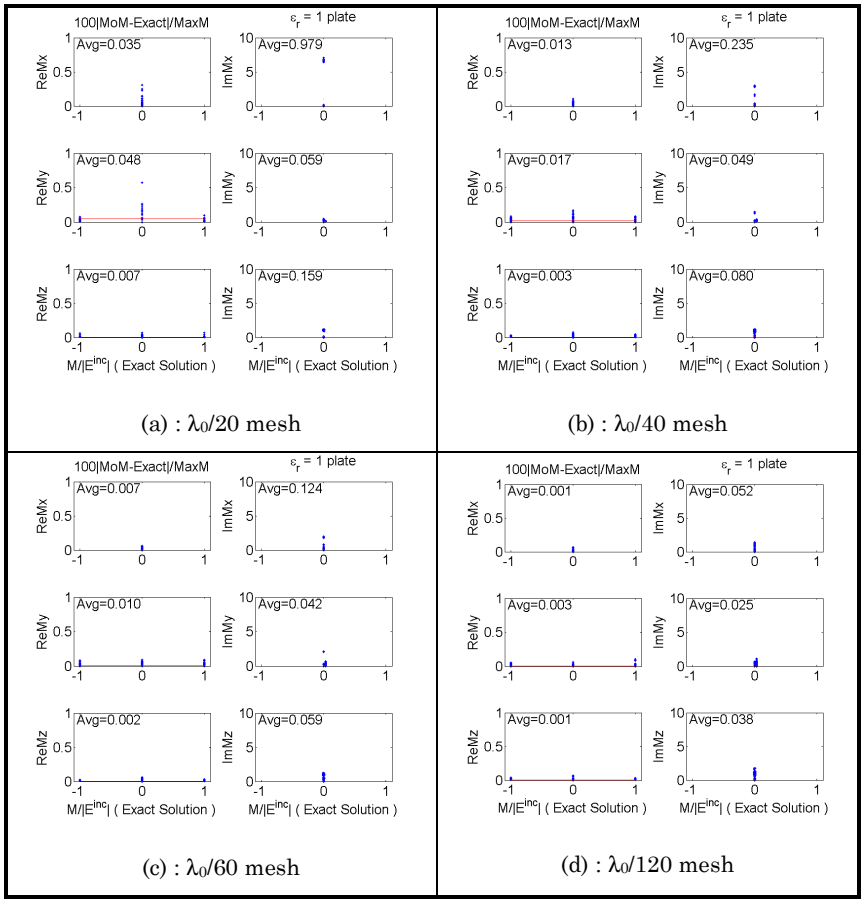

Figure 113 : Relative error on the M current density for the $\varepsilon_r = 1$ plate

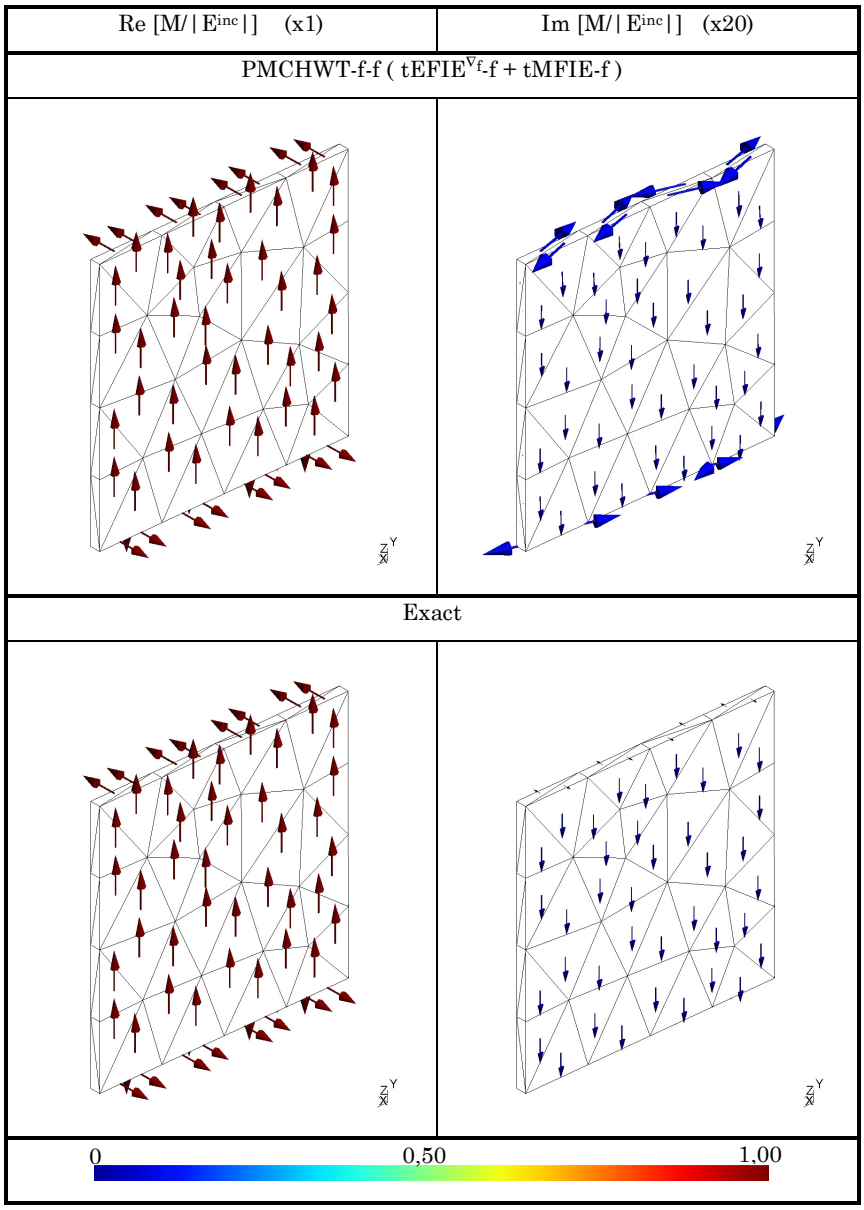

Figure 114 : M/|E^{inc}| for the $\varepsilon_r = 1$ plate with $\lambda_0/20$ mesh

As can be seen in Figure 112 (p.189), Figure 114 (p.191) and Figure 115, the large error on the vertical thin sides is related to the orientation of the single pairs of triangles meshing the thickness of the plate. We mention also that the same behavior is observed if PMCHWT-f-f (tEFIE$^{\nabla G}$-f + tMFIE-f) is used instead of PMCHWT-f-f (tEFIE$^{\nabla f}$-f + tMFIE-f), even if more nodes are used in the inner and outer integrals.

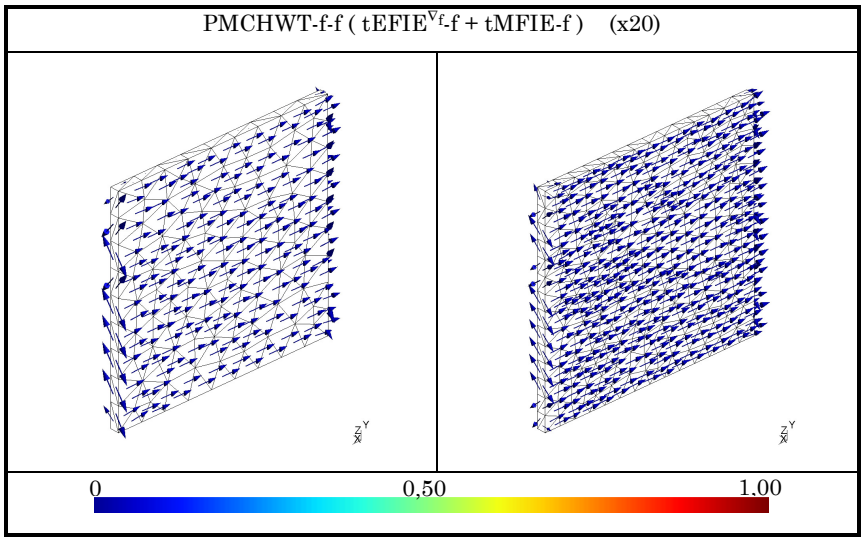

Figure 115 : Large error on the vertical thin sides

The explanation is quite simple. The exact solution requires a normal component varying from positive to negative along the diagonal, zero on the horizontal edges and constant on the vertical edges. The RWG's impose a normal component constant all along every edge (§2.2.8). This limitation is not a problem for the horizontal and vertical edges, but on the diagonal the RWG's choose for a zero normal component. The "best" RWG solution for this situation is depicted in Figure 116.

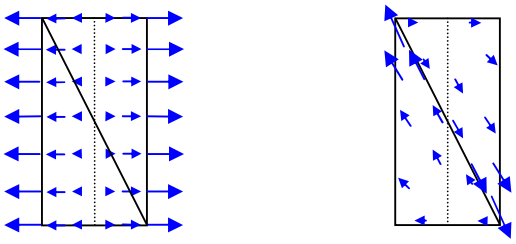

(a) Exact solution (b) Best RWG approximation

Figure 116 : RWG solution on the thin vertical sides of the plate

6.7.2 PEC plate

On the four next pages we show $J/|H^{inc}|$ obtained by the tEFIE$^{\nabla_f}$-f and tMFIE-nxf for the four meshes presented in Figure 110 (p.186).

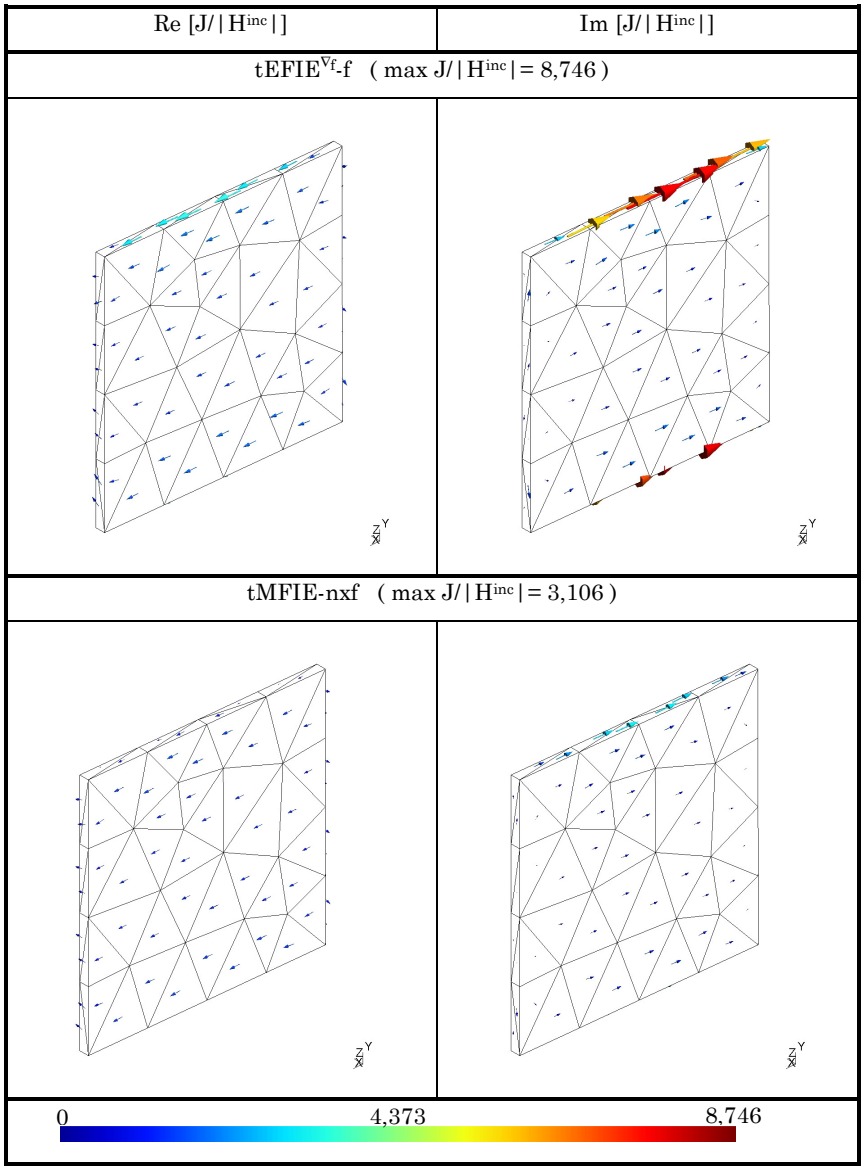

Figure 117 : $J/|H^{inc}|$ on the PEC plate ($\lambda_0/20$ mesh)

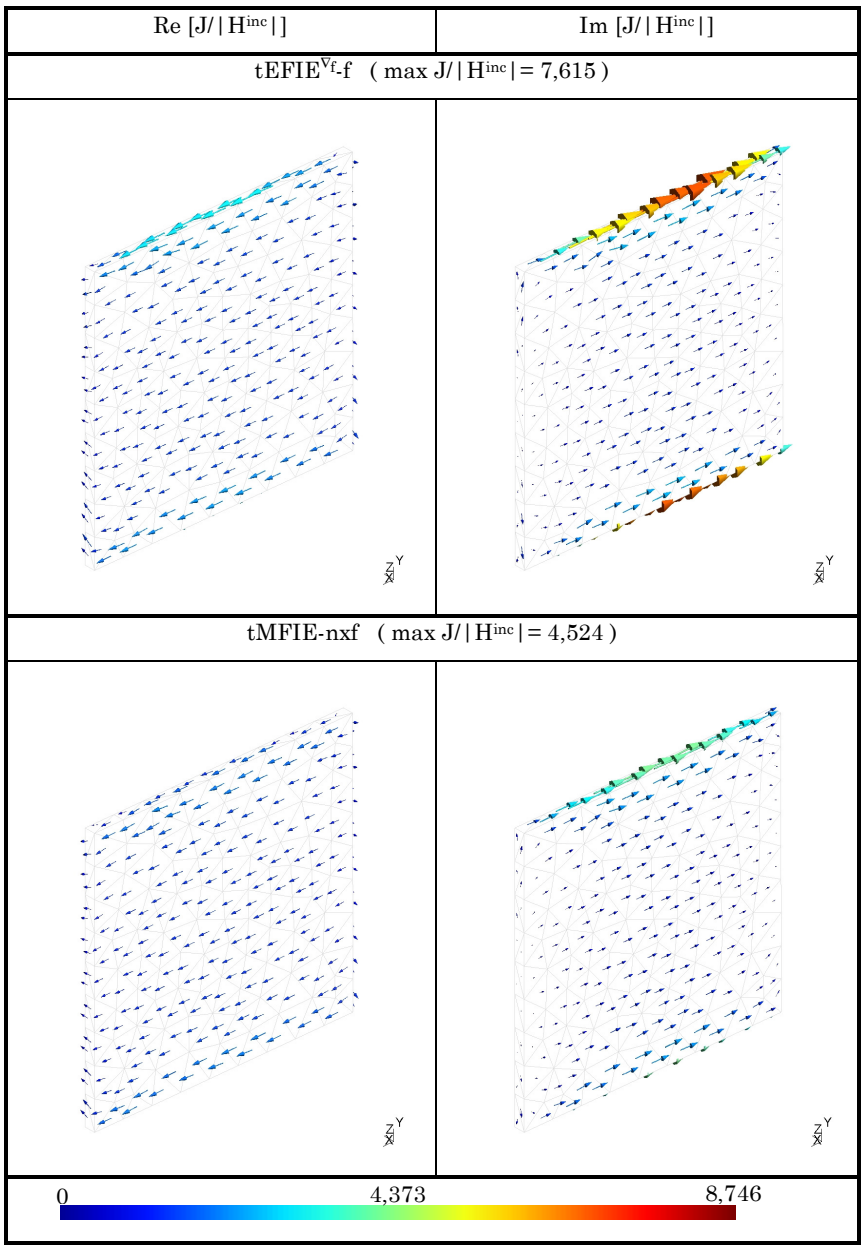

Figure 118 : J/|H^inc| on the PEC plate (λ_0/40 mesh)

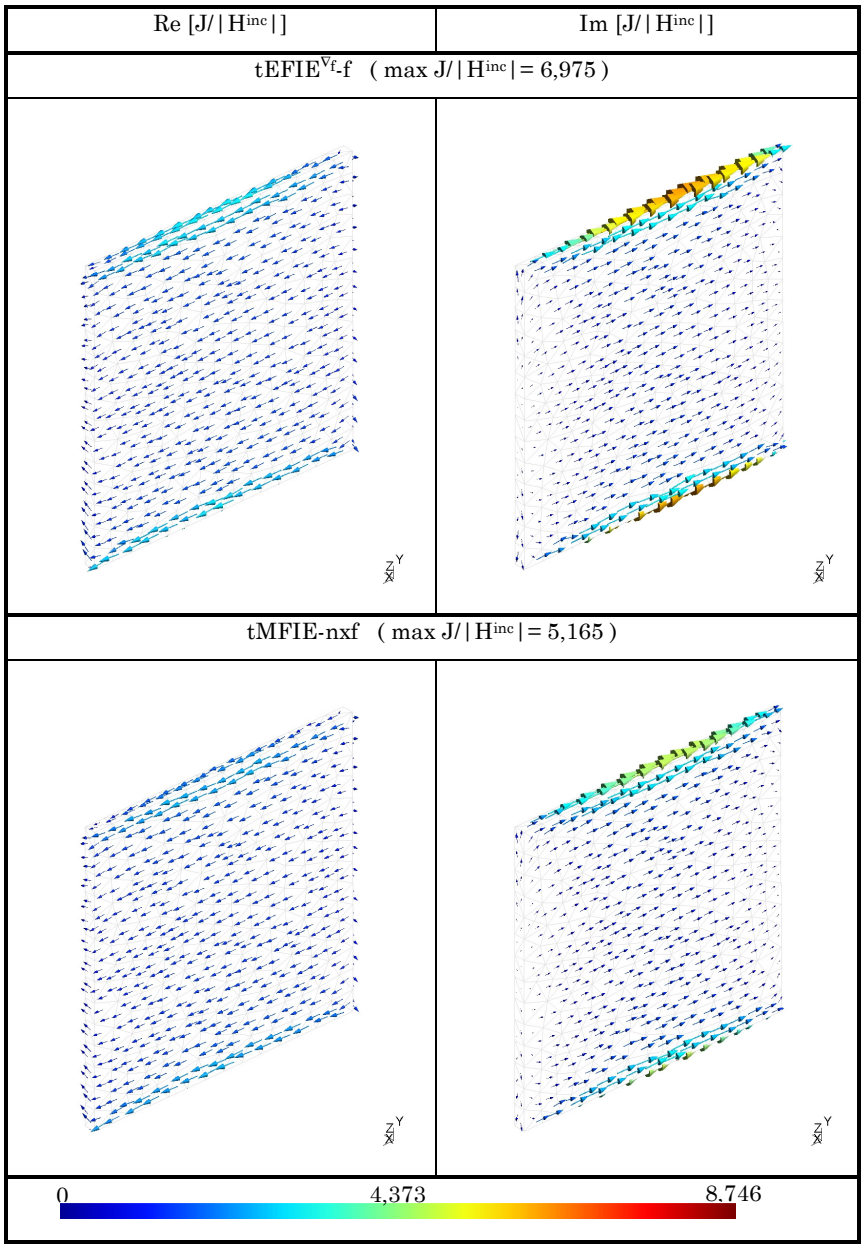

Figure 119 : $J/|H^{inc}|$ on the PEC plate ($\lambda_0/60$ mesh)

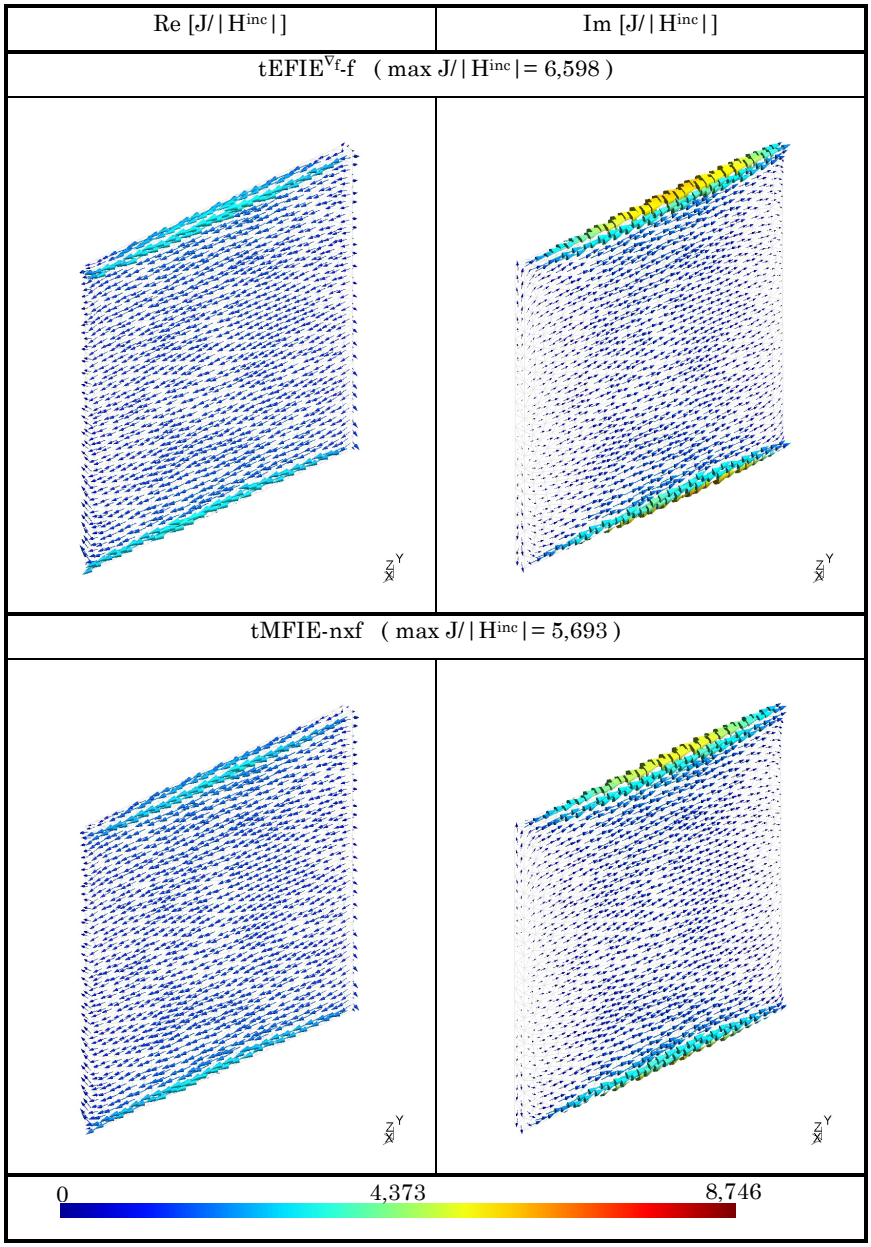

Figure 120 : $J/|H^{inc}|$ on the PEC plate ($\lambda_0/120$ mesh)

Figure 117 (p.193) to Figure 120 (p.196) clearly show that the highest tEFIE$^{\nabla_f}$-f and tMFIE-nxf electric current densities observed on the top and bottom thin edges are very different from each other for the $\lambda_0/20$ mesh, but converge to each other when the mesh is refined, as summarized in Table 26 :

Table 26 : Max [J/|H^{inc}|]

	$\lambda_0/20$	$\lambda_0/40$	$\lambda_0/60$	$\lambda_0/120$
tEFIE$^{\nabla_f}$-f	8,746	7,615	6,975	6,598
tMFIE-nxf	3,106	4,524	5,165	5,693

It seems that, in presence of elongated triangles, the tEFIE$^{\nabla_f}$-f overestimates the high edge current densities while the tMFIE-nxf underestimates them. It can be anticipated that a mesh finer than $\lambda_0/120$ would further favour the convergence of the tEFIE$^{\nabla_f}$-f and tMFIE-nxf solutions. Unfortunately, such mesh densities require prohibitive computer resources and are far beyond the "best practice" density of $\lambda_0/10$.

The condition numbers (CN) presented in Table 27 confirm the observations made previously in §§6.2.3, 6.2.4 and 6.5.2, namely :

- CN is much lower for the tMFIE-nxf than for the tEFIE$^{\nabla_f}$-f
- CN is quasi independent of the mesh fineness for tMFIE-nxf
- CN increases with $1/h$ for tEFIE$^{\nabla_f}$-f, if h is the characteristic length of the mesh (see Table 24, p.187)

Table 27 : Condition numbers

h	$\lambda_0/20$	$\lambda_0/40$	$\lambda_0/60$	$\lambda_0/120$
tEFIE$^{\nabla_f}$-f	1316	2041	2974	7812
tMFIE-nxf	103	68.8	66.1	70.4

It is also worth noting that the CN of Table 27 are quite similar to those reported in Table 25 (p.187) for the same structures filled with dielectric material instead of PEC, and analyzed with a PMCHWT-f-f based on tEFIE$^{\nabla_f}$-f.

Figure 121 gives quantitative evidence that the lower current densities are more similar with tEFIE$^{\nabla f}$-f and tMFIE-nxf.

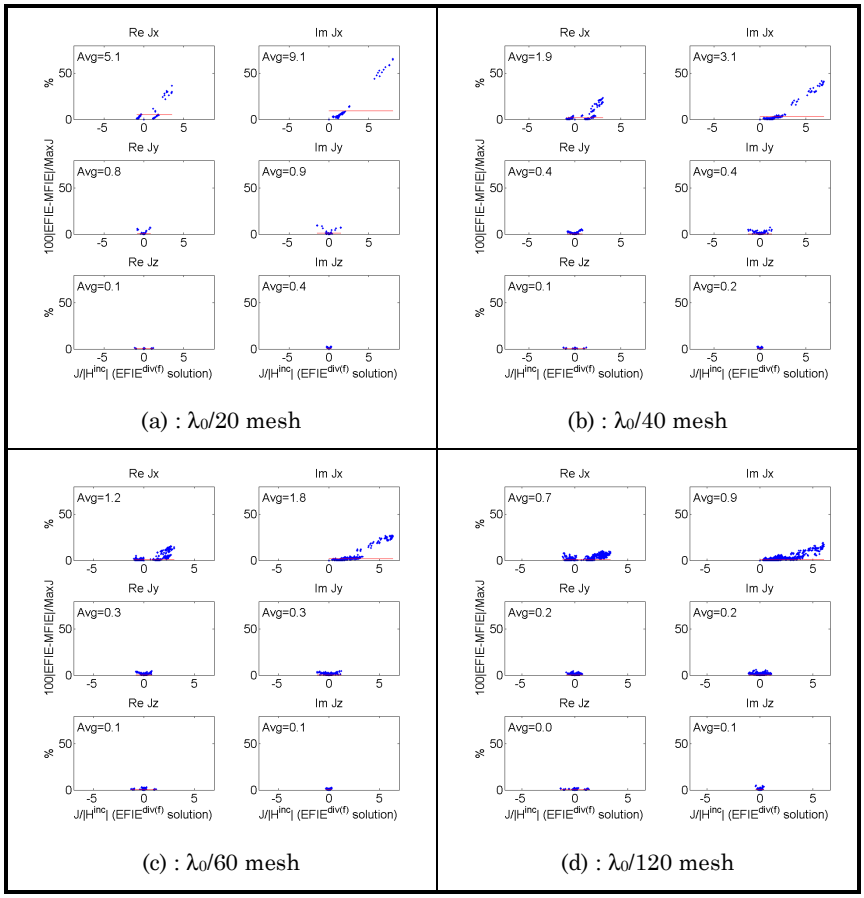

Figure 121 : Comparison tEFIE$^{\nabla f}$-f and tMFIE-nxf on the PEC plate

6.8 Thin plate : log-distributed mesh

In this paragraph we present MoM results obtained with the log-distributed mesh depicted in Figure 122 (p.199). For the Level 2 mesh, [0,5] means that the constraining rectangular grid is located at a distance (0,5)xT/2 from every edge, where T=λ_0/100 is the thickness of the plate. The Level 1 mesh is the λ_0/60 mesh used in §6.7. A λ_0/60 mesh is also used for the level 2, which means that the elongated triangles squeezed between the grid along the edges have two long sides of dimension around λ_0/60 and one very thin side.

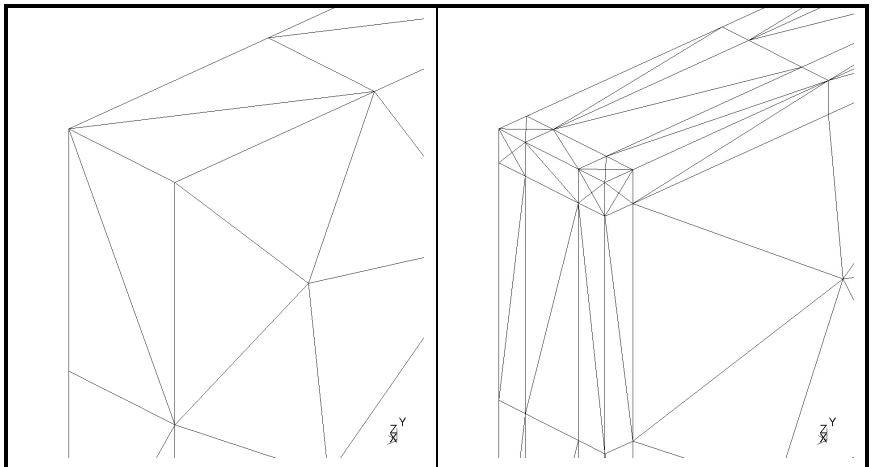

(a) : Level 1

- 1022 triangles -

(b) : Level 2 [0,5]

-1594 triangles -

Figure 122 : Two log-distributed meshes for the plate

6.8.1 Dielectric thin plate : $\varepsilon_r = 1$

In this paragraph we quantify the accuracy of the MoM solution for the two log-distributed meshes of Figure 122 by comparing it to the exact solution in the case $\varepsilon_r = 1$. The solution is obtained with PMCHWT-f-f, using tMFIE-f and $tEFIE^{\nabla f}$-f.

The following integration scheme has been used :

	Self Term	$R_{min} < \lambda/100$	$R_{min} \in [\lambda/100; \lambda/10]$	$R_{min} > \lambda/10$	V
Inner	3		3	3	--
Outer	16		16	3	3

The exact solution in the case $\varepsilon_r = 1$ gives maximum normalized current densities $J/|H^{inc}|$ and $M/|E^{inc}|$ equal to 1 (see §6.1.4). The MoM solutions for the maximum normalized *J* and *M* current densities are also equal to 1,00 , with an accuracy better than 1%.

Figure 123 summarizes the relative errors for the Level 1 and Level 2 meshes. They are both very small and quite similar to each other. We see in Figure 124 (p.201) and Figure 125 (p.202) that the very small current densities on the thin vertical (ImJ) or horizontal (ImM) side are quite erroneous. The same phenomenon has already been observed with the regular mesh of the plate (§6.7.1) : it is due to the limitations of the RWG representation. We refer to Figure 116 (p.192) for a detailed explanation.

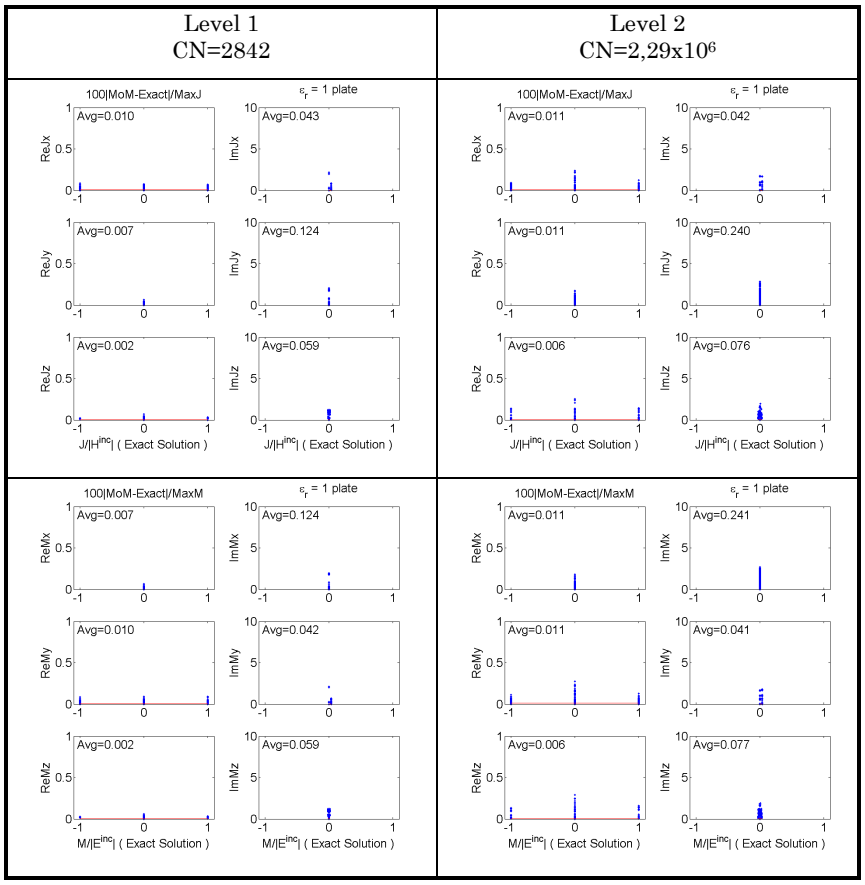

Figure 123 : Relative error on the J and M current density
for the $\varepsilon_r = 1$ plate

As already observed with the cube in §6.6.1, the condition number increases by a factor close to 1000 between the regular mesh and the log-distributed mesh.

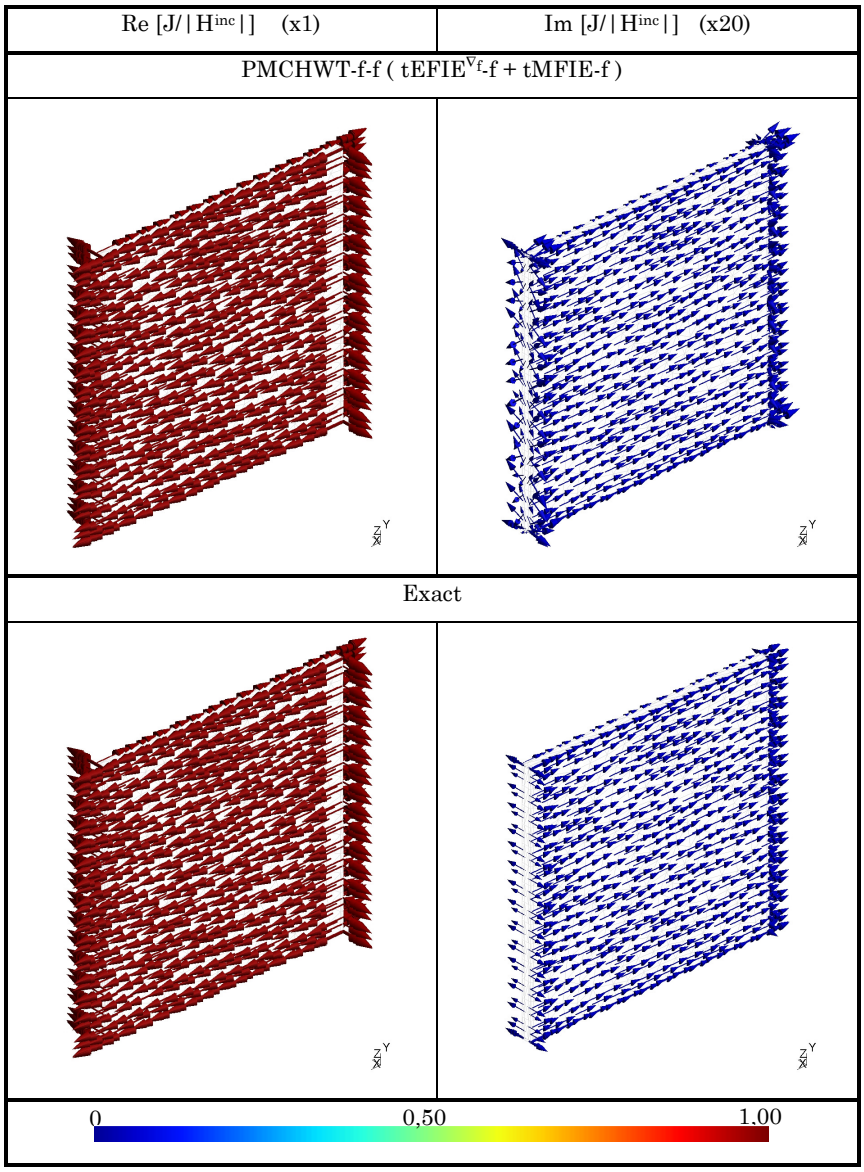

Figure 124 : $J/|H^{inc}|$ for the $\varepsilon_r = 1$ plate with Level 2 mesh

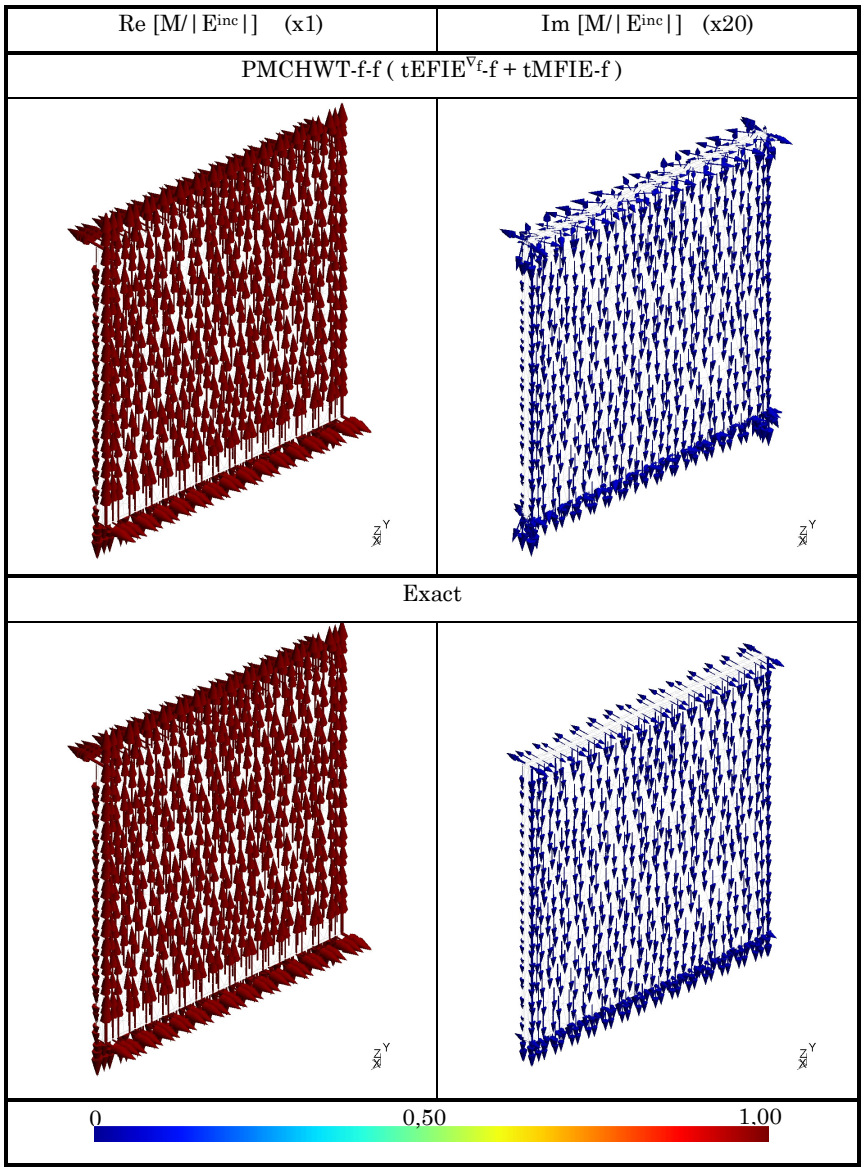

Figure 125 : $M/|E^{inc}|$ for the $\varepsilon_r = 1$ plate with Level 2 mesh

6.8.2 Dielectric thin plate : $\varepsilon_r = 9$

For the PMCHWT and Müller combination scheme, the tEFIE$^{\nabla G}$ is used.

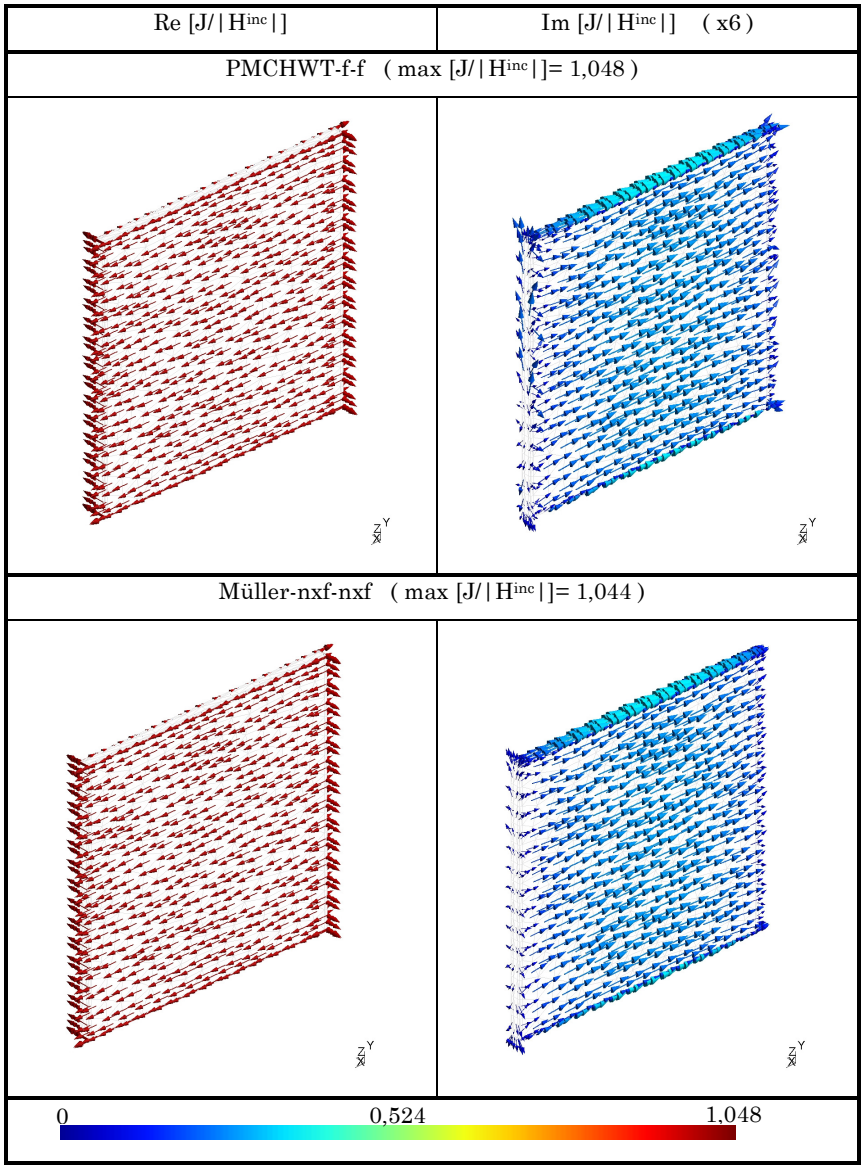

Figure 126 : $J/|H^{inc}|$ on the $\varepsilon_r = 9$ plate (Level 2 mesh)

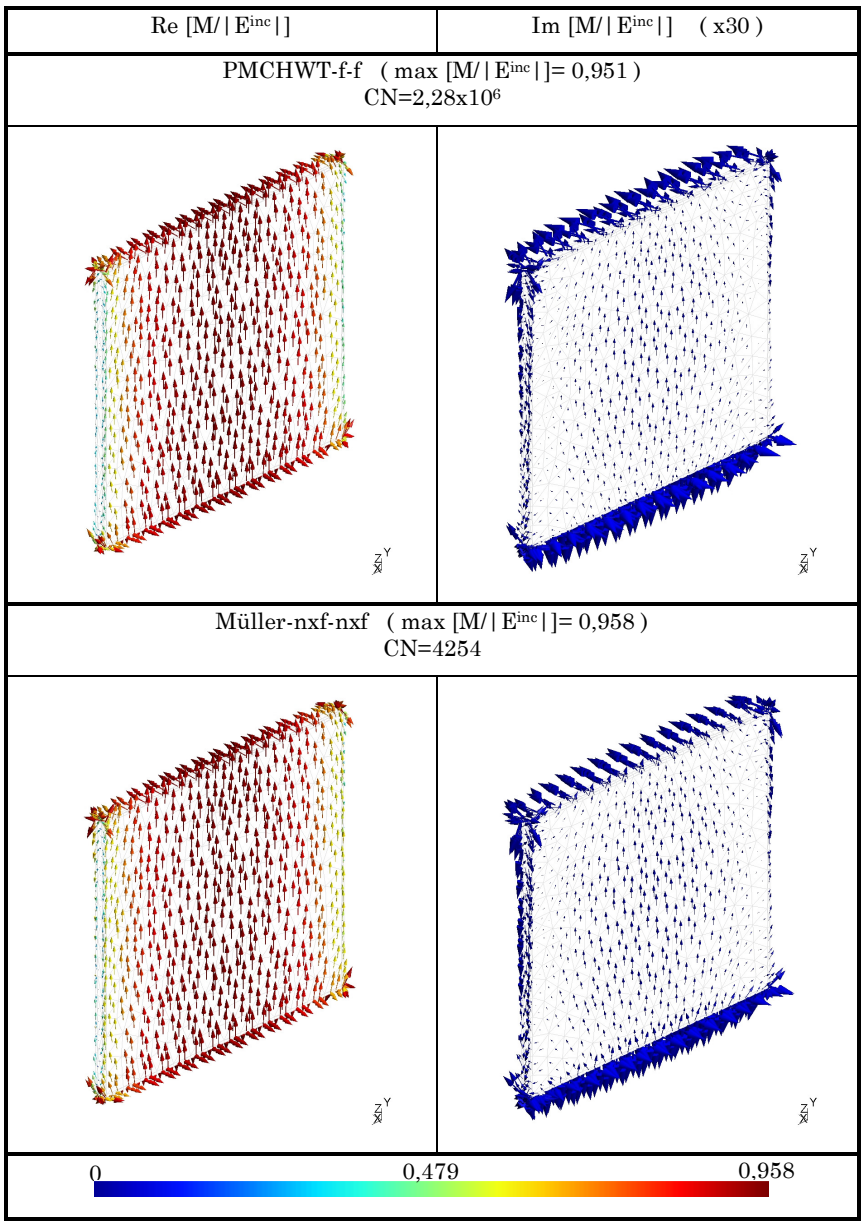

Figure 127 : $M/|E^{inc}|$ on the $\varepsilon_r = 9$ plate (Level 2 mesh)

The condition number in the Müller-nxf-nxf case is approximately 500 times lower than in the PMCHWT-f-f case, as already observed in §6.2.5.

Both solutions, PMCHWT-f-f and Müller-nxf-nxf, are quasi identical.

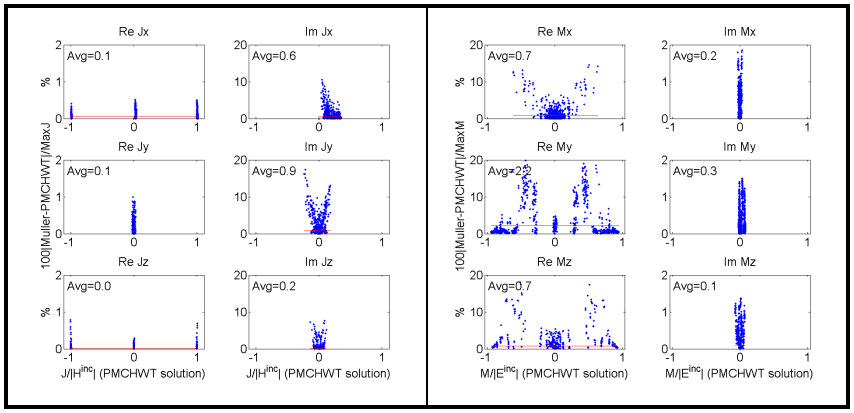

Figure 128 : Comparison PMCHWT-f-f / Müller-nxf-nxf for $\varepsilon_r = 9$ plate

As we already noted and explained in §§6.7.1 and 6.8.1, we can see in Figure 129 that RWG functions are not adequate to model the smallest current density pattern on the thin sides of the plate (Im[M]) : the arrows are zigzagging somewhat erratically. The largest current density pattern (Re[M]) is similar on the vertical and horizontal thin sides to the patterns observed on the cube (see Figure 104, p.180). It is worth mentioning that the circular pattern of the magnetic current density on the vertical side couldn't be modelled with linear basis functions (e.g. RWG) and the Level 1 mesh of Figure 122a (p.199).

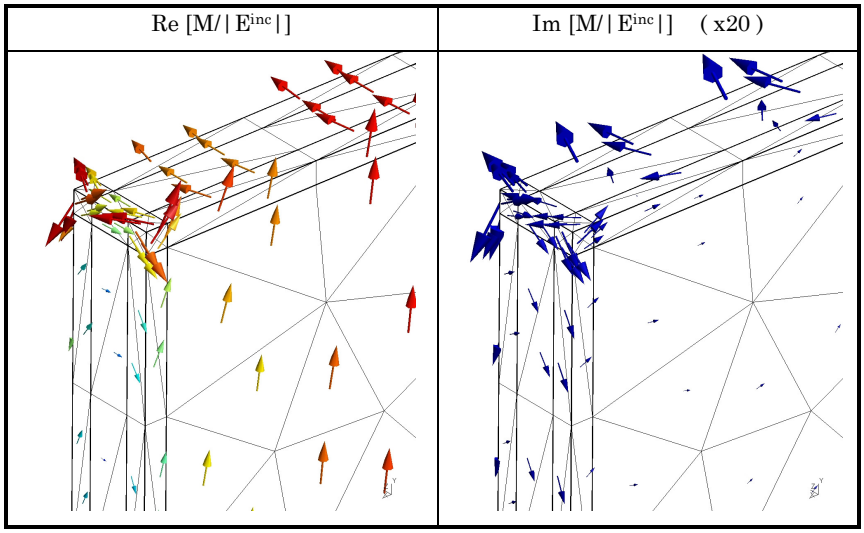

Figure 129 : Details of $M/|E^{inc}|$ on the $\varepsilon_r = 9$ plate

6.8.3 PEC thin plate

Figure 130 shows $J/|H^{inc}|$ obtained by the tEFIE$^{\nabla G}$-f and tMFIE-nxf for the Level 2 mesh presented in Figure 122 (p.199).

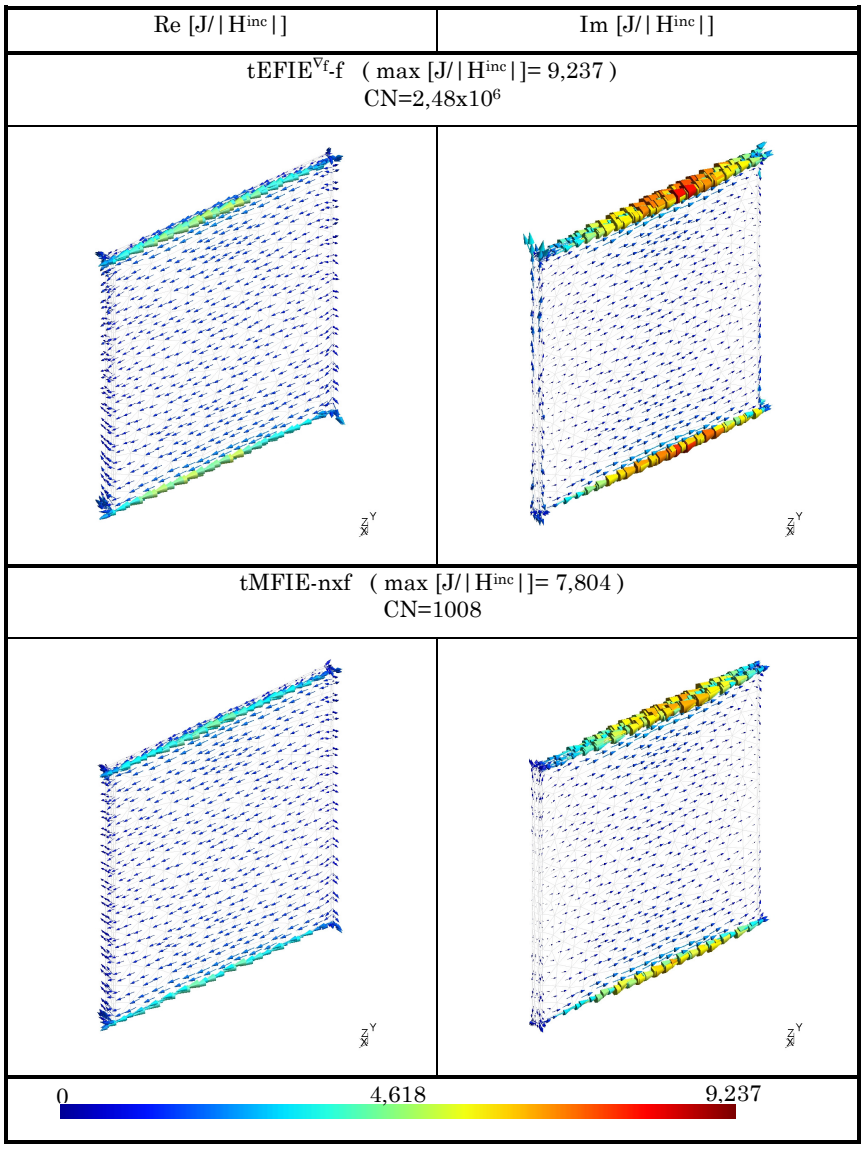

Figure 130 : $J/|H^{inc}|$ on the PEC plate (Level 2 mesh)

The condition number is again much lower for the tMFIE-nxf than for the tEFIE$^{\nabla f}$-f.

The following integration scheme has been used :

	Self Term	$R_{min} < \lambda/100$	$R_{min} \in [\lambda/100; \lambda/10]$	$R_{min} > \lambda/10$	V
Inner	3		3	3	--
Outer	16		16	3	3

In Figure 131 we present the differences between tEFIE-f and the tMFIE-nxf solutions, for the Level 1 and Level 2 meshes of the thin PEC plate. The comparison is not entirely correct here as the tEFIE$^{\nabla G}$-f is used for the Level 2 mesh while the tEFIE$^{\nabla f}$-f is used for the Level 1, but it allows the following observations namely :

- The average relative difference between the tEFIE$^{\nabla G}$-f and tMFIE-nxf solutions is not too much affected if a higher level log-distributed mesh is used
- The maximum difference between the tEFIE$^{\nabla G}$-f and tMFIE-nxf solutions becomes slightly higher for the higher current densities that are computed closer to the edges with the higher order log-distributed meshes

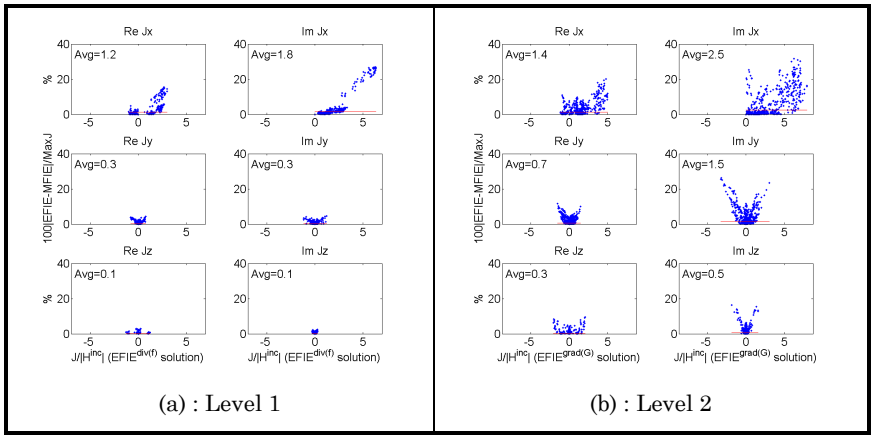

(a) : Level 1 (b) : Level 2

Figure 131 : Comparison tEFIE-f and tMFIE-nxf for Level 1 and 2 meshes

6.9 Very thin and infinitely thin PEC plate : edge currents

6.9.1 Introduction

The E-MFIE formulation (see §4.4) allows to compute the individual (electric) current densities on both sides of any (PEC) sheet. To demonstrate it, we will shrink the very thin plate analyzed in §6.7, using this time two types of very symmetric meshes, identical for the two large faces of the plate and the opposite faces of the sheet. These meshes are shown in Figure 132 (p.209). They will allow :

- to compare the current densities on the plate and on the sheet
- to compute the difference between the current densities on both sides at similar locations
- to respect the symmetry of the geometry and the plane wave illumination

The tEFIE$^{\nabla G}$-f and tMFIE-nxf solutions for the very thin plates will be compared against each other, and with the E-MFIE solution for the sheet. The E-MFIE solution is a combination of the tEFIE$^{\nabla G}$-f and tMFIE-nxf. The same integration schemes have been used for the tEFIE$^{\nabla G}$-f for the plate and the tEFIE$^{\nabla G}$-f used in the E-MFIE for the sheet. The same applies for the tMFIE-nxf. The integration schemes are :

for the tEFIE$^{\nabla G}$-f

	Self Term	$R_{min} < \lambda/100$	$R_{min} \in [\lambda/100; \lambda/10]$	$R_{min} > \lambda/10$	V
Inner	3		3	3	--
Outer	42		42	3	3

for the tMFIE-nxf

	Self Term	$R_{min} < \lambda/100$	$R_{min} \in [\lambda/100; \lambda/10]$	$R_{min} > \lambda/10$	V
Inner	3		3	3	--
Outer	16		16	3	3

For the large $\lambda_0/4$ faces of the plate and for the two opposite faces of the sheet, we use a linearly or a logarithmically distributed mesh. The local coordinates of the Log grid inside the $C = \lambda_0/4$ faces, according to the notation introduced in §6.6, is [-900 -892 -800 -600 -250 +250 +600 +800 +892 +900]/900x(C/2).

For the thin sides of the plate, we use at all times a linearly distributed mesh, with stretched triangles. The thickness of the plate will be $\lambda_0/100$, $\lambda_0/1000$ or $\lambda_0/10000$.

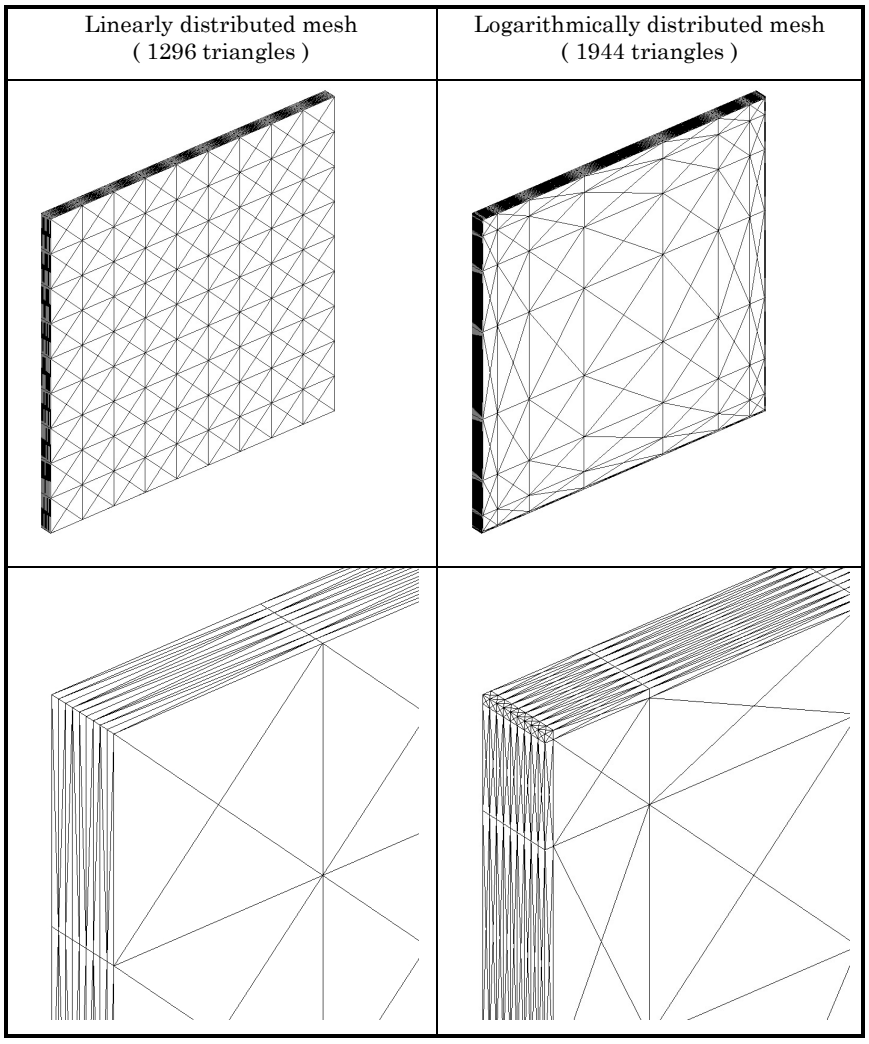

Figure 132 : Lin and Log Mesh for the (¼ x ¼ x 1/100)λ_0 plate and sheet

On the four next pages we present in Figure 133 and Figure 134 (Figure 135 and Figure 136) the solutions obtained with the linearly (logarithmically) distributed mesh, and comment them. Because of the large difference between high and low current densities, the color scale is logarithmic.

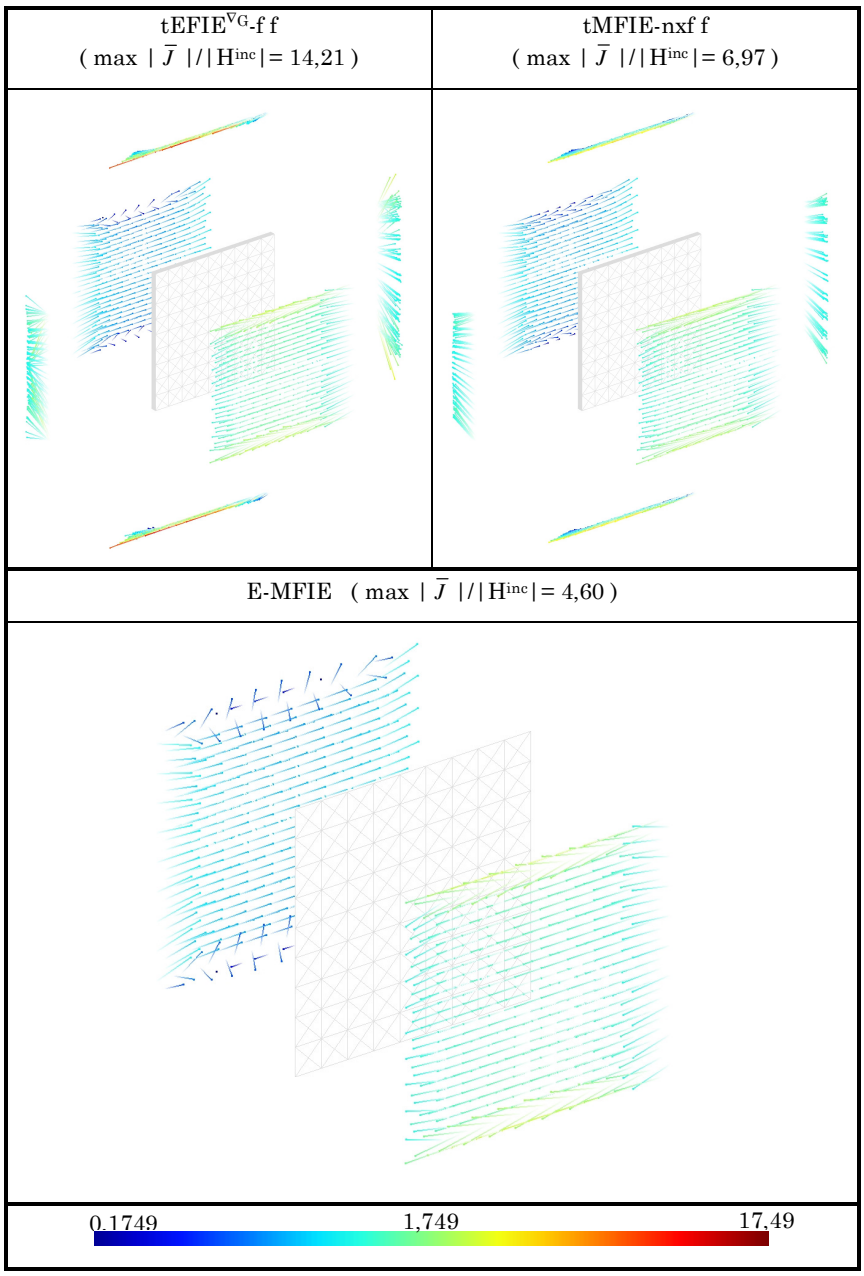

Figure 133 : Re(J) /|H^{inc}| on a (¼ x ¼ x 1/100)λ_0 PEC plate / sheet with linearly distributed mesh

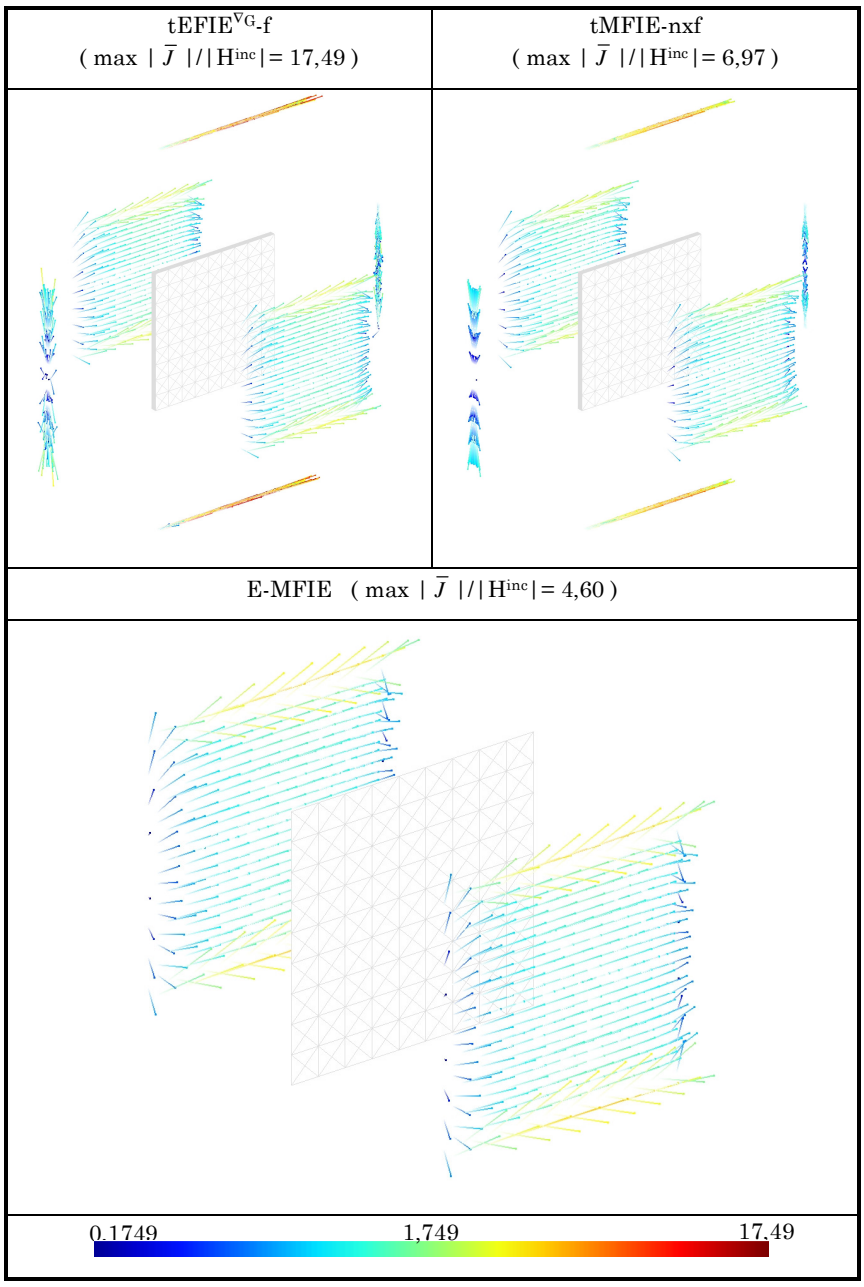

Figure 134 : Im(J) /|H^{inc}| on a (¼ x ¼ x 1/100)λ_0 PEC plate / sheet with linearly distributed mesh

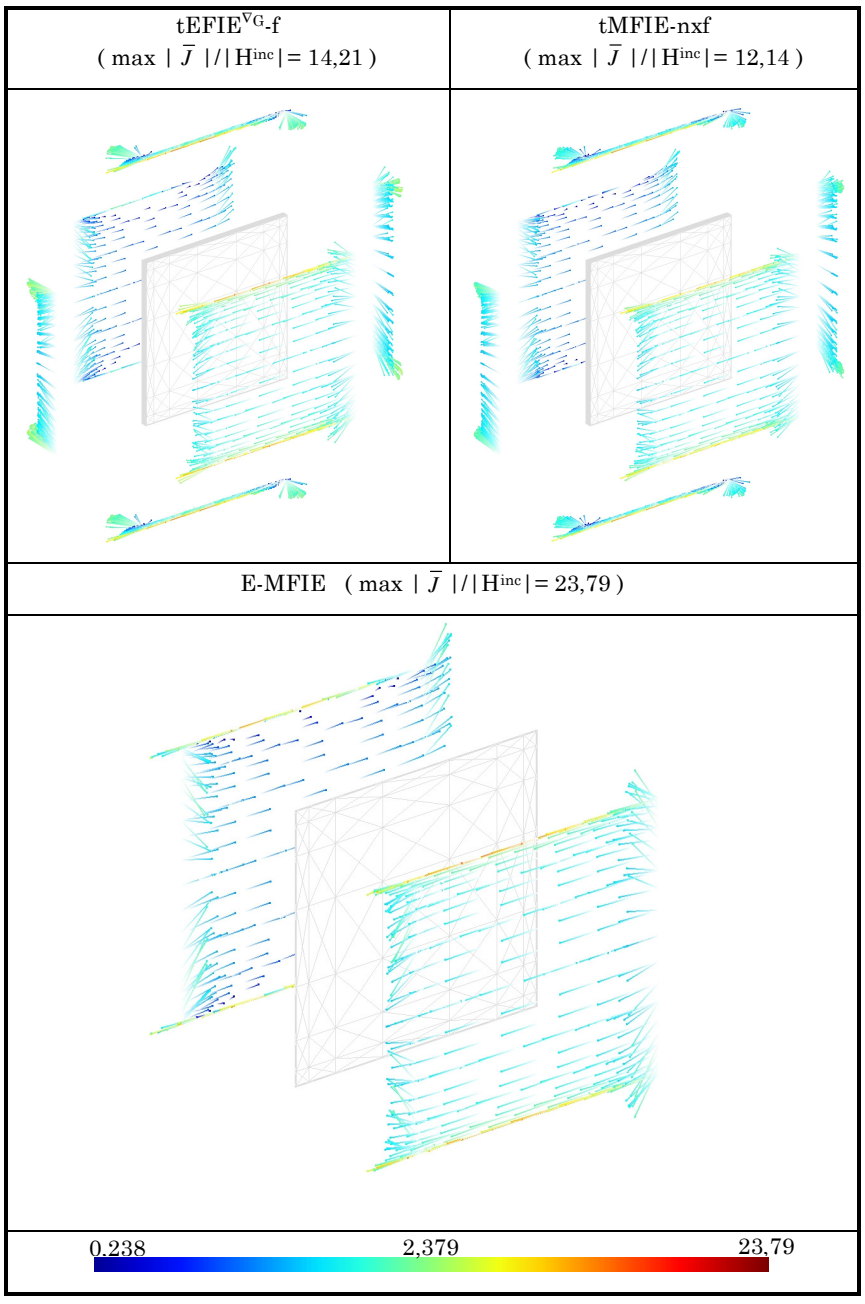

Figure 135 : Re(J) /|H^{inc}| on a (¼ x ¼ x 1/100)λ_0 PEC plate / sheet with logarithmically distributed mesh

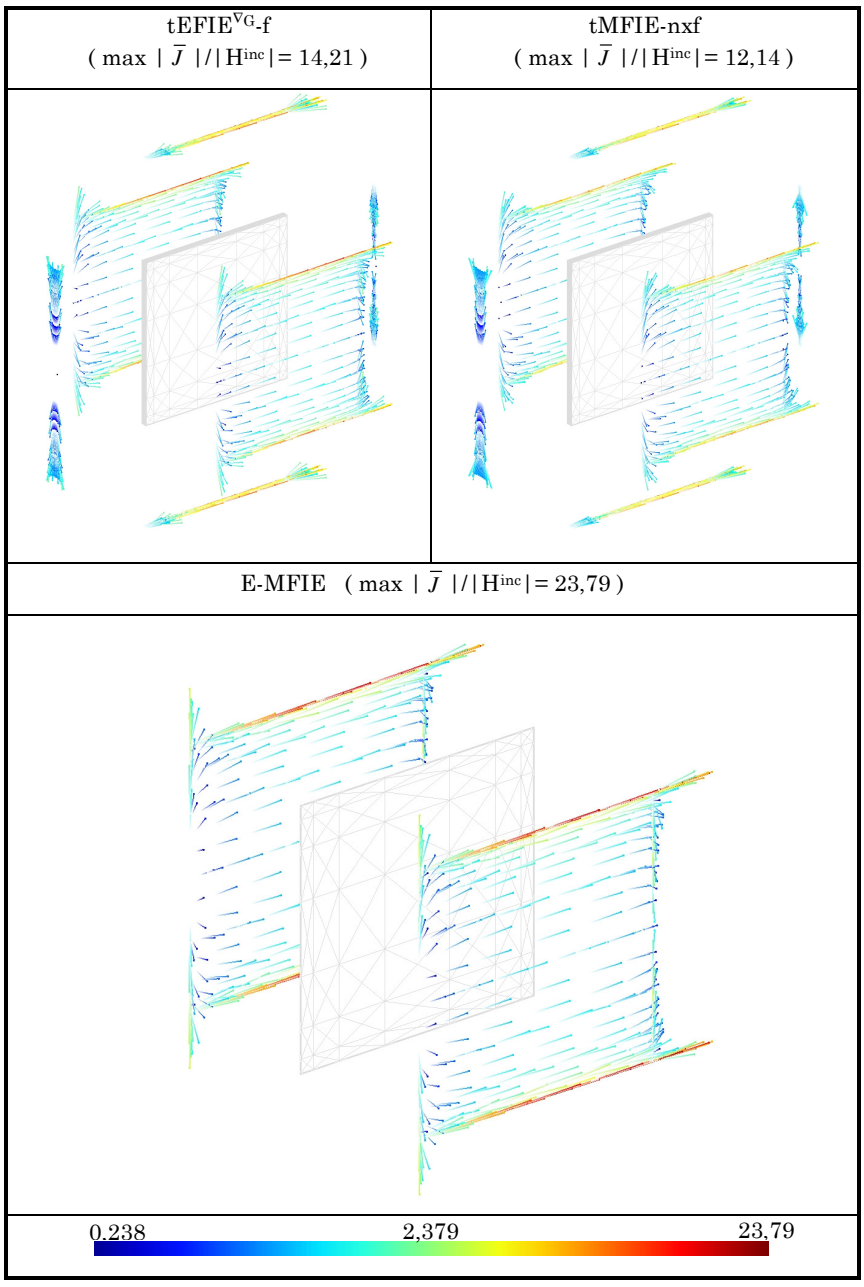

Figure 136 : Im(J) /|H^{inc}| on a (¼ x ¼ x 1/100)λ_0 PEC plate / sheet with logarithmically distributed mesh

On the Lin distributed mesh, max $|\bar{J}|/|H^{inc}|$ is much lower for the E-MFIE (4,60) than for the tEFIE$^{\nabla G}$-f (17,49) and tMFIE-nxf (6,97), as opposed to what is observed on the Log distributed mesh. This is explained by the fact that on the Lin distributed mesh of the plate, the highest current density is obtained on the top thin sides of the plate, computed much closer to the edge than on the large flat vertical face. These high current densities cannot be computed with the E-MFIE as the thin sides are excluded in the sheet model. With the Log distributed mesh, the grid is defined such that the highest current density is computed at the same distance from the edge on the large vertical flat face as well (see Figure 132, p.209). If we visually compare in Figure 137 the highest current densities on the large vertical face, represented on an identical linear scale, they are much more similar with tEFIE$^{\nabla G}$-f, tMFIE-nxf and E-MFIE, except in the last triangles very close to the edge, where the E-MFIE computes (much) higher current densities than on the plate with the tEFIE$^{\nabla G}$-f and tMFIE-nxf. These higher E-MFIE current densities, very close to the edges, seem to compensate for the absence in the sheet model of the current densities flowing on the thin sides of the plate.

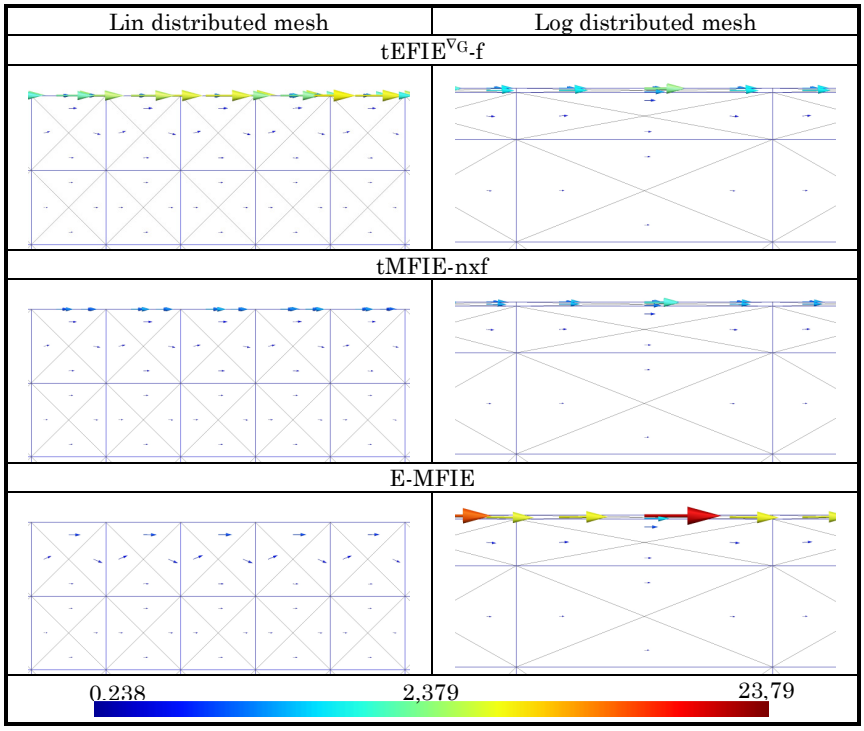

Figure 137 : Max (Im[J]) /$|H^{inc}|$ on the sheet and on the plate

We also make the following qualitative observations :

- The tEFIE$^{\nabla G}$-f and tMFIE-nxf solutions look very similar on the two large $\lambda_0/4$ faces, but differ significantly on the four thin edges. This phenomenon had already been noted in §6.7.
- On the large faces, in a small strip close to the upper and lower edges, the current density zigzag instead of flowing smoothly along a quasi straight line. This nonphysical behavior is due again to the limited linear representation of RWG functions. Close to the edges the current density exhibits a large transversal gradient with regard to the current flow direction. In §2.2.8 we explain why such a gradient cannot be modelled with RWG functions. As a consequence, in the triangles extending across the zone where this gradient is very large, the current density (orange) as modelled with RWG's is forced to zigzag to maintain a constant normal component with their two neighbours (red and yellow arrows), where very different current densities are flowing. Note that there is no zigzag behavior in these neighbouring triangles : their base is parallel to the current density flow and the two other sides are crossed by current densities having similar norms.

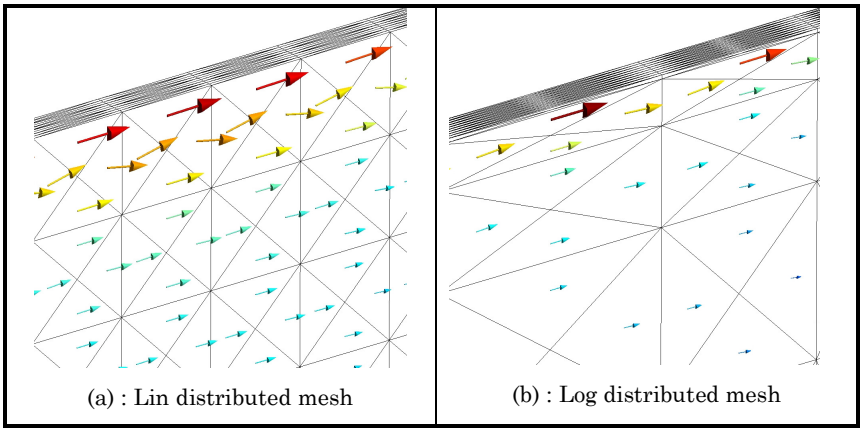

(a) : Lin distributed mesh

(b) : Log distributed mesh

Figure 138 : RWG and zigzag current densities near edges

0n Figure 138 this zigzag effect appears to be less pronounced with the Log distributed mesh. Actually it is still present - see the very light zigzag of the yellow arrows - but it is better constrained in triangles with a very small dimension across the large gradient zone.

As can be seen in Figure 135 (p.212) and Figure 136 (p.213) the Log distributed mesh brings the tEFIE$^{\nabla G}$-f and tMFIE-nxf solutions much closer to each other, while allowing to better model the large transversal current density gradient close to the edges. The color scale for the current densities is logarithmic though, somewhat masking the quantitative differences between these three solutions. As we used identical meshes for the upper and lower faces of the plate and for the

sheet, we can present a quantitative comparison of the tEFIE$^{\nabla G}$-f, tMFIE-nxf and E-MFIE solutions.

Before that, we summarize in Table 28 the condition numbers for all cases :

Table 28 : Condition numbers

	tEFIE$^{\nabla G}$-f	tMFIE-nxf	tEFIE$^{\nabla G}$-f	tMFIE-nxf
$\lambda_0/100$	1,02x10^6	1693	2,41x10^8	3,50x10^5
$\lambda_0/1000$	2,33x10^8	93301	1,21x10^{10}	2,08x10^7
$\lambda_0/10000$	5,34x10^{10}	5,48x10^6	1,68x10^{12}	1,74x10^9
E-MFIE	890		6,17x10^7	
	Lin-distributed mesh		Log-distributed mesh	

As usual we observe that tMFIE-nxf is much better conditioned than tEFIE$^{\nabla G}$-f, but this time the condition number of both formulations increases nearly proportionally with $(1/t)^2$, if t is the thickness of the plate.

With the E-MFIE formulation, the condition number is very low for the Lin-distributed mesh, better than the tEFIE$^{\nabla G}$-f and the tMFIE-nxf ones, but increases by five orders of magnitude for the Log-distributed mesh, where it only increases by two orders of magnitude for both the tEFIE$^{\nabla G}$-f and the tMFIE-nxf.

Despite the poorer condition numbers reported in Table 28, in the next paragraph we restrict the analysis to the Log-distributed meshes. For the same number of unknowns, those meshes drastically reduce the zigzag effect close to edges, even though they do not eliminate it. They also provide a better mesh refinement only where it is necessary and they reduce the differences between the tEFIE$^{\nabla G}$-f and the tMFIE-nxf solutions.

6.9.2 EFIE / MFIE and E-MFIE comparisons on Log-distributed meshes

If we call (-*Z*) the illuminated face and (+*Z*) the shadowed face, the 36 comparisons to make are summarized in Table 29 :

Table 29 : Comparison list for the plate and sheet

Log mesh	EFIE v MFIE	EFIE v E-MFIE	MFIE v E-MFIE
(-Z) face	$\lambda_0/100$ (Re + Im)		
(+Z) face			
Log mesh	EFIE v MFIE	EFIE v E-MFIE	MFIE v E-MFIE
(-Z) face	$\lambda_0/1000$ (Re + Im)		
(+Z) face			
Log mesh	EFIE v MFIE	EFIE v E-MFIE	MFIE v E-MFIE
(-Z) face	$\lambda_0/10000$ (Re + Im)		
(+Z) face			

To reduce the number of comparisons we consider the properties (315) to (318), valid for flat PEC sheets, and demonstrated in §1.13. As $\bar{H}^i = \bar{H}^i_y$ is purely real everywhere on (both faces of) the flat PEC sheet, we have that :

$$\mathrm{Re}[J_x^{(-Z)}] - \mathrm{Re}[J_x^{(+Z)}] = 2\,|H_i| \tag{315}$$

$$\mathrm{Im}[J_x^{(-Z)}] - \mathrm{Im}[J_x^{(+Z)}] = 0 \tag{316}$$

$$\mathrm{Re}[J_y^{(-Z)}] - \mathrm{Re}[J_y^{(+Z)}] = 0 \tag{317}$$

$$\mathrm{Im}[J_y^{(-Z)}] - \mathrm{Im}[J_y^{(+Z)}] = 0 \tag{318}$$

We can expect these properties to be nearly fulfilled for the very thin PEC plates as well. In Figure 139 (p.218) we observe that the property (315) is fulfilled for the E-MFIE on the sheet, to the numerical errors introduced by the MoM. The same property is better and better fulfilled for the $\lambda_0/100$, $\lambda_0/1000$ and $\lambda_0/10000$ plates except close to the edges, where the highest current density is flowing (+*Y* and −*Y* edges). Similar observations apply for property (316), in Figure 140 (p.219). Having measured how well these properties are fulfilled by the numerical implementation, it suffices to observe the current density on the illuminated face (-*Z*) only.

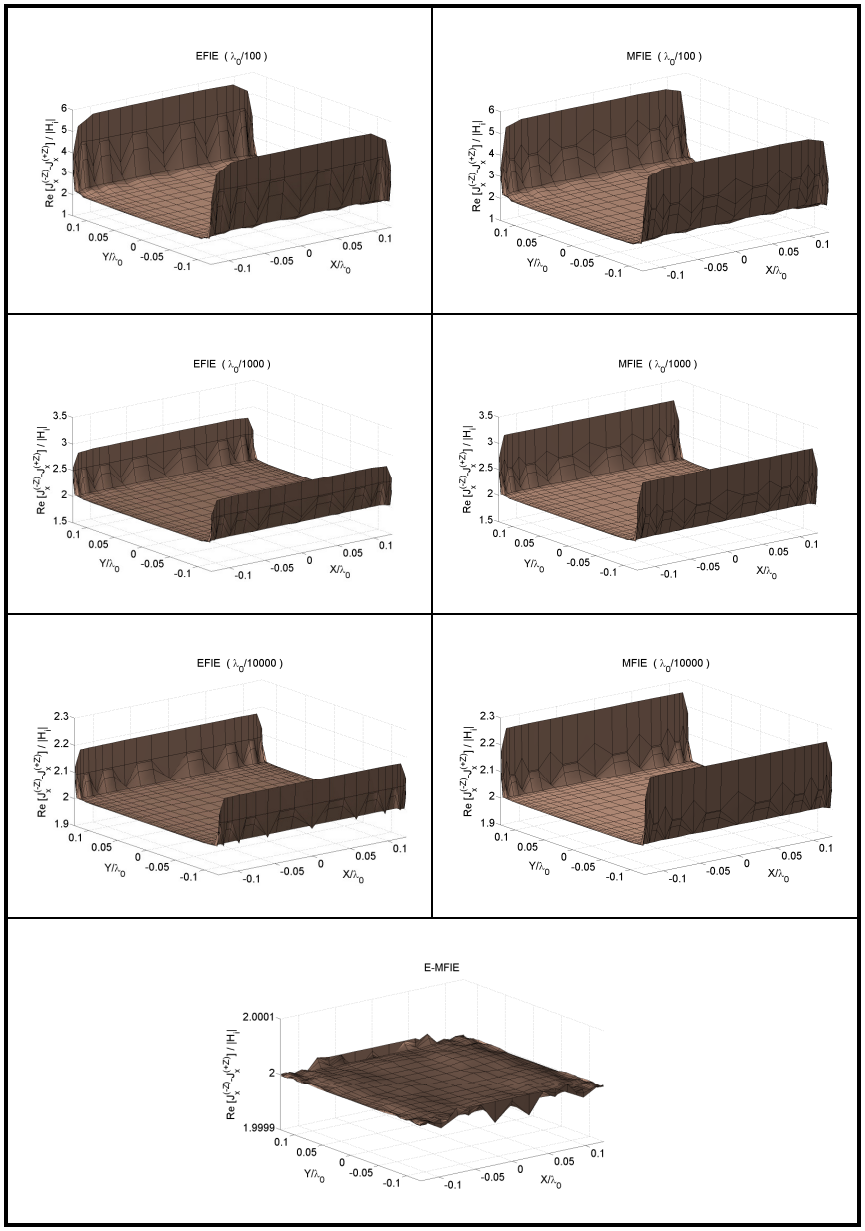

Figure 139 : $\mathrm{Re}[J_x^{(-Z)}] - \mathrm{Re}[J_x^{(+Z)}] = 2H_i$

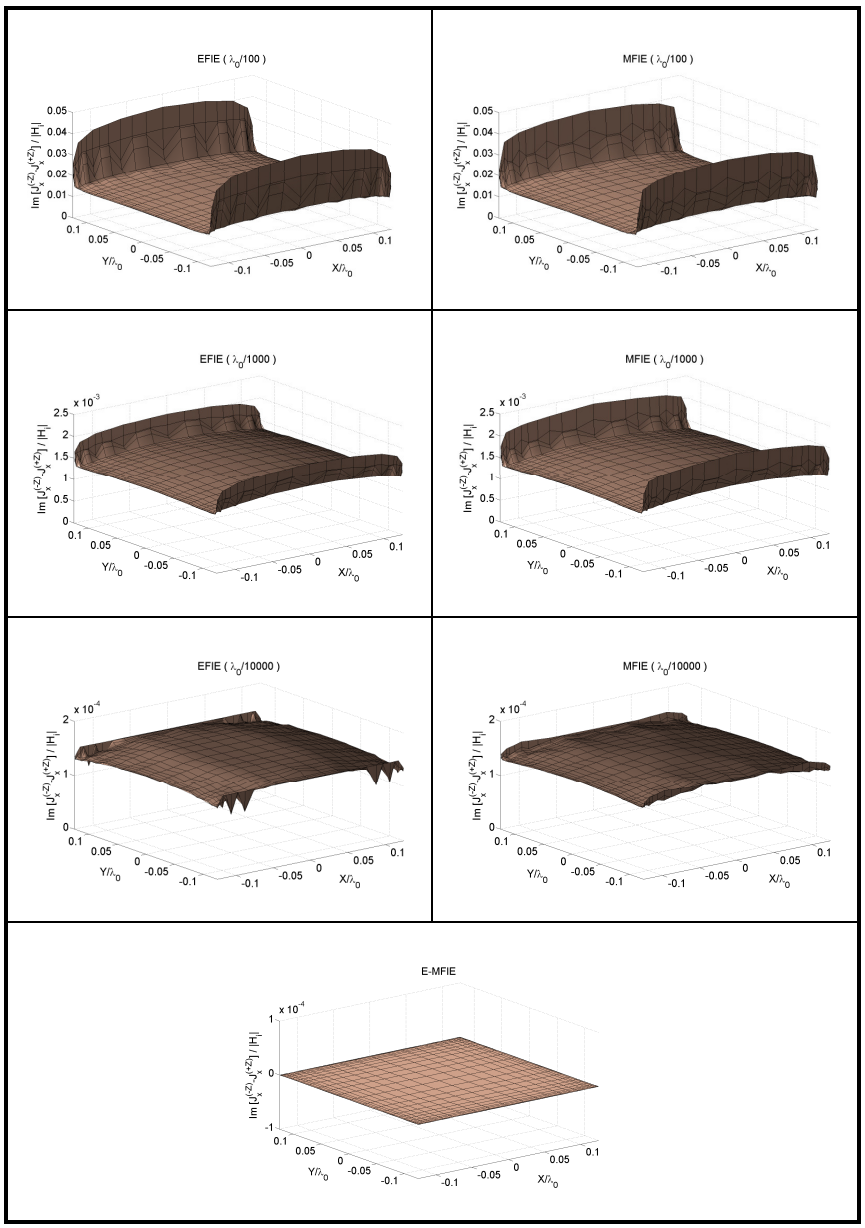

Figure 140 : $\mathrm{Im}[J_x^{(-Z)}] - \mathrm{Im}[J_x^{(+Z)}] = 0$

In Figure 141 we show $J_x/|H^{inc}|$ on the (-*Z*) face of the Log distributed mesh. The thin sides of the plate, absent on the sheet, are not considered here. J_x is the main component of the electric current density except close to the vertical edges. In the coloured plots of Figure 141, the 27x27=729 regularly distributed locations actually correspond to the Log distributed locations where $J_x/|H^{inc}|$ has been computed, namely at the centroids of all 9x9x4=324 triangles in the Log distributed mesh, or linearly interpolated between these 324 location to complete the regular 27x27 grid (refer to Figure 138b, p.215).

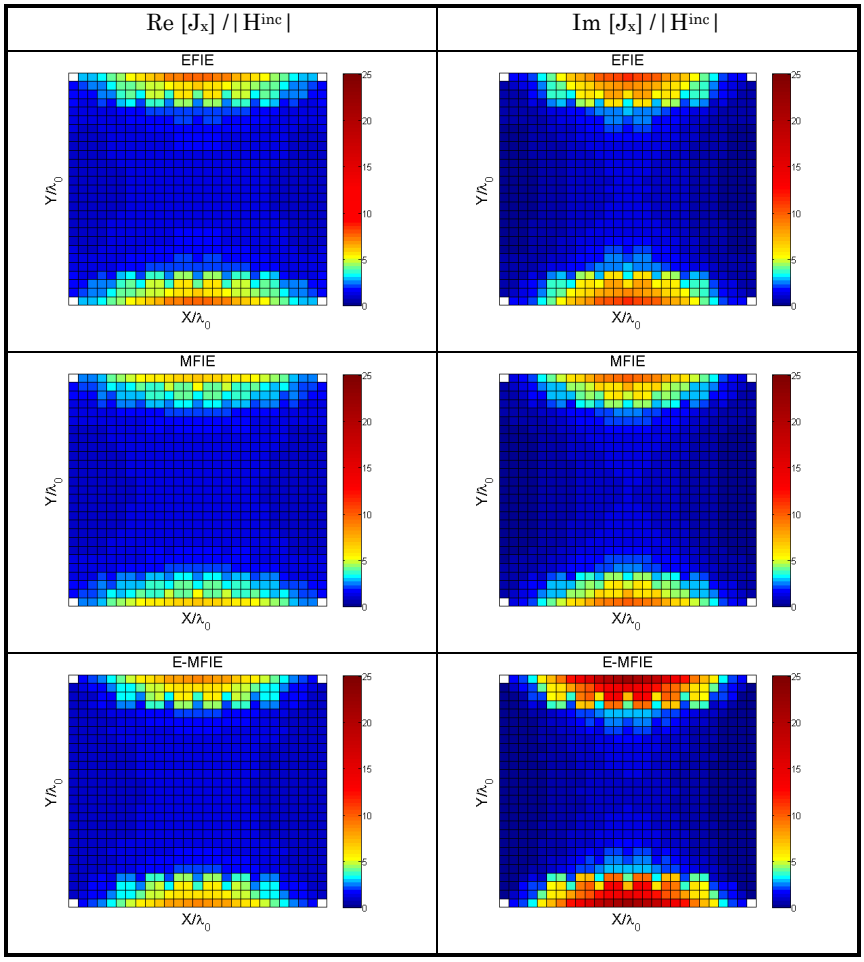

Figure 141 : $J_x/|H^{inc}|$ on the illuminated face (λ_0/100 plate)

In Figure 142 we compare $J_x/|H^{inc}|$ on the illuminated face (-Z) obtained with the tEFIE$^{\nabla G}$-f and tMFIE-nxf. Both solutions agree within 15%, except :

– For Re[J_x] and Im[J_x], in the "zigzag" area, where we know that the current density is badly approximated. We recall, with Figure 138 (p.215), that the zigzag area does not extend until the last triangles attached to the horizontal edge, where the difference between tEFIE$^{\nabla G}$-f and tMFIE-nxf does not exceed 15%

– For Im[J_x] only, in the middle of the vertical edge. But $J_x/|H^{inc}|$ is very low there (EFIE : 0,375 / MFIE : 0,280).

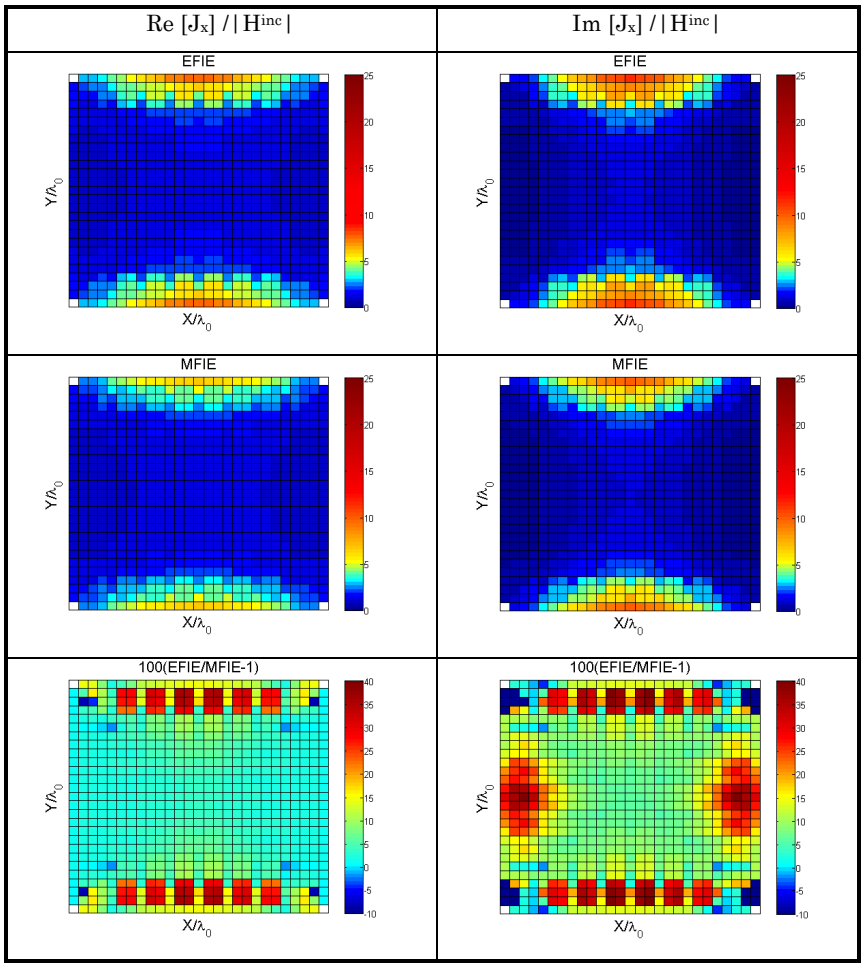

Figure 142 : $J_x/|H^{inc}|$ on the illuminated face (λ_0/100 plate)

In Figure 143 we show $J_y/|H^{inc}|$ on the illuminated face (*-Z*). Globally over the plate, J_y is ten times lower than J_x, except in the vicinity of the vertical edge, where J_y is higher than J_x.

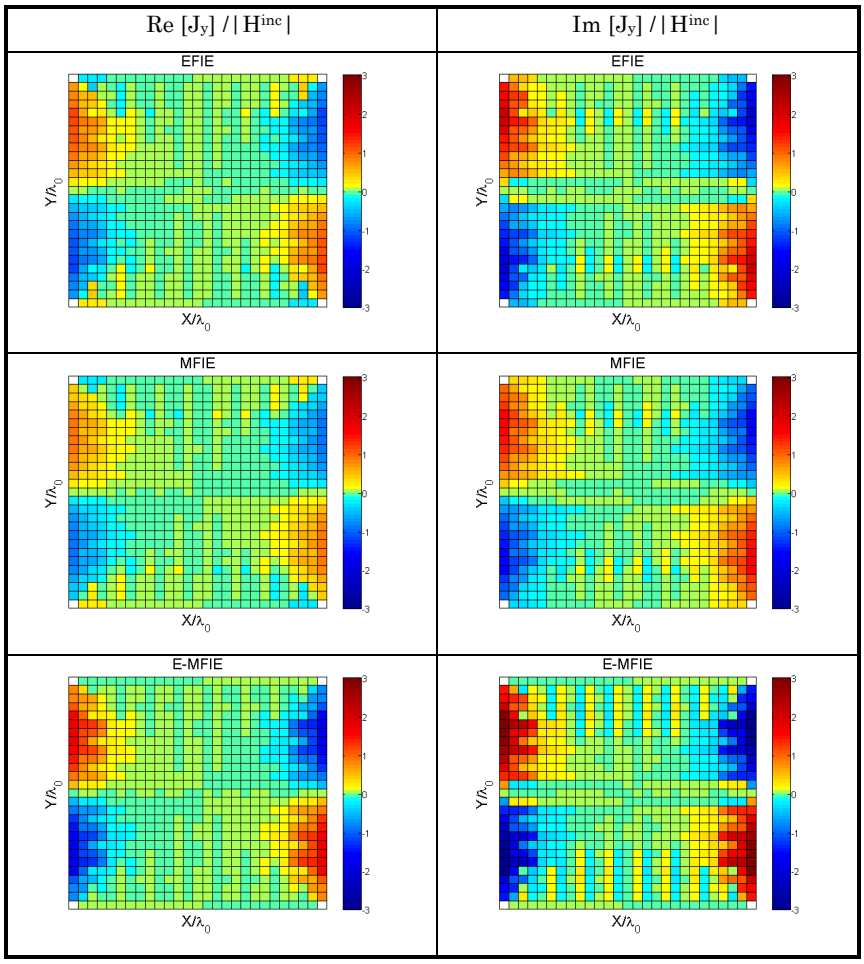

Figure 143 : $J_y/|H^{inc}|$ on the illuminated face (λ_0/100 plate)

In Figure 144 we compare $J_y/|H^{inc}|$ on the illuminated face (-*Z*) obtained with the tEFIE$^{\nabla G}$-f and tMFIE-nxf. As J_y is quite small over the sheet, the relative errors can become quite high and lose signification. Instead we present the absolute difference, showing that it remains quite small (~0,2) as compared to the actual value of the J_y and J_x current densities. Figure 146 (p.225) gives more insight and perspective in the actual differences between both solutions.

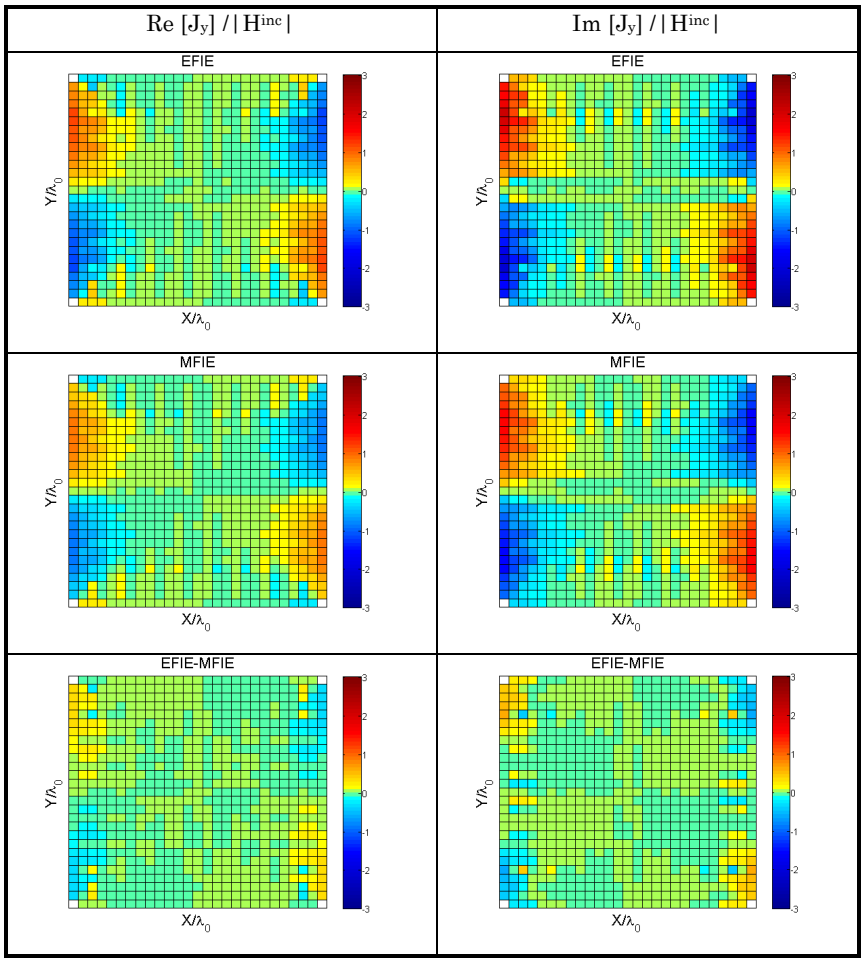

Figure 144 : Absolute difference EFIE-MFIE for $J_y/|H^{inc}|$

The electric surface current densities obtained with the tEFIE$^{\nabla G}$-f and tMFIE-nxf on the $\lambda_0/100$ PEC plate are superimposed in Figure 145. The color and size scaling is identical for the tEFIE$^{\nabla G}$-f and tMFIE-nxf solution on every picture, but it is different from one picture to the other, to optimize the color contrast in each of the three selected zones. In all three cases, the largest arrows correspond to the tEFIE$^{\nabla G}$-f solution.

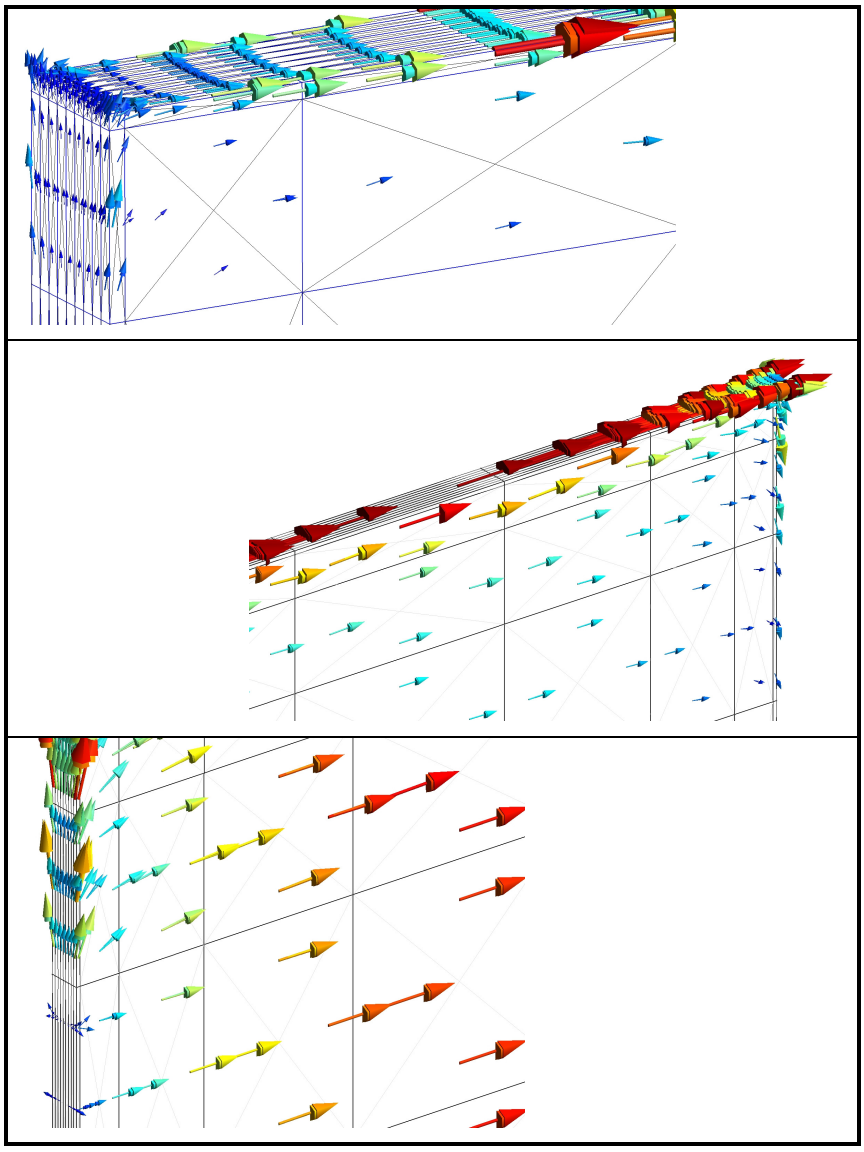

Figure 145 : Zoom on Im[J_x] close to the edges and corners

In Figure 146 we show how the tEFIE$^{\nabla G}$-f and tMFIE-nxf solutions for Im[J_x] evolve when the thickness of the plate is reduced. The tEFIE$^{\nabla G}$-f largest current density grows towards the E-MFIE solution, while the tMFIE-nxf largest current density slowly diminishes.

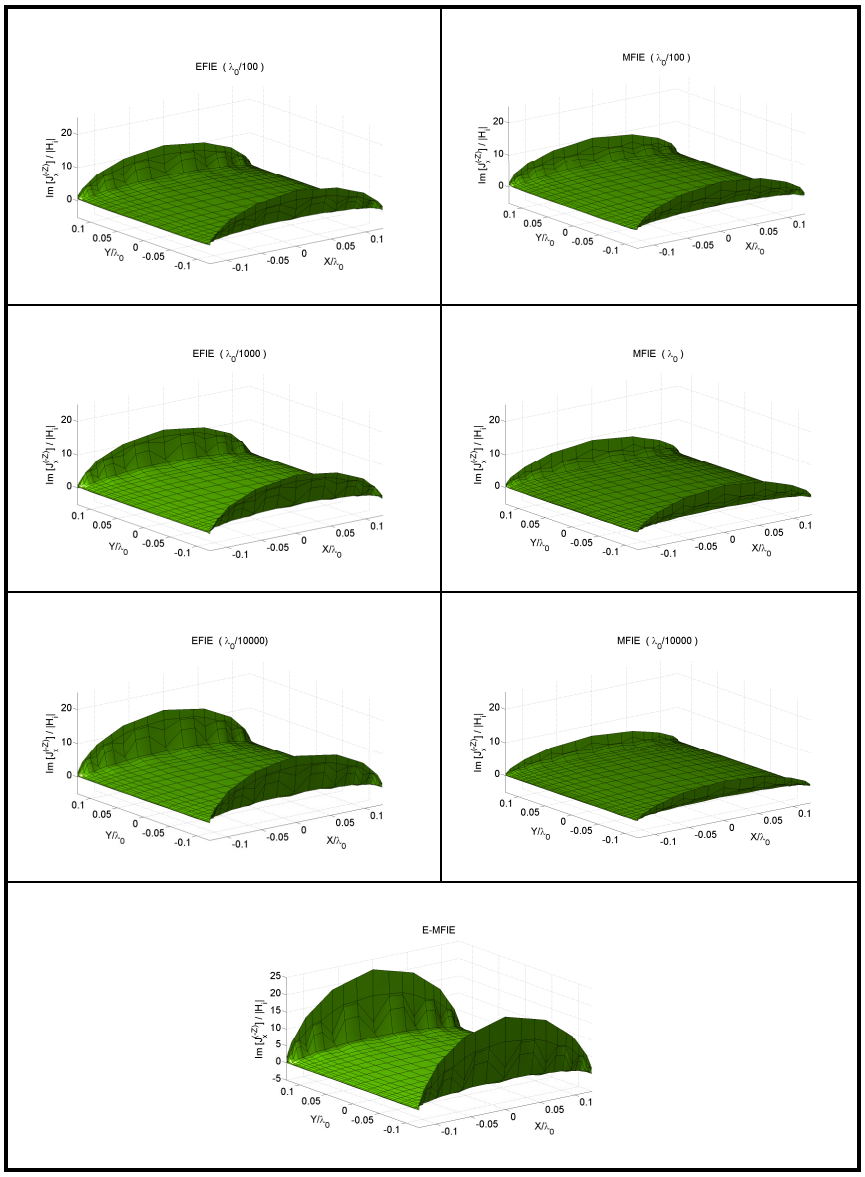

Figure 146 : Influence of the plate thickness on Im[J_x]/| H^{inc} |

In Figure 147 we quantify how the tEFIE$^{\nabla G}$-f solution for the thin PEC plate gets closer and closer to the E-MFIE solution for the PEC sheet, for the highest current density component : Im[J_x]. The pictures on the left cover the whole plate, including the edges where the high differences mask the lower differences on the rest of the plate. The pictures on the right exclude a small portion of the plate along the four edges, to better reveal the differences tEFIE$^{\nabla G}$-f / E-MFIE on the rest of the plate. It is apparent that the tEFIE$^{\nabla G}$-f converges towards the E-MFIE solution, but quite slowly along the four edges of the plate.

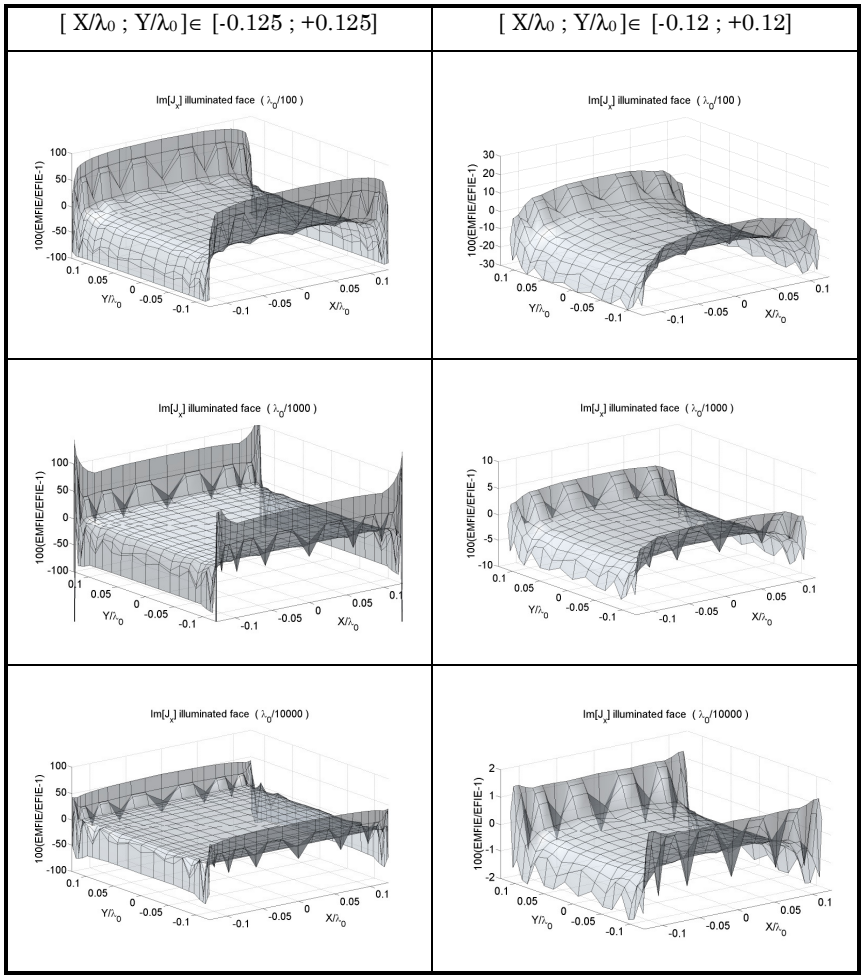

Figure 147 : Difference E-MFIE / EFIE for several plate thicknesses

6.10 PEC sheet on a thin dielectric plate

We analyze now the combination of the plate and the sheet already analyzed separately in §6.9, with the same Log distributed mesh to allow comparisons. The plate (in white and unmeshed in Figure 148) acts as a thin dielectric substrate while the PEC sheet (in grey, meshed) can be seen as a coating deposited just on top of the substrate, in contact with it, on the illuminated (-*Z*) side of the plate.

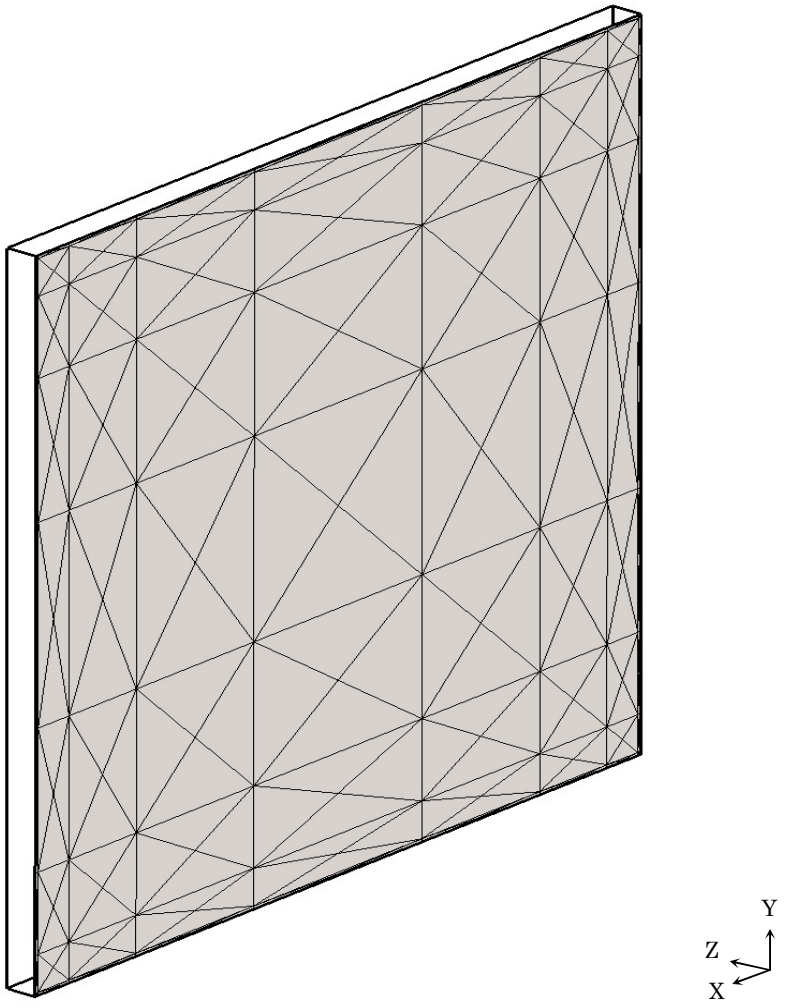

Figure 148 : PEC sheet on a dielectric plate

In this problem there are three domains : O is free space, D is the dielectric substrate and P is the PEC sheet. To refer to §3.3 and Table 5 (p.68), there are four types of sectors :

Table 30 : Sector table

D	P	O	Type	Nature
X		X	I	D
	X	X	II	E
X	X		III	E
X	X	X	IV	E

The type IV sectors correspond to the border (1-)edges of the PEC sheet. The type III (resp. : II) sectors correspond to the inner (2-)edges of the PEC sheet in contact with the substrate (resp. : free space) on the $+Z$ (resp. : $-Z$) side. None of the inner or border edges of the PEC sheet are fully embedded in only one domain, so the E-MFIE scheme is not required here. For all three 'E' sector types we may use either the EFIE-f or the MFIE-nxf (or a CFIE).

The Type I sectors correspond to all remaining (1-)edges that are not in contact with the PEC sheet. As dielectric sectors, they require a pair of independent integro-differential equations.

Finally, for sector types containing several dielectric domains (I and IV), a combination scheme must also be chosen (see §3.6), like PMCHWT or Müller.

6.10.1 PEC sheet on a $\varepsilon_r = 1$ substrate

Similarly to the example of the sphere in a half spherical $\varepsilon_r = 1$ shell (§6.3.1), the substrate is transparent and the electric current density on the PEC sheet should be identical to the current density obtained on the isolated PEC sheet.

For the isolated PEC sheet, the results obtained with the E-MFIE in §6.9 are re-used. For the PEC sheet on a transparent dielectric substrate, either the tEFIE$^{\nabla G}$-f or the tMFIE-nxf is used for the PEC sectors (II, III, IV) while the tEFIE$^{\nabla G}$-f and the tMFIE-f are used together for the dielectric sectors (I) in the PMCHWT-f-f scheme.

The integration scheme is :

	Self Term	$R_{min} < \lambda/100$	$R_{min} \in [\lambda/100; \lambda/10]$	$R_{min} > \lambda/10$	V
Inner	3		3	3	--
Outer	16		16	3	3

In Figure 149 we show $J_x/|H^{inc}|$ on the (-Z) face of the Log-distributed mesh. The thin sides of the plate, absent on the sheet, are not considered here. J_x is the main component of the electric surface current density except close to the vertical edges (see Figure 151, p.231). In the coloured plots of Figure 149, the 27x27=729 regularly distributed locations actually correspond to the Log distributed locations where $J_x/|H^{inc}|$ has been computed, namely at the centroids of all 9x9x4=324 triangles in the Log-distributed mesh, or linearly interpolated between these 324 location to complete the regular 27x27 grid.

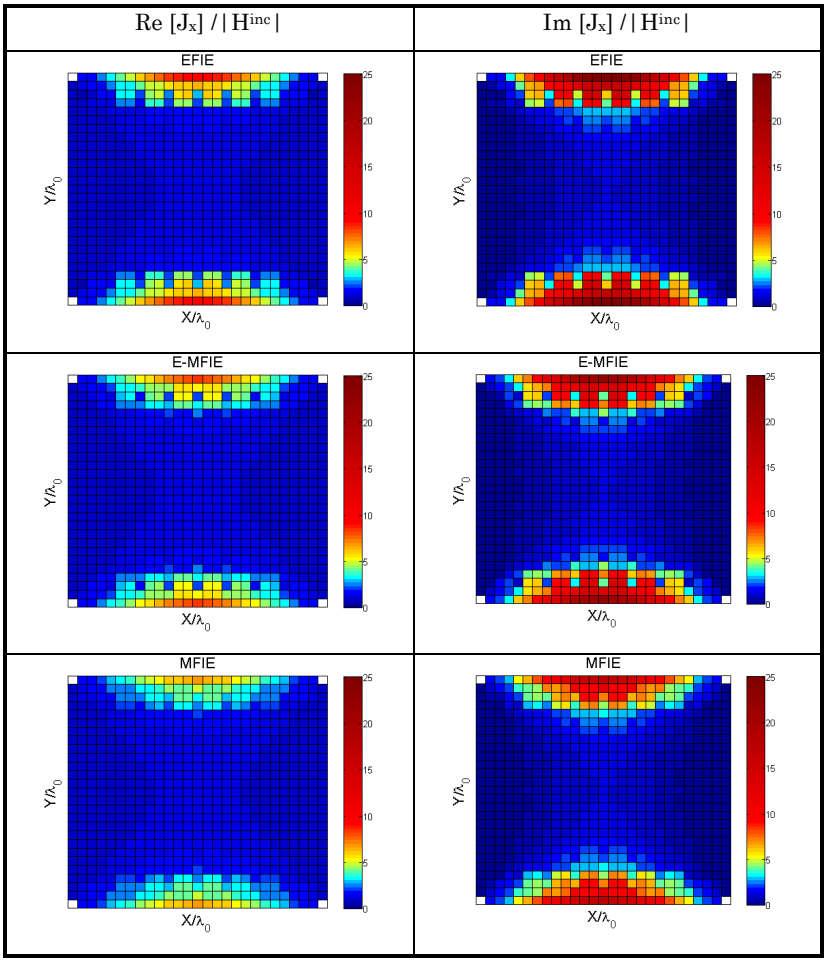

Figure 149 : J_x on the illuminated face with tEFIE$^{\nabla G}$-f ("EFIE" above), tMFIE-nxf ("MFIE" below) for the PEC sheet on the $\varepsilon_r = 1$ plate (PMCHWT-f-f based on tEFIE$^{\nabla G}$-f and tMFIE-f) and "E-MFIE" (in the middle) for the isolated PEC sheet

In Figure 150 we zoom on the very high current density flowing closest to the (top) horizontal edge. In the E-MFIE case the pair of quasi identical large arrows on the top correspond to the current density flowing on both sides of the sheet, visible there because of their large size. In the tEFIE$^{\nabla G}$-f case, the pair of large arrows across the horizontal edge have very dissimilar sizes (red and light blue). In the tMFIE-nxf case, the same pair of arrows exhibits quasi identical sizes (yellow).

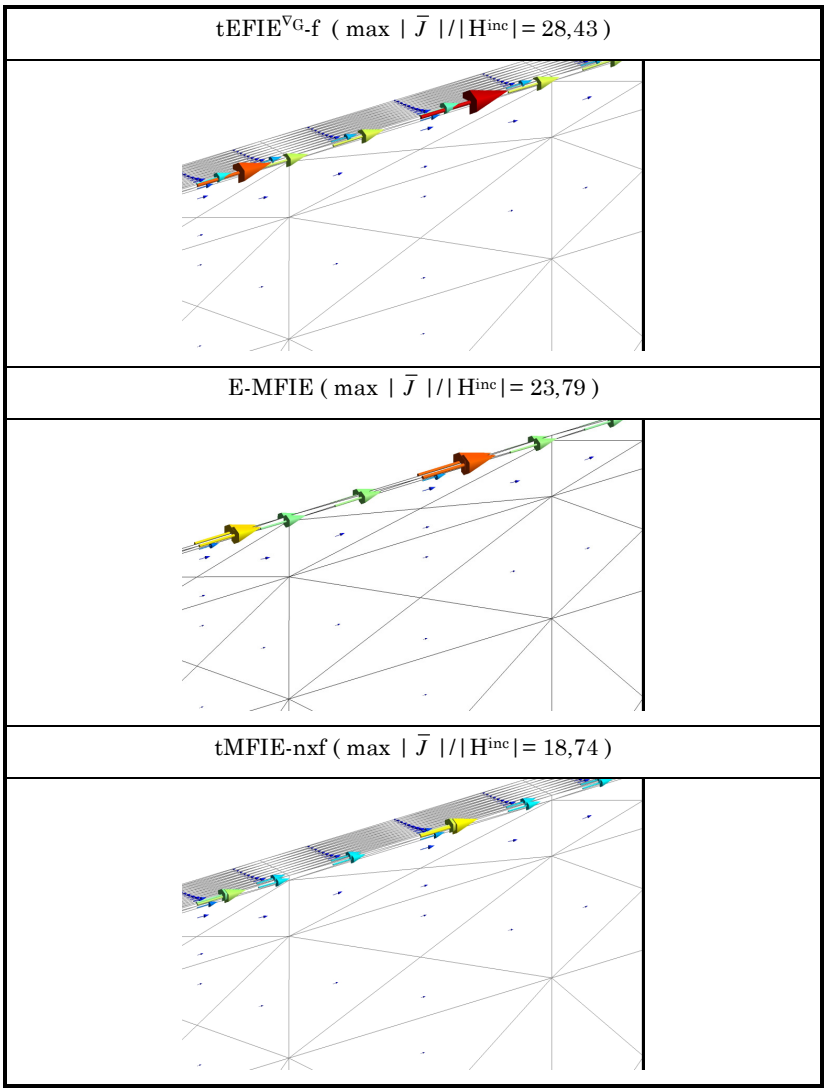

Figure 150 : Zoom on Im[J_x]/| H^{inc} | close to the horizontal edge

In Figure 151 we zoom on the high current density flowing closest to the (top) horizontal edge. The observations made for Figure 150 (p.230) can be transposed here. Note that these high currents flowing upwards (Y axis) cannot be seen on Figure 149 (p.229), where only J_x is shown.

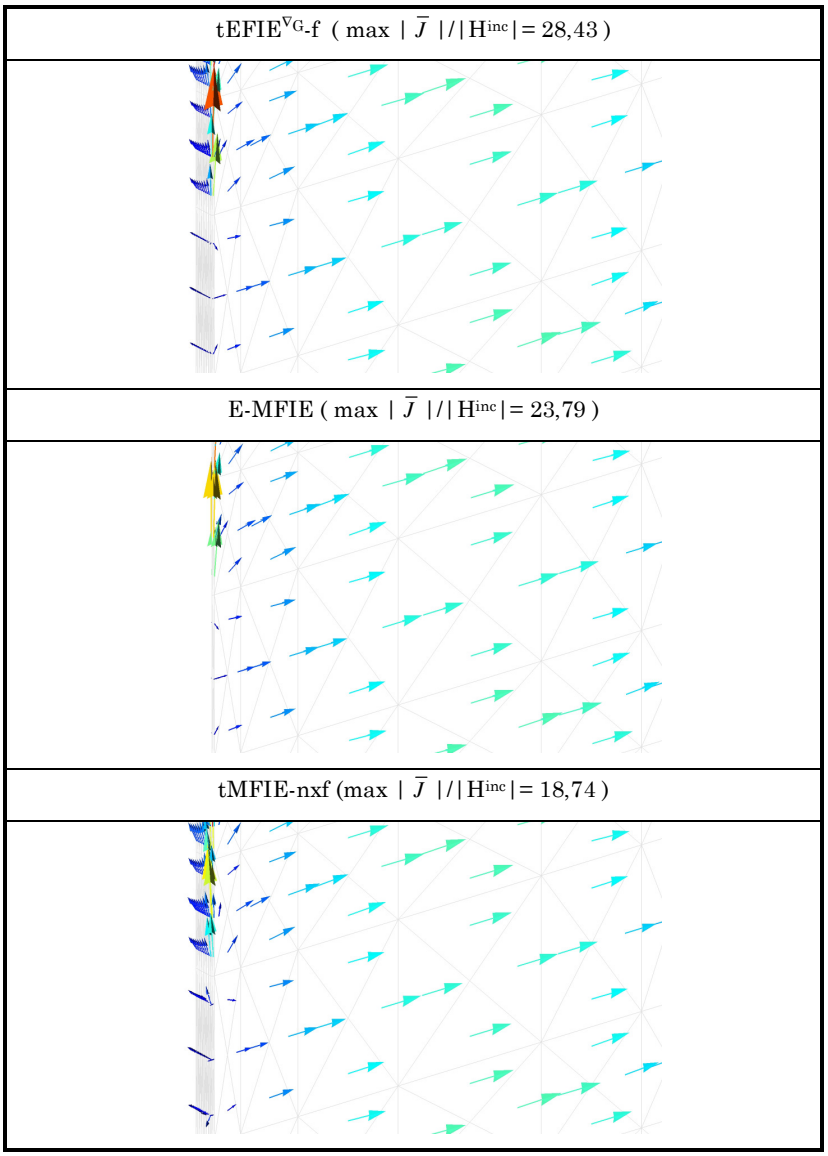

Figure 151 : Zoom on Im[J_x]/| H^{inc} | close to the vertical edge

We present in Figure 152 a quantitative comparison between tEFIE$^{\nabla G}$-f, tMFIE-nxf and E-MFIE for Re[J_x] and Im[J_x] on the illuminated face. Globally, they all agree within ±5% inside the plate, and within +50% for the largest current densities on the horizontal edges and for the very low currents close to the vertical edges. Again, the most significant differences occur in the "zigzag" area (see also Figure 142, p.221).

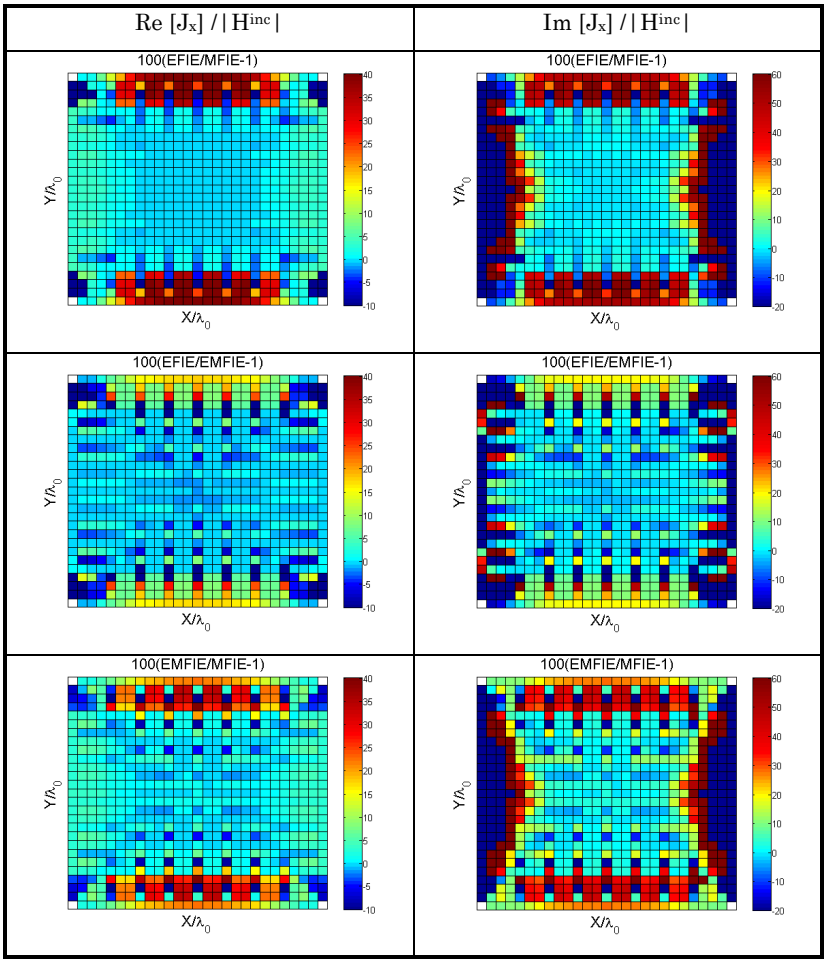

Figure 152 : Difference in percent between tEFIE$^{\nabla G}$-f, tMFIE-nxf and E-MFIE for J_x on the illuminated face of a PEC sheet deposited on a $\varepsilon_r = 1$ plate

There is no magnetic current density on the PEC sheet. Therefore we present in Figure 153 the magnetic current density M on the shadowed face (+Z) of the dielectric substrate. Due to the very large value of M close to the (corners of the) PEC sheet, the scale is logarithmic.

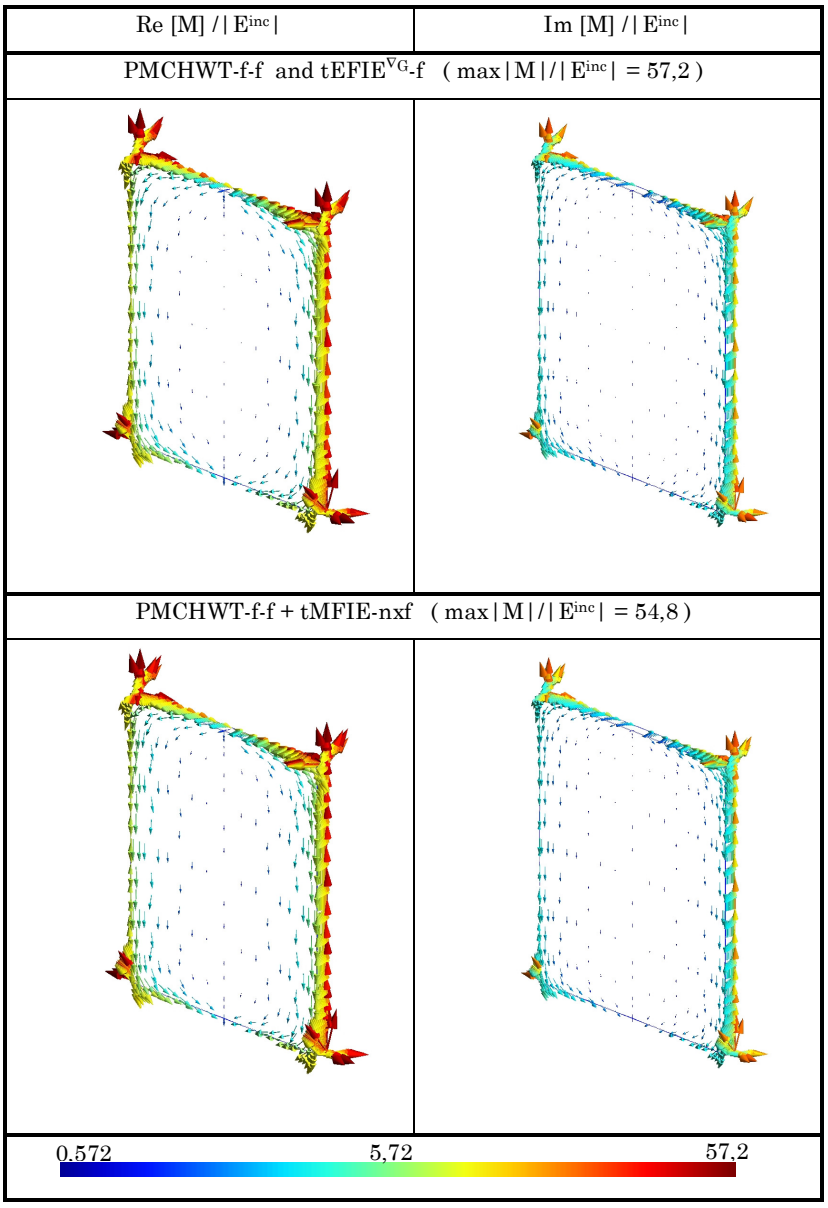

Figure 153 : M/| E^inc | on the shadow face of the $\varepsilon_r = 1$ plate + PEC sheet

6.10.2 PEC sheet on a $\varepsilon_r = 2$ substrate

In the next figures, we simply present the current densities on the plate and PEC sheet, with logarithmic scale.

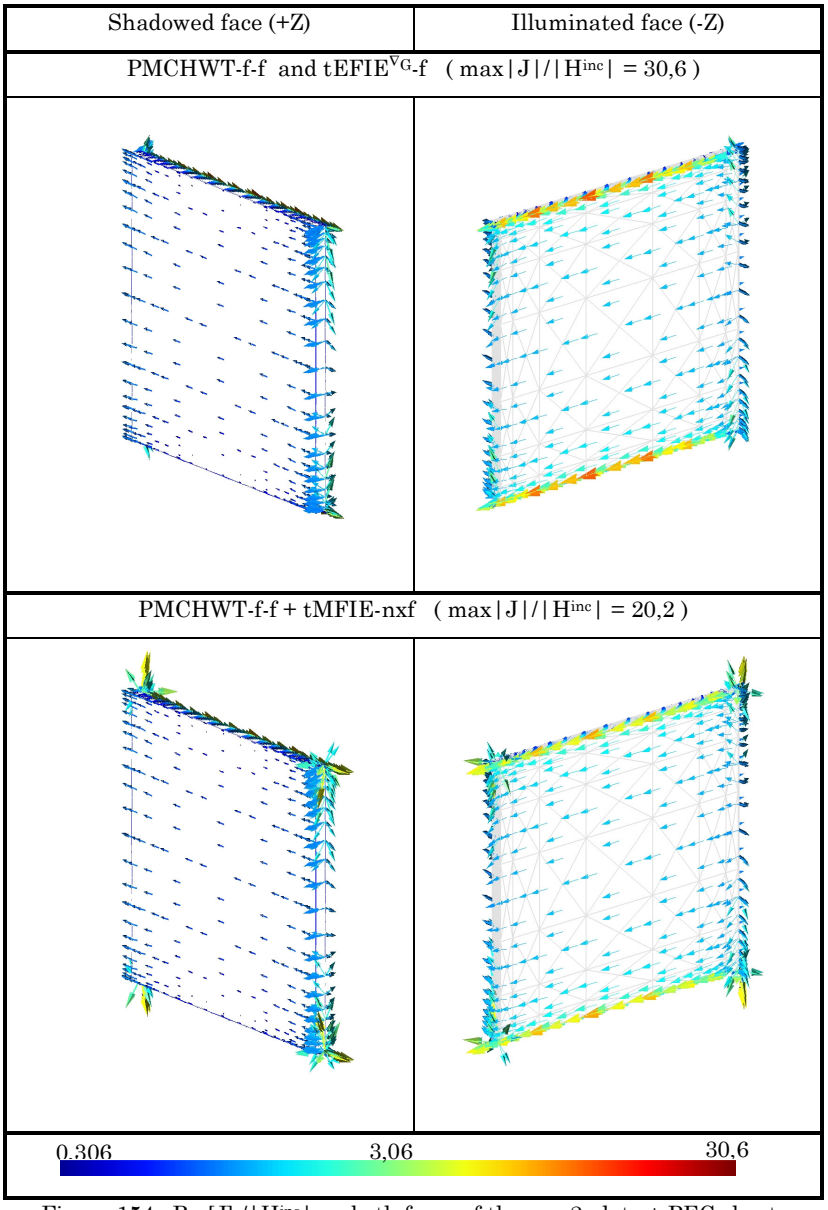

Figure 154 : Re [J] /|H^{inc}| on both faces of the $\varepsilon_r = 2$ plate + PEC sheet

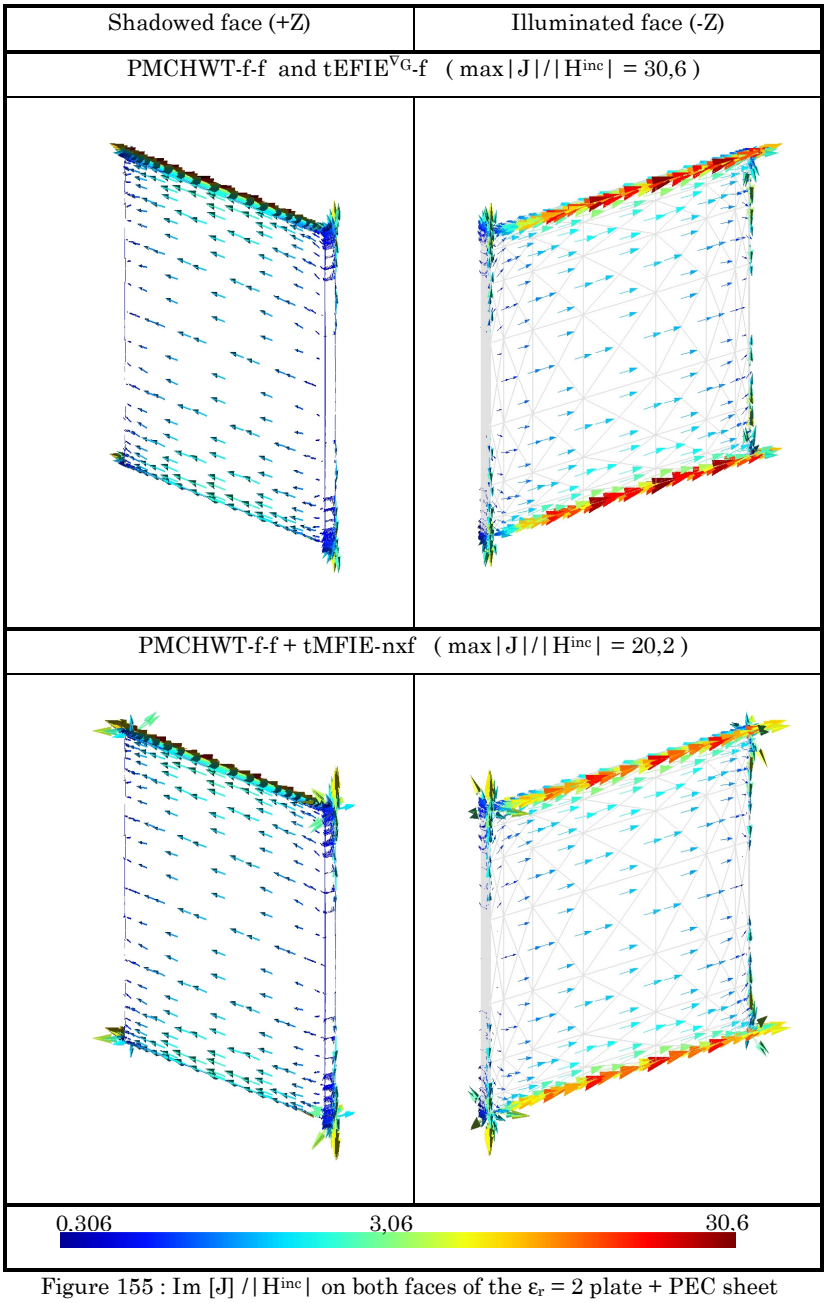

Figure 155 : Im [J] /|H^{inc}| on both faces of the ε_r = 2 plate + PEC sheet

In Figure 156 we present the magnetic current density on the shadowed face obtained with the PMCHWT-f-f and tEFIE$^{\nabla G}$-f, and compare it with the $\varepsilon_r = 1$ case.

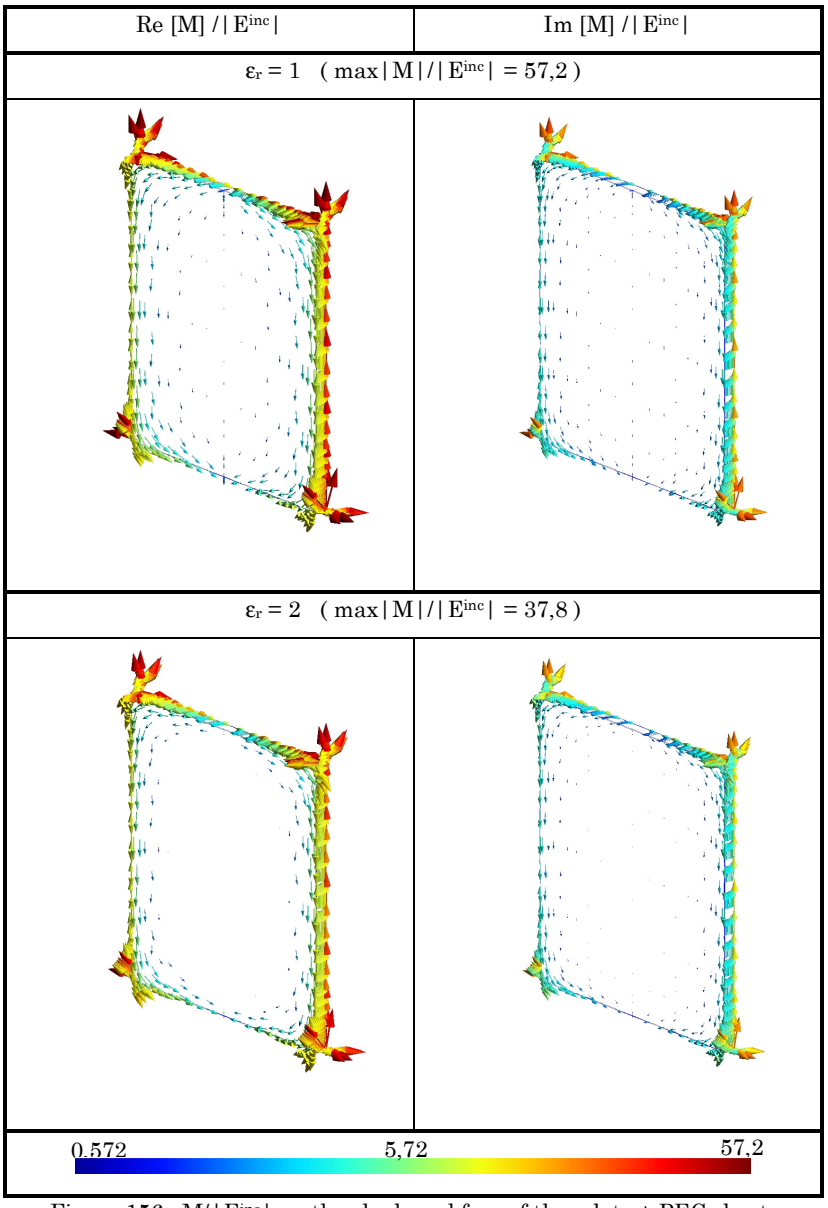

Figure 156 : M/ | E^{inc} | on the shadowed face of the plate + PEC sheet

In Figure 157 we present the magnetic current density on the shadowed face obtained with the PMCHWT-f-f + tMFIE-nxf, and compare it with the $\varepsilon_r = 1$ case.

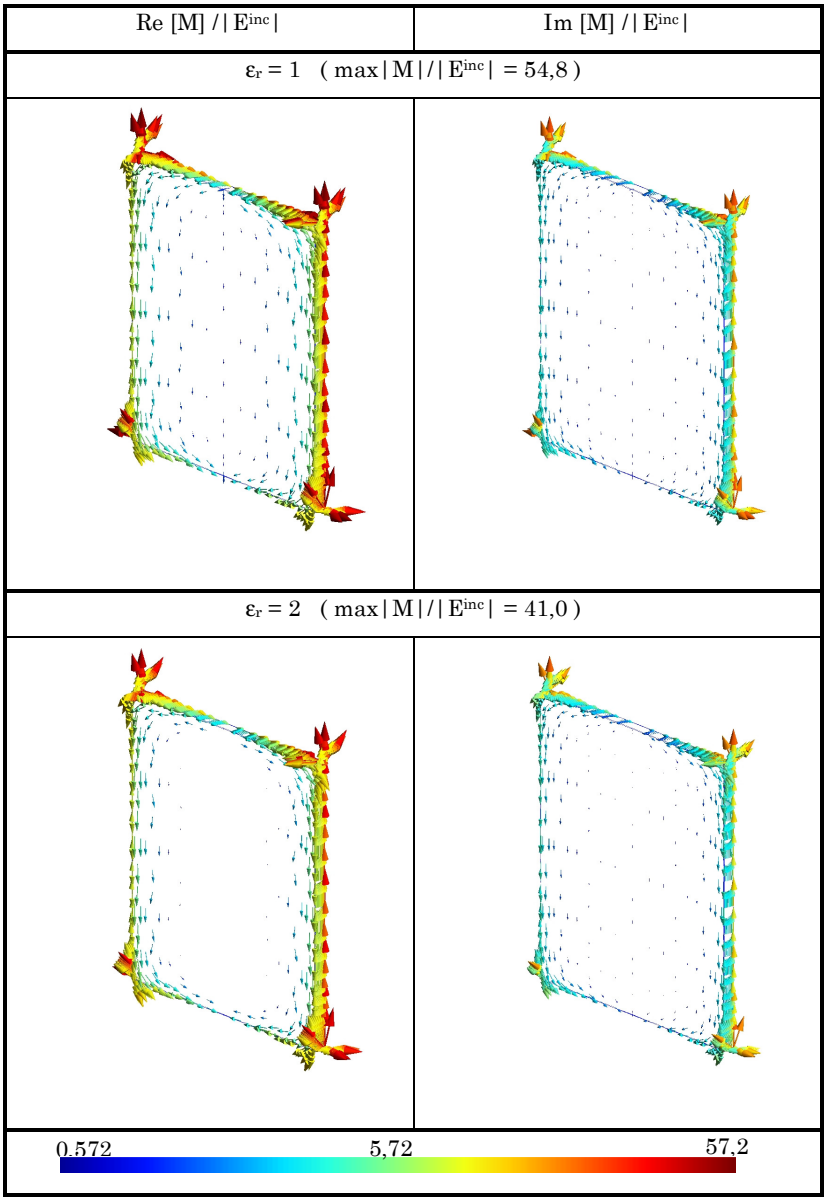

Figure 157 : $M/|E^{inc}|$ on the shadowed face of the dielectric plate

6.11 Solder Line

To illustrate the notion of solder line (§3.3.2), we analyze now a PEC bowtie, with gap or without gap, but with an air or a PEC solder line.

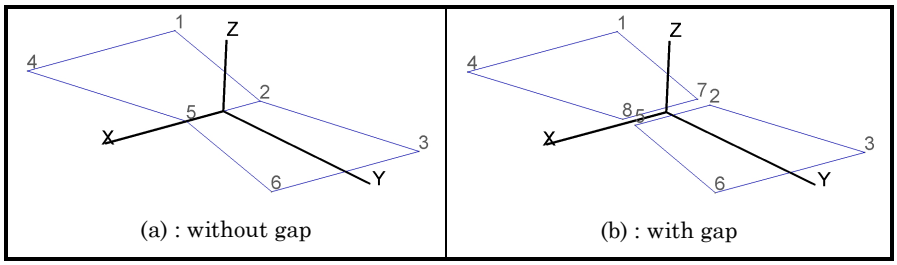

Figure 158 : Bowtie geometry

It is illuminated by a plane wave incoming from the spherical coordinates $(\theta, \varphi) = (45°,90°)$ and is polarized along X ($\alpha = 90°$).

The coordinates of the 6 nodes defining the bowtie of Figure 158a are :

	1	2	3	4	5	6
X/λ_0	-1/4	-1/8	-1/4	+1/4	+1/8	+1/4
Y/λ_0	-1/2	0	+1/2	-1/2	0	+1/2
Z/λ_0	0	0	0	0	0	0

The coordinates of the 8 nodes defining the bowtie of Figure 158b are :

	1	2	3	4	5	6	7	8
X/λ_0	-1/4	-1/8	-1/4	+1/4	+1/8	+1/4	-1/8	+1/8
Y/λ_0	-1/2	+1/40	+1/2	-1/2	+1/40	+1/2	-1/40	-1/40
Z/λ_0	0	0	0	0	0	0	0	0

The largest side of any triangle in the mesh is $\lambda_0/10$. To obtain the current densities on both sides of the sheet, the E-MFIE formulation has been used (see §4.4). The following integration scheme has been used :

	Self Term	$R_{min} < \lambda/100$	$R_{min} \in [\lambda/100; \lambda/10]$	$R_{min} > \lambda/10$	V
Inner	3		3	3	--
Outer	16		3	3	3

Figure 159 (p.239) and Figure 160 (p.240) show that the electric current densities on both sides of a $\lambda_0/20$ air gap, or its limit case, the air solder line, are flowing independently. When the two PEC parts of the bowtie are joined with a PEC solder line, making it a unique PEC sheet, the electrical current density exhibits a continuous flow across the PEC solder line.

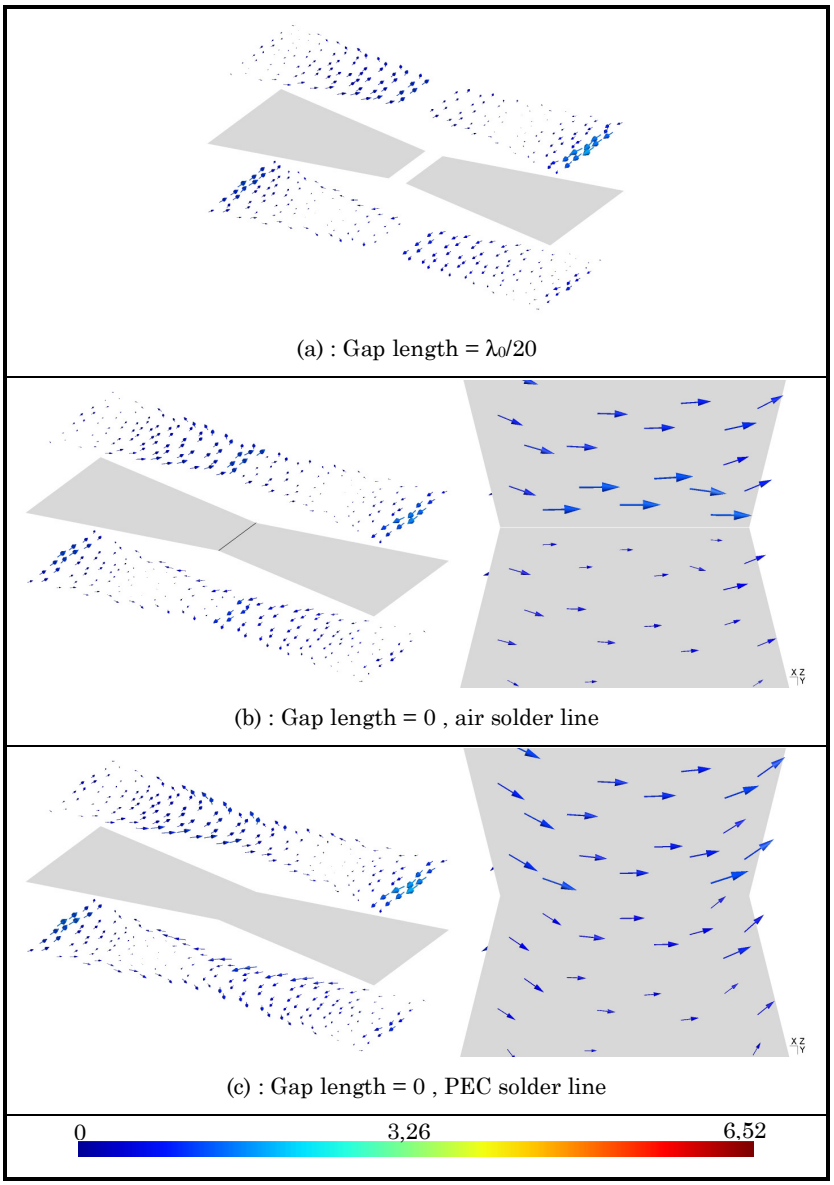

Figure 159 : Re[J]/|H^{inc}| on both sides of the PEC sheet(s)

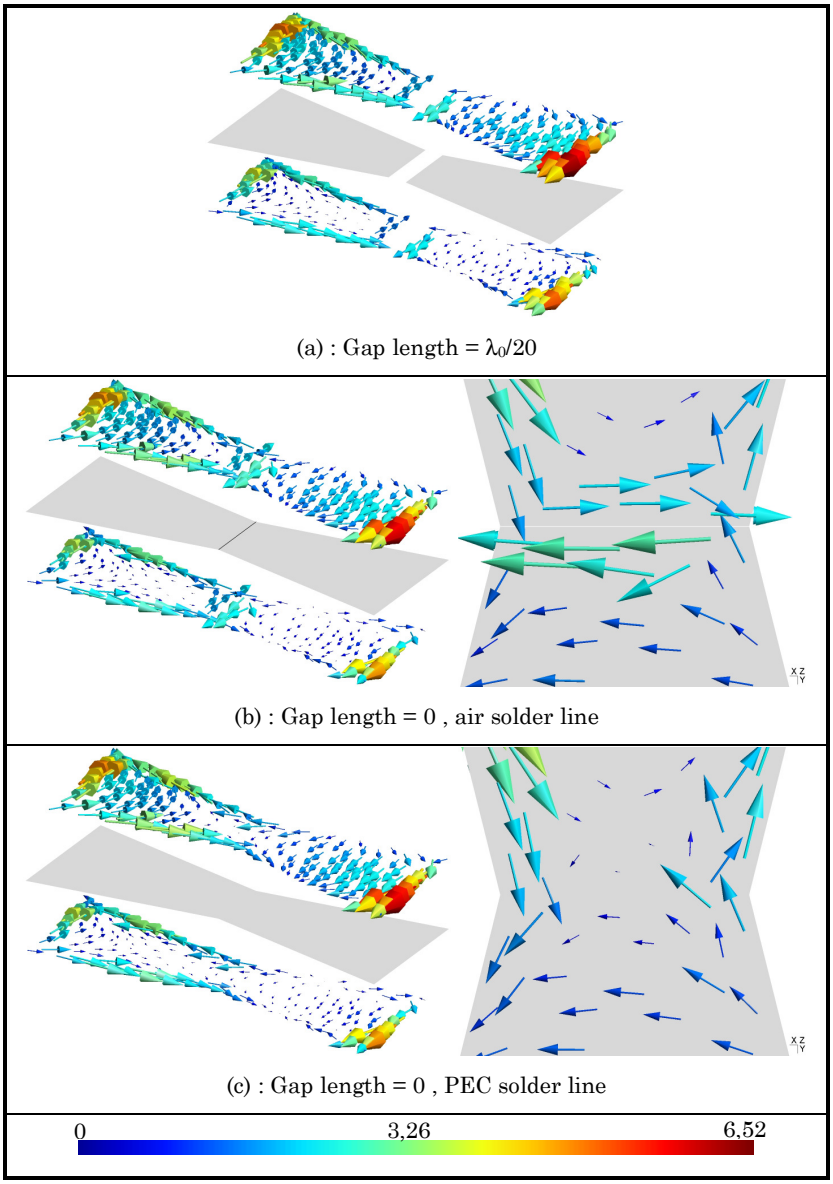

Figure 160 : Im[J]/|H^{inc}| on both sides of the PEC sheet(s)

6.12 Examples where a 16 nodes quadrature is necessary

6.12.1 Thin dielectric $\varepsilon_r = 1$ plate

A ($\lambda_0/4$ x $\lambda_0/4$ x $\lambda_0/500$) plate is illuminated by a plane wave characterized by (θ, φ, α) = (45°, 0°, 180°)[7]. The mesh is regular with characteristic dimension $\lambda_0/40$. The MoM solutions obtained with the following integration schemes are compared against the exact analytical solution (see §6.1.4) :

	Self Term	$R_{min} < \lambda/100$	$R_{min} \in [\lambda/100; \lambda/10]$	$R_{min} > \lambda/10$	V
Inner	3		3	3	--
Outer	variable		3	3	3

The average relative errors obtained in function of the number of nodes in the outer integral when $R_{min} < \lambda/100$ are listed in Table 31. The necessity to use at least 16 nodes quadrature is made even more evident in Figure 161 (p.242) and Figure 162 (p.243).

Table 31 : Average relative error with PMCHWT-f-f (tEFIE$^{\nabla_f}$-f)

	Re			Im			Re			Im		
	Jx	Jy	Jz	Jx	Jy	Jz	Mx	My	Mz	Mx	My	Mz
3	16,2	13,3	4,52	13,0	16,9	4,10	19,8	24,7	6,01	22,4	17,1	5,99
7	16,0	14,9	4,16	9,52	6,76	2,41	10,8	8,01	3,14	22,6	19,5	5,89
12	3,51	3,45	0,77	2,69	2,98	0,61	2,90	2,69	0,56	5,15	5,24	1,01
16	0,48	0,54	0,05	1,11	1,34	0,06	0,64	0,72	0,09	1,31	1,31	0,19
19	0,78	0,81	0,14	1,49	1,62	0,23	1,19	1,07	0,15	1,86	2,01	0,26
25	0,47	0,52	0,05	1,18	1,36	0,10	0,69	0,62	0,08	1,45	1,57	0,20
42	0,33	0,43	0,02	1,04	1,28	0,05	0,34	0,48	0,06	1,18	1,20	0,18
61	0,37	0,42	0,03	1,09	1,28	0,07	0,52	0,46	0,07	1,29	1,36	0,19
73	0,33	0,40	0,02	1,03	1,24	0,05	0,39	0,43	0,06	1,19	1,24	0,18

[7] See §6.1.1 for the definition of those angles

PMCHWT-f-f (tEFIE$^{\nabla f}$-f)	PMCHWT-f-f (tEFIE$^{\nabla G}$-f)
3 integration nodes	
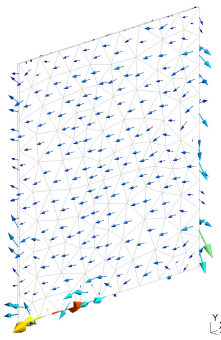	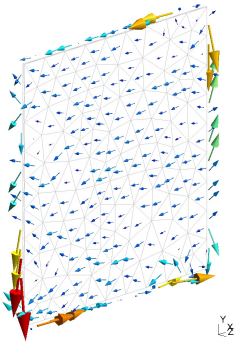
7 integration nodes	
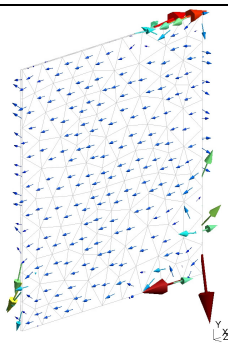	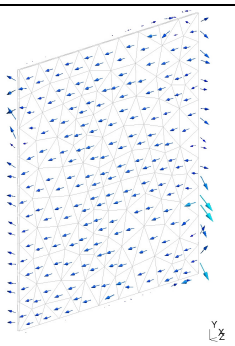
16 integration nodes	
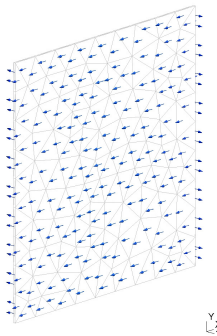	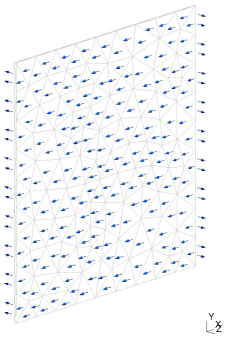

Figure 161 : Re[J]/|H^{inc}| on a ($\lambda_0/4$ x $\lambda_0/4$ x $\lambda_0/500$) plate with $\varepsilon_r = 1$

PMCHWT-f-f and tEFIE$^{\nabla f}$-f	PMCHWT-f-f and tEFIE$^{\nabla G}$-f
3 integration nodes	
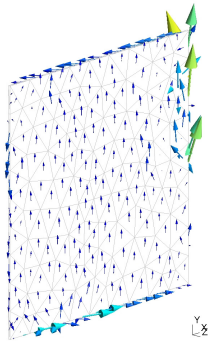	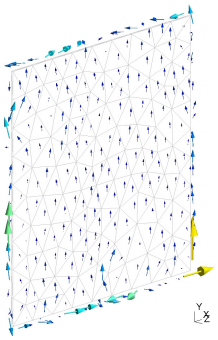
7 integration nodes	
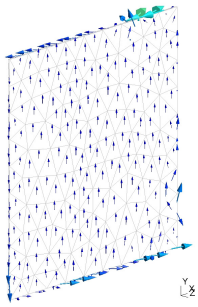	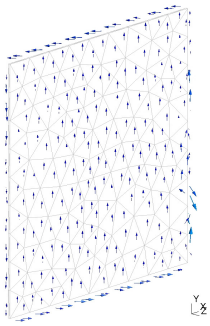
16 integration nodes	
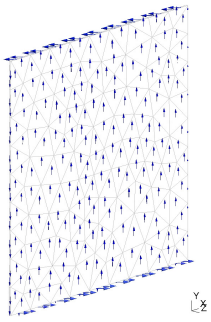	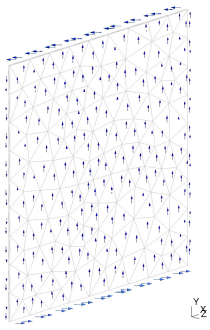

Figure 162 : Re[M]/|E^{inc}| on a ($\lambda_0/4$ x $\lambda_0/4$ x $\lambda_0/500$) plate with $\varepsilon_r = 1$

6.12.2 PEC and dielectric pyramids

We analyze a PEC pyramid on top of a dielectric $\varepsilon_r = 1$ pyramid, to show that accurate integration of the singular terms in the Z matrix is indispensable, even for such a simple example.

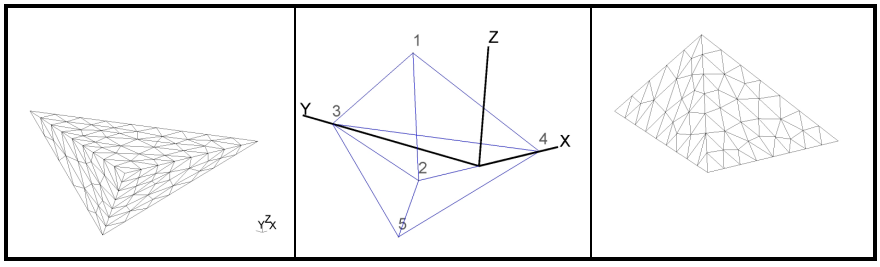

Figure 163 : Lower dielectric and higher PEC pyramid with meshes

It is illuminated by a plane wave incoming from the spherical coordinates $(\theta, \varphi) = (45°,90°)$ and is polarized in the YZ plane ($\alpha = 0°$).

The coordinates of the 5 nodes defining the two pyramids are :

	X/λ_0	Y/λ_0	Z/λ_0
1	0	1/30	1/30
2	-1/30	0	0
3	0	2/30	0
4	1/30	0	0
5	0	1/30	-1/30

The largest side of any triangle in the mesh is $\lambda_0/81$. The following integration schemes have been used :

	Self Term	$R_{min} < \lambda/100$	$R_{min} \in [\lambda/100; \lambda/10]$	$R_{min} > \lambda/10$	V
Inner	3		3	3	--
Outer	variable		3	3	3

In Figure 164 (p.245) we limit the comparisons to Im[J], though similar observations can be made for Re[J]. In Figure 165 (p.246) we also give the tEFIE$^{\nabla G}$-f and tMFIE-nxf solution for the PEC pyramid alone, obtained with a 16 nodes quadrature in the outer integral when $R_{min} < \lambda/100$. The solution for J on the PEC pyramid on top of the $\varepsilon_r = 1$ pyramid must be very similar, as in §6.10.1.

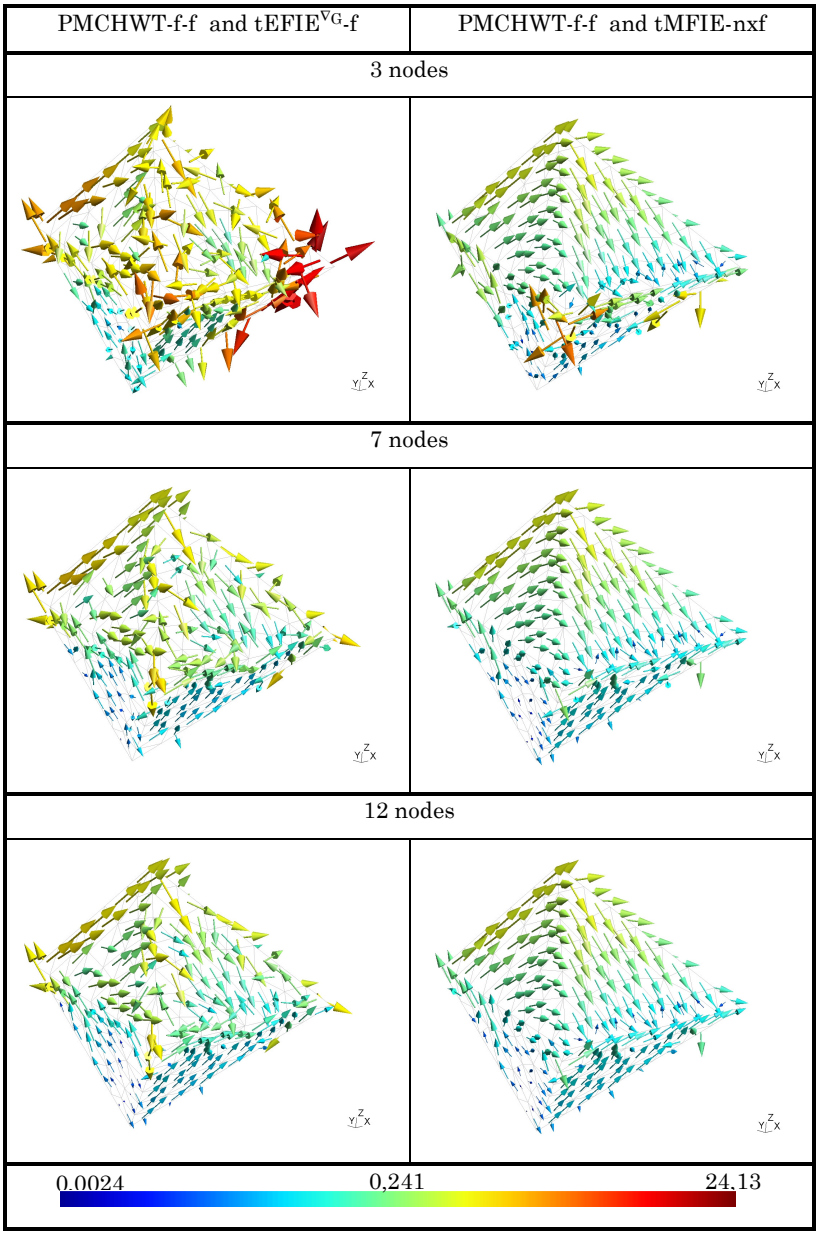

Figure 164 : Im[J]/|H^{inc}| : poor solutions with 3, 7 and 12 nodes

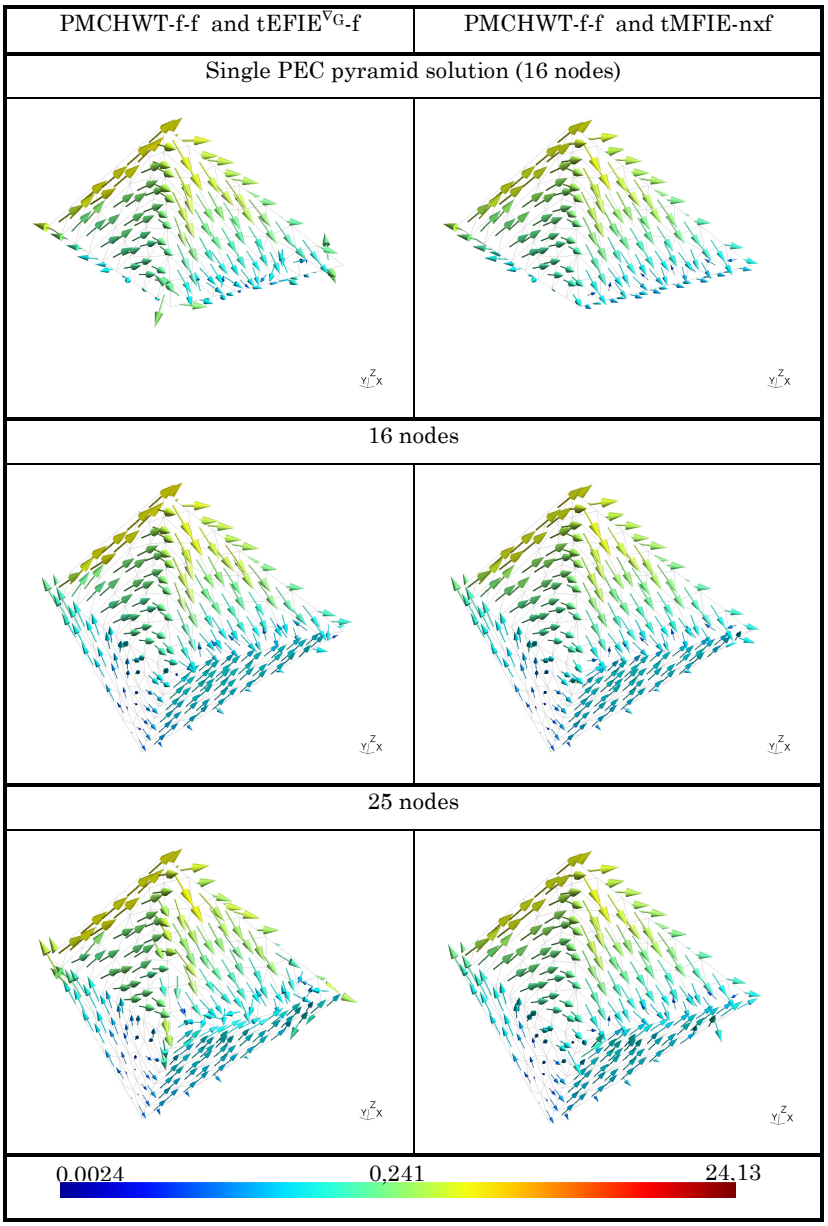

Figure 165 : Im[J]/|H^{inc}| : Reference and good solutions (16, 25 nodes)

6.13 Summary

In this chapter many examples have been selected to illustrate the theories and concepts exposed in every chapter of Part I : the new theorems about flat perfectly conducting sheets demonstrated in chapter 1, the issues raised in chapter 2 regarding the use of RWG or curl conforming basis functions, the solder line introduced in chapter 3, as well as the solution for composite bodies, the E-MFIE formulation elaborated in chapter 4, two examples supporting the accuracy analysis in chapter 5.

To fulfill one of the main objectives of this book, the presentation of those examples in an evolutive sequence, from the sphere to the thin plate via a rounded cube and then a regular cube, allowed to measure and compare the accuracy and performances of various formulations for most examples. Aside the exact Mie solution for dielectric or perfectly conducting spheres, the void dielectric reference solution and the existence of two independent solutions for perfectly conducting volumes, the tEFIE and the tMFIE, were of valuable help in this process. The lowest average and maximum errors were observed for the homogeneously meshed sphere. A progressive degradation of these errors from several percent up to fifty percent was put in evidence across the successive examples, due to the presence of rounded or sharp edges and tips, or to the inhomogeneity of the mesh.

The presented and analyzed results are exclusively the current densities, as opposed to the usual practice where global values are preferred, such as radiation patterns, scattering coefficients or impedances. We believe that those aggregate values hide many of the behaviors and phenomenons revealed only with careful observation of the current densities. This way we were able to precisely localize and quantify the differences between the tEFIE and the tMFIE, showing that the tEFIE overestimates current densities close to edges while the opposite is true for the tMFIE. We also observed quantitatively how these differences are attenuated when the mesh density is increased. Only a close look at the current densities could reveal the weaknesses of RWG basis functions close to edges, but also on the thin side of a dielectric plate and even on the sphere. Finally, the necessity to perform careful evaluation of the singular integrals - using for example our 16 or 42 nodes polynomial quadratures - could only be detected and explained by the observation of localized erratic current densities.

To greatly reduce the amount of triangles required to finely mesh the close vicinity of edges and tips, while allowing a detailed capture of the high gradients in current density flowing there, original log-distributed meshes have been proposed that use (very) elongated triangles. Though irregular triangles are mostly considered as bad elements to be avoided in a mesh, we have shown in this book that they can be used in confidence, provided the integrations are performed with enough accuracy and that the condition number is maintained below an acceptable level.

[1] G.Mie, *Ann. Physik*, 25, 377, 1908.

[2] K.F. Warnick, *Numerical Analysis for Electromagnetic Integral Equations*, Artech House, 2008.

Conclusion

This book was devoted to the resolution of the electromagnetic scattering by linear, homogeneous and isotropic three-dimensional bodies with the Method of Moments. Despite the fact that this problem has been tackled in many ways by hundreds of researchers for more than half a century now, significant improvements or even new contributions to the vast amount of already available results proved to be possible.

The exact electromagnetic theory underlying the Method of Moments has been reviewed, extended and generalized. In this process, Maxwell's equations are transformed into integral equations where the unknowns appear under the form of equivalent current densities, electric and/or magnetic, defined at the bounding surface of every non perfectly conducting volumic homogenous region. The correct vector forms of the electric and magnetic integral equations valid in the case of arbitrary sheets have been established through an original demonstration, taking into account the edge singularities. Those new equations have permitted to demonstrate a dual theorem that constitutes the exact generalisation of the physical optics approximation. They also allowed to fully understand why the MFIE cannot be used to solve sheets, with the additional consequence that a new formulation was added to the arsenal of the Method of Moments, named E-MFIE, that fully solves perfectly conducting sheets on both faces. With the introduction of new contracted notations, the exact theory and equations describing any combination of geometries (volumes or sheets) and materials (dielectric or perfect conductors) has been cast into canonical forms, putting in evidence the duality between the electric and magnetic formulations. Starting from the full vector expressions, new formulations based on the normal components has been proposed aside the already existing ones, based on the tangential components.

The Method of Moments was then introduced in a practical way by discretizing the canonical expressions based on the tangential components, while maintaining the highest level of generality to allow a detailed and critical review of the basis and testing functions. Curl conforming basis functions are sometimes encountered in the literature, but we explain in Part I and illustrate in Part II why they must be banned. Also the widely used Rao Wilton Glisson (RWG) basis functions are shown to be only partly linear, and the consequences thereof are explained in Part I and visualized by several concrete examples in Part II. Finally, a series of considerations about the crucial step of testing reveal why some choices are optimal, acceptable or catastrophic for both the tangential and normal components based formulations. Again, many examples and comparisons from Part II support the assertions made in Part I.

Similarly to the generalization step made with the exact theory, the Method of Moments has been generalized and made applicable to any combination of perfectly conducting and dielectric material within a simple and universal resolution framework. To this end, the original concepts of singular edge, solder line, and RWG sector table have been introduced in Part I and illustrated in Part II. The construction of the global Z matrix, and in particular the combination step, is fully explained in the most general case of dielectric sectors. Perfectly conducting sectors are presented as a special case of dielectric sectors, with the exception of embedded sheets, that required the development of the E-MFIE, a novel method combining the electric and magnetic formulations. With the

E-MFIE, sheets can now be solved in the same universal way as dielectric or perfectly conducting volumes.

Having at our disposal an all purpose and very general method with solid theoretical foundations, we naturally selected for the practical computation of the many integrals involved in the Method of Moments an all purpose integration strategy with an easy and universal implementation scheme. To fulfill another important objective of this book, the accuracy of the selected high efficiency polynomial quadratures has been carefully evaluated in several original ways. For the first time analytical exact reference solutions have been derived for the representative cases of a pair of orthogonal adjacent triangles, regular or very elongated. This exact analytical analysis allowed to precisely quantify the modest accuracy attained by polynomial quadratures when integrating singular integrals, as compared to their performances with regular integrals. It also revealed an unexpected and superior performance of the 16 and 42 nodes quadratures. This observation was further confirmed by several examples, two of them showing in Part II that the accuracy provided by these two quadratures is necessary to avoid localized erratic current densities in the final solution.

After careful control of their accuracy, the electric and magnetic field integral equations have been extensively compared, against exact solutions when available, or against each other via a convergence analysis, for example. A great accuracy or similarity was observed, except in the vicinity of sharp edges, where both solutions seem to diverge from the expectations. Metallic sheets are unavoidably surrounded by sharp edges. As the magnetic formulation cannot deal with sheets, we found another incentive to investigate the foundations of these apparent contradictions to the duality principle.

In Part II, a series of evolutive examples have been presented to support and illustrate the theories developed in Part I, but also to provide many quantitative and comparative measurements of the local and average accuracy of various formulations available in the Method of Moments, including unused ones that we chose to apply anyway in this book. Instead of showing far-field based results, we deliberately chose to analyze the current densities themselves, as only they provide the most detailed insight . The electric and magnetic field integral equations are shown to provide equivalent accuracy, except in the vicinity of sharp edges. The use of regular meshes with various densities, but also the introduction of meshes using elongated triangles close to those edges, revealed that the electric formulation seems to overestimate the surface current densities and oppositely for the magnetic formulation. As we could show how unreliable RWG basis functions are in the vicinity of edges, no definitive conclusion could be drawn, except that other basis functions should be used there if a more accurate modelling of these strong current densities is required.

For dielectric domains, the PMCHWT and Müller combinations based on the *nxf* testing schemes were found to be as accurate as the *f* testing scheme, while exhibiting a much better condition number, at least in the two analyzed situations. For perfectly conducting volumes, the magnetic field integral equation also proved to exhibit a much lower condition number insensitive to mesh refinements. Considering also that the magnetic field integral equation is not prone to low frequency breakdown, as opposed to the electric field integral equation, we conclude by saying that those less popular formulations deserve much more consideration by the electromagnetic community.

Appendix A

We consider the flat circle F_{fa} centered on $\overline{r}_{fa}$:

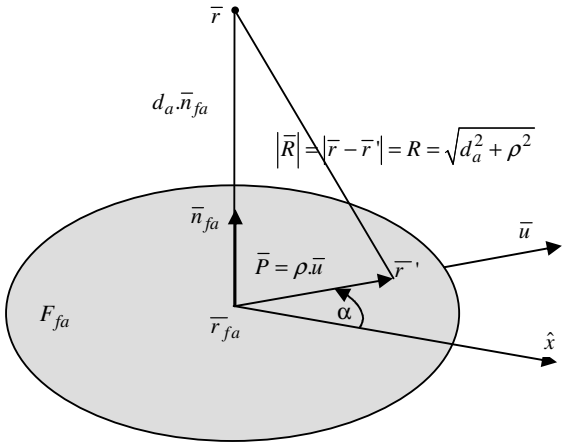

Figure 166 : Integrals on F_{fa}

The vector $\overline{r} = \overline{r}_{fa} + d_a.\overline{n}_{fa}$ is on the positive side ($d_a \geq 0$) of $\overline{n}_{fa}$, the unit normal to F_{fa}. Referring to Figure 166 we first decompose the integral (42) into :

$$\iint_{F_a} \frac{\overline{R}}{4\pi R^3}.dS' = \iint_{F_a} \frac{d_a.\overline{n}_{fa}}{4\pi R^3}.dS' - \iint_{F_a} \frac{\overline{P}}{4\pi R^3}.dS'$$

From $\overline{r}$ the surface F_{fa} is viewed under a signed solid angle $\Omega(\overline{r}, F_a)$, given by :

$$\Omega(\overline{r}, F_{fa}) = d_a \iint_{F_{fa}} \frac{dS'}{R^3}$$

The limit for $\overline{r} \to \overline{r}_{fa}$ of the first integral is therefore :

$$\lim_{\overline{r} \to \overline{r}_{fa}} \left(d_a.\overline{n}_{fa} \iint_{F_a} \frac{dS'}{4\pi R^3} \right) = \overline{n}_{fa}.\lim_{\overline{r} \to \overline{r}_{fa}} \left\{ sign(d_a).\frac{\Omega(\overline{r}, F_a)}{4\pi} \right\} = +\frac{\overline{n}_a}{2}$$

The second integral is identically zero :

$$\iint_{F_a} \frac{\overline{P}}{R^3} dS = \hat{x} \int_0^{2\pi} d\alpha \int_0^{\rho_a} \rho.d\rho \frac{-\rho\cos\alpha}{\left(d_a^2 + \rho^2\right)^{3/2}}$$

$$+\hat{y} \int_0^{2\pi} d\alpha \int_0^{\rho_a} \rho.d\rho \frac{-\rho\sin\alpha}{\left(d_a^2 + \rho^2\right)^{3/2}} = 0$$

Note that the second integral reduces to zero because $\overline{r}$ is on the normal above the centre of a symmetric shape F_{fa}.

Appendix B

$$\frac{+1}{j\omega\varepsilon}\bar{\nabla}\nabla\bullet\int_S G\left(\bar{n}\times\bar{H}\right)dS'$$

$$=\frac{+1}{j\omega\varepsilon}\bar{\nabla}\int_S \nabla\bullet\left[G\left(\bar{n}\times\bar{H}\right)\right]dS'$$

$$=\frac{+1}{j\omega\varepsilon}\bar{\nabla}\int_S \left(\bar{n}\times\bar{H}\right)\cdot\bar{\nabla}G\,dS'$$

$$=\frac{-1}{j\omega\varepsilon}\bar{\nabla}\int_S \left(\bar{n}\times\bar{H}\right)\cdot\bar{\nabla}'G\,dS'$$

$$=\frac{-1}{j\omega\varepsilon}\bar{\nabla}\int_S \left(\bar{n}\times\bar{H}\right)\cdot\bar{\nabla}'_s G\,dS'$$

$$=\frac{-1}{j\omega\varepsilon}\bar{\nabla}\int_S \left\{\nabla'_s\left[G\left(\bar{n}\times\bar{H}\right)\right]-G\nabla'_s\left[\bar{n}\times\bar{H}\right]\right\}dS'$$

$$=\frac{-1}{j\omega\varepsilon}\bar{\nabla}\int_S \nabla'_s\left[G\left(\bar{n}\times\bar{H}\right)\right]dS'+\frac{1}{j\omega\varepsilon}\int_S\bar{\nabla}\left[G\nabla'_s\left[\bar{n}\times\bar{H}\right]\right]dS'$$

$$=\frac{-1}{j\omega\varepsilon}\bar{\nabla}\oint_{\partial S}\underbrace{\left[G\left(\bar{n}\times\bar{H}\right)\right].\bar{n}}_{=0}dS'+\frac{1}{j\omega\varepsilon}\int_S\bar{\nabla}\left[G\nabla'_s\left[\bar{n}\times\bar{H}\right]\right]dS'$$

$$=\frac{1}{j\omega\varepsilon}\int_S\bar{\nabla}G.\nabla'_s\left[\bar{n}\times\bar{H}\right]dS'$$

$$=\int_S\left(\bar{\nabla}'G\right)\left[\frac{-1}{j\omega\varepsilon}\nabla'_s\cdot\left(\bar{n}\times\bar{H}\right)\right]dS'$$

$$=\int_S\left(\bar{\nabla}'G\right)\left[\bar{n}\cdot\bar{E}\right]dS'$$

Appendix C

$$\bar{R}=\begin{pmatrix}x-x'\\ y-y'\\ z-z'\end{pmatrix} \qquad R=\sqrt{(x-x')^2+(y-y')^2+(z-z')^2} \qquad \hat{R}=\frac{\bar{R}}{R}$$

$$\partial_x R=\frac{x-x'}{R}$$

$$G=\frac{e^{-jkR}}{4\pi R}=k\frac{e^{-j(kR)}}{4\pi(kR)}$$

$$\bar{\nabla}G=-\frac{1+jkR}{4\pi R^3}e^{-jkR}\bar{R}=k^2\left(\frac{-1}{(kR)^2}-\frac{j}{kR}\right)G\begin{pmatrix}x-x'\\ y-y'\\ z-z'\end{pmatrix}=k^2 f_2(kR)\begin{pmatrix}x-x'\\ y-y'\\ z-z'\end{pmatrix}$$

$$\frac{1}{k^2}\partial_x\left(\nabla_x G\right)=\partial_x\left[\left(x-x'\right)f_2(kR)\right]=\left(x-x'\right)\partial_x\left[f_2(kR)\right]+f_2(kR)$$

$$\frac{1}{k^2}\partial_x\left(\nabla_y G\right)=\partial_x\left[\left(y-y'\right)f_2(kR)\right]=\left(y-y'\right)\partial_x\left[f_2(kR)\right]$$

$$\partial_x\left[f_2(kR)\right]=(x-x')k^2\left\{\frac{3+3j(kR)-(kR)^2}{(kR)^4}\right\}G=(x-x')k^2 f_4(kR)$$

$$\frac{\bar{\nabla}\nabla\bullet}{k^2}\int_S G(\bar{r}-\bar{r}')\bar{J}(\bar{r}')\,dS'=\frac{1}{k^2}\int_S\bar{\nabla}\nabla\bullet(G\bar{J})\,dS'=\frac{1}{k^2}\int_S\bar{\nabla}\left[\underbrace{G(\nabla\bullet\bar{J})}_{0}+\bar{J}\cdot\bar{\nabla}G\right]dS'$$

$$\frac{1}{k^2}\int_S\bar{\nabla}\left[\bar{J}\cdot\bar{\nabla}G\right]dS'=\frac{1}{k^2}\int_S\bar{\nabla}\left[J_x\nabla_x G+J_y\nabla_y G+J_z\nabla_z G\right]dS'$$

$$=\frac{1}{k^2}\int_S\begin{bmatrix}\partial_x\left(J_x\nabla_x G+J_y\nabla_y G+J_z\nabla_z G\right)\\ \partial_y\left(J_x\nabla_x G+J_y\nabla_y G+J_z\nabla_z G\right)\\ \partial_z\left(J_x\nabla_x G+J_y\nabla_y G+J_z\nabla_z G\right)\end{bmatrix}dS'$$

$$=\frac{1}{k^2}\int_S\begin{bmatrix}J_x\partial_x\left(\nabla_x G\right)+J_y\partial_x\left(\nabla_y G\right)+J_z\partial_x\left(\nabla_z G\right)\\ J_x\partial_y\left(\nabla_x G\right)+J_y\partial_y\left(\nabla_y G\right)+J_z\partial_y\left(\nabla_z G\right)\\ J_x\partial_z\left(\nabla_x G\right)+J_y\partial_z\left(\nabla_y G\right)+J_z\partial_z\left(\nabla_z G\right)\end{bmatrix}dS'$$

$$=\int_S\begin{bmatrix}J_x\left(x-x'\right)\partial_x\left[f_2(kR)\right]+J_x f_2(kR)+J_y\left(y-y'\right)\partial_x\left[f_2(kR)\right]+J_z\left(z-z'\right)\partial_x\left[f_2(kR)\right]\\ J_x\left(x-x'\right)\partial_y\left[f_2(kR)\right]+J_y\left(y-y'\right)\partial_y\left[f_2(kR)\right]+J_y f_2(kR)+J_z\left(z-z'\right)\partial_y\left[f_2(kR)\right]\\ J_x\left(x-x'\right)\partial_z\left[f_2(kR)\right]+J_y\left(y-y'\right)\partial_y\left[f_2(kR)\right]+J_z\left(z-z'\right)\partial_z\left[f_2(kR)\right]+J_z f_2(kR)\end{bmatrix}dS'$$

$$=\int_S\left[\bar{J}\,f_2(kR)+k^2 f_4(kR)\left(\bar{J}.\bar{R}\right)\bar{R}\right]dS'$$

$$j\omega\mu\left(1+\frac{\bar{\nabla}\nabla\bullet}{k^2}\right)\int_S G\bar{J}\,dS'$$

$$= jZk\int_S\left[G\bar{J}+G\bar{J}\left(\frac{-1}{(kR)^2}-\frac{j}{kR}\right)+k^2\left\{\frac{3+3j(kR)-(kR)^2}{(kR)^4}\right\}G\left(\bar{J}.\bar{R}\right)\bar{R}\right]dS'$$

$$= jZk\int_S\left[G\bar{J}\,k\left(\frac{1}{kR}+\frac{-1}{(kR)^3}-\frac{j}{(kR)^2}\right)\frac{e^{-jkR}}{4\pi}+k\left(\frac{3+3j(kR)-(kR)^2}{(kR)^3}\right)\frac{e^{-jkR}}{4\pi}\left(\bar{J}.\hat{R}\right)\hat{R}\right]dS'$$

$$= Zk^2\int_S\left[G\bar{J}\left(\frac{j}{kR}+\frac{1}{(kR)^2}-\frac{j}{(kR)^3}\right)\frac{e^{-jkR}}{4\pi}-\left(\frac{j}{(kR)}+\frac{3}{(kR)^2}-\frac{3j}{(kR)^3}\right)\frac{e^{-jkR}}{4\pi}\left(\bar{J}.\hat{R}\right)\hat{R}\right]dS'$$

$$j\omega\varepsilon\left(1+\frac{\bar{\nabla}\nabla\bullet}{k^2}\right)\int_S G\bar{J}\,dS' = Yk^2\int_S\left[G\bar{J}\,f_3-\left(\bar{J}.\hat{R}\right)\hat{R}\,f_{3r}\right]dS'$$

With :

$$f_3=\left(\frac{j}{kR}+\frac{1}{(kR)^2}-\frac{j}{(kR)^3}\right)\frac{e^{-jkR}}{4\pi}$$

$$f_{3r}=\left(\frac{j}{kR}+\frac{3}{(kR)^2}-\frac{3j}{(kR)^3}\right)\frac{e^{-jkR}}{4\pi}$$

Appendix D

Analytical and numerical integration of the principal value term

D.1. $\bar{f}_m \neq \bar{f}_n$

On the triangle T_m depicted in Figure 167, having a surface A, and two RWG functions defined on edges m and n of length respectively L_m and L_n.

$$\bar{f}_m = \frac{\pm L_m}{2A}(\bar{r} - \bar{p})$$
$$\bar{f}_n = \frac{\pm L_n}{2A}(\bar{r} - \bar{q})$$

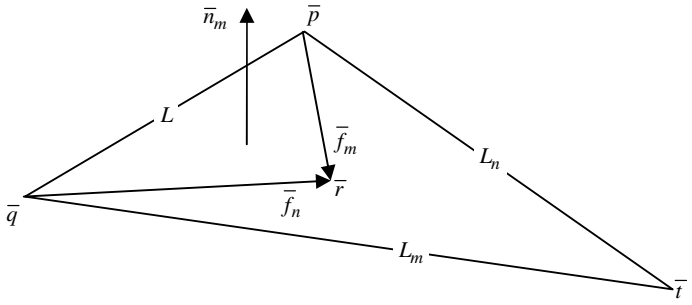

Figure 167 : principal value term (1)

We have the following integrals :

(1) $$\int_{T_m} \bar{f}_m . \frac{\bar{n}_m \times \bar{f}_n}{2} . dS = \frac{\pm L_m . \pm L_n}{12}$$

(2) $$\int_{T_m} \bar{n}_m \times \bar{f}_m . \frac{\bar{n}_m \times \bar{f}_n}{2} . dS = \frac{\pm L_m . \pm L_n}{96A}\left[L_m^2 + L_n^2 - 3L^2 \right]$$

where

$$L = norm(\bar{q} - \bar{p})$$
$$A = norm(\bar{t} - \bar{p}) \times (\bar{q} - \bar{p})/2$$

Numerical integration with Dunavant quadratures shows that only one node is sufficient to obtain the exact value of (1), but three nodes are needed for (2).

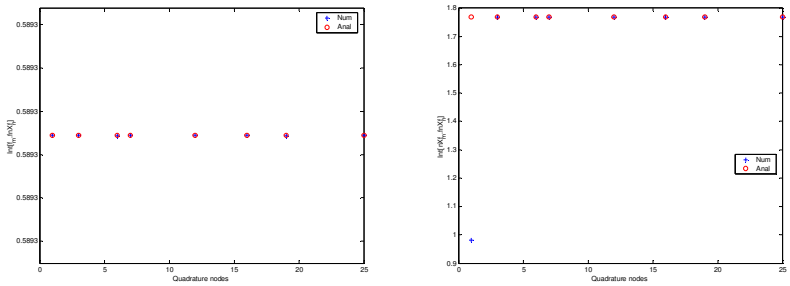

In this example, L = 1, X = -2 and Y = 1

=> L_m = 3,1623 and L_n = 2,2361

If we consider that L_m and $L_n < \lambda/10$ and T_m is quasi equilateral, then :

(1) < $\lambda^2/1200$

(2) < $\lambda^2/4160$

Note though that for a given L_m and L_n, (1) is unaffected by the shape of the triangle, but (2) is !

D.2. $\bar{f}_m = \bar{f}_n$

If $\bar{f}_m = \bar{f}_n$, then (1) and (2) become :

(1) $\int_{T_m} \bar{f}_m . \frac{\bar{n}_m \times \bar{f}_m}{2} . dS = 0$

(2) $\int_{T_m} \bar{n}_m \times \bar{f}_m . \frac{\bar{n}_m \times \bar{f}_m}{2} . dS = \frac{1}{2} \int_{T_m} \left| \bar{f}_m \right|^2 . dS = \frac{L_m^2}{96A} \left[3\left(L_n^2 + L^2 \right) - L_m^2 \right]$

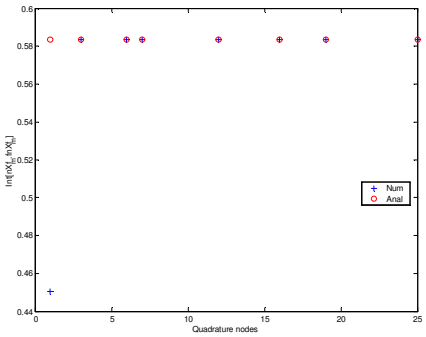

Numerical integration with Dunavant quadratures shows that three nodes are needed for (2).

Appendix E

E.1 Surface gradient and surface divergence theorems

Considering :

- A surface S with normal $\bar{n}$ and with closed oriented contour C
- The normal $\bar{m}$ on C pointing outside S
- A vector $\bar{l} = \bar{n} \times \bar{m}$ defining the sense of integration everywhere on C
- A vector function $\bar{A}$ continuously differentiable on S
- A scalar function B continuously differentiable on S

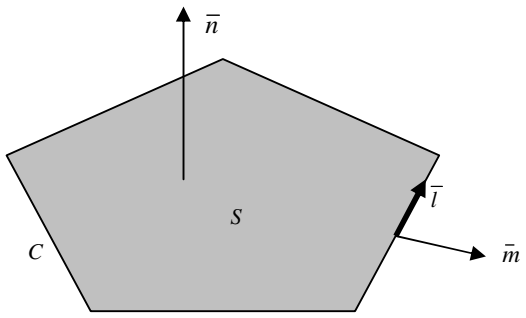

Figure 168 : Geometry for the surface divergence and gradient theorems

We have the following equalities :

$$\iint_S \left(\nabla_s \cdot \bar{A}\right) dS = \oint_C \left(\bar{A} \cdot \bar{m}\right) dl$$
$$\iint_S \left(\bar{\nabla}_s B\right) dS = \oint_C \left(B \cdot \bar{m}\right) dl$$

Note that the surface S does neither have to be polygonal nor flat, as depicted in Figure 168.

The surface divergence and gradient are defined as :

$$\nabla_s = \nabla - \nabla_n$$
$$\bar{\nabla}_s = \bar{\nabla} - \bar{\nabla}_n$$

In the case of a flat surface S lying in the XY plane, they are given by :

$$\nabla_s = \nabla_x + \nabla_y$$
$$\bar{\nabla}_s = \bar{\nabla}_x + \bar{\nabla}_y$$

E.2 Examples of a surface gradient and a surface divergence

To illustrate the **surface divergence** notion, we prove below that :

$$R^n = \nabla_S \left(\frac{\bar{P}}{P^2} \frac{R^{n+2}}{n+2} \right) = \nabla_{S'} \left(\frac{\bar{P}'}{P'^2} \frac{R^{n+2}}{n+2} \right)$$

Where the vectors $\bar{R}$, $\bar{P}$ and $\bar{P}'$ are depicted in Figure 169.

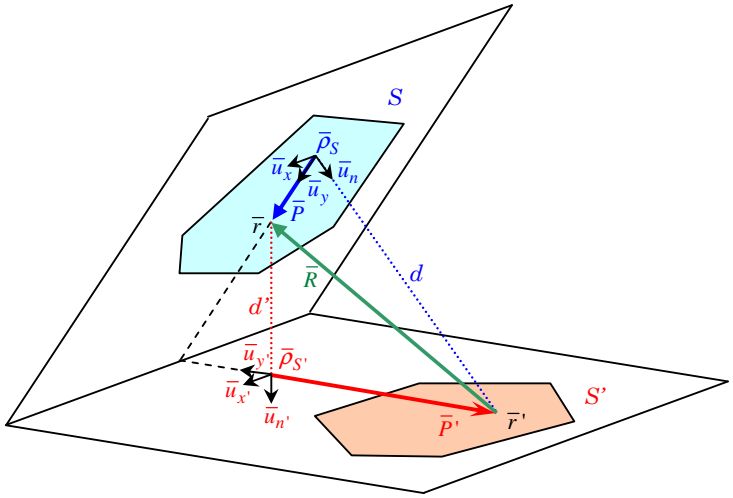

Figure 169 : Surface divergence

To calculate the surface divergence related to S, lying in the xy plane, let us express the vectors in the (x,y,n) coordinate system having its origin in $\bar{\rho}_S$, the projection of $\bar{r}'$ on S :

$$\bar{r} = x.\bar{u}_x + y.\bar{u}_y + 0.\bar{u}_n = \bar{P} = \bar{r} - \bar{\rho}_S$$

$$\bar{r}' = 0.\bar{u}_x + 0.\bar{u}_y + d.\bar{u}_n$$

$$R = \left\| \bar{R} \right\| = \left\| \bar{r} - \bar{r}' \right\| = \sqrt{x^2 + y^2 + (-d)^2} \quad \Rightarrow \quad \frac{\partial R}{\partial x} = \frac{x}{R} \qquad \frac{\partial R}{\partial y} = \frac{y}{R}$$

$$P^2 = \left\| \bar{P} \right\|^2 = x^2 + y^2 \quad \Rightarrow \quad \frac{\partial P^2}{\partial x} = 2x \qquad \frac{\partial P^2}{\partial y} = 2y$$

We have :

$$\nabla_S\left(\frac{\bar{P}}{P^2}\frac{R^{n+2}}{n+2}\right)=\frac{\partial}{\partial x}\left(\frac{R^{n+2}}{n+2}\frac{x}{P^2}\right)+\frac{\partial}{\partial y}\left(\frac{R^{n+2}}{n+2}\frac{y}{P^2}\right)$$

$$=\frac{R^{n+2}}{n+2}\frac{2}{P^2}+\frac{x}{n+2}\frac{\partial}{\partial x}\left(\frac{R^{n+2}}{P^2}\right)+\frac{y}{n+2}\frac{\partial}{\partial y}\left(\frac{R^{n+2}}{P^2}\right)$$

$$=\frac{R^{n+2}}{n+2}\frac{2}{P^2}+\frac{x}{n+2}\frac{\left[P^2(n+2)R^{n+1}\partial R/\partial x-R^{n+2}\partial P^2/\partial x\right]}{P^4}$$

$$+\frac{y}{n+2}\frac{\left[P^2(n+2)R^{n+1}\partial R/\partial y-R^{n+2}\partial P^2/\partial y\right]}{P^4}$$

$$=\frac{R^{n+2}}{n+2}\frac{2}{P^2}+\frac{x^2P^2R^n-2x^2R^{n+2}/(n+2)}{P^4}+\frac{y^2P^2R^n-2y^2R^{n+2}/(n+2)}{P^4}$$

$$=\frac{R^{n+2}}{n+2}\frac{2}{P^2}+\frac{\left(x^2+y^2\right)R^n}{P^2}-2R^{n+2}\frac{x^2+y^2}{(n+2)P^4}$$

$$=R^n$$

To calculate the surface divergence related to *S'*, lying in the x'y' plane, let us express the vectors in the (x',y',n') coordinate system having its origin in $\bar{\rho}_{S'}$, the projection of $\bar{r}$ on *S'*:

$$\bar{r}=0.\bar{u}_{x'}+0.\bar{u}_{y'}+d'.\bar{u}_{n'}$$

$$\bar{r}'=x'.\bar{u}_{x'}+y'.\bar{u}_{y'}+0.\bar{u}_{n'}=\bar{P}'=\bar{r}'-\bar{\rho}_{S'}$$

$$R=\left\|\bar{R}\right\|=\left\|\bar{r}-\bar{r}'\right\|=\sqrt{(-x')^2+(-y')^2+d'^2}\quad\Rightarrow\quad\frac{\partial R}{\partial x'}=\frac{x'}{R}\qquad\frac{\partial R}{\partial y}=\frac{y'}{R}$$

$$P'^2=\left\|\bar{P}'\right\|^2=(x')^2+(y')^2\qquad\Rightarrow\quad\frac{\partial P'^2}{\partial x'}=2x'\quad\frac{\partial P'^2}{\partial y'}=2y'$$

We have :

$$\nabla'_{S'}\left(\frac{\bar{P}'}{P'^2}\frac{R^{n+2}}{n+2}\right)=\frac{\partial}{\partial x'}\left(\frac{R^{n+2}}{n+2}\frac{x'}{P'^2}\right)+\frac{\partial}{\partial y'}\left(\frac{R^{n+2}}{n+2}\frac{y'}{P'^2}\right)$$

$$=\frac{R^{n+2}}{n+2}\frac{2}{P'^2}+\frac{x'}{n+2}\frac{\partial}{\partial x'}\left(\frac{R^{n+2}}{P'^2}\right)+\frac{y'}{n+2}\frac{\partial}{\partial y'}\left(\frac{R^{n+2}}{P'^2}\right)$$

$$=\frac{R^{n+2}}{n+2}\frac{2}{P'^2}+\frac{x'}{n+2}\frac{\left[P'^2(n+2)R^{n+1}\partial R/\partial x'-R^{n+2}\partial P'^2/\partial x'\right]}{P'^4}$$

$$+\frac{y'}{n+2}\frac{\left[P'^2(n+2)R^{n+1}\partial R/\partial y'-R^{n+2}\partial P'^2/\partial y'\right]}{P'^4}$$

$$=\frac{R^{n+2}}{n+2}\frac{2}{P'^2}+\frac{x'^2P'^2R^n-2x'^2R^{n+2}/(n+2)}{P'^4}+\frac{y'^2P'^2R^n-2y'^2R^{n+2}/(n+2)}{P'^4}$$

$$=\frac{R^{n+2}}{n+2}\frac{2}{P'^2}+\frac{\left(x'^2+y'^2\right)R^n}{P'^2}-2R^{n+2}\frac{x'^2+y'^2}{(n+2)P'^4}$$

$$=R^n$$

To illustrate the **surface gradient** notion, we prove that :

$$\bar{P}R^n=\bar{\nabla}_S\left(\frac{R^{n+2}}{n+2}\right)\quad\text{and}\quad\bar{P}'R^n=\bar{\nabla}'_{S'}\left(\frac{R^{n+2}}{n+2}\right)$$

$$\bar{\nabla}_S\left(\frac{R^{n+2}}{n+2}\right)=\frac{\partial}{\partial x}\left(\frac{R^{n+2}}{n+2}\right)\bar{u}_x+\frac{\partial}{\partial y}\left(\frac{R^{n+2}}{n+2}\right)\bar{u}_y$$

$$=R^{n+1}\left[\frac{\partial R}{\partial x}\bar{u}_x+\frac{\partial R}{\partial y}\bar{u}_y\right]$$

$$=R^n\left[x.\bar{u}_x+y.\bar{u}_y\right]$$

$$=R^n\bar{P}$$

$$\bar{\nabla}'_{S'}\left(\frac{R^{n+2}}{n+2}\right)=\frac{\partial}{\partial x'}\left(\frac{R^{n+2}}{n+2}\right)\bar{u}_{x'}+\frac{\partial}{\partial y'}\left(\frac{R^{n+2}}{n+2}\right)\bar{u}_{y'}$$

$$=R^{n+1}\left[\frac{\partial R}{\partial x'}\bar{u}_{x'}+\frac{\partial R}{\partial y'}\bar{u}_{y'}\right]$$

$$=R^n\left[x'.\bar{u}_{x'}+y'.\bar{u}_{y'}\right]$$

$$=R^n\bar{P}'$$

Note though that : $\bar{R}.R^n=\bar{\nabla}\left(\frac{R^{n+2}}{n+2}\right)$ and $\bar{R}.R^n=-\bar{\nabla}'\left(\frac{R^{n+2}}{n+2}\right)$

There is a sign difference for the full gradient, as opposed to the surface gradient ! This is due to the definition of $\bar{P} = \bar{r} - \bar{\rho}_S$ and $\bar{P}' = \bar{r}' - \bar{\rho}'_S$. These vectors end on $\bar{r}$ and $\bar{r}'$ respectively, as opposed to $\bar{R} = \bar{r} - \bar{r}'$ that always end on $\bar{r}$.

E.3 Complete derivation of the integral of R^n on S'

To obtain a general analytical expression, we make use of the surface divergence theorem to transform the surface integral into a line integral. If $\bar{\rho}_{S'}$, the projection on *S'* of $\bar{r}$, lies inside *S'* or anywhere on its boundary $\partial S'$, then the surface divergence theorem cannot be used at *P'=0* and a decomposition into two integrals on $S' - S'_\varepsilon$ and S'_ε is necessary as the function $\frac{R^{n+2}}{P'^2}\bar{P}'$ is not continuously differentiable at *P'=0*. In general, we may write :

$$\iint_{S'} R^n dS' = \iint_{S'-S'_\varepsilon} R^n dS' + \iint_{S'_\varepsilon} R^n dS'$$

$$= \iint_{S'-S'_\varepsilon} \nabla'_s \left(\frac{\bar{P}'}{P'^2} \frac{R^{n+2}}{n+2} \right) dS' + \iint_{S'_\varepsilon} R^n dS'$$

$$= \frac{1}{n+2} \int_{\partial(S'-S'_\varepsilon)} \frac{R^{n+2}}{P'^2} \left(\bar{P}'.\bar{m}' \right) dl' + \iint_{S'_\varepsilon} R^n dS'$$

$$= \underbrace{\frac{1}{n+2} \int_{\partial S'} \frac{R^{n+2}}{P'^2} \left(\bar{P}'.\bar{m}' \right) dl'}_{(1)} + \underbrace{\frac{1}{n+2} \int_{\partial S'_\varepsilon} \frac{R^{n+2}}{P'^2} \left(\bar{P}'.\bar{m}' \right) dl'}_{(2)} + \underbrace{\iint_{S'_\varepsilon} R^n dS'}_{(3)}$$

Note that writing : $\int_{\partial(S'-S'_\varepsilon)} \left[\bar{P}'.\bar{m}' \right] .dl' = \int_{\partial S'} \left[\bar{P}'.\bar{m}' \right] dl' + \int_{\partial S'_\varepsilon} \left[\bar{P}'.\bar{m}' \right] dl'$ implies that $\bar{m}'$ must point outside *S'*-S'_ε on $\partial S'$ and $\partial S'_\varepsilon$, as depicted in Figure 171 (p.264).

When $\bar{\rho}_{S'}$ is located outside S', (2) and (3) vanish and only (1) remains.

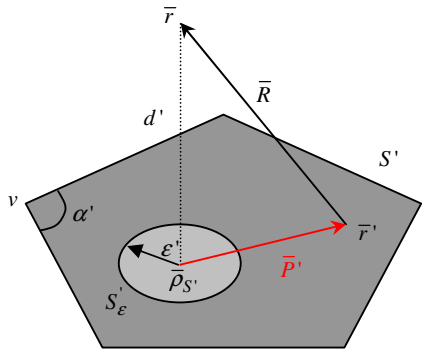

Figure 170 : Geometry for the integral of R^n on S'

Let us integrate the two last terms (2) and (3), knowing that in the most general case, when $\bar{\rho}_{S'}$ is the vertex *v* for example, then S'_ε is a portion of a circle with

opening angle α'. If $\bar{\rho}_{S'}$ is located on $\partial S'$ but not on a vertex, then α' = π (S'_ε is a half circle), and if $\bar{\rho}_{S'}$ lies inside S', then α' = 2π (S'_ε is a full circle, as depicted in Figure 170)

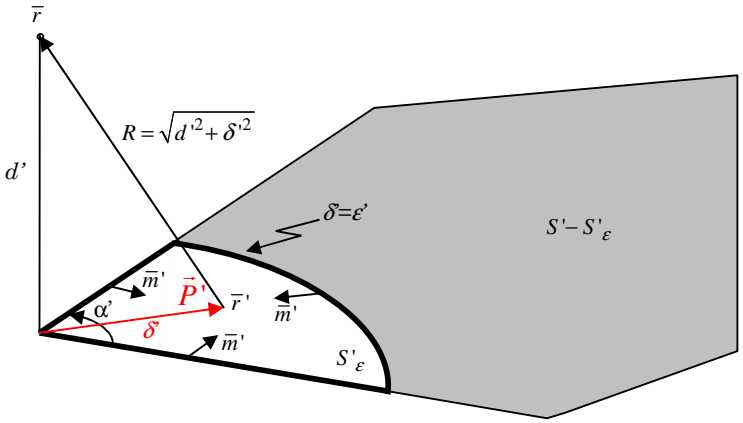

.

Figure 171 : Geometry for integrals (2) and (3)

$$(2)=\frac{1}{n+2}\int_{\partial S'_\varepsilon}\frac{R^{n+2}}{P'^2}\left(\bar{P}'.\bar{m}'\right)dl'$$

$$=\frac{1}{n+2}\int_0^{\varepsilon'}\frac{R^{n+2}}{P'^2}(0)d\delta'+\frac{\left(\sqrt{d'^2+\varepsilon'^2}\right)^{n+2}}{n+2}\int_0^{\alpha'}\frac{\left(-\varepsilon'\bar{m}'\right).\bar{m}'}{\varepsilon'^2}\varepsilon'.d\alpha'+\frac{1}{n+2}\int_{\varepsilon'}^{0}\frac{R^{n+2}}{P'^2}(0)d\delta'$$

$$=-\alpha'.\frac{\left(\sqrt{d'^2+\varepsilon'^2}\right)^{n+2}}{n+2}$$

$$(3)=\iint_{S'_\varepsilon}R^n dS'=\int_0^{\alpha'}d\alpha'\int_0^{\varepsilon'}\delta'.d\delta'\left(d'^2+\delta'^2\right)^{n/2}=\alpha'\left[\frac{\left(d'^2+\delta'^2\right)^{(n+2)/2}}{n+2}\right]_0^{\varepsilon'}$$

$$=\alpha'\left[\frac{\left(\sqrt{d'^2+\varepsilon'^2}\right)^{n+2}-|d'|^{n+2}}{n+2}\right]$$

Inserting (2) and (3) into the expression of $\iint_{S'}R^n dS'$, we get :

$$\iint_{S'}R^n dS'=\frac{1}{n+2}\int_{\partial S'}\frac{R^{n+2}}{P'^2}\left(\bar{P}'.\bar{m}'\right)dl'-\alpha'\frac{|d'|^{n+2}}{n+2}$$

We can now build a recursive formula for these integrals as follows :

$$K'^{n} = \iint_{S'} R^n dS' = \frac{1}{n+2}\left\{\int_{\partial S'} \frac{R^{n+2}}{P'^2}\left(\bar{P}'.\bar{m}'\right)dl' - \alpha'\left|d'\right|^{n+2}\right\}$$

$$= \frac{1}{n+2}\left\{\int_{\partial S'}\left(R^n + d'^2\frac{R^n}{P'^2}\right)\left(\bar{P}'.\bar{m}'\right)dl' - \alpha'\left|d'\right|^{n+2}\right\}$$

$$= \frac{1}{n+2}\left\{\int_{\partial S'} R^n\left(\bar{P}'.\bar{m}'\right)dl' + d'^2\left[\int_{\partial S'}\left(\frac{R^n}{P'^2}\right)\left(\bar{P}'.\bar{m}'\right)dl' - \alpha'\left|d'\right|^n\right]\right\}$$

$$= \frac{1}{n+2}\left\{\int_{\partial S'} R^n\left(\bar{P}'.\bar{m}'\right)dl' + n.d'^2.K'^{n-2}\right\}$$

If S' is a polygon, then $\partial S' = \Sigma(\partial S'_i)$ where every $\partial S'_i$ is a straight line on which $\bar{P}'(\bar{r}').\bar{m}'_i(\bar{r}') = P'^0_i = cst$.

Then :

$$K'^{n} = \iint_{S'} R^n dS' = \frac{1}{n+2}\left\{\sum_i P'^0_i.I'^n_i + n.d'^2\,K'^{n-2}\right\}$$

For a polygon S', we can also build a recursive formula for the line integral I'^n_i, noting that $R^2 = \left(R'^0_i\right)^2 + l'^2$:

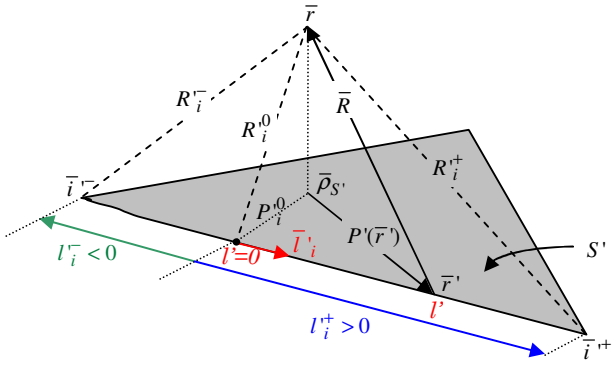

Figure 172 : Geometry for the line integral

$$I'^{n}_{i} = \int_{\partial S'_i} R^n dl' = \int_{\partial S'_i} \left(\frac{d}{dl'} \left[\frac{R^{n+1}}{n+1} \right] \Big/ \frac{dR}{dl'} \right) dl' = \frac{1}{n+1} \int_{\partial S'_i} \left(\frac{R}{l'} . \frac{d}{dl'} \left[R^{n+1} \right] \right) dl'$$

$$= \frac{1}{n+1} \left\{ \left[\frac{R^{n+2}}{l'} \right]_{l'^-_i}^{l'^+_i} - \int_{\partial S'_i} \left(\frac{-\left(R'^0_i \right)^2}{Rl'^2} . R^{n+1} \right) dl' \right\}$$

$$= \frac{1}{n+1} \left\{ \left[R^n \frac{\left(R'^0_i \right)^2 + l'^2}{l'} \right]_{l'^-_i}^{l'^+_i} + \left(R'^0_i \right)^2 \int_{\partial S'_i} \left(R^n . \frac{d}{dl'} \left[\frac{-1}{l'} \right] \right) dl' \right\}$$

$$= \frac{1}{n+1} \left\{ \left[l' R^n \right]_{l'^-_i}^{l'^+_i} + \left(R'^0_i \right)^2 \left[\left[\frac{R^n}{l'} - \frac{R^n}{l'} \right]_{l'^-_i}^{l'^+_i} + n \int_{\partial S'_i} R^{n-2} dl' \right] \right\}$$

$$= \frac{1}{n+1} \left\{ l'^+_i \left(R'^+_i \right)^n - l'^-_i \left(R'^-_i \right)^n + n \left(R'^0_i \right)^2 I'^{n-2}_i \right\}$$

If we determine $I'^{-1}_i = \int_{\partial S'_i} \frac{dl'}{R}$ and $K'^{-3} = \iint_{S'} \frac{dS'}{R^3}$, the recursive expressions for I'^{n}_i and K'^{m} allow to deduce easily $I'^{+1}_i = \int_{\partial S'_i} R.dl'$ and subsequently $K'^{-1} = \iint_{S'} \frac{dS'}{R}$ and $K'^{+1} = \iint_{S'} R.dS'$.

The expression of I'^{-1}_i is obtained easily :

$$I'^{-1}_i = \int_{\partial S'_i} \frac{dl'}{R} = \int_{l'^-_i}^{l'^+_i} \frac{dl'}{\sqrt{\left(R'^0_i \right)^2 + l'^2}} = \left[\ln \left(l' + \sqrt{\left(R'^0_i \right)^2 + l'^2} \right) \right]_{l'^-_i}^{l'^+_i} = \ln \left(\frac{l'^+_i + R'^+_i}{l'^-_i + R'^-_i} \right)$$

The function I'^{-1}_i is everywhere continuous(ly) differentiable and finite, except on the boundary $\partial S'$ of the surface S', where it is infinite.

On the contrary I'^{+1}_i is everywhere finite and continuous(ly) differentiable :

$$I'^{+1}_i = \int_{\partial S'_i} R.dl' = \frac{1}{2} \left\{ l'^+_i R'^+_i - l'^-_i R'^-_i + \left(R'^0_i \right)^2 \ln \left(\frac{l'^+_i + R'^+_i}{l'^-_i + R'^-_i} \right) \right\}$$

To derive a compact expression for K'^{-3}, we will use the fact that the function α' for a flat polygon S' can be expressed as :

$\alpha' = \sum_i \alpha'_i$, where $\alpha'_i = \tan^{-1} \frac{l'^+_i}{P'^0_i} - \tan^{-1} \frac{l'^-_i}{P'^0_i}$.

As required, with this expression for α' we have :

- $\alpha' = 0$ if $\bar{\rho}_{S'}$ is outside S'
- $\alpha' = 2\pi$ if $\bar{\rho}_{S'}$ is inside S'
- $\alpha' = \pi$ if $\bar{\rho}_{S'}$ is on $\partial S'$ but not on a vertex
- α' = inner opening angle of the polygon S' if $\bar{\rho}_{S'}$ is a vertex

$$K'^{-3} = \iint_{S'} R^{-3} dS' = \frac{1}{-3+2}\left\{\int_{\partial S'} \frac{R^{-3+2}}{P'^2}\left(\bar{P}'.\bar{m}'_i\right)dl' - \alpha'\left|d'\right|^{-3+2}\right\}$$

$$= \frac{\alpha'}{|d'|} - \sum_i \left(\bar{P}'.\bar{m}'_i\right)\int_{\partial S'_i} \frac{1}{P'^2 R} dl'$$

$$= \frac{\alpha'}{|d'|} - \sum_i P'^0_i \int_{l'^-_i}^{l'^+_i} \frac{1}{\left(l'^2 + \left(P'^0_i\right)^2\right)\sqrt{l'^2 + \left(P'^0_i\right)^2 + d'^2}} dl'$$

$$= \frac{\alpha'}{|d'|} - \sum_i P'^0_i \left[\frac{1}{d' P'^0_i} \tan^{-1} \frac{d' l'}{P'^0_i \sqrt{l'^2 + \left(P'^0_i\right)^2 + d'^2}}\right]_{l'^-_i}^{l'^+_i}$$

$$= \frac{1}{|d'|}.\sum_i \left[\tan^{-1}\frac{l'^+_i}{P'^0_i} - \tan^{-1}\frac{l'^-_i}{P'^0_i}\right] - \frac{1}{|d'|}\sum_i \left[\tan^{-1}\frac{|d'|l'^+_i}{P'^0_i R'^+_i} - \tan^{-1}\frac{|d'|l'^-_i}{P'^0_i R'^-_i}\right]$$

$$= \frac{1}{|d'|}.\sum_i \left[\tan^{-1}\frac{l'^+_i P'^0_i}{\left(P'^0_i\right)^2 + d'^2 + |d'|R'^+_i} - \tan^{-1}\frac{l'^-_i P'^0_i}{\left(P'^0_i\right)^2 + d'^2 + |d'|R'^-_i}\right]$$

$$= \frac{1}{|d'|}.\sum_i \left[\tan^{-1}\frac{l'^+_i P'^0_i}{\left(R'^0_i\right)^2 + |d'|R'^+_i} - \tan^{-1}\frac{l'^-_i P'^0_i}{\left(R'^0_i\right)^2 + |d'|R'^-_i}\right]$$

The integral K'^{-3} is singular (infinite) when d' = 0.

In practice, the function $d'K'^{-3}$ is encountered. We give hereafter the physical meaning of this function.

The solid angle sustended from the observation point $\bar{r}$ by an oriented surface S' is given by :

$$\Omega_{S'}(\bar{r}) = \int_{S'}\left[\frac{\bar{u}_n(\bar{r}').\bar{u}_R(\bar{r}')}{R^2}\right]dS'$$

where $\bar{r}'$ is the integration point on S', $R = |\bar{r} - \bar{r}'|$, $\bar{u}_n$ is a unit vector indicating the arbitrarily chosen orientation of the surface S' at $\bar{r}'$ and the unit vector

$\bar{u}_R = \dfrac{\bar{R}}{R} = \dfrac{\bar{r} - \bar{r}'}{|\bar{r} - \bar{r}'|}$. $\Omega_{S'}$ can be positive or negative, depending on the relative orientations of $\bar{u}_n$ and $\bar{u}_R$.

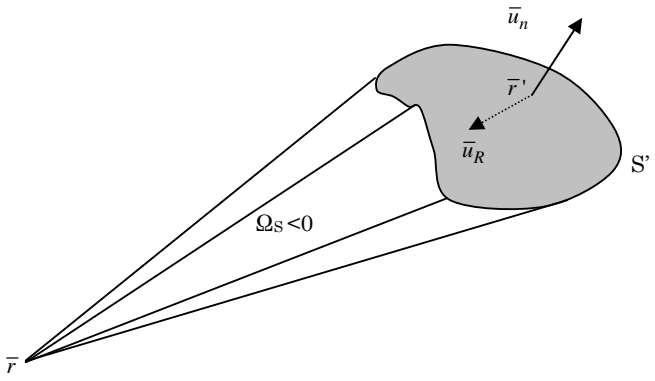

Figure 173 : Solid angle

In the case of a flat surface S' :

$$\Omega_{S'} = \int_{S'} \left[\frac{\bar{u}_n . \bar{u}_R}{R^2} \right] dS' = \int_{S'} \left[\frac{d'/R}{R^2} \right] dS' = d' \int_{S'} \left[R^{-3} \right] dS' = d' . K'^{-3}$$

With this "signed solid angle" interpretation for $d' K'^{-3}$, it is now easy to understand that this function is

- bounded between -2π and +2π (for a flat surface S')
- continuous(ly) differentiable everywhere except on the surface S', where it undergoes discontinuous jumps between positive values on the $+\bar{u}_n$ side and negative values on the $-\bar{u}_n$ side

The functions K'^{-1} and $d' K'^{-1}$ are both everywhere finite and continuous(ly) differentiable :

$$K'^{-1} = \iint_{S'} R^{-1} dS' = \sum_i P_i'^{0} . I_i'^{-1} - d'^{2} K'^{-3}$$

E.4 Complete derivation of the integral of $\bar{P} R^n$ on S'

To obtain a general analytical expression, we make use of the surface gradient theorem to transform the surface integral into a line integral. If n≤-3 and $\bar{r}$ lies inside *S'* or anywhere on its boundary $\partial S'$, then the surface gradient theorem cannot be used at *R=0* and a decomposition into two integrals on $S' - S'_\varepsilon$ and S'_ε is necessary as the function R^{n+2} is not continuously differentiable at *R=0*. In general, we may write :

$$\iint_{S'} \bar{P}'R^n dS'$$

$$= \iint_{S'-S'_\varepsilon} \bar{\nabla}'_{S'}\left(\frac{R^{n+2}}{n+2}\right) dS' + \iint_{S'_\varepsilon} \bar{P}'R^n dS' = \int_{\partial(S'-S'_\varepsilon)} \frac{R^{n+2}}{n+2}.\bar{m}'dl' + \iint_{S'_\varepsilon} \bar{P}'R^n dS'$$

$$= \underbrace{\int_{\partial S'} \frac{R^{n+2}}{n+2}.\bar{m}'dl'}_{(1)} + \underbrace{\int_{\partial S'_\varepsilon} \frac{R^{n+2}}{n+2}.\bar{m}'dl'}_{(2)} + \underbrace{\iint_{S'_\varepsilon} \bar{P}'R^n dS'}_{(3)}$$

To show that (2)+(3)=0, we place $\bar{r}$ above S' and let d' tend to 0.

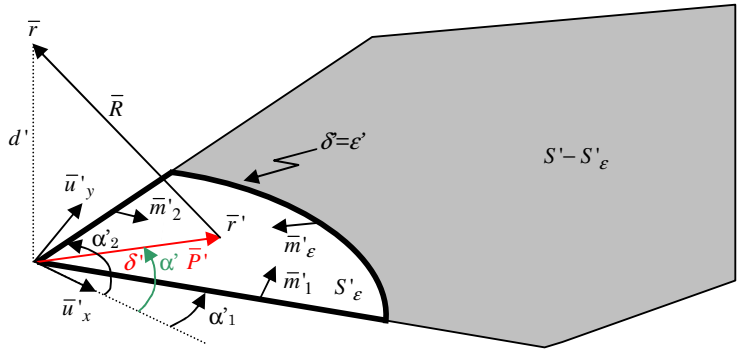

Figure 174 : Geometry for the gradient theorem

With Figure 174 we can write :

- $\bar{m}'_1 = -\sin\alpha'_1.\bar{u}'_x + \cos\alpha'_1.\bar{u}'_y$
- $\bar{m}'_\varepsilon = -\cos\alpha'.\bar{u}'_x - \sin\alpha'.\bar{u}'_y$
- $\bar{m}'_2 = -\sin\alpha'_2.\bar{u}'_x + \cos\alpha'_2.\bar{u}'_y$
- $\bar{P}' = \delta'\cos\alpha'.\bar{u}'_x + \delta'\sin\alpha'.\bar{u}'_y$
- $R = \sqrt{d'^2 + \delta'^2}$

$$(2)=\int_{\partial S'_\varepsilon}\frac{R^{n+2}}{n+2}.\bar{m}'dl'$$

$$=\left(-\sin\alpha'_1.\bar{u}'_x+\cos\alpha'_1.\bar{u}'_y\right)\frac{1}{n+2}\int_0^{\varepsilon'}\left(d'^2+\delta'^2\right)^{n/2+1}d\delta'$$

$$-\left(d'^2+\varepsilon'^2\right)^{n/2+1}\frac{1}{n+2}\int_{\alpha'_1}^{\alpha'_2}\left(\cos\alpha'.\bar{u}'_x+\sin\alpha'.\bar{u}'_y\right)\varepsilon'.d\alpha'$$

$$+\left(-\sin\alpha'_2.\bar{u}'_x+\cos\alpha'_2.\bar{u}'_y\right)\frac{1}{n+2}\int_{\varepsilon'}^{0}\left(d'^2+\delta'^2\right)^{n/2+1}d\delta'$$

$$=\frac{1}{n+2}\int_0^{\varepsilon'}\left(d'^2+\delta'^2\right)^{n/2+1}d\delta'\left\{\left(\sin\alpha'_2.\bar{u}'_x-\cos\alpha'_2.\bar{u}'_y\right)-\left(\sin\alpha'_1.\bar{u}'_x-\cos\alpha'_1.\bar{u}'_y\right)\right\}$$

$$-\varepsilon'\left(d'^2+\varepsilon'^2\right)^{n/2+1}\frac{1}{n+2}\left(\left(\sin\alpha'_2-\sin\alpha'_1\right).\bar{u}'_x-\left(\cos\alpha'_2-\cos\alpha'_1\right).\bar{u}'_y\right)$$

$$=\frac{1}{n+2}\left[\int_0^{\varepsilon'}\left(d'^2+\delta'^2\right)^{n/2+1}d\delta'-\varepsilon'\left(d'^2+\varepsilon'^2\right)^{n/2+1}\right]\left(\left(\sin\alpha'_2-\sin\alpha'_1\right).\bar{u}'_x-\left(\cos\alpha'_2-\cos\alpha'_1\right).\bar{u}'_y\right)$$

$$(3)=\iint_{S'_\varepsilon}\bar{P}'R^n dS'$$

$$=\int_{\alpha'_1}^{\alpha'_2}d\alpha'\int_0^{\varepsilon'}\delta'.d\delta'.\delta'\cos\alpha'\left(d'^2+\delta'^2\right)^{n/2}.\bar{u}'_x+\int_{\alpha'_1}^{\alpha'_2}d\alpha'\int_0^{\varepsilon'}\delta'.d\delta'.\delta'\sin\alpha'\left(d'^2+\delta'^2\right)^{n/2}.\bar{u}'_y$$

$$=\left\{\int_{\alpha'_1}^{\alpha'_2}\cos\alpha'.d\alpha'.\bar{u}'_x+\int_{\alpha'_1}^{\alpha'_2}\sin\alpha'.d\alpha'.\bar{u}'_y\right\}.\int_0^{\varepsilon'}(\delta')^2\left(d'^2+\delta'^2\right)^{n/2}d\delta'$$

$$=\left\{\left(\sin\alpha'_2-\sin\alpha'_1\right).\bar{u}'_x-\left(\cos\alpha'_2-\cos\alpha'_1\right).\bar{u}'_y\right\}.\int_0^{\varepsilon'}(\delta')^2\left(d'^2+\delta'^2\right)^{n/2}d\delta'$$

Integration by parts shows that (2)+(3)=0, regardless of d', ε' and n.

In the specific case of n=-3, we have for example :

$$\int_0^{\varepsilon'}(\delta')^2\left(d'^2+\delta'^2\right)^{-3/2}d\delta'=\frac{-\varepsilon}{\sqrt{d^2+\varepsilon^2}}+\ln\left[\frac{\varepsilon+\sqrt{d^2+\varepsilon^2}}{|d|}\right]$$

$$\frac{1}{-3+2}\left[\int_0^{\varepsilon'}\left(d'^2+\delta'^2\right)^{-3/2+1}d\delta'-\varepsilon'\left(d'^2+\varepsilon'^2\right)^{-3/2+1}\right]=-\ln\left[\frac{\varepsilon'+\sqrt{d'^2+\varepsilon'^2}}{|d'|}\right]+\frac{\varepsilon'}{\sqrt{d'^2+\varepsilon'^2}}$$

These two expressions would be singular (infinite) for d' = 0, but as their sum is identically zero for any d' ≠ 0, it must remain so when d' = 0.

We can now write, for any n and $\bar{r}$:

$$\iint_{S'}\bar{P}'R^n dS'=\int_{\partial S'}\frac{R^{n+2}}{n+2}.\bar{m}'dl'$$

If S' is a polygon, then : $\iint_{S'}\bar{P}'R^n dS'=\sum_i\bar{m}'_i\int_{\partial S'_i}\frac{R^{n+2}}{n+2}.dl'=\frac{1}{n+2}\sum_i\bar{m}'_i I_i'^{n+2}$

Appendix F

In general :

$$Z_{mn,i}^{EJ} = -\frac{jZ_i}{k_i}\int_{S_{m,i}} \bar{T}_{m,i}(\bar{r}).\left[\int_{S_{n,i}} \left\{ k_i^2 G_i(R)\bar{f}_{n,i}(\bar{r}') - \nabla'_s \cdot \bar{f}_{n,i}(\bar{r}')\ \ \bar{\nabla}' G_i(R)\right\}.dS'\right].dS$$

We choose $\bar{T}_{m,i}(\bar{r}) = \bar{f}_{m,i}(\bar{r}) = RWG$ and split the complete integral into :

$$\int_{S_{m,i}} \bar{f}_{m,i}(\bar{r}).\left[\int_{T_{n,i}^+} + \int_{T_{n,i}^-}\right].dS = \int_{T_{m,i}^+} \bar{f}_{m,i}^+(\bar{r}).\left[\int_{T_{n,i}^+} + \int_{T_{n,i}^-}\right].dS + \int_{T_{m,i}^-} \bar{f}_{m,i}^-(\bar{r}).\left[\int_{T_{n,i}^+} + \int_{T_{n,i}^-}\right].dS$$

Let us consider the integral involving $T_{m,i}^+$, $T_{n,i}^+$ and $\bar{\nabla}' G_i(R)$:

$$\int_{T_{m,i}^+} \bar{f}_{m,i}^+(\bar{r}).\left[\int_{T_{n,i}^+} -\nabla'_s \cdot \bar{f}_{n,i}^+(\bar{r}')\ \ \bar{\nabla}' G_i(R).dS'\right].dS$$

$$= \left(\nabla'_s \cdot \bar{f}_{n,i}^+\right)\left\{\int_{T_{m,i}^+} \bar{f}_{m,i}^+(\bar{r}).\left[\int_{T_{n,i}^+} \bar{\nabla} G_i(R).dS'\right].dS\right\}$$

$$= \left(\nabla'_s \cdot \bar{f}_{n,i}^+\right)\left\{\int_{T_{m,i}^+}\left[\int_{T_{n,i}^+} \bar{f}_{m,i}^+(\bar{r}).\bar{\nabla}_s G_i(R).dS'\right].dS\right\}$$

$$= \left(\nabla'_s \cdot \bar{f}_{n,i}^+\right)\left\{+\int_{T_{m,i}^+}\left[\int_{T_{n,i}^+} \left(\nabla_s\left(G_i(R)\bar{f}_{m,i}^+(\bar{r})\right) - G_i(R)\nabla_s \cdot \bar{f}_{m,i}^+\right).dS'\right].dS\right\}$$

$$= \left(\nabla'_s \cdot \bar{f}_{n,i}^+\right)\left\{+\int_{T_{m,i}^+}\left[\nabla_s \int_{T_{n,i}^+} G_i(R)\bar{f}_{m,i}^+(\bar{r}).dS' - \int_{T_{n,i}^+} G_i(R)\nabla_s \cdot \bar{f}_{m,i}^+.dS'\right].dS\right\}$$

$$= \left(\nabla'_s \cdot \bar{f}_{n,i}^+\right)\left\{\begin{array}{l} +\int_{\partial T_{m,i}^+}\left(\bar{f}_{m,i}^+(\bar{r}).\bar{m}_{m,i}^+\right)\left[\int_{T_{n,i}^+} G_i(R).dS'\right].dS \\ -\int_{T_{m,i}^+}\left[\int_{T_{n,i}^+} G_i(R)\nabla_s \cdot \bar{f}_{m,i}^+.dS'\right].dS \end{array}\right\}$$

Similarly :

$$\int_{T_{m,i}^-} \bar{f}_{m,i}^-(\bar{r}).\left[\int_{T_{n,i}^+} -\nabla'_s \cdot \bar{f}_{n,i}^+(\bar{r}')\ \ \bar{\nabla}' G_i(R).dS'\right].dS$$

$$= \left(\nabla'_s \cdot \bar{f}_{n,i}^+\right)\left\{\begin{array}{l} +\int_{\partial T_{m,i}^-}\left(\bar{f}_{m,i}^-(\bar{r}).\bar{m}_{m,i}^-\right)\left[\int_{T_{n,i}^+} G_i(R).dS'\right].dS \\ -\int_{T_{m,i}^-}\left[\int_{T_{n,i}^+} G_i(R)\nabla_s \cdot \bar{f}_{m,i}^-.dS'\right].dS \end{array}\right\}$$

As RWG functions have no component normal to the four edges of $\partial S_{m,i}$ the line integral on $\partial T_{m,i}^+$ and $\partial T_{m,i}^-$ reduce to integrals on the edge common to $T_{m,i}^+$ and $T_{m,i}^-$. The divergence conforming property of the RWG (see §2.2.5) then ensures that $\int_{\partial T_{m,i}^+} + \int_{\partial T_{m,i}^-} = 0$.

Finally :

$$\int_{S_{m,i}} \overline{f}_{m,i}(\overline{r}).\left[\int_{T_{n,i}^{+}}\right].dS =$$
$$-\nabla_s \cdot \overline{f}_{m,i}^{+}\nabla'_s \cdot \overline{f}_{n,i}^{+}\int_{T_{m,i}^{+}}\int_{T_{n,i}^{+}} G_i(R).dS'.dS - \nabla_s \cdot \overline{f}_{m,i}^{-}\nabla'_s \cdot \overline{f}_{n,i}^{+}\int_{T_{m,i}^{-}}\int_{T_{n,i}^{+}} G_i(R).dS'.dS$$

Similarly :

$$\int_{S_{m,i}} \overline{f}_{m,i}(\overline{r}).\left[\int_{T_{n,i}^{-}}\right].dS =$$
$$-\nabla_s \cdot \overline{f}_{m,i}^{+}\nabla'_s \cdot \overline{f}_{n,i}^{-}\int_{T_{m,i}^{+}}\int_{T_{n,i}^{-}} G_i(R).dS'.dS - \nabla_s \cdot \overline{f}_{m,i}^{-}\nabla'_s \cdot \overline{f}_{n,i}^{-}\int_{T_{m,i}^{-}}\int_{T_{n,i}^{-}} G_i(R).dS'.dS$$

The total integral can now be rewritten in contracted form :

$$Z_{mn,i}^{EJ} = -\frac{jZ_i}{k_i}\int_{S_{m,i}} \overline{f}_{m,i}(\overline{r}).\left[\int_{S_{n,i}} \left\{ k_i^2 G_i(R)\overline{f}_{n,i}(\overline{r}') - \nabla'_s \cdot \overline{f}_{n,i}(\overline{r}')\ \ \overline{\nabla}' G_i(R)\right\}.dS'\right].dS$$
$$= -\frac{jZ_i}{k_i}\int_{S_{m,i}}\int_{S_{n,i}} \left\{ k_i^2 \overline{f}_{m,i}(\overline{r}).\overline{f}_{n,i}(\overline{r}') + \nabla_s \cdot \overline{f}_{m,i}\nabla'_s \cdot \overline{f}_{n,i}\right\} G_i(R).dS'.dS$$

In this alternative and equivalent expression, the derivative of the free-space Green's function has been transferred to the test function $\overline{T}_{m,i}(\overline{r}) = \overline{f}_{m,i}(\overline{r}) = RWG$.

A similar transformation is not possible with $\overline{T}_{m,i}(\overline{r}) = \overline{n}_{m,i}(\overline{r}) \times \overline{f}_{m,i}(\overline{r})$ because this function is not divergence conforming.

Appendix G

This Appendix gives every detail of the analytical solution summarized and analyzed in §5.5.1

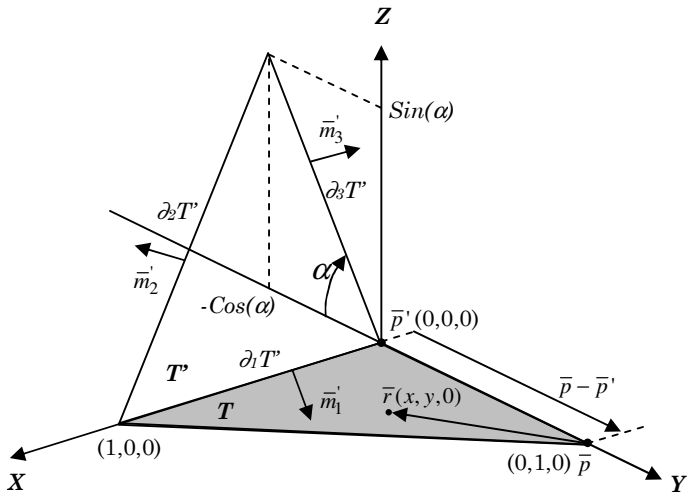

$$I = +\frac{C'}{4\pi}\iint_T \bar{w}(\bar{r}).(\bar{r}-\bar{p}')\times\left(\iint_{T'}\frac{-\bar{P}'}{R^3}.dS'\right)dS$$

$$= +\frac{C'}{4\pi}\iint_T \bar{w}(\bar{r}).(\bar{r}-\bar{p}')\times\left(\sum_i \bar{m}_i'.Q_i'\right)dS$$

$$= +\frac{C'}{4\pi}\sum_i\iint_T \bar{w}(\bar{r}).\left[(\bar{r}-\bar{p}')\times\bar{m}_i'\right]Q_i'dS$$

with $C' = \pm\frac{L'}{2A'} = \pm\sqrt{2}$ and $Q_i' = \ln\left[\frac{R_i'^{+}(\bar{r})+l_i'^{+}(\bar{r})}{R_i'^{-}(\bar{r})+l_i'^{-}(\bar{r})}\right]$.

Considering :

$$\bar{m}_1' = \begin{pmatrix} 0 \\ +\cos\alpha \\ -\sin\alpha \end{pmatrix} \qquad \bar{m}_2' = \begin{pmatrix} 1 \\ -\cos\alpha \\ +\sin\alpha \end{pmatrix} \qquad \bar{m}_3' = \begin{pmatrix} -1 \\ 0 \\ 0 \end{pmatrix}$$

$\bar{f} = C(\bar{r}-\bar{p}) = (\bar{r}-\bar{p})$ is the RWG defined on T from vertex $\bar{p}$.

	$\bar{w} = \bar{f}$	$\bar{w} = \bar{n} \times \bar{f}$
$\bar{w}.(\bar{r} - \bar{p}') \times \bar{m}_1' =$	$-x.\sin\alpha$	$\sin\alpha(x^2 + y^2 - y)$
$\bar{w}.(\bar{r} - \bar{p}') \times \bar{m}_2' =$	$\frac{x.\sin\alpha}{\sqrt{2}}$	$\frac{-\sin\alpha}{\sqrt{2}}(x^2 + y^2 - y)$
$\bar{w}.(\bar{r} - \bar{p}') \times \bar{m}_3' =$	0	0

After computation of the vector cross and dot products, (284) reduces to the sum of only two integrals on edges $\partial_1 T'$ and $\partial_2 T'$, the integral on $\partial_3 T'$ being identically zero :

$$I = \frac{\sqrt{2}\sin\alpha}{4\pi}\left\{\iint_T P(x,y).Q_1'(\bar{r})dS - \frac{1}{\sqrt{2}}.\iint_T P(x,y).Q_2'(\bar{r})dS\right\} = \frac{\sqrt{2}\sin\alpha}{4\pi}\{I_1 - I_2\}$$

with $P_{\bar{w}=\bar{f}}(x,y) = -x$ and $P_{\bar{w}=\bar{n}\times\bar{f}}(x,y) = x^2 + y^2 - y$

Integrals on $\partial_1 T'$

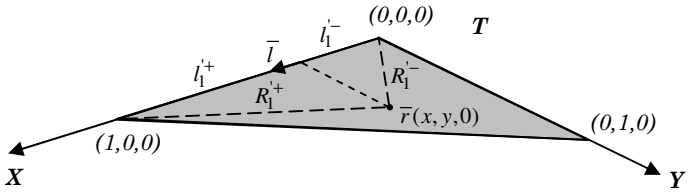

$$R_1'^+(\bar{r}) + l_1'^+(\bar{r}) = \sqrt{(1-x)^2 + y^2} + (1-x)$$

$$R_1'^-(\bar{r}) + l_1'^-(\bar{r}) = \sqrt{x^2 + y^2} - x$$

$R_1'^+(\bar{r}) + l_1'^+(\bar{r})$ is always strictly positive for any position of $\bar{r}$ inside T, except for $\bar{r}$ = (1,0,0). The integrand of I_1^+ is singular only at (1,0,0).

$R_1'^-(\bar{r}) + l_1'^-(\bar{r})$ is always strictly positive for any position of $\bar{r}$ inside T, except all along the common edge $\partial_1 T'$ (y = 0). The integrand of I_1^- is not singular though in $\bar{r}$ = (0,0,0) because $P(0,0) = 0$ premultiplies $Q_1'(\bar{r})$.

$$I_1 = \left\{\begin{array}{l} \int_0^1\int_0^{1-y} P(x,y).\ln\left[\sqrt{(1-x)^2 + y^2} + (1-x)\right]dxdy \\ -\int_0^1\int_0^{1-x} P(x,y).\ln\left[\sqrt{x^2 + y^2} - x\right]dydx \end{array}\right\} = I_1^+ - I_1^-$$

The integrands related to $\partial_1 T'$ are depicted in Figure 175.

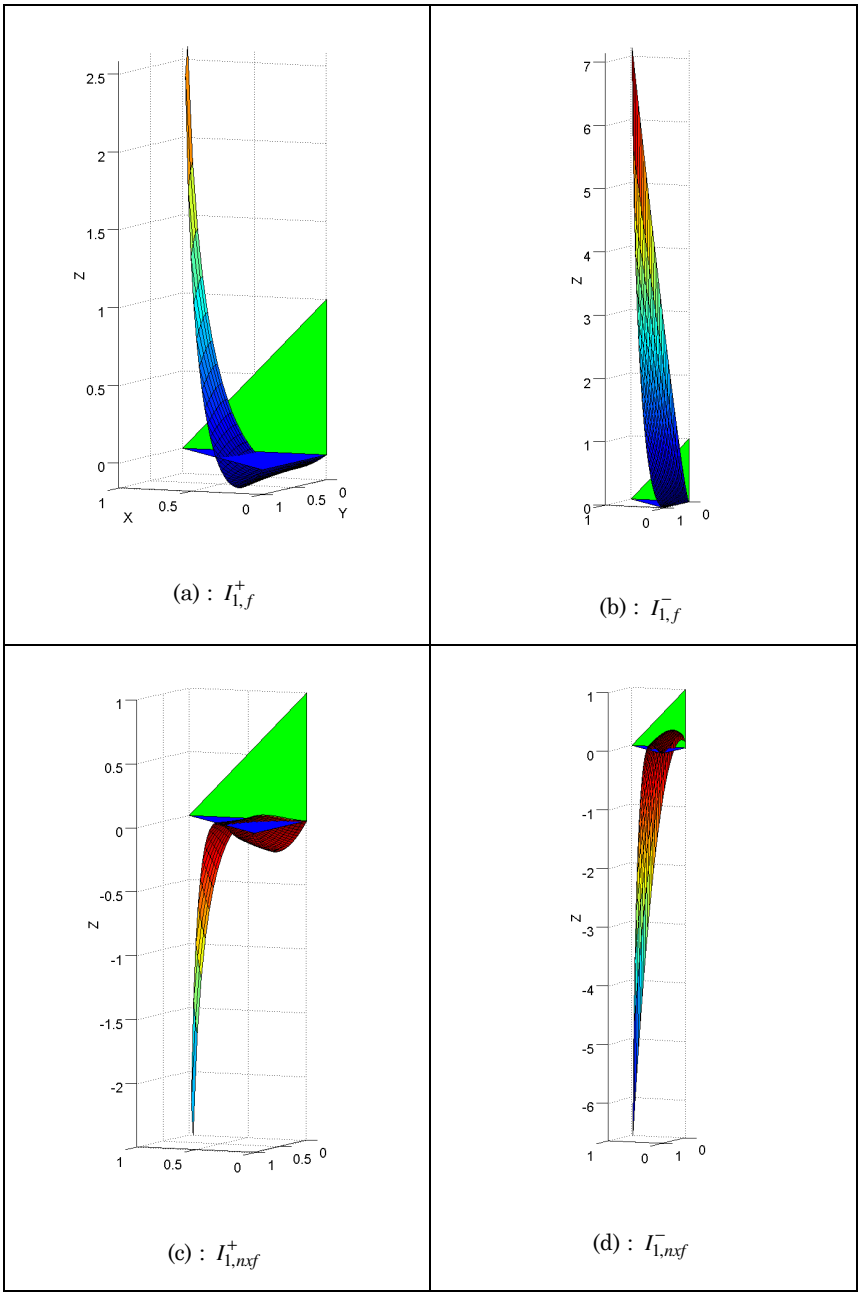

(a) : $I^{+}_{1,f}$

(b) : $I^{-}_{1,f}$

(c) : $I^{+}_{1,nxf}$

(d) : $I^{-}_{1,nxf}$

Figure 175 : Integrands related to $\partial_1 T'$

If $\overline{w} = \overline{f}$:

$$I^{+}_{1,f} = \int_0^1 \int_0^{1-y} x.\ln\left[\sqrt{(1-x)^2+y^2}+(1-x)\right] dx dy$$

$$= \frac{1}{4}\int_0^1 \left[\begin{array}{l} 2x^2.\ln\left[\sqrt{(1-x)^2+y^2}+(1-x)+(x+3)\sqrt{(1-x)^2+y^2}\right] \\ -(y^2-2).\ln\left[\sqrt{(1-x)^2+y^2}-(1-x)\right] \end{array}\right]_0^{1-y} dy$$

$$= \frac{1}{4}\int_0^1 \left[\begin{array}{l} 2(1-y)^2.\ln\left[y\left(\sqrt{2}+1\right)\right]-(y^2-2).\ln\left[y\left(\sqrt{2}-1\right)\right] \\ +(y^2-2).\ln\left[\sqrt{1+y^2}-1\right]+(4-y)y\sqrt{2}-3\sqrt{1+y^2} \end{array}\right] dy$$

$$= \frac{1}{4}\left[\begin{array}{l} -y^3\left(\frac{\sqrt{2}}{3}+\frac{2}{9}\right)+y^2\left(2\sqrt{2}+1\right)-2y-\frac{5}{3}y\sqrt{y^2+1} \\ +\frac{2(y^3-3y+3)y}{3}\ln\left[y\left(\sqrt{2}+1\right)\right]+\frac{y(y^2-6)}{3}.\ln\left[\sqrt{1+y^2}-1\right] \\ -\frac{y(y^2-6)}{3}\ln\left[y\left(\sqrt{2}-1\right)\right]+\frac{2}{3}.\ln\left[\sqrt{1+y^2}+y\right] \end{array}\right]_0^1$$

$$= \frac{-11+12\ln\left(\sqrt{2}+1\right)}{36} = -0,011764359882374 60...$$

$$I^{-}_{1,f} = \int_0^1 \int_0^{1-x} x.\ln\left[\sqrt{x^2+y^2}-x\right] dy dx$$

$$= \int_0^1 \left[xy.\ln\left[\sqrt{x^2+y^2}-x\right]-xy-x^2\ln\left[\sqrt{x^2+y^2}+y\right]\right]_0^{1-x} dx$$

$$= \int_0^1 \left[\begin{array}{l} x(1-x).\ln\left[\sqrt{x^2+(1-x)^2}-x\right]-x(1-x) \\ -x^2\ln\left[\sqrt{x^2+(1-x)^2}+(1-x)\right]+x^2\ln[x] \end{array}\right] dy$$

$$= \frac{1}{36}\left[\begin{array}{l} 8x^3+12x^3\ln\left[\sqrt{x^2+(1-x)^2}+1-x\right]+12x^3\ln[x]-21x^2-6x \\ -6x^2(2x-3)\ln\left[\sqrt{x^2+(1-x)^2}-x\right]-12\ln[1-x] \\ +3\sqrt{2}\sinh^{-1}[1-2x]+6(x+1)\sqrt{x^2+(1-x)^2}+6\ln\left[\sqrt{x^2+(1-x)^2}+x\right] \end{array}\right]_0^1$$

$$= \frac{-11-9\sqrt{2}\ln\left(\sqrt{2}+1\right)}{36} = -0,617168175625671...$$

If $\overline{w} = \overline{n} \times \overline{f}$:

$$I^{+}_{1,n\times f} = \int_0^1 \int_0^{1-y} (x^2 + y^2 - y).\ln\left[\sqrt{(1-x)^2 + y^2} + (1-x)\right] dxdy$$

$$= \frac{1}{18}\int_0^1 \left[\begin{array}{l} 6x(x^2 + 3y^2 - 3y).\ln\left[\sqrt{(1-x)^2 + y^2} + (1-x)\right] \\ +3(3y^2 - 6y + 2).\ln\left[\sqrt{(1-x)^2 + y^2} - (1-x)\right] \\ +(2x^2 + 5x + 14y^2 - 18y + 11)\sqrt{(1-x)^2 + y^2} \end{array}\right]_0^{1-y} dy$$

$$= \frac{1}{18}\int_0^1 \left[\begin{array}{l} 6(1-y)(4y^2 - 5y + 1).\ln\left[y(\sqrt{2}+1)\right] \\ +3(3y^2 - 6y + 2).\left\{\ln\left[y(\sqrt{2}+1)\right] - \ln\left[y(\sqrt{1+y^2} - 1)\right]\right\} \\ \sqrt{2}y(16y^2 - 27y + 18) - \sqrt{1+y^2}\,(14y^2 - 18y + 11) \end{array}\right] dy$$

$$= \frac{1}{18}\left[\begin{array}{l} \left(4\sqrt{2} + \frac{3}{2}\right)y^4 - y^3\left(9\sqrt{2} + 6\right) + y^2\left(9\sqrt{2} + 9\right) - 6y \\ -\sqrt{y^2+1}\left(\frac{-7y^3}{2} + 6y^2 - \frac{23y}{4} - 3\right) - 6y(y-1)^3 \ln\left[y\left(\sqrt{2}+1\right)\right] \\ -3y(y^2 - 3y + 2)\left\{\ln\left[y\left(\sqrt{2}-1\right)\right] - \ln\left[\sqrt{1+y^2} - 1\right]\right\} + \frac{3}{4}\sinh^{-1} y \end{array}\right]_0^1$$

$$= \frac{2 - 3\sqrt{2} + \ln\left(\sqrt{2}+1\right)}{24} = -0,056719463...$$

$$I^{-}_{1,n\times f} = \int_0^1 \int_0^{1-y} (x^2 + y^2 - y).\ln\left[\sqrt{x^2 + y^2} - x\right] dxdy$$

$$= \frac{1}{9}\int_0^1 \left[\sqrt{x^2 + y^2}\,(x^2 + 7y^2 - 9y) + 3x(x^2 + 3y^2 - 3y).\ln\left[\sqrt{x^2 + y^2} - x\right]\right]_0^{1-y} dy$$

$$= \frac{1}{9}\int_0^1 \left[\begin{array}{l} \sqrt{2y^2 - 2y + 1}(8y^2 - 11y + 1) - 7y^3 + 9y^2 \\ +3(1-y)(4y^2 - 5y + 1).\ln\left[\sqrt{2y^2 - 2y + 1} - 1 + y\right] \end{array}\right] dy$$

$$= \frac{1}{9}\left[\begin{array}{l} -y^4 + \frac{9}{2}y^2 - 3y - 3(y-1)^3 \ln\left[\sqrt{2y^2 - 2y + 1} - 1 + y\right] \\ +\frac{9}{16\sqrt{2}}\sinh^{-1}\left[1 - 2y\right] + \sqrt{2y^2 - 2y + 1}\,(2y^3 - \frac{7}{2}y^2 - \frac{1}{8}y + \frac{21}{16}) \end{array}\right]_0^1$$

$$= \frac{-2 - \sqrt{2}\ln\left(\sqrt{2}+1\right)}{16} = -0,202903155...$$

Integrals on $\partial_2 T'$

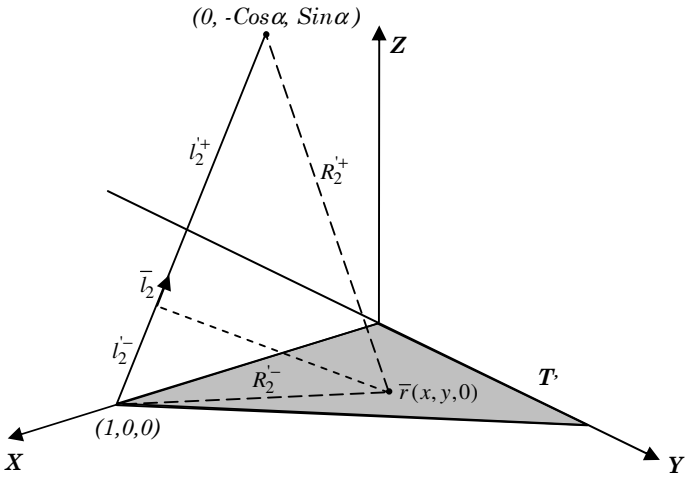

$$R'^+_2(\bar{r}) + l'^+_2(\bar{r}) = \sqrt{x^2 + y^2 + 2y\cos\alpha + 1} + (x + y\cos\alpha + 1)/\sqrt{2}$$

$$R'^-_2(\bar{r}) + l'^-_2(\bar{r}) = \sqrt{(1-x)^2 + y^2} + (x + y\cos\alpha - 1)/\sqrt{2}$$

$R'^+_2(\bar{r}) + l'^+_2(\bar{r})$ is always strictly positive for any position of $\bar{r}$ inside T. The integrand of I_2^+ is regular everywhere.

$R'^-_2(\bar{r}) + l'^-_2(\bar{r})$ is always strictly positive for any position of $\bar{r}$ inside T, except for $\bar{r}$ = (1,0,0). The integrand of I_1^+ is singular only at (1,0,0).

$$I_2 = \frac{1}{\sqrt{2}} \left\{ \begin{array}{l} \int_0^1 \int_0^{1-y} P(x,y).\ln\left[\sqrt{x^2 + y^2 + 2y\cos\alpha + 1} + (x + y\cos\alpha + 1)/\sqrt{2}\right] dxdy \\ -\int_0^1 \int_0^{1-x} P(x,y).\ln\left[\sqrt{(1-x)^2 + y^2} + (x + y\cos\alpha - 1)/\sqrt{2}\right] dxdy \end{array} \right\}$$
$$= I_2^+ - I_2^-$$

The integrands related to $\partial_2 T'$ are depicted in Figure 176 (p.279).

We could not solve the symbolic integrals for any arbitrary value of α. In the case α = 90°, we could solve exactly $I_{2,f}^-$ and $I_{2,n\times f}^-$ but no analytic solution could be found for $I_{2,f}^+$ and $I_{2,n\times f}^+$. Fortunately $I_{2,f}^+$ and $I_{2,n\times f}^+$ can be estimated very accurately with polynomial quadratures, as the integrand is regular.

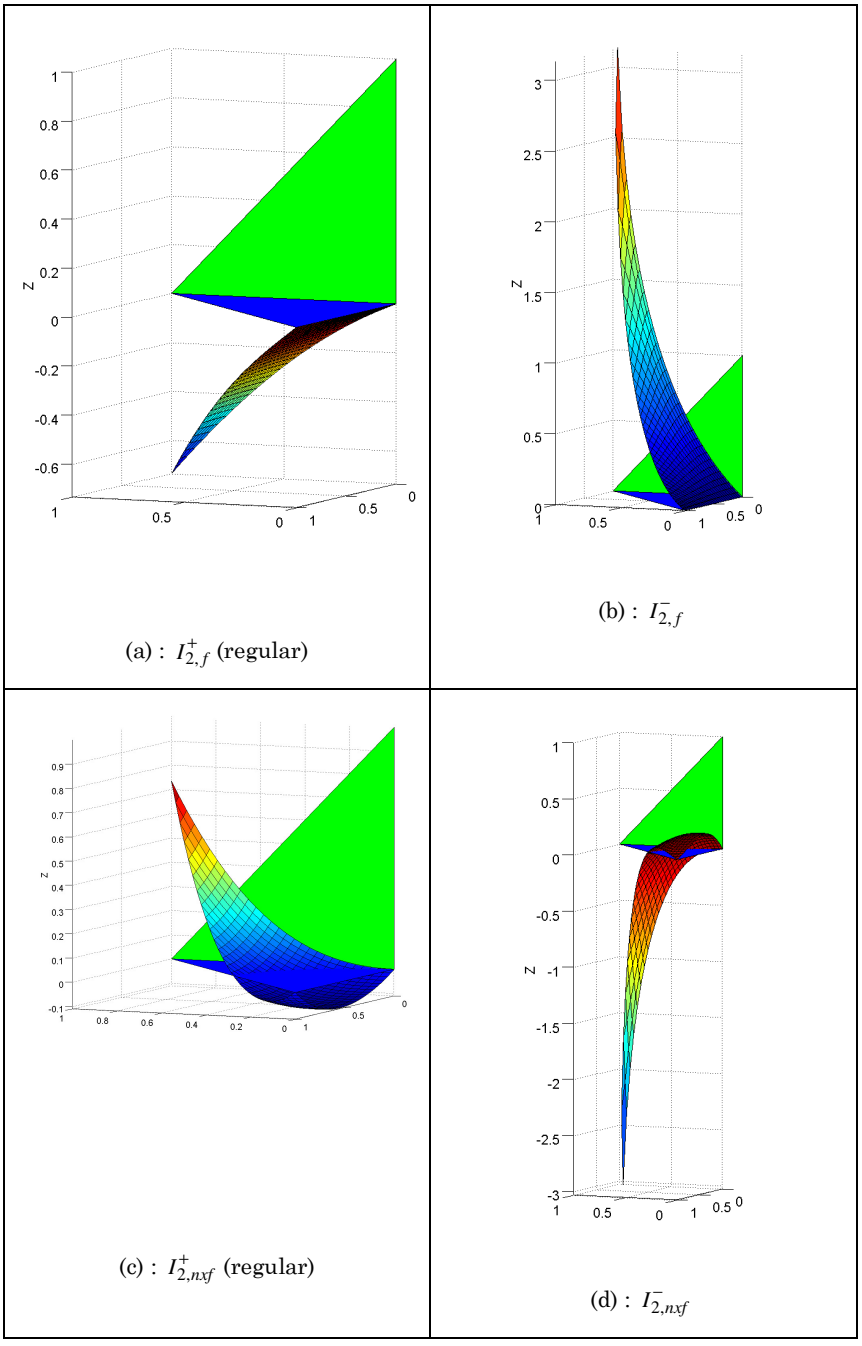

(a) : $I^{+}_{2,f}$ (regular)

(b) : $I^{-}_{2,f}$

(c) : $I^{+}_{2,nxf}$ (regular)

(d) : $I^{-}_{2,nxf}$

Figure 176 : Integrands related to $\partial_2 T$"

If $\overline{w} = \overline{f}$:

$$I_{2,f}^{-} = \int_0^1 \int_0^{1-x} x.\ln\left[\sqrt{(1-x)^2+y^2} - (1-x)/\sqrt{2}\right] dy dx$$

$$= \int_0^1 x \left[\begin{array}{l} y.\ln\left[\sqrt{(1-x)^2+y^2} - (1-x)/\sqrt{2}\right] - y - \dfrac{1-x}{\sqrt{2}} \ln\left[\sqrt{(1-x)^2+y^2} + y\right] \\ + \dfrac{1-x}{\sqrt{2}}\left(\tan^{-1}\left[\dfrac{y}{\sqrt{(1-x)^2+y^2}}\right] + \tan^{-1}\left[\dfrac{y\sqrt{2}}{(1-x)}\right]\right) \end{array} \right]_0^{1-x} dx$$

$$= \int_0^1 x \left[\begin{array}{l} (1-x).\ln\left[(1-x)/\sqrt{2}\right] - (1-x) - \dfrac{(1-x)}{\sqrt{2}} \ln\left[\left(\sqrt{2}+1\right)(1-x)\right] \\ + \dfrac{(1-x)}{\sqrt{2}} \ln\left[1-x\right] + \dfrac{(1-x)}{\sqrt{2}}\left(\tan^{-1}\left[\dfrac{1}{\sqrt{2}}\right] + \tan^{-1}\left[\sqrt{2}\right]\right) \end{array} \right] dx$$

$$= \int_0^1 x(1-x) \left[.\ln\left[(1-x)/\sqrt{2}\right] + \left(\frac{\pi}{2\sqrt{2}} - 1 - \frac{\ln\left[\sqrt{2}+1\right]}{\sqrt{2}} \right) \right] dx$$

$$= \int_0^1 x(1-x) \left[.\ln\left[1-x\right] + \underbrace{\left(\frac{\pi}{2\sqrt{2}} - 1 - \frac{\ln\left[\sqrt{2}+1\right]}{\sqrt{2}} - \ln\left[\sqrt{2}\right] \right)}_{C} \right] dx$$

$$= \left[\frac{-x^3}{9}(3C-1) - \frac{x^2}{12}(1-6C) - \frac{x}{6} - \frac{(2x^3-3x^2+1)}{6}\ln(1-x) \right]_0^1$$

$$= \frac{-11-3\sqrt{2}\ln(\sqrt{2}+1) - 3\ln 2 + 3\sqrt{2}\,\pi/2}{36} = -0{,}199452599692466$$

If $\bar{w} = \bar{n} \times \bar{f}$:

$$I^{-}_{2,n\times f} = \frac{1}{\sqrt{2}} \int_0^1 \int_0^{1-x} (x^2 + y^2 - y).\ln\left[\sqrt{(1-x)^2 + y^2} - (1-x)/\sqrt{2}\right] dy dx$$
$$= I^{-}_{2,n\times f}(x^2) + I^{-}_{2,n\times f}(y^2) - I^{-}_{2,n\times f}(y)$$

$$I^{-}_{2,n\times f}(x^2) = \frac{1}{\sqrt{2}} \int_0^1 \int_0^{1-x} x^2.\ln\left[\sqrt{(1-x)^2 + y^2} - (1-x)/\sqrt{2}\right] dy dx$$
$$= \frac{1}{\sqrt{2}} \int_0^1 x^2 \left[\begin{array}{l} y.\ln\left[\sqrt{(1-x)^2 + y^2} - (1-x)/\sqrt{2}\right] - y - \frac{1-x}{\sqrt{2}} \ln\left[\sqrt{(1-x)^2 + y^2} + y\right] \\ + \frac{1-x}{\sqrt{2}} \left(\tan^{-1}\left[\frac{y}{\sqrt{(1-x)^2 + y^2}}\right] + \tan^{-1}\left[\frac{y\sqrt{2}}{(1-x)}\right] \right) \end{array} \right]_0^{1-x} dx$$
$$= \frac{1}{\sqrt{2}} \int_0^1 x^2 \left[\begin{array}{l} (1-x).\ln\left[(1-x)/\sqrt{2}\right] - (1-x) - \frac{(1-x)}{\sqrt{2}} \ln\left[\left(\sqrt{2}+1\right)(1-x)\right] \\ + \frac{(1-x)}{\sqrt{2}} \ln\left[1-x\right] + \frac{(1-x)}{\sqrt{2}} \left(\tan^{-1}\left[\frac{1}{\sqrt{2}}\right] + \tan^{-1}\left[\sqrt{2}\right] \right) \end{array} \right] dx$$
$$= \frac{1}{\sqrt{2}} \int_0^1 x^2 (1-x) \left[.\ln\left[(1-x)/\sqrt{2}\right] + \left(\frac{\pi}{2\sqrt{2}} - 1 - \frac{\ln\left[\sqrt{2}+1\right]}{\sqrt{2}} \right) \right] dx$$
$$= \int_0^1 x^2 (1-x) \left[.\ln\left[1-x\right] + \underbrace{\left(\frac{\pi}{2\sqrt{2}} - 1 - \frac{\ln\left[\sqrt{2}+1\right]}{\sqrt{2}} - \ln\left[\sqrt{2}\right] \right)}_{C} \right] dx$$
$$= \frac{1}{\sqrt{2}} \left[\frac{x^4}{16}(1-4C) - \frac{x^3}{36}(1-12C) - \frac{x^2}{24} - \frac{x}{12} - \frac{(3x^4 - 4x^3 + 1)}{12} \ln(1-x) \right]_0^1$$
$$= \frac{1}{\sqrt{2}} \frac{-25 - 6\sqrt{2}\ln(\sqrt{2}+1) - 6\ln 2 + 3\sqrt{2}\pi}{144}$$

$$I^{-}_{2,n\times f}(y^2)=\frac{1}{\sqrt{2}}\int_0^1\int_0^{1-x} y^2.\ln\left[\sqrt{(1-x)^2+y^2}-(1-x)/\sqrt{2}\right]dydx$$

$$=\frac{1}{36\sqrt{2}}\int_0^1\left[\begin{array}{l}12y^3\ln\left[\sqrt{(1-x)^2+y^2}-(1-x)/\sqrt{2}\right]-3\sqrt{2}\,y(1-x)\sqrt{(1-x)^2+y^2}\\+6\sqrt{2}(1-x)^3\ln\left[\sqrt{(1-x)^2+y^2}+y\right]-4y^3+6(1-x)^2y\\-3\sqrt{2}(1-x)^3\left(\tan^{-1}\left[\frac{y}{\sqrt{(1-x)^2+y^2}}\right]+\tan^{-1}\left[\frac{y\sqrt{2}}{(1-x)}\right]\right)\end{array}\right]_0^{1-x}dx$$

$$=\frac{1}{36\sqrt{2}}\int_0^1(1-x)^3\left[12\ln[1-x]+\underbrace{\left(-4+6\sqrt{2}\ln\left[\sqrt{2}+1\right]-6\ln 2-3\sqrt{2}\,\frac{\pi}{2}\right)}_{C}\right]dx$$

$$=-\frac{1}{\sqrt{2}}\frac{1}{144}\left[(1-x)^4(C+12\ln(1-x)-3)\right]_0^1$$

$$=\frac{1}{\sqrt{2}}\frac{-7+6\sqrt{2}\ln(\sqrt{2}+1)-6\ln 2-3\sqrt{2}\,\pi/2}{144}$$

$$I^{-}_{2,n\times f}(y)=\frac{1}{\sqrt{2}}\int_0^1\int_0^{1-x} y.\ln\left[\sqrt{(1-x)^2+y^2}-(1-x)/\sqrt{2}\right]dydx$$

$$=\frac{1}{\sqrt{2}}\int_0^1\frac{1}{4}\left[\begin{array}{l}-y^2-(1+\ln 2)(1-x)^2-\sqrt{2}(1-x)\sqrt{(1-x)^2+y^2}\\+((1-x)^2+2y^2)\ln\left[\sqrt{(1-x)^2+y^2}-(1-x)/\sqrt{2}\right]\end{array}\right]_0^{1-x}dx$$

$$=\frac{1}{\sqrt{2}}\int_0^1\frac{(1-x)^2}{4}\left[2\ln[1-x]+\underbrace{\left(-3+\sqrt{2}-\ln\left[\sqrt{2}-1\right]-\ln 2\right)}_{C}\right]dx$$

$$=-\frac{1}{\sqrt{2}}\frac{1}{36}\left[(1-x)^3(3C+6\ln(1-x)-2)\right]_0^1$$

$$=\frac{1}{\sqrt{2}}\frac{-44+12\sqrt{2}-12\ln(\sqrt{2}-1)-12\ln 2}{144}$$

Finally :

$$I^{-}_{2,n\times f}=I^{-}_{2,n\times f}(x^2)+I^{-}_{2,n\times f}(y^2)-I^{-}_{2,n\times f}(y)$$

$$=\frac{1}{12\sqrt{2}}(1+\ln(\sqrt{2}-1)-\sqrt{2}+\sqrt{2}\,\pi/8)=-0,043618281..$$

Appendix H

This Appendix gives every detail of the analytical solution summarized and analyzed in §5.5.3

$$I^{+}_{1,n\times f} =$$

$$\int_0^T \int_0^{S(1-y/T)} \left(x^2+y^2-yT\right) \ln\left[S-x+\sqrt{(S-x)^2+y^2}\right] dx dy =$$

$$\int_0^T \frac{1}{18} \left\{ \begin{array}{l} (11S^2+5xS+2x^2+14y^2-18yT)\sqrt{(S-x)^2+y^2} + \\ (6x^3+18xy^2-9y^2S-18xyT+18yST-6T^3) \ln\left[S-x+\sqrt{(S-x)^2+y^2}\right] \end{array} \right\}_0^{S(1-y/T)} dy =$$

$$\frac{1}{18} \left\{ \begin{array}{l} \frac{S}{8T^3} \left(\begin{array}{l} 36S^2T^4+36y^2T^4-72ST^4\sqrt{S^2+y^2}-32y^3T^3-48yS^2T^3 \\ +24yT^3(2S^2+y^2-3yT)\ln\left[S+\sqrt{S^2+y^2}\right] \\ +12yST^3\sqrt{S^2+y^2}+36S^3T^3\ln\left[y+\sqrt{S^2+y^2}\right]+9y^4T^2+36y^2S^2T^2-16y^3S^2T+3y^4S^2 \\ -12y^2\left((y^2-4yT+6T^2)S^2+3y(y-2T)T^2\right)\ln\left[y\left(S/T+\sqrt{(S/T)^2+1}\right)\right] \end{array} \right) \\ + \\ \left(\begin{array}{l} -\frac{15S^4}{4}\ln\left[y+\sqrt{S^2+y^2}\right]+9y^2S^2\sqrt{(S/T)^2+1}+y^4\frac{(S^2+7T^2)}{2T^2}\sqrt{(S/T)^2+1} \\ -3y^3\frac{(S^2+2T^2)}{T}\sqrt{(S/T)^2+1}-\left(\frac{7}{2}y^3-6y^2T+\frac{29}{4}yS^2-6S^2T\right)\sqrt{S^2+y^2} \end{array} \right) \end{array} \right\}_0^T =$$

$$\frac{ST}{144}\left[12(S^2-T^2)\ln\left[S+\sqrt{S^2+T^2}\right]+6\frac{S^3}{T}\ln\left[T/S+\sqrt{(T/S)^2+1}\right]-18S\sqrt{S^2+T^2}-S^2+13T^2\right]$$

$$I^{-}_{2,n\times f} =$$

$$\int_0^S \int_0^{T(1-x/S)} \left(x^2+y^2-yT\right) \ln\left[\sqrt{(S-x)^2+y^2}-\frac{S(S-x)}{\sqrt{S^2+Z^2}}\right] dy dx$$

$$= \int_0^S x^2 \int_0^{T(1-x/S)} \ln\left[\sqrt{(S-x)^2+y^2}-\frac{S(S-x)}{\sqrt{S^2+Z^2}}\right] dy dx$$

$$+\int_0^S \int_0^{T(1-x/S)} y^2 \ln\left[\sqrt{(S-x)^2+y^2}-\frac{S(S-x)}{\sqrt{S^2+Z^2}}\right] dy dx$$

$$-\int_0^S \int_0^{T(1-x/S)} yT \ln\left[\sqrt{(S-x)^2+y^2}-\frac{S(S-x)}{\sqrt{S^2+Z^2}}\right] dy dx$$

$$(1)=\int_0^S \frac{x^2}{\sqrt{S^2+Z^2}}\left\langle \begin{array}{l} y\sqrt{S^2+Z^2}\left\{\ln\left[\sqrt{(S-x)^2+y^2}-\dfrac{S(S-x)}{\sqrt{S^2+Z^2}}\right]-1\right\} \\ +(S-x)\left\{Z\left(\tan^{-1}\left[\dfrac{y\sqrt{S^2+Z^2}}{Z(S-x)}\right]+\tan^{-1}\left[\dfrac{yS}{Z\sqrt{(S-x)^2+y^2}}\right]\right)\right\} \\ +S\ln\left[\sqrt{(S-x)^2+y^2}+y\right] \end{array}\right\rangle_0^{T(1-x/S)}$$

$$=\frac{T}{S}\int_0^S x^2(S-x)\left\{\ln(S-x)+C_{x^2}\right\}$$

$$=\frac{T}{S}\left\langle -\frac{S^4}{12}\ln(S-x)-\frac{xS^3}{12}-\frac{x^2S^2}{24}+\frac{x^3S}{36}(12C_{x^2}-1)+\frac{x^4}{16}(1-4C_{x^2})-\frac{x^3}{12}(3x-4S)\ln(S-x)\right\rangle_0^S$$

$$=\frac{S^3T}{144}\left[12\ln S-13+12C_{x^2}\right]$$

$C_{x^2}=$

$$\ln\left[\sqrt{1+(T/S)^2}-\frac{1}{\sqrt{1+(Z/S)^2}}\right]+\frac{S/T}{\sqrt{1+(S/Z)^2}}\left(\tan^{-1}\left[T/S\sqrt{1+(S/Z)^2}\right]+\tan^{-1}\left[\frac{T/Z}{\sqrt{1+(T/S)^2}}\right]\right)$$

$$-\frac{S/T}{\sqrt{1+(Z/S)^2}}\ln\left[T/S+\sqrt{1+(T/S)^2}\right]-1$$

$$(2)=\int_0^S \frac{dx}{18}\left\langle \begin{array}{l} \dfrac{-6(S-x)^3Z^3}{(S^2+Z^2)^{3/2}}\left(\tan^{-1}\left[\dfrac{y\sqrt{S^2+Z^2}}{Z(S-x)}\right]+\tan^{-1}\left[\dfrac{yS}{Z\sqrt{(S-x)^2+y^2}}\right]\right) \\ +\dfrac{3S(S^2+3Z^2)(S-x)^3}{(S^2+Z^2)^{3/2}}\ln\left[\sqrt{(S-x)^2+y^2}+y\right]-2y^3 \\ +6y^3\ln\left[\sqrt{(S-x)^2+y^2}-\dfrac{S(S-x)}{\sqrt{S^2+Z^2}}\right]-\dfrac{3S(S-x)y\sqrt{(S-x)^2+y^2}}{\sqrt{S^2+Z^2}}+\dfrac{6(S-x)^2yZ^2}{S^2+Z^2} \end{array}\right\rangle_0^{T(1-x/S)}$$

$$=\frac{1}{36}\left(\frac{T}{S}\right)^3\int_0^S(S-x)^3\left\{12\ln(S-x)+C_{y^2}\right\}$$

$$=\frac{1}{36}\left(\frac{T}{S}\right)^3\left\langle -\frac{1}{4}(S-x)^4\left(12\ln(S-x)+C_{y^2}-3\right)\right\rangle_0^S$$

$$=\frac{ST^3}{144}\left[12\ln S+C_{y^2}-3\right]$$

$C_{y^2}=$

$$\frac{12(S/T)^2}{1+(S/Z)^2}-\frac{6(S/T)\sqrt{1+(S/T)^2}}{\sqrt{1+(Z/S)^2}}-\frac{12(S/T)^3}{\left[1+(S/Z)^2\right]^{3/2}}\left(\tan^{-1}\left[T/S\sqrt{1+(S/Z)^2}\right]+\tan^{-1}\left[\frac{T/Z}{\sqrt{1+(T/S)^2}}\right]\right)$$

$$+12\ln\left[\sqrt{1+(T/S)^2}-\frac{1}{\sqrt{1+(Z/S)^2}}\right]+\frac{6(S/T)^3\left[1+3(Z/S)^2\right]}{\left[1+(Z/S)^2\right]^{3/2}}\ln\left[T/S+\sqrt{1+(T/S)^2}\right]-4$$

$$(3) = -\frac{T}{4}\int_0^S \left\langle \begin{array}{l} 2\left[(S-x)^2+y^2\right]\ln\left[\sqrt{(S-x)^2+y^2}-\dfrac{S(S-x)}{\sqrt{S^2+Z^2}}\right]-\dfrac{2S(S-x)\sqrt{(S-x)^2+y^2}}{\sqrt{S^2+Z^2}} \\ +\dfrac{2S^2(S-x)^2\sqrt{(S-x)^2+y^2}}{S^2+Z^2}\arg th\left[\dfrac{\sqrt{S^2+Z^2}\sqrt{(S-x)^2+y^2}}{S(S-x)}\right] \\ -\dfrac{S^2(S-x)^2}{S^2+Z^2}\ln\left[S^2(y^2+Z^2)+(x^2+y^2)Z^2-2SZ^2x\right]-(S-x)^2-y^2 \end{array} \right\rangle_0^{T(1-x/S)}$$

$$= \frac{T}{4}\left(\frac{T}{S}\right)^2\int_0^S (S-x)^2\left\{-2\ln(S-x)+C_{yT}\right\}dx$$

$$= \frac{T}{4}\left(\frac{T}{S}\right)^2\left\langle -\frac{1}{9}(S-x)^3(3C_{yT}-6\ln(S-x)+2)\right\rangle_0^S$$

$$= \frac{T}{4}\left(\frac{T}{S}\right)^2\frac{1}{9}S^3(3C_{yT}-6\ln S+2)$$

$$= \frac{ST^3}{144}(12C_{yT}-24\ln S+8)$$

$C_{yT} =$

$$\frac{(S/T)^2}{1+(Z/S)^2}\left\{\ln\left[1+\left(\frac{T}{Z}\right)^2+\left(\frac{T}{S}\right)^2\right]-\ln\left[\frac{\sqrt{1+(T/S)^2}\sqrt{1+(Z/S)^2}+1}{\sqrt{1+(T/S)^2}\sqrt{1+(Z/S)^2}-1}\bullet\frac{\sqrt{1+(Z/S)^2}-1}{\sqrt{1+(Z/S)^2}+1}\right]\right\}$$

$$+2\left(\frac{S}{T}\right)^2\ln\left[1-\frac{1}{\sqrt{1+(Z/S)^2}}\right]-2\left[1+\left(\frac{S}{T}\right)^2\right]\ln\left[\sqrt{1+(T/S)^2}-\frac{1}{\sqrt{1+(Z/S)^2}}\right]$$

$$+2\left(\frac{S}{T}\right)^2\frac{\sqrt{1+(T/S)^2}-1}{\sqrt{1+(Z/S)^2}}+1$$